Rice University

Spectroscopy of ^{87}Sr Rydberg Atoms and Molecules

by

Roger Ding

A Thesis Submitted
in Partial Fulfillment of the
Requirements for the Degree

Doctor of Philosophy

Approved, Thesis Committee:

F. Barry Dunning, *Adviser*
Sam and Helen Worden Professor of Physics and Astronomy

Thomas C. Killian, *Co-Adviser*
Professor of Physics and Astronomy

Han Pu
Professor of Physics and Astronomy

Houston, Texas
August 2019

Rice University

Spectroscopy of ^{87}Sr Rydberg Atoms and Molecules

by

Roger Ding

A Thesis Submitted
in Partial Fulfillment of the
Requirements for the Degree

Doctor of Philosophy

Approved, Thesis Committee:

F. Barry Dunning, *Adviser*
Sam and Helen Worden Professor of Physics and Astronomy

Thomas C. Killian, *Co-Adviser*
Professor of Physics and Astronomy

Han Pu
Professor of Physics and Astronomy

Houston, Texas
August 2019

Abstract

Spectroscopy of ^{87}Sr Rydberg Atoms and Molecules

by

Roger Ding

This dissertation describes the development of an apparatus to undertake spectroscopic studies of ^{87}Sr Rydberg states and their application in the production of ultra-long-range Rydberg molecules (ULRRMs). Most previous spectroscopic studies of strontium have been performed with the bosonic isotope ^{88}Sr which has no nuclear spin ($I = 0$), resulting in a relatively simple and well-understood Rydberg excitation spectrum. In contrast, fermionic ^{87}Sr has a large nuclear spin ($I = 9/2$) that leads to strong hyperfine interactions which greatly complicate the Rydberg excitation spectrum. In order to understand the Rydberg states in ^{87}Sr, two-photon spectroscopy was performed to measure and identify the $(5sns)\,^3S$ and $(5snd)\,^3D$ hyperfine Rydberg states for $30 \lesssim n \lesssim 99$. Working with theory collaborators, a detailed understanding of how the hyperfine interaction affects the Rydberg levels is developed and used to extract revised quantum defects.

The detailed understanding of the ^{87}Sr hyperfine Rydberg structure was then utilized to produce the first ULRRMs in a fermionic gas. Unlike traditional molecular binding mechanisms, ULRRMs comprised of one or more ground-state atoms embedded in the electron cloud of a Rydberg atom with the entire system bound together through the weak Rydberg electron-neutral atom scattering. Therefore, production of ULRRMs is dependent on both the principal quantum number (n) of the parent Rydberg atom and the initial spatial distribution of atoms. At low temperatures, the effects of quantum statistics becomes important and result in bunching (bosons) and antibunching (fermions). These differences in spatial distributions can influence the excitation rates of ULRRMs. Current progress in exploring the role of quantum statistics in the excitation of ULRRMs using cold, dense strontium gases is described, with an emphasis on ^{87}Sr, and how such measurements can

be used to extract the pair correlation function $g^{(2)}(R)$.

Acknowledgments

Acknowledgments go here.

Person 1 Person 1 description.

Person 2 Person 2 description.

Person 3 Person 3 description.

Person 4 Person 4 description.

Table of Contents

1. Introduction

Advances in laser cooling have paved the way towards the creation of cold, ultracold, and quantum degenerate gases of atoms, which are ideal for studying quantum systems with unprecedented levels of control. Compared to many other systems where the challenge is separating the influences of a particular interaction from a myriad of other effects, ultracold quantum gas systems follow a "bottom-up" approach where interactions are carefully (and often painstakingly) introduced. So far, from the observation of the BEC-BCS crossover [1–3] to the superfluid-Mott insulator transition in an optical lattice [4] to the formation of matter-wave solitons [5, 6], most of these effects arise from an isotropic, two-body short-range contact interaction that can be described by the pseudopotential

$$\hat{V}(\mathbf{r})\,\psi(\mathbf{r}) \;=\; \left[g\delta(\mathbf{r})\,\frac{\partial}{\partial r}r\right]\psi(\mathbf{r}) \tag{1.1}$$

where $\mathbf{r}$ is the relative distance between two colliding particles, g is the interaction strength[1], and $\delta(\mathbf{r})$ is the Dirac delta function [7, 8]. Due to the $\delta(\mathbf{r})$ term, this requires the particle wave functions to overlap for interactions to occur.

An recent trend in the field of ultracold gases has been the introduction of long-range interactions into systems that have been generally well-described by Eq. (1.1). These long-range interactions can typically be expanded as

$$\hat{V}(\mathbf{r})\,\psi(\mathbf{r}) \;=\; \left[\sum_k \frac{C_k(\mathbf{r})}{|\mathbf{r}|^{\,k}}\right]\psi(\mathbf{r}) \tag{1.2}$$

with interaction strength $C_k(\mathbf{r})$ and the "long-range" coming from the $\hat{V} \sim 1/|\mathbf{r}|^{\,k}$ dependence [7]. Some common interactions are $k = 1$ for Coulomb, $k = 3$ for dipole-dipole, and $k = 6$ for van der Waals. These can also have an angular dependence as well, which leads

[1] The effective interaction for two particles of equal mass is $g = 4\pi\hbar^2 a_s/m$ with a_s is the s-wave scattering length [7].

to isotropic and anisotropic interactions that adds additional "richness" to the system. The provides the opportunity to study a wide variety of phenomena including those with applications towards quantum computing [9, 10], quantum simulation [11, 12], and tests of theory. There are several methods for incorporating long-range interactions into ultracold systems, each of which has trade-offs between production, manipulation, and duration (i.e., how difficult is it to get cold enough to study the interactions of interest, how controllable are the samples and the interactions, and and how long can the effect be studied). Some of the most prominent methods are (e.g., see [13]):

Polar molecules

Typically heteronuclear, these molecules can have both large (permanent) electric dipole moments [14] and, ignoring chemical reactions, extremely long lifetimes. The major disadvantage is that their additional complexity generally makes it very difficult to produce ultracold and quantum degenerate samples and control their interactions. In spite of these challenges, a degenerate Fermi gas of ^{40}K^{87}Rb was recently achieved by combining atoms from a BEC of ^{87}Rb and a degenerate Fermi gas of ^{40}K [15]. Additionally, steady progress continues to be made towards direct laser cooling of molecules [16–18].

Magnetic atoms

Atoms themselves can have permanent dipole moments that can be exploited to study long-range interactions with quantum degeneracy having been achieved in chromium [19, 20], erbium [21, 22], and dysprosium [23, 24]. Although simpler than molecules and have (essentially) infinite lifetimes, their dipolar interactions are limited by the magnetic moment of the atoms and typically requires tuning of the short-range interaction strength to be weaker than the dipole-dipole interaction in order to observe their effects. There is also a recent proposal for creating ultracold dysprosium atoms which exhibits both an electric and a magnetic dipole moment [25].

Coupling atoms to a high-finesse cavity

An ingenious way of inducing long-range interactions in atomic systems is by placing the atoms in a high-finesse optical cavity such that they couple to the cavity mode, which in turn causes the atoms to experience position-dependent forces [26, 27]. Although the interactions are (essentially) infinite-range, they are likely restricted to only that case. They are also constrained by the geometry of the experiment which could make it difficult to tune between isotropic and anisotropic interactions.

Rydberg states

Highly excited Rydberg states of atoms (and molecules) with principal quantum numbers $n \gg 1$ can also exhibit strong dipole-dipole interactions [28]. (Rydberg states have also been observed in solid state systems [29], opening another avenue for studying long-range interactions.) Since many of the properties of Rydberg atoms scale with n, their interactions can be tuned in strength and anisotropy simply by exciting to different states. Rydberg atoms can also leverage well-established techniques for producing quantum degenerate gases of atoms so that their interactions can be readily incorporated into existing experimental setups. The major disadvantage of Rydberg systems is their sensitivity to stray electric fields and their limited lifetime due to spontaneous decay and to both blackbody and Rydberg-Rydberg interactions.

This thesis will be focused on the latter by studying Rydberg systems in ultracold strontium gases. Most ultracold Rydberg experiments have predominantly focused on the alkali metal atoms rubidium, cesium, and potassium. With their hydrogen-like electronic structure, there are well-established methods for both calculating their properties (e.g., see [30]) and techniques for producing ultracold and quantum degenerate gases, making them a staple of ultracold gas experiments. But since Rydberg interactions are long-ranged, generally comparable to the interparticle separation in the gas, the particular atomic species used should only affect the details of the interactions but not their overall form. As will be discussed below, strontium has some properties that make it a very attractive system for studying Rydberg physics.

1.1 Rydberg Atoms

A Rydberg atom can be loosely defined as an atom in an excited state with very large principal quantum number n such that $n \gg 1$. Starting in the late 1800's, it was observed that the wavenumbers of atomic levels ($\nu_{n,l}$) could be described by the formula

$$\nu_{n,j,l} = \nu_{\infty,j,l} - \frac{R}{(n - \delta_{n,j,l})^2} = \nu_{\infty,j,l} - \frac{R}{n^{*2}} \tag{1.3}$$

where $\nu_{\infty,j,l}$ is the series limit, $\delta_{n,j,l}$ is the "quantum defect", and R is the Rydberg constant [28, 31, 32]. (The subscripts in Eq. (1.3) indicate a common dependency of the values on n, j, and l.) Oftentimes, the principal quantum number and quantum defect are combined into an "effective quantum number" $n^* = n - \delta_{n,j,l}$. This is the Rydberg formula. Conceptually, a Rydberg atom can be thought of as being comprised of a core ion and a highly-excited valence electron that spends the majority of its time far away from the core. As a result, the Rydberg electron has only a small probability of being found near the core, which allows its effects to be characterized by a (nearly) constant parameter $\delta_{n,j,l}$ due to it primarily experiencing the long-range Coulomb interaction of the core ion. While the details of the core ion and electrons are important, causing $\delta_{n,j,l}$ to vary from atom-to-atom and from orbital-to-orbital, interactions with the core generally do not have a large effect on the overall properties of the Rydberg atoms.

While the effects due to the core are usually small, the principal quantum number does greatly affect the atomic wave function. As a result, n sets the energy scale for many interactions and leads to the properties of Rydberg atoms becoming exaggerated when n becomes large. Table 1.1 gives the n dependence for a few properties of Rydberg atoms.

1.1.1 Ultra-Long-Range Rydberg Molecules (ULRRMs)

One key aspect to focus on from Tab. 1.1 is that the size of a Rydberg atom increases very rapidly with n^*. In a dense enough gas, the $\langle r \rangle \sim (n^*)^2$ scaling means the Rydberg orbital radius can quickly become comparable to or larger than the interparticle separations.

Table 1.1: Some properties of rubidium and strontium Rydberg atoms [28, 33, 34]. Unless otherwise noted, the rubidium and strontium values in the table are calculated from the ionization energies, Rydberg constants, and quantum defects presented in [35] and [36], respectively.

Property	n^* scaling	Rb: $(38s)\,^2S$	Sr: $(5s38s)\,^3S_1$
Binding energy (E_{n^*})	$(n^*)^{-2}$	11.19 meV	11.35 meV
Coulomb splitting ($E_{n^*} - E_{(n+1)^*}$)	$(n^*)^{-3}$	148.77 GHz	151.84 GHz
Orbital radius ($\langle r \rangle$)	$(n^*)^{2}$	1823.74 a_0	1798.74 a_0
Lifetime (τ)	$(n^*)^{3}$	28.6(11) µs [37]	21(1) µs [38]

It was in this context, when an atom (or multiple atoms) could be located inside the Rydberg electron's orbit, that a density-dependent shift was first observed in the spectral lines of alkali atoms with the direction of the shift, relative to the unperturbed atomic line, also dependent on the buffer gas used [39–42]. Figure 1.1 shows $\langle r \rangle$ and $1/\langle r \rangle^3$ for a

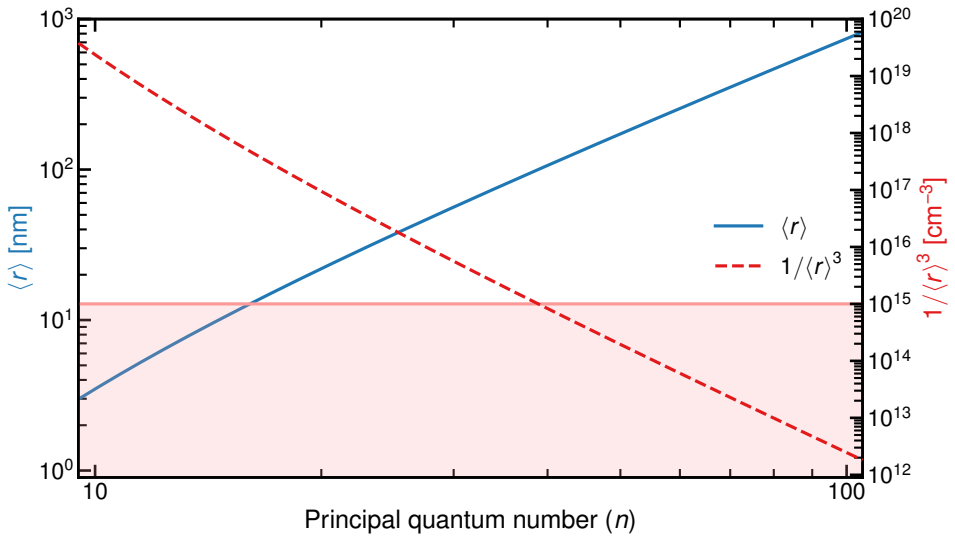

Figure 1.1: Orbital radius $\langle r \rangle$ for a strontium Rydberg atom in the $(5sns)\,^3S_1$ state and the corresponding density $1/\langle r \rangle^3$. The shaded region represents the range of densities typically achievable in ultracold strontium gas experiments with a maximum of about $1 \times 10^{15}\,\mathrm{cm}^{-3}$ occurring in a ^{88}Sr BEC [43, 44].

strontium atom in the $(5sns)\,^3S_1$ state and the typical densities achievable in ultracold gas experiments. Notice that, even for modest principal quantum numbers and densities, it's easily possible to excite Rydberg atoms much larger than the interparticle separations.

This shift was first explained by Fermi [45], and later generalized by Omont [46], to be the result of low-energy scattering of the Rydberg electron off nearby neutral atoms, describing the electron-atom interaction with the pseudopotential

$$\hat{V}(\mathbf{R}) = \sum_i \frac{2\pi\hbar^2 A_s[k(\mathbf{R})]}{m_e}\delta(\mathbf{r}_i - \mathbf{R}) + \frac{6\pi\hbar^2 A_p^3[k(\mathbf{R})]}{m_e}\overleftarrow{\boldsymbol{\nabla}}\delta(\mathbf{r}_i - \mathbf{R})\overrightarrow{\boldsymbol{\nabla}} \tag{1.4}$$

where $\mathbf{r}_i$ is the position of the Rydberg valence electron(s) and $\mathbf{R}$ is the position of the ground-state atom relative to the Rydberg core [41, 42, 47]. On the right hand side, the first term is the s-wave contribution and the second term is the p-wave contribution with momentum-dependent scattering lengths $A_s(k)$ and $A_p(k)$, respectively. The semiclassical Rydberg electron momentum is given by $\hbar k(\mathbf{r}) = \sqrt{2m_e[e^2/(4\pi\epsilon_0\mathbf{r}) - E_b]}$ for an unperturbed Rydberg electron with binding energy E_b [47]. Evaluating the interaction with the Rydberg electron wave function $|\Psi_{nl}\rangle$ leads to an effective molecular potential

$$\langle\hat{V}(\mathbf{R})\rangle \simeq \sum_i \frac{2\pi\hbar^2 A_s(k)}{m_e}|\Psi_{nl}(\mathbf{r}_i = \mathbf{R})|^2 + \frac{6\pi\hbar^2 A_p^2(k)}{m_e}|\boldsymbol{\nabla}\Psi_{nl}(\mathbf{r}_i = \mathbf{R})|^2 \tag{1.5}$$

experienced by a ground-state atom [47]. A very nice derivation of the interaction is presented in [48][2] along with review articles [42, 50, 51].

We are particularly interested in the case when, in the low-energy scattering regime, $A_s < 0$ because the interaction is attractive and can lead to the formation of bound states involving nearby ground state atoms located in the Rydberg electron wave function. These objects are known as "ultra-long-range Rydberg molecules"[3] (ULRRMs) and were theoretically predicted by Greene et al., [52] in 2000. Instead of the more conventional binding mechanisms (e.g., ionic or covalent), the ground state atoms are bound to the Rydberg atom by low-energy Rydberg electron-neutral atom scattering. The first experimental detection of ULRRMs occurred in ^{87}Rb [53] with subsequent observations in Cs [54] and Sr [47]. Figure 1.2 provides an illustrative example of a molecular potential together with the resulting radial molecular vibrational wave functions and a typical Rydberg excitation spectrum seen experimentally. Starting from the atomic line and tuning the laser below

[2] She references [49] which has more details of Fermi's approach.

[3] Other objects can also be called "Rydberg molecules" (e.g., a molecule electronically excited to a high principal quantum number) but for the purposes of this thesis, a Rydberg molecule refers to the binding of neutral atoms to a Rydberg atom due to Rydberg electron-neutral atom scattering.

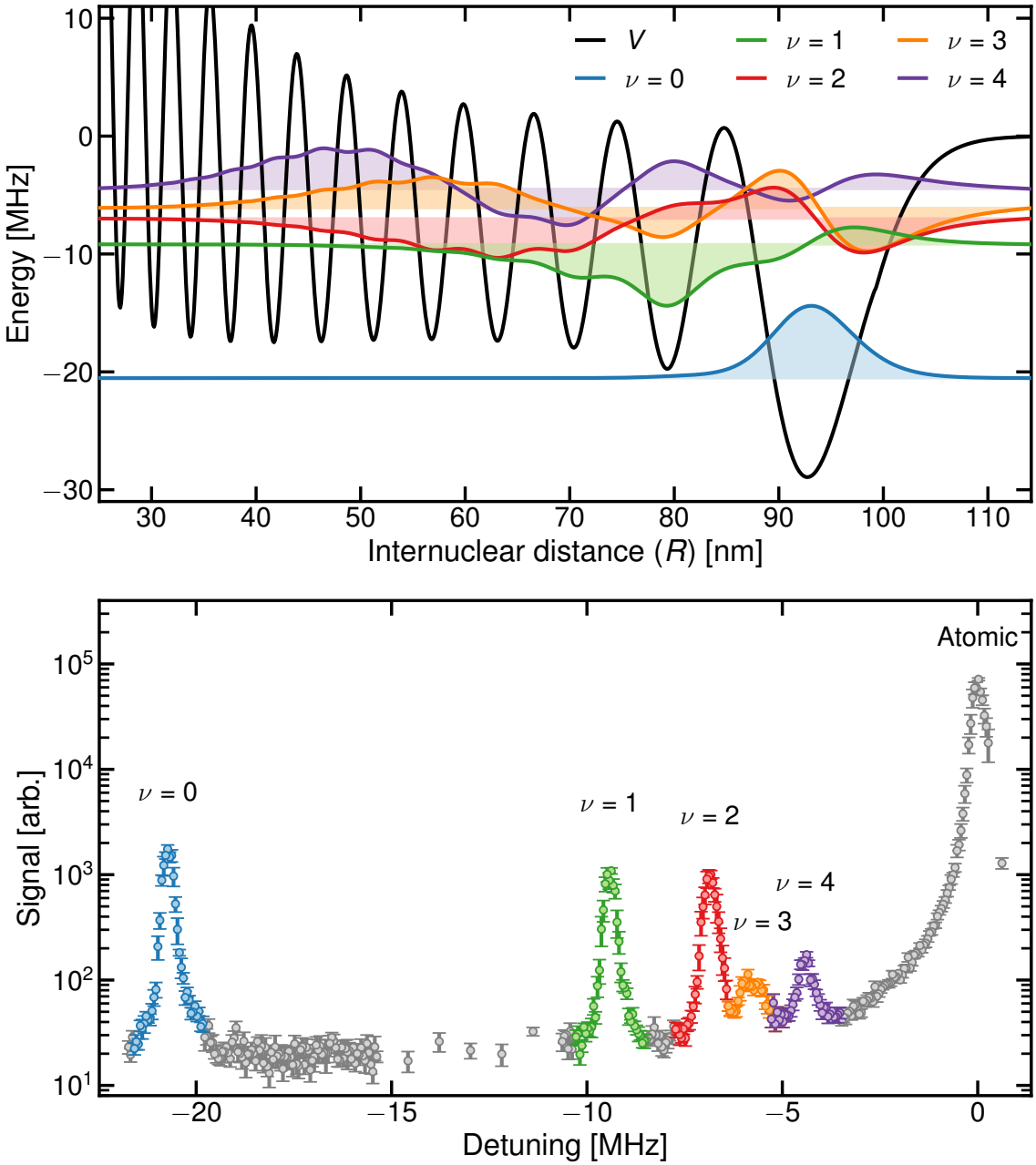

Figure 1.2: (Top) Calculated molecular potential $\langle \hat{V}(R) \rangle$ for a $(5s34s)\,^3S_1 + (5s^2)\,^1S_0$ atom pair together with the radial wave functions for the $\nu = 0$, 1, 2, 3, and 4 vibrational states. (Bottom) Rydberg excitation signal for an unpolarized gas of ^{87}Sr with the various dimer vibrational states as indicated.

resonance, additional peaks appear which correspond to the various radial vibrational states (labeled by ν) of the ULRRM. Note that the binding energies of ULRRMs are typically a few to a few-tens of megahertz and scale as $E_b \sim 1/(n^*)^6$[4], meaning that ULRRMs can only be created in ultracold, dense samples.

Although Fig. 1.2 only shows "dimer" data with one Rydberg atom in the $(5s34s)\,^3S_1$ state bound to a single nearby $(5s^2)\,^1S_0$ atom, this effect is generalizable to multiple bodies bound to the Rydberg atom. A "trimer" is a Rydberg atom containing two bound ground-state atoms, a "tetramer" is a Rydberg atom with three embedded ground-state atoms, and so on (e.g., see [55]). Once a macroscopic occupation of the bound molecular states occurs, it makes more sense to describe the system in the quasiparticle picture with the Rydberg atom and the bound ground-state atoms forming a "polaron" [56, 57].

1.2 Strontium Rydberg Atoms

Strontium offers several benefits over the alkali atoms with perhaps the most obvious, as seen in Fig. 1.3, being the existence of singlet and triplet Rydberg series due to the presence of two valence electrons. Starting from the $(5s^2)\,^1S_0$ ground state, two-photon excitation can be used to access the myriad of ^1S, ^3S, ^1D, and ^3D Rydberg levels. In addition to the anisotropies associated with a particular Rydberg orbital, the C_6 coefficients have been calculated for these states and exhibit both attractive ($C_6 < 0$) and repulsive ($C_6 > 0$) interactions [59]. The second valence electron also introduces additional complexity due to there being multiple Rydberg series which can interact and perturb one another. The treatment of such perturbations typically requires multichannel quantum defect theory (MQDT) [28, 60, 61] and/or a two-active-electron (TAE) model [62]. There also exists the opportunity to produce doubly-excited and autoionizing states [28] which, besides being

[4]Since $\langle \hat{V}(\mathbf{R}) \rangle \propto |\Psi_{nl}(\mathbf{R})|^2$, the $1/(n^*)^6$ scaling can be understood as the electron probability being "spread out" over a volume which scale as $V \sim \langle r \rangle^3 \sim (n^*)^6$.

[5]Based on the energy level diagrams presented in [58] and by the Weidemüller strontium Rydberg experiment at University of Science and Technology of China (USTC) Shanghai Institute for Advanced Studies.

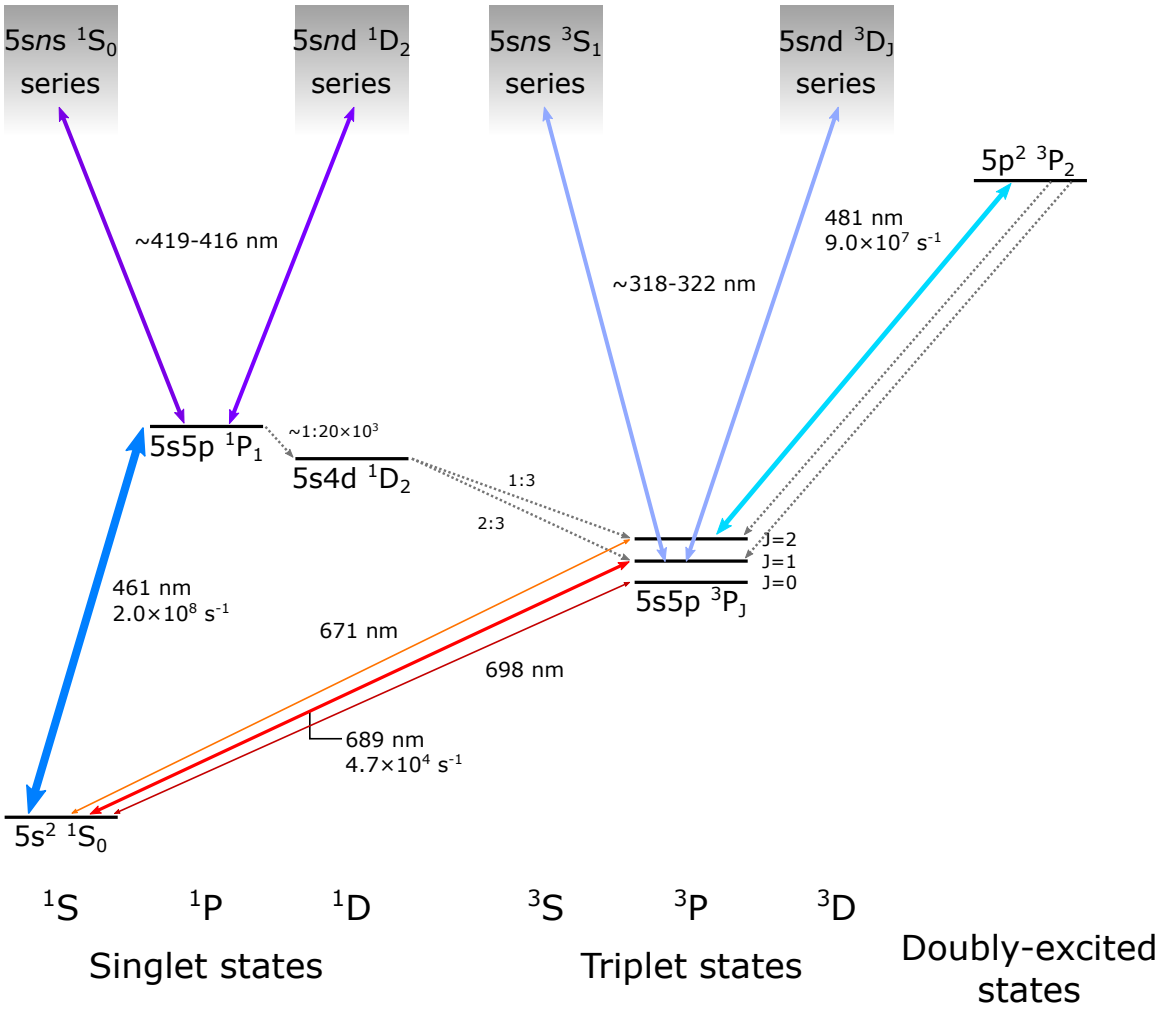

Figure 1.3: Energy level diagram for (bosonic) strontium with preference given to levels relevant to our experimental setup[5]. Driven transitions are indicated by double arrows. Spontaneous decays are indicated dashed single arrows.

interesting in their own right (e.g., see [63]), have proven to be a sensitive tool for detecting Rydberg atoms [64–67].

Another significant advantage of strontium is the narrow $(5s^2)\,{}^1S_0 \rightarrow (5s5p)\,{}^3P_1$ transition with a $\Gamma/2\pi = 7.5\,\mathrm{kHz}$ ($\tau = 21\,\mu\mathrm{s}$) linewidth. Not only does this transition enable us to easily produce samples with temperatures below $2\,\mu\mathrm{K}$, it also provides a convenient first step for two-photon excitation to Rydberg states. Considering the two-photon coupling between states (in a three-level system) $\Omega \sim \Gamma/\Delta$ and the photon scattering rate $\Gamma_{\mathrm{sc}} \sim (\Gamma/\Delta)^2$ for a detuning Δ (e.g., see [68–72]), the narrow linewidth enables stronger coupling for

comparable scattering rates. Active research is also progressing towards exciting strontium Rydberg atoms using the even narrower $(5s^2)\,^1S_0 \rightarrow (5s5p)\,^3P_0$ clock transition [73]. In principle, the ultranarrow $(5s^2)\,^1S_0 \rightarrow (5s5p)\,^3P_2$ transition could also be used to excite Rydberg states and a direct measurement of the transition frequency was recently reported [74].

A third, more subtle, aspect of strontium is the range of stable isotopes available, both bosonic ($I = 0$) and fermionic ($I = 9/2$). Since all the bosonic isotopes (^{88}Sr, ^{86}Sr, and ^{84}Sr) have been Bose condensed [75–79] and a degenerate Fermi gas ^{87}Sr has also been produced [79, 80], strontium provides a unique opportunity for incorporating Rydberg interactions into both ultracold Bose and Fermi gases (as well as Bose-Bose and Bose-Fermi mixtures). For the bosons, the lack of nuclear spin means there is no hyperfine structure which greatly simplifies their Rydberg spectra whereas the hyperfine structure of ^{87}Sr makes its spectra significantly more complicated. However, ^{87}Sr provides a unique opportunity for approximating an ultracold classical gas since, in an unpolarized gas of ^{87}Sr, the atomic population is distributed among the $(2I + 1) = 10$ degenerate $(5s^2)\,^1S_0, F, m_F$ spin states.

Many of the advantages (and challenges) discussed above for strontium generally apply to other alkaline earth-like atoms as well (e.g., calcium, barium, ytterbium). One other advantage of strontium in particular[6] is the lack of a scattering resonance between the Rydberg electron and nearby perturbing atoms. It was observed that the lifetimes of rubidium ULRRMs were significantly shorter than the lifetime of the parent Rydberg atom with the difference attributed to the occurrence of a p-wave scattering resonance [81, 82]. In contrast, strontium ULRRMs exhibit lifetimes similar to the parent Rydberg state, indicating a much weaker (or absent) p-wave scattering resonance [38]. It should be noted that in very dense gases (e.g., in a BEC), even strontium ULRRMs exhibit reduced lifetimes with the likely cause being collisions between ground-state atoms and the Rydberg core ion [83].

[6] At the time of writing, ULRRMs of other alkaline earth-like atoms have not yet been reported.

1.3 Thesis Outline

The goal of this thesis is to document experiments towards utilizing the unusual characteristics of ULRRMs as probes of long-range spatial correlations in ultracold gases. At ultracold temperatures, the atoms in the gas are expected to exhibit the effects of quantum statistics that affect the likelihood of finding two (or more) strontium atoms within a certain radius (i.e., a "spatial correlation function"). This "bunching" or "antibunching" of atoms should then be reflected in the excitation rates to ULRRM states. Towards that end, Ch. 2 outlines the techniques used to produce ultracold gases of strontium as well as documenting the current state of the Rydberg experiment. It also aims to provide a (small) collection of references regarding laser cooling strontium in general, noting several methods that are not implemented on our current system but may be of interest for future upgrades. Chapter 3 includes a reproduction of the paper [84] which details efforts in understanding the hyperfine Rydberg states of ^{87}Sr. Understanding the Rydberg states of ^{87}Sr is of high importance because it is used to represent both a Fermi gas and a (nearly) classical gas. Additional material and details are provided that were not included in the published paper. Current work exploring the effects of spatial correlations on ULRRMs is presented in Ch. 4, describing experiments examining the effects of spatial correlations on production of vibrationally-excited dimer ULRRMs. Lastly, Ch. 5 provides a summary of this thesis and some potential avenues for future exploration. Hopefully this thesis serves as a valuable resource for future studies of strontium Rydberg atoms and molecules.

2. Strontium Rydberg Experiment

This chapter describes the Rydberg apparatus used in this thesis with the purpose of providing an overview of the current state of various systems for producing ultracold and quantum degenerate gases of strontium as well as providing references that may be helpful for future upgrades. Being the third ultracold strontium experiment at Rice, we leveraged lessons learned from the other experiments, colloquially referred to as "Neutral" and "Plasma", to build a capable and flexible system[7].

Although the Rydberg system looks very similar to other ultracold strontium experiments, what makes it uniquely suited for studying Rydberg physics is the inclusion of systems for creating, manipulating, and detecting charged particles. In particular, in-vacuum electric field plates can both cancel stray electric fields as well as apply field ionization ramps and direct the resulting electrons (or ions) towards a microchannel plate (MCP) detector.

2.1 Producing Ultracold Gases of Strontium

We follow the well-established laser cooling and trapping sequence for producing ultracold gases of strontium. An energy level diagram for (bosonic) strontium primarily focused on the transitions relevant for laser cooling and trapping is provided in Fig. 2.1. Briefly, laser cooling and trapping of strontium gases proceeds in the following steps:

Cooling and trapping on the $(5s^2)\,{}^1S_0 \rightarrow (5s5p)\,{}^1P_1$ transition

[7] Collectively, the three experiments work with ultracold atomic strontium in all forms: from the ground state (Neutral) to the ions (Plasma), and everything in between (Rydberg). There is also the strontium atomic beam experiment, which produces some of highest n Rydberg atoms ever reported.

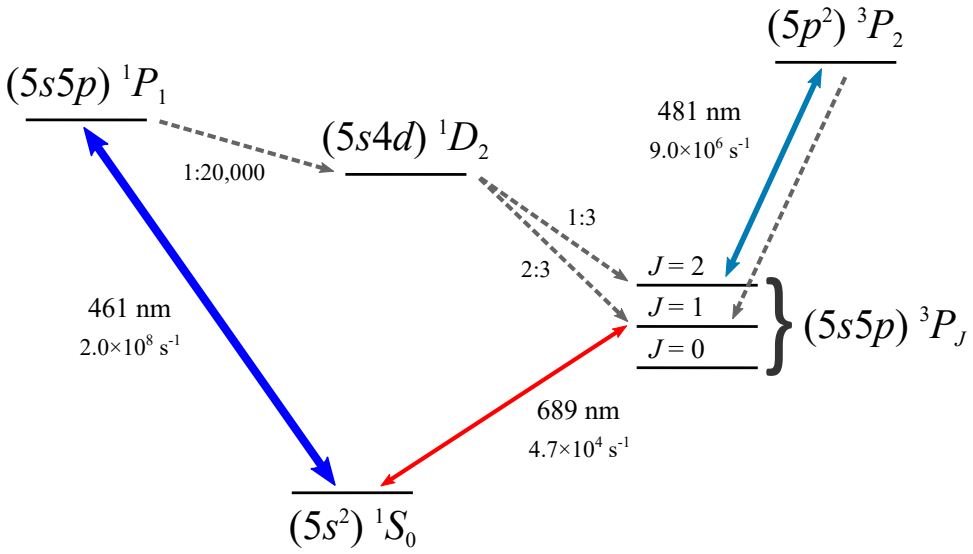

Figure 2.1: A simplified level diagram of (bosonic) strontium focusing on the transitions relevant for laser cooling and trapping. Solid and dashed arrows representing driven transitions and decays, respectively.

The broad $\Gamma/2\pi = 30.5\,\text{MHz}$ transition at 461 nm is used for the first stage of cooling due to its ability to scatter many photons very rapidly, exerting large radiative forces on the atoms. A "blue" magneto-optical trap (MOT) driving this transition typically produces samples with temperatures of about $(1-2)\,\text{mK}$. The blue MOT also loads the magnetic trap, formed by the MOT quadrupole field, with atoms in the metastable $(5s5p)\,^3P_2$ state due a small leak ($\approx 1{:}\,20\,000$) of atoms following the $(5s5p)\,^1P_1 \rightarrow (5s4d)\,^1D_2 \rightarrow (5s5p)\,^3P_2$ decay path. The trapped $(5s5p)\,^3P_2$ atoms are returned to the ground state by repumping at 481 nm

Cooling and trapping on the $(5s^2)\,^1S_0 \rightarrow (5s5p)\,^3P_1$ transition

Second-stage cooling is achieved by a MOT driving the narrow $\Gamma/2\pi = 7.5\,\text{kHz}$ transition at 689 nm. Due to the narrower linewidth, the 689 nm transition scatters photons much more slowly than the 461 nm transition, making it unsuitable for capturing large numbers of atoms from the strontium oven. However, it is well-suited for bridging between the millikelvin temperatures of the blue MOT and the microkelvin trap depths of optical traps. A 689 nm "red" MOT easily produces samples with temperatures around $(1-2)\,\mu\text{K}$, ideal for efficient loading into optical traps.

Optical trapping and evaporative cooling

Further cooling requires evaporative cooling in a conservative trap. Optical dipole traps (ODTs) are used to create a conservative potential for strontium because ground-state strontium atoms have no magnetic moment and, therefore, cannot be magnetically trapped. Optical dipole traps work by inducing energy shifts of atomic sates via off-resonantly coupling and, therefore, require high powers to achieve sufficient trap depths. As a result, lasers at 532 nm or 1064 nm are commonly employed. Once cold atoms from the red MOT are loaded in to an ODT, evaporative cooling can be used to produce ultracold and quantum degenerate gases with temperatures below 1 µK.

Detailed explanations of the various techniques and a variety of setups are available from numerous sources (e.g., see [58, 65, 85–90]).

2.1.1 Cooling on the 461 nm "Blue" Transition

At room temperature, strontium is a solid metal with negligible vapor pressure and thus requires an oven to sublimate strontium into a gaseous form. Although oven temperatures vary from setup-to-setup, they are typically around $(450 - 750)\,^{\circ}\mathrm{C}$[8] [58, 85, 89–94]. As a result, the first step in laser cooling and trapping strontium utilizes the 461 nm $(5s^2)\,{}^1S_0 \rightarrow (5s5p)\,{}^1P_1$ transition with its broad $\Gamma/2\pi = 30.5$ MHz linewidth, which enables high photon scattering rates. Table 2.1 gives the isotope shifts of the 461 nm transitions referenced to ^{88}Sr.

Immediately after the atoms exit the oven, they pass through a two-dimensional (2D) collimator which applies transverse optical molasses [95–99] to reduce the divergence of the atomic beam. Some experiments have incorporated a 2D magneto-optical trap (MOT) that can not only focus the atomic beam but can also deflect the atoms so that only cold atoms

[8] If the setup has a nozzle heater, its temperature is generally higher than the main oven to reduce the likelihood of clogging.

Table 2.1: Isotope shifts of the 461 nm $(5s^2)\,{}^1S_0 \rightarrow (5s5p)\,{}^1P_1$ transition relative to ^{88}Sr. Calculated from the weighted averages of values presented in Tabs. B.3 and B.4. g-factors for the upper state are also included.

Isotope	Lower level	Upper level	$\nu - \nu_{88}$ [MHz]	g_J or g_F
^{88}Sr	$(5s^2)\,{}^1S_0$	$(5s5p)\,{}^1P_1$	0	1
^{87}Sr	$(5s^2)\,{}^1S_0, F = 9/2$	$(5s5p)\,{}^1P_1, F = 7/2$	−11.3(16)	−2/9
		$(5s5p)\,{}^1P_1, F = 11/2$	−53.4(16)	2/11
		$(5s5p)\,{}^1P_1, F = 9/2$	−70.6(16)	4/99
^{86}Sr	$(5s^2)\,{}^1S_0$	$(5s5p)\,{}^1P_1$	−124.7(6)	1
^{84}Sr	$(5s^2)\,{}^1S_0$	$(5s5p)\,{}^1P_1$	−270.9(7)	1

enter the experiment region [100][9]. In order to maximize the efficiency of the 2D collimator, elliptical beams are used to increase the intensity along the atomic beam.

Since the 2D collimator has no effect on the longitudinal velocity, they atoms are still moving at about $v_{\text{avg}} \approx 500\,\text{m}\,\text{s}^{-1}$[10], much too quickly to be trapped by a MOT operating on the 461 nm transition which has a capture velocity of about $v_C \approx 14\,\text{m}\,\text{s}^{-1}$[11] [68, 105]. The atoms are slowed longitudinally with a Zeeman slower where a spatially-varying magnetic field keeps the slowing atoms in resonance with a 461 nm beam counterpropagating to their direction of travel [106]. Because the magnetic field is axial, a circularly polarized 461 nm beam is used. Several ideas and considerations for Zeeman slowing an atomic beam can be found in [107–114].

Now that a significant portion of the atoms have been slowed by the Zeeman slower, they enter the main chamber where they are cooled and trapped by a standard six-beam 461 nm "blue" MOT. The MOT uses a quadrupole magnetic field and light detuned below atomic resonance to provide both position-dependent and velocity-dependent forces that capture and cool the atoms [68, 70, 115]. Blue MOTs typically produce samples of atoms around

[9] The designs presented in [101–104] are probably the more "traditional" 2D MOT which forms a cold line of atoms that are then "pushed" to the main chamber.

[10] Assuming the atomic beam leaves the oven at $T = 425\,^\circ\text{C}$: $v_{\text{mp}} \approx 445\,\text{m}\,\text{s}^{-1}$, $v_{\text{avg}} \approx 483\,\text{m}\,\text{s}^{-1}$, and $v_{\text{rms}} \approx 514\,\text{m}\,\text{s}^{-1}$ [68].

[11] The capture velocity defined as $v_C \equiv \Gamma/k$ where Γ is the transition linewidth and k is the transition wavevector [68].

$(1-2)$ mK. Some experiments (e.g., [89]) implement a "cold" blue MOT stage where the

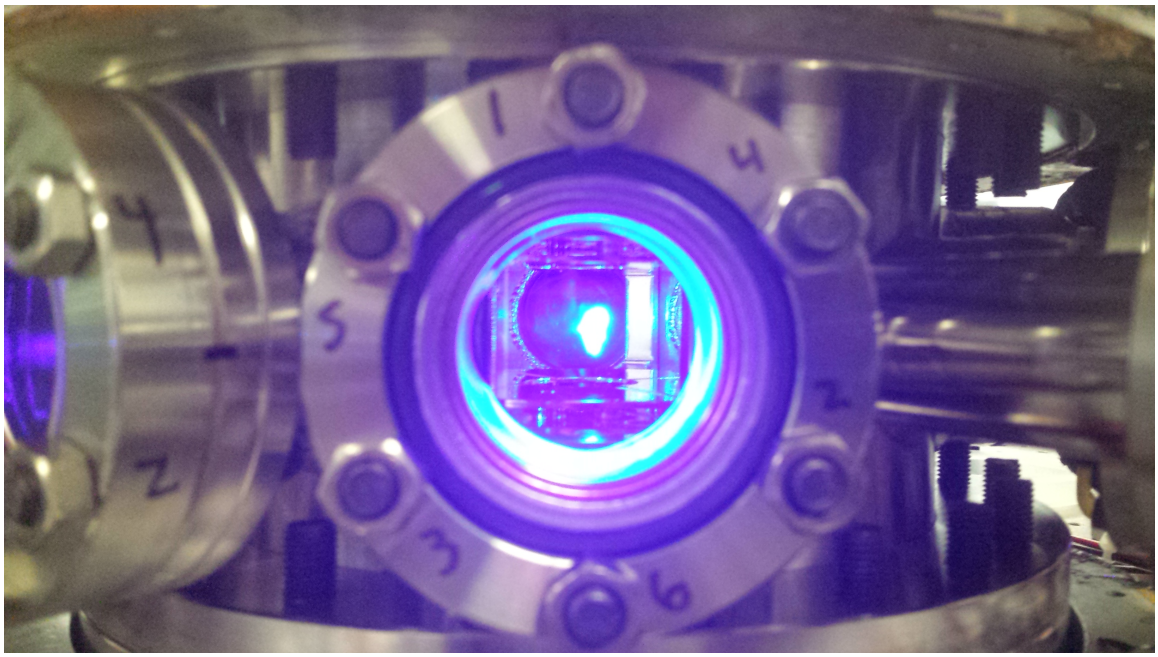

Figure 2.2: A picture of the ^{88}Sr blue MOT taken on 2014/08/29 through the 2.75 in absorption imaging viewport. The strontium oven and Zeeman slower are located off to the right. With the electric field plates separated by about 1 in, this blue MOT likely has a vertical height close to 0.5 in.

detuning, intensity, and quadrupole gradient are ramped to obtain colder temperatures for improved transfer efficiency to the red MOT. No such stage is implemented on our current setup as we found the blue MOT temperatures sufficient for decent transfer.

Although the 461 nm light is capable of scattering many photons per second, the Doppler limit of this transition is about $T_D = 732\,\mu\text{K}$[12] [68] with typical temperatures closer to 1 mK. While sub-Doppler cooling is not available in the bosonic isotopes, it has been observed in ^{87}Sr where the blue MOT temperature was measured to be about 300 µK [116, 117]. Interestingly, as noted in [116], cooling bosonic alkaline-earth atoms on the $^1S_0 \rightarrow {}^1P_1$ transition typically yields temperatures a few times the Doppler cooling limit [117–119].

[12] For the 461 nm transition: $k_B T_D \equiv \hbar\Gamma/2 = 732\,\mu\text{K}$, $k_B T_r \equiv \hbar^2 k^2/2M = 512\,\text{nK}$.

2.1.2 Magnetic Trap and Repumping

The $(5s^2)\,{}^1S_0 \rightarrow (5s5p)\,{}^1P_1$ transition is not completely closed where $(5s5p)\,{}^1P_1$ atoms can leak to the $(5s4d)\,{}^1D_2$ state. The branching ratio for this decay path was found to be $A\big({}^1P_1 \rightarrow {}^1S_0\big)/A\big({}^1P_1 \rightarrow {}^1D_2\big) \approx 20 \times 10^3$ [120][13]. About 2/3 of the $(5s4d)\,{}^1D_2$ atoms then decay to the $(5s5p)\,{}^3P_1$ which subsequently decay to the $(5s^2)\,{}^1S_0$ and return to the 461 nm cooling cycle. The remaining 1/3 decay to the long-lived metastable $(5s5p)\,{}^3P_2$ state with a lifetime of about 520 s [122], effectively removing them from the blue MOT cooling cycle. Of the $(5s5p)\,{}^3P_2$ states, the low-field seeking $m_J = 1, 2$ states can become trapped in the quadrupole magnetic field of the blue MOT [123, 124]. This decay path, initially seen as a loss from the blue MOT, ends up being a powerful tool for accumulating atoms in a metastable reservoir at roughly the same temperature as the blue MOT and was an essential tool in overcoming the ≈0.5 % natural abundance of ^{84}Sr to produce the first strontium BECs [75, 76].

The magnetic trap is also crucial for laser cooling and trapping multiples isotopes. As seen in Tab. 2.1, the isotope shifts are comparable to the 461 nm linewidth meaning a blue MOT can only efficiently trap a single isotope at a time. The key to trapping multiple isotopes is to utilize the automatic accumulation of $(5s5p)\,{}^3P_2$ metastable atoms, which are dark to the 461 nm cooling light, in the magnetic trap. Multiple isotopes can be loaded in to the magnetic trap by simply operating a blue MOT tuned for a particular isotope and then tuning the laser to trap another isotope. This sequential loading process typically starts with the most abundant isotope, since those atoms will spend the most time the magnetic trap, before tuning the 461 nm laser to cool and trap subsequent isotopes. Loading rates into the magnetic trap could be improved by implementing a "depumping" laser that prevents $(5s5p)\,{}^3P_1$ atoms from returning to the ground state by optically pumping them to the $(5s5p)\,{}^3P_2$ [125].

Before moving on to the next cooling stage, atoms in the metastable reservoir need

[13] Previous measurements suggested that this branching ratio was about 1 : 50 000 [121]

to be returned to the $(5s^2)\,^1S_0$ ground state. Several transitions have been explored for repumping atoms out of the metastable reservoir, each of which has varying advantages and disadvantages [58, 85, 90, 91, 93, 105, 120, 125–133][14]. On our experiment, we drive the $(5s5p)\,^3P_2 \rightarrow (5p^2)\,^3P_2$ transition at 481 nm. One of the key advantages of this transition is that the upper state is $^3P_2$ so it only requires a single laser to clear out the magnetic trap because the $(5p^2)\,^3P_2$ atoms can only decay to either the $(5s5p)\,^3P_1$ or $(5s5p)\,^3P_2$ states. Another advantage of this transition is that the ^{87}Sr hyperfine structure of the doubly-excited $(5p^2)\,^3P_2$ state is expected to be small meaning the shifts of the 481 nm transition should be predominantly due to the hyperfine structure of the $(5s5p)\,^3P_2$ state which are known [74, 134]. As seen in Fig. 2.3, the $A = -212.765(1)$ MHz and $B = 67.215(15)$ MHz

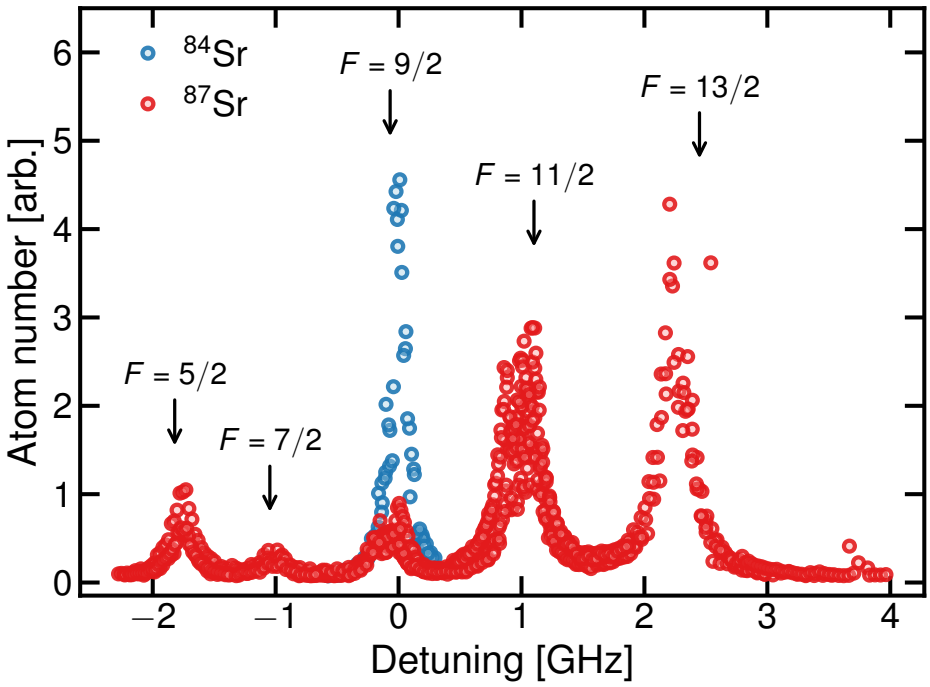

Figure 2.3: Representative number of ^{84}Sr and ^{87}Sr atoms returned to the $(5s^2)\,^1S_0$ ground state from the magnetic trap varying the 481 nm laser frequency. The labeled arrows indicate the expected energy shifts of the $(5s5p)\,^3P_2, F \rightarrow (5p^2)\,^3P_2$ transition in ^{87}Sr calculaed using only the hyperfine A and B constants of the $(5s5p)\,^3P_2$ state from [134].

hyperfine constants of the $(5s5p)\,^3P_2$ state [134] captures the observed energy splittings in

[14] An excellent overview of the various strontium repumping transitions is presented in [58].

the $(5s5p)\,^3P_2, F \rightarrow (5p^2)\,^3P_2$ transitions quite well. When multiple isotopes are loaded into the magnetic trap, it will be necessary to apply the appropriate frequency shifts to the repump laser so that all isotopes are recovered efficiently.

Other uses for the magnetically trapped metastable strontium could be for magnetic transport of atoms from a "collection" chamber to a "science" chamber. It should also be mentioned that the magnetic trap is not always necessary nor preferred depending on the particular isotope and experiment being performed. Keeping a repumper on can result in higher initial blue MOT loading rates by preventing accumulation of atoms in the metastable reservoir, drastically reduce experimental cycle times. This approach may be of interest for experiments looking to have repetition rates such as in optical tweezer experiments working with ^{88}Sr [120, 135–137]. An interesting idea is mentioned in [138] where atoms in the magnetic trap are laser cooled using the $(5s5p)\,^3P_2 \rightarrow (5s4d)\,^3D_3$ transition at 2.92 µm before being returned to the $(5s^2)\,^1S_0$ state for loading in to an optical lattice.

2.1.3 Cooling on the 689 nm "Red" Transition

After the 461 nm cooling stage, the strontium atoms are typically around $(1-2)$ mK whereas efficient loading of atoms in to optical dipole traps require sample temperatures closer to $(1-2)$ µK. A "red" MOT operating on the narrow $(5s^2)\,^1S_0 \rightarrow (5s5p)\,^3P_1$ transition at 689 nm bridges this gap. With $\Gamma/2\pi = 7.5$ kHz, the Doppler limit $T_D \approx 180$ nK is comparable to the recoil limit of $T_r \approx 230$ nK. Following [139], MOTs can be characterized by the ratio of the transition linewidth (Γ) to the single photon recoil frequency shift (ω_R) with typical MOTs operating in the $\Gamma/\omega_R \gg 1$ regime compared to narrow line MOTs where $\Gamma/\omega_R \sim 1$. Operating in the $\Gamma/\omega_R \sim 1$ regime, where a few photon recoils can kick an atom out of resonance with the cooling lasers, leads to very different dynamics. The differences in dynamics are especially apparent in the shape of bosonic red MOTs where the atoms are trapped on a thin ellipsoidal shell where the laser detuning matches the Zeeman shift from the quadrupole field [44, 58]. Conversely, the fermionic red MOT looks similar to

Table 2.2: Isotope shifts of the 689 nm $(5s^2)\,{}^1S_0 \rightarrow (5s5p)\,{}^3P_1$ transition, relative to ^{88}Sr. Calculated from the weighted averages of the values in Tab. B.5. g-factors for the upper state are also included.

Isotope	Lower level	Upper level	$\nu - \nu_{88}$ [MHz]	g_J or g_F
^{88}Sr	$(5s^2)\,{}^1S_0$	$(5s5p)\,{}^3P_1$	0	3/2
^{87}Sr	$(5s^2)\,{}^1S_0, F = 9/2$	$(5s5p)\,{}^3P_1, F = 7/2$	1351.937(27)	−1/3
		$(5s5p)\,{}^3P_1, F = 9/2$	221.689(13)	2/33
		$(5s5p)\,{}^3P_1, F = 11/2$	−1241.465(18)	3/11
^{86}Sr	$(5s^2)\,{}^1S_0$	$(5s5p)\,{}^3P_1$	−163.814 43(26)	3/2
^{84}Sr	$(5s^2)\,{}^1S_0$	$(5s5p)\,{}^3P_1$	−351.59(11)	3/2

"traditional" $\Gamma/\omega_R \gg 1$ MOTs but it's shape is due to complications arising from hyperfine structure. An excellent description of how the narrow 689 nm "red" MOT works for both the bosons and fermion is presented in [58][15] with additional resources in [44, 85].

Considering first the bosonic case, the $\Gamma/2\pi = 7.5$ kHz transition is a bit too narrow to effectively capture the ∼2 mK atoms from the blue MOT. In order to increase the capture efficiency, the spectrum of the red MOT light is artificially broadened by frequency modulation, typically by a few megahertz, which enables addressing of multiple velocity classes of atoms from the blue MOT. Once enough atoms have been captured in the "broadband" red MOT, the frequency modulation and intensity are ramped down[16] to a narrow or single-frequency red MOT which increases the sample density and reduces the temperature. At the end, temperatures are typically below about 2 µK. Our ^{84}Sr red MOT system is documented in [93].

While the bosonic isotopes of strontium behave like an ideal $J = 0 \rightarrow J = 1$ MOT described in texts (e.g., see [68, 70]), the hyperfine structure of ^{87}Sr poses a challenge. Since the ground state has (essentially) no magnetic moment, the position-dependent Zeeman shift is only experienced by the $^3P_1$ state with a $g_F m_F$-dependent magnitude. This is very different than the case for alkali atoms where the g-factors of the lower and upper

[15] The "Red MOT Bible".

[16] Reducing the frequency modulation essentially increases the intensity of each comb tooth in the FM spectrum.

states are comparable. As a result, some positions experience a restoring force whereas the forces are anti-trapping at other locations. Narrow line laser cooling of ^{87}Sr was first achieved by the Tokyo group through the use of a "trap" laser resonant with the $(5s^2)\,^1S_0, F = 9/2 \rightarrow (5s5p)\,^3P_1, F = 11/2$ transition and a second "stir" laser resonant with $(5s^2)\,^1S_0, F = 9/2 \rightarrow (5s5p)\,^3P_1, F = 9/2$ to quickly redistribute the population and take advantage of the Clebsch-Gordan coefficients so that, on-average, the atoms experience a trapping force [58, 140].

Due to the large isotope shifts compared to the linewidth of the transition (see Tab. 2.2), red MOTs for multiple isotopes can be operated simultaneously. This ability compliments the metastable reservoir exceedingly well since, when switching from the blue MOT to the red MOT, the magnetic field gradient is lowered from about $(30 - 70)\,\mathrm{G\,cm^{-1}}$ to about $(1 - 10)\,\mathrm{G\,cm^{-1}}$ which releases the atoms from the magnetic trap. It is during this switching time that the 481 nm repump light is applied so all the isotopes released from the metastable reservoir are returned to the $(5s^2)\,^1S_0$ ground state. Since the repumped atoms can be an mixture of isotopes, this ability to simultaneously laser cool and trap with the red MOT is critical.. After laser cooling on the 689 nm transition, our sample temperatures are typically $(1 - 2)\,\mu\mathrm{K}$, which is sufficient for loading into an optical dipole trap (ODT).

An alternative method to the broadband red MOT is saw-tooth wave adiabatic passage (SWAP) cooling which eschews the traditional broadband red MOT in favor of carefully designed frequency ramps that adiabatically transfer atoms between the $^1S_0$ and $^3P_1$ states [141–144]. The advantage of this method is particularly apparent for ^{87}Sr which eliminates the need for the "stir" laser. The drawback is that the temperatures achieved seem to be limited to about 10 µK due to the need to maintain efficient adiabatic transfer [141]. A promising technique is to use SWAP cooling instead of the broadband red MOT to capture atoms from the blue MOT before transferring to a single-frequency red MOT to reach colder temperatures [145].

2.1.4 Optical Dipole Trap (ODT)

Strontium in the $(5s^2)\,{}^1S_0$ ground state has no magnetic moment meaning it cannot be magnetically trapped [17] and requires the use of optical dipole traps (ODTs). Since ODTs are (generally) conservative, the trapped atoms remain at approximately the same temperature as when the are loaded (typically $\sim$1 µK). If further cooling is required, evaporative cooling can be performed to attain temperatures sufficient for quantum degeneracy.

Optical dipole traps work by using intense, off-resonant light to shift atomic energy levels. Since the amount of shift is dependent on the intensity, an spatially-varying intensity $I(\mathbf{r})$ leads to force gradient such that, when appropriately designed, will attract (or repel) atoms to the area of highest intensity. For a two-state atom with ground state $|g\rangle$ and excited state $|e\rangle$ separated by energy $\hbar\omega_0$ and coupled by a laser at frequency ω, this shift can be written as (e.g., see [71, 150])

$$\Delta E(\mathbf{r}) = -\frac{3\pi c^2}{2\omega_0}\left(\frac{\Gamma}{\omega_0-\omega}+\frac{\Gamma}{\omega_0+\omega}\right)I(\mathbf{r}) = -\frac{1}{2\epsilon_0 c}\,\mathrm{Re}\left[\alpha(\omega)\right]I(\mathbf{r}) \tag{2.1}$$

Oftentimes, the details of the transition are collected in to a complex frequency-dependent "polarizability" $\alpha(\omega)$. A quick and easy way to generalize Eq. (2.1) to a multilevel atom is to treat the multiple levels as individual two-level systems and then sum the contributions due to off-resonant coupling in each two-level system (e.g., [85, 151, 152]). A more accurate calculation of the AC Stark shift would require diagonalizing the Hamiltonian which includes all the states in the atom coupled by the laser.

For strontium, the red MOT spatial distribution and the particular isotope(s) being loaded needs to be taken in to account when designing an ODT. While the fermionic red MOT traps atoms in an ellipsoidal volume around the MOT quadrupole center, the atoms in a bosonic red MOT tend to form a thin shell below the quadrupole center [44, 79]. As a result, improved loading of atoms into an ODT can be obtained by "mode-matching"

[17] There is interest in producing quantum degenerate gases of alkaline-earth atoms in metastable states [146], some of which are magnetically trappable. Quantum degenerate gases of metastable atoms have been realized for helium [147–149].

the trapping volume of the ODT to the spatial distribution of atoms in the red MOT. For strontium, the preferred ODT geometry appears to be a high-aspect ratio horizontal "pancake" or "light sheet" where the tight axis is along gravity as this matches well with the shape of the bosonic red MOT [58, 79, 89, 90, 153]. Single-beam traps typically provide very weak confinement along the beam so secondary vertical or horizontal ODT beams are generally added to increase confinement along weak axes.

The specific isotope(s) being trapped also have an effect on both loading into an ODT as well as on their evaporation due to their wildly varying intra- and inter-isotope scattering lengths. Table 2.3 lists the s-wave scattering lengths for various combinations of isotopes. The first strontium BECs were achieved with ^{84}Sr, which has a convenient $a_s = 123\,a_0$

Table 2.3: . Measured s-wave scattering lengths (a_s) of strontium for various pairs of isotopes given in a_0 from [154]. An extended version is given in Tab. B.2.

	^{84}Sr	^{86}Sr	^{87}Sr	^{88}Sr
^{84}Sr	122.762(92)	31.65(14)	−57.61(61)	1658(54)
^{86}Sr	31.65(14)	798(12)	162.25(21)	97.374(69)
^{87}Sr	−57.61(61)	162.25(21)	96.198(68)	54.819(92)
^{88}Sr	1658(54)	97.374(69)	54.819(92)	−2.00(27)

scattering length, was easily evaporated to quantum degeneracy in low aspect ratio traps [75, 76]. An unpolarized degenerate Fermi gas of ^{87}Sr was also obtained in a nearly-circular ODT [80] but spin-polarized degenerate Fermi gases requires sympathetic cooling and thus requires trapping multiple isotopes [79]. Early work towards producing quantum degenerate gases of ^{88}Sr and ^{86}Sr were hindered by the tight waists of the ODT beams which leads to inelastic losses of ^{86}Sr [155, 156]. It was only by going to a large-volume high-aspect-ratio ODT was a BEC of ^{86}Sr realized [78]. The first BEC of ^{88}Sr was achieved by sympathetic cooling with (unpolarized) ^{87}Sr in a nearly spherical trap [77].

Some recent work towards developing systems for trapping strontium in optical tweezer arrays showed results that an ODT around $(501-520)\,\mathrm{nm}$ is close to a "magic" wavelength[18]

[18] A wavelength is "magic" when two (or more) states experience the same shift such that there is no differential shift between them [152, 157].

for the $(5s^2)\,{}^1S_0 \rightarrow (5s5p)\,{}^3P_1$ transition [120, 135]. It should be noted that both our current 1064 nm ODT and a "green" ODT are both expected to be repulsive for strontium Rydberg states [158, 159].

2.2 Vacuum System

An overview of our vacuum system is shown in Fig. 2.4 with the some of the components labeled. Perhaps the most distinctive aspect of our vacuum system is that it was designed

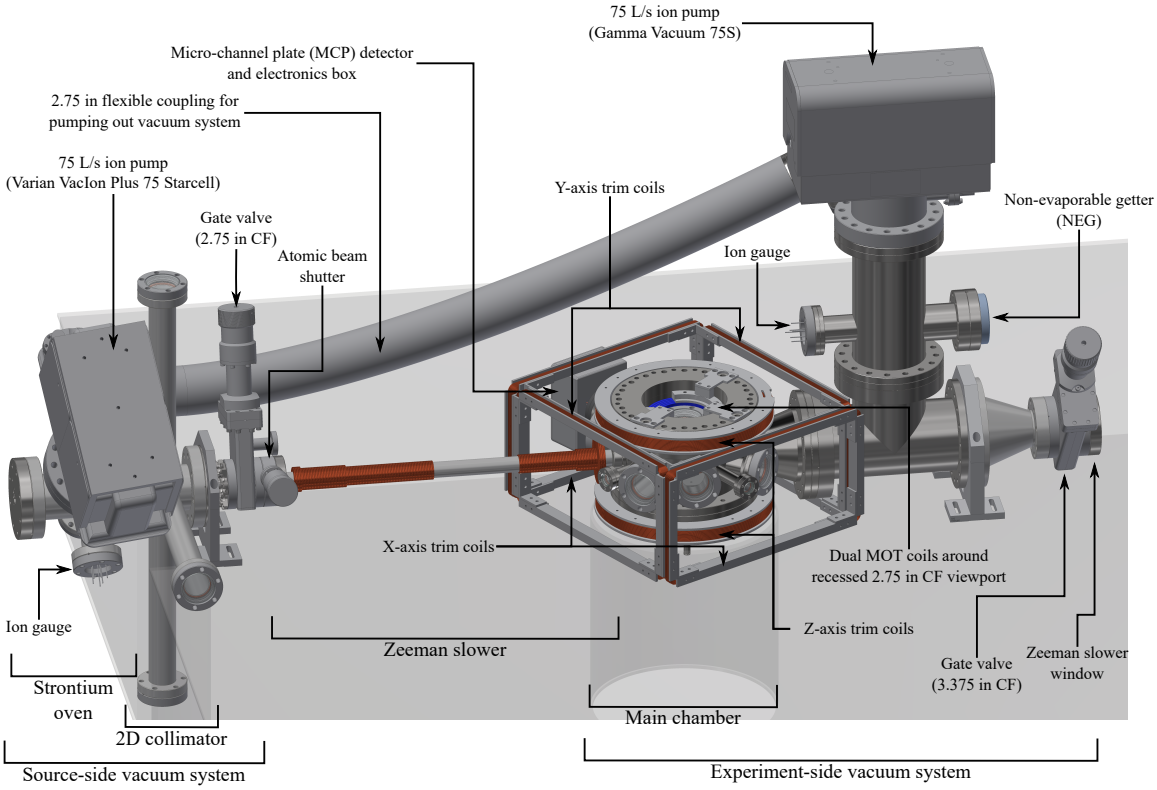

Figure 2.4: Overview of the strontium Rydberg apparatus highlighting the main sections of the vacuum system and various components.

to have the majority of the horizontal laser beams about 3.5 in = 8.89 cm from the surface of the optical table. Keeping the beams at this height eliminated the need for rigid supporting structures to elevate the entire vacuum system along with the associated requirement for raised optical platforms. This should also improve beam pointing stability as there is

reduced need for periscopes to raise laser beams to the level of the vacuum chamber.

To facilitate vertically propagating beams, two holes were cut through the table with a semicircle at the end of the table for the vertical 2D collimator arm and a 10 in diameter circle under the main chamber for MOT and dipole trap beams. We had originally planned on mounting vertical optics directly to the main chamber but decided instead to mount them to a single elevated platform above the main chamber and another platform on the underside of the table. Adding the breadboard under the table required tapping threads on the underside of the table. The major disadvantage of our current setup is the long distance between the undertable breadboard and the bottom of the main chamber, about 12 in[19], which makes it difficult to design, install, and align sensitive vertical beams.

2.2.1 Source-side Vacuum System

This section of the vacuum chamber is where the strontium oven and 2D collimator are located and produces the atomic beam of strontium for cooling and trapping. Although there are various designs for strontium ovens [92, 160] (and even commercial systems), we used a simple design that has shown success on the older strontium experiments in the laboratory. The design is simple with a single Watlow FIREROD cartridge heater[20] providing the majority of the heating power to the oven. An array of capillary tubes form a nozzle to provide some degree of collimation and resistive heater wire is wrapped around them to reduce the effects of strontium building up in the capillary tubes and clogging. We typically run our main FIREROD oven heater around 425 °C with the nozzle heater around 390 °C[21]. Figure 2.5 shows a recently fabricated strontium oven made to replace the one on the Neutral apparatus and is very similar to the one on our setup with the major difference being that it is mounted on the smaller 2.75 in flange whereas ours is mounted on a 3.375 in

[19] The thickness of the optical table.

[20] These are neat little devices which come with leads for both the resistive heating element and an integrated thermocouple.

[21] Ideally, the nozzle should be hotter than the reservoir to reduce the likelihood of clogging the capillary tubes but it's likely that our actual oven temperature is a bit lower due to the FIREROD thermocouple sensor being buried in the cartridge heater body rather than at the location of the strontium.

flange. The larger flange provides extra room for various feedthroughs without being too

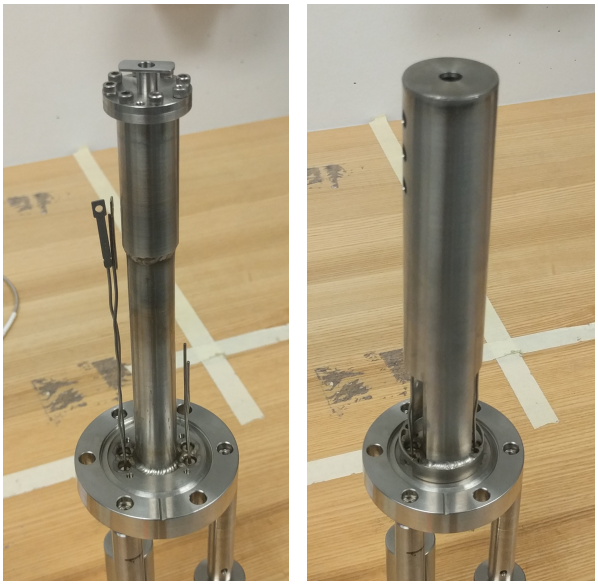

Figure 2.5: Neutral's new strontium oven during construction before the nozzle thermocouple and heating wires were attached. The design is very similar to our oven but is mounted on a 2.75 in flange instead of a 3.375 in flange. Oven without (left) and with (right) the heat shield.

cramped.

Immediately after the atoms exit the oven, they pass through the two-dimensional (2D) collimator stage which applies transverse optical molasses to increase the flux of atoms down the Zeeman slower. To maximize the effectiveness of the limited 461 nm laser power, the beams have elliptical intensity profiles to maximize the intensity on the atomic beam and a single beam is recycled through the four arms of the 2D collimator. The long arms also help to prevent strontium buildup on the AR coated viewports.

Before the atoms leave this section of the vacuum system and enter the Zeeman slower, they pass through a differential pumping tube[22] with a conductance $C \approx 0.85\,\mathrm{L\,s^{-1}}$ that helps maintain the pressure differential between the source and experiment sides of the system. The pressure in the source side is typically higher than the experiment side and

[22] A cylinder of OFHC (oxygen-free high thermal conductivity) copper with a coaxial through hole with approximate dimensions of $\varnothing = 0.3$ in by $L = 2.4650$ in.

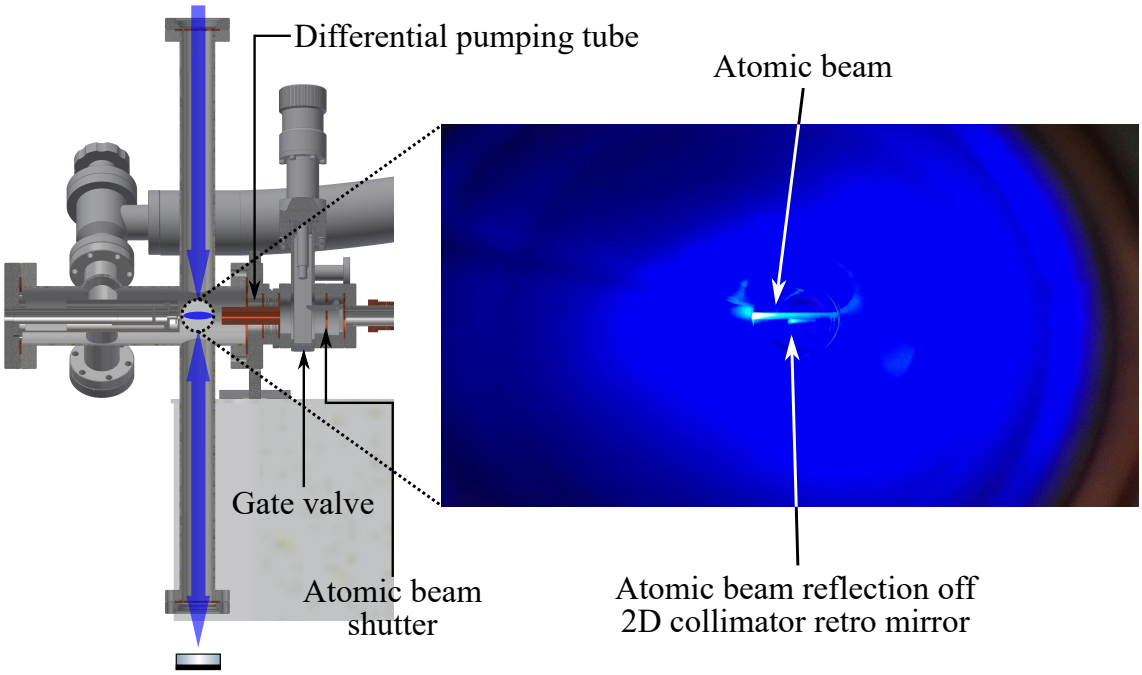

Figure 2.6: (Left) Cross-section image of the source-side vacuum system. (Right) Picture of the fluorescing atomic beam as viewed down the vertical arm of the two-dimensional (2D) collimator. A reflection of the atomic beam off the vertical retro mirror is also visible.

is currently around 7.6×10^{-9} Torr[23]. We suspect the ion pump on the source side is being restricted by the zero-length reducer which adapts the 4.5 in flange on the source-side vacuum chamber to the 6 in flange on the Varian ion pump.

A shutter and a gate valve was also installed between the source-side vacuum system and the Zeeman slower. The shutter allows us to physically block the atomic beam and extend the time between needing to change the entrance window for the 461 nm Zeeman slower beam. The gate valve should, in principle, allow us to isolate the source-side vacuum system from the rest of the chamber to facilitate reloading the strontium oven without venting the entire vacuum chamber but we found this valve to be somewhat leaky during our initial pumped out [24].

[23] MiniVac ion pump controller outputting 7.9 mV $= 7.9 \times 10^{-6}$ A for the rebuilt VacIon Plus 75 Starcell on 2019/06/13.

[24] Something similar was noticed by the Weld group at UCSB and they used two gate valves to separate their atomic source from their UHV main chamber [94].

2.2.2 Zeeman Slower

Since an oven is required to produce enough strontium vapor for trapping, a Zeeman slower is needed to slow the atoms down so that they can be captured by the MOT. Our Zeeman slower is detailed in [105] so it will only be briefly covered here. The Zeeman slower uses a spatially-varying axial magnetic field to keep the atoms resonant with a circularly-polarized 461 nm beam propagating counter to the direction of the atoms so that they continuously scatter photons as they slow [106]. Our particular design is a "spin-flip"-type where the amplitude of the axial magnetic field crosses zero between the ends. The Zeeman slower coil was constructed in multiple layers to allow tailoring of the resulting field to match the desired profile. Each layer was affixed to the Zeeman slower with thermally-conductive epoxy[25] and the resulting magnetic field measured before wrapping the next layer. Due to its length[26], it's conductance is reduced ($C \approx 1.4\,\mathrm{L\,s^{-1}}$) which should help maintain the differential pressure between the source and experiment sides.

For cooling, the Zeeman slower was custom made with a double wall that acts as a water cooling jacket. The inner wall separates the cooling water from UHV and the magnetic field coils are wrapped around the outer wall. Due to space constraints, the source-side is welded to a 2.75 in flange whereas it's connected to the main chamber by a 2.125 in flange. These flanges are also where cooling water enters and exits the jacket. It's possible to avoid water-cooling by using a permanent magnet Zeeman slower [109–111, 161] but the magnetic field would likely require significant shielding and/or more demanding cancellation efforts in order for it to not interfere with other aspects of the experiment.

2.2.3 Experiment-side Vacuum System

The experiment-side vacuum system can be broken down in to the main chamber where experiments take place and a "pumping tower" which provides a high-conductance path to

[25] Emerson and Cuming STYCAST 2762 or STYCAST 2762 FT with Catalyst 14, 17, or 17M-1.
[26] The inner wall of the Zeeman slower is about $\varnothing = 0.6940$ in by $L = 18.8296$ in.

the vacuum pumps. The custom main chamber [27] features:

- Recessed top and bottom flanges which bring the 2.75 in viewports closer to the center of the chamber while providing room for the MOT coils to fit around the viewports. The in-vacuum electric field plates are mounted to the bottom flange which has eleven 10 kV safe high voltage (SHV) feedthroughs for the electric field system.

- Six (6) 2.75 in horizontal viewports provide optical access for the various trapping (e.g., MOT and ODT) beams and the imaging system.

- Three (3) 1.33 in ("mini") horizontal viewports used for the various 689 nm and 320 nm excitation beams. These are oriented perpendicular and parallel to the MCP, allowing us to apply bias magnetic fields along the MCP axis to reduce electron deflection by the Lorentz force.

- Room for a Photonis miniTOF micro-channel plate (MCP) detector.

- A conical expansion to a 6 in flange for increased conductance to the vacuum pumps.

Most of the viewports were anti-reflection (AR) coated for 461 nm, 689 nm, and 1064 nm with the transmission shown in Fig. 2.7. Vacuum pressure on the experiment-side is maintained by a $75\,\mathrm{L\,s^{-1}}$ ion pump[29] located at the top of the pumping tower. The ion pump current suggests the vacuum on this side is at about 3.4×10^{-9} Torr[30]. Additional pumping is provided by a non-evaporable getter (NEG)[31] located about halfway up the pumping tower. In retrospect, we should have also included a titanium sublimation pump (TSP) for additional pumping capability.

[27] Fabricated by Huntington Mechanical Labs.

[28] I would like to thank Robyn Miller at Reynard Corporation for finding and sending me the reflection and transmission data from the order we placed six years ago.

[29] Gamma Vacuum TiTan 75S-CVX-6S-SC-N-N.

[30] MiniVac ion pump controller outputting $-4.8\,\mathrm{mV} = 4.8 \times 10^{-6}\,\mathrm{A}$ for the Gamma Vacuum TiTan 75S on 2019/06/13.

[31] SAES CapaciTorr D 200.

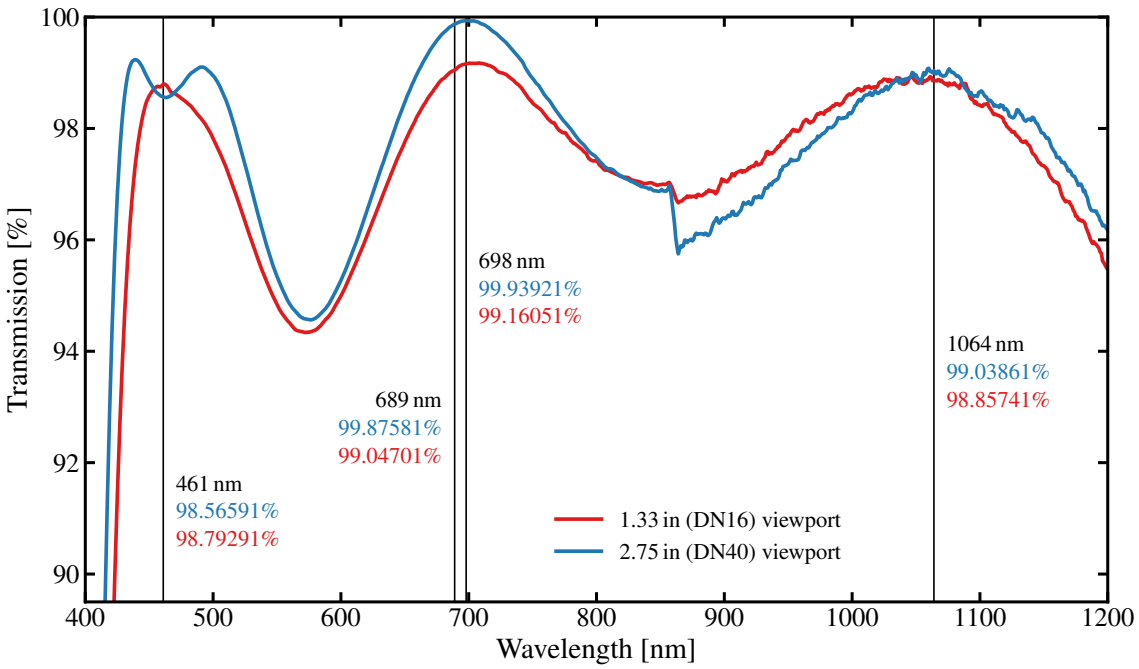

Figure 2.7: Transmission data of the 1.33 in and 2.75 in viewports with the anti-reflection (AR) coating by Reynard Corporation[28]. Although the AR coating was specified for 461 nm, 689 nm, and 1064 nm, it's fortuitous that the coating should be very good for the 698 nm clock transition and acceptable for 532 nm and 813 nm should we ever decide to use traps at those wavelengths.

Since we do not have a 2D deflection MOT, strontium from the atomic beam will deposit on the Zeeman slower entrance viewport overtime[32]. A 3.375 in gate valve separates the Zeeman slower viewport from the main chamber to facilitate changing this viewport once it gets coated with strontium.

2.3 Magnetic Field Trim Coils

Three pairs of Helmholtz coils are used to cancel stray magnetic fields and to apply a bias field and are shown in Fig. 2.8. The X-axis and Y-axis coil pairs produce fields in the horizontal plane parallel to the table surface and are oriented such that the X-axis produces a field towards or away from the MCP whereas the Y-axis produces a field perpendicular

[32]Neutral has tried using Plasma's pulsed Nd:YAG laser to perform ablation on their coated Zeeman viewport with a moderate level of success.

to this axis. The Z-axis coils produces a field along the vertical axis perpendicular to the surface of the table.

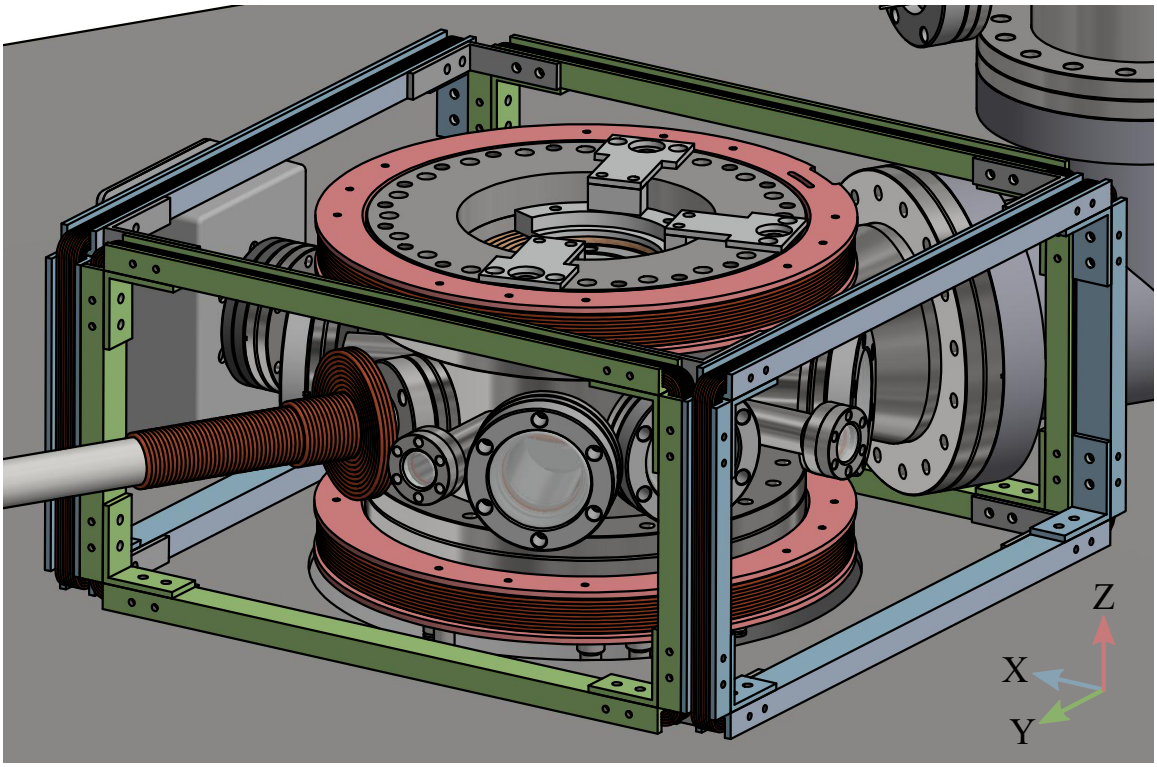

Figure 2.8: Magnetic field trim coils around main chamber for nulling stray fields and/or applying bias fields. The trim coil axes are defined relative to the MCP (equivalently, the 1.33 in viewports for the Rydberg excitation lasers) and gravity with the X-axis (blue) oriented towards the MCP, the Z-axis (red) pointing upwards perpendicular to the table surface, and the Y-axis (green) perpendicular to the X and Z axes (following the right-hand rule, of course).

Both the horizontal (X-axis and Y-axis) trim coils are constructed from 17.5 AWG wire[33] with 45 turns wound on aluminum U-channels and compressed together with polyimide tape. Due to the choice of keeping the center of the chamber at 3.5 in above the table surface, this required the horizontal (X-axis and Y-axis) trim coils to be centered at this height leading to their rectangular geometry instead of square or circular.

The vertical (Z-axis) coils were wound on circular aluminum U-channel forms and fit around the outside of the top and bottom flanges of the main chamber. This geometry

[33] MWS Wire Industries 17.5 HAPT-200 (NEMA MW 35-C).

allowed us to put 76 turns of 14 AWG rectangular wire[34] on them on them. The circular U-channels forms also feature a radial slice to mitigate the generation of eddy currents. In retrospect, we should made the horizontal coils beefier (especially along the X-axis) in order generate larger bias fields along the MCP axis. We found that having bias fields along other directions (i.e., not towards/away from the MCP) reduced our detection efficiency, likely due to the Lorentz force steering electrons away from the MCP.

2.4 Dual MOT Coils

One of the things we did differently from the previous strontium experiments is that we have two pairs of MOT coils instead of a single pair where the larger pair is used for the blue MOT while the smaller pair for the red MOT (see Fig. 2.9). This allows us to use two different current drivers without needing a single supply with enough dynamic range to supply both the ∼40 A to generate the ∼40 G cm^{-1} gradient for the blue MOT and also generating a low-noise ∼1 A for the ∼1 G cm^{-1} gradient for the red MOT. A drawing of the

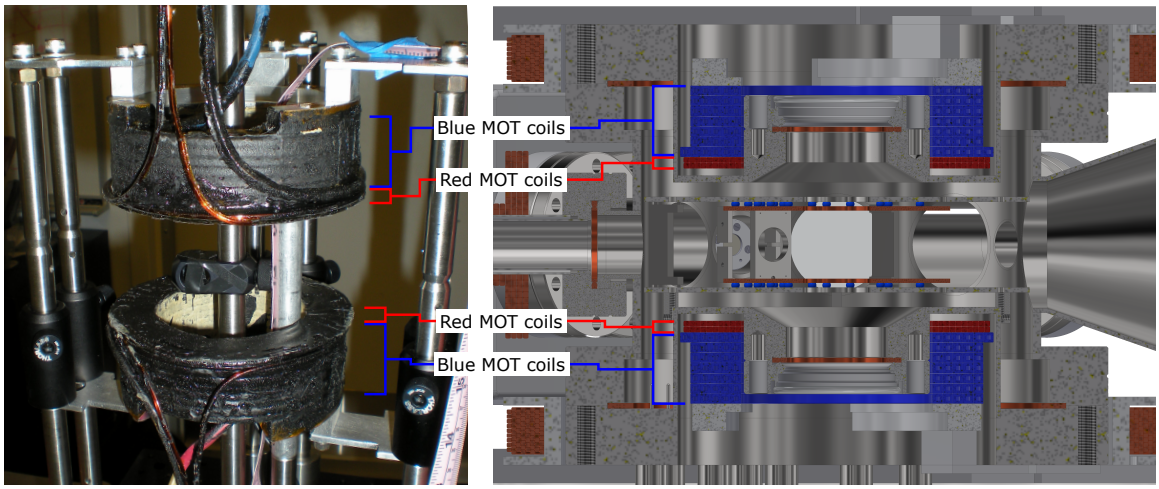

Figure 2.9: (Left) Picture of our assembled dual MOT coils on a test setup. (Right) CAD rendering of how they are centered around the windows of the recessed flanges on the main chamber.

dual MOT coils can be found in Appendix C.1.

[34] MWS Wire Industries 14 SQ HML-240 (NEMA MW 20C).

The blue MOT coils are constructed from square tubular wire[35] which is hollow inside for cooling water and produce a magnetic field gradient of about $1.25\,\mathrm{G\,cm^{-1}\,A^{-1}}$ along the tight axis (the Z-axis). The coils are typically run with around $(40-50)\,\mathrm{A}$ from a power supply[36] set for fixed-current output. A power MOSFET[37] is used for quickly turning the current on and off.

The red MOT coils are constructed from square 13 AWG copper wire[38] and are epoxied to the undersides of the blue MOT coils, placing them closer to the center of the vacuum chamber. A homebuilt voltage-controlled current driver[39] provides the current but we should be able to use any current driver capable of supplying up to about 5 A. The red MOT coils produce a magnetic field gradient of about $1\,\mathrm{G\,cm^{-1}\,A^{-1}}$.

2.5 Laser Systems for Producing Cold and Ultracold Strontium Gases

Figure 2.11 gives an overview of the orientation of our various laser cooling and trapping beams.

2.5.1 461 nm "Blue" Laser System

The experiment currently has three blue diode lasers in a master-slave configuration that provides all the 461 nm power for our experiment. In a master-slave setup, a single (typically low-power) frequency-stabilized "master" external cavity diode laser (ECDL) is used to injection lock higher-power "slave" lasers to increase the available laser power [162, 163]. The blue master laser is locked relative to the $(5s^2)\,{}^1S_0 \rightarrow (5s5p)\,{}^1P_1$ transition in a homebuilt strontium cell using Doppler-free saturated absorption spectroscopy. The error signal is obtained by modulating the axial magnetic field in the saturated absorption cell

[35] S&W Wire 125SQ DPG/BARE (NEMA 46-C).
[36] TDA-Lambda Genesys 8-90-IS510-U which can supply up to 8 V and 90 A.
[37] An IXYS IXFN 340N07.
[38] MWS Wire Industries 13 SQ HML-240 (NEMA MW 20-C).
[39] Powered by an APEX PA12(A) power operational amplifier.

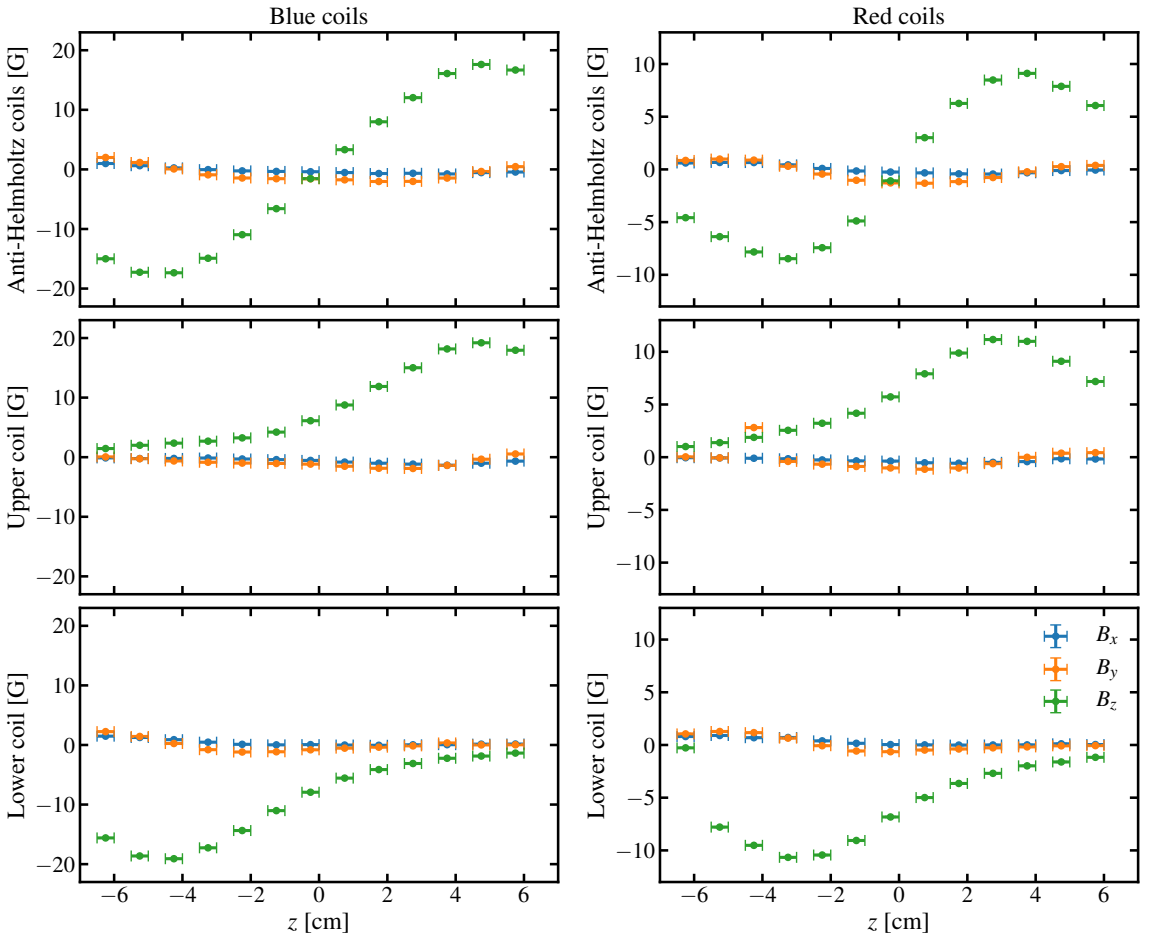

Figure 2.10: Blue MOT coil (left) and red MOT coil (right) magnetic fields measured along the z-axis on the test setup shown in Fig. 2.9 with $I = 4\,\mathrm{A}$. The uncertainties are estimated to be $\pm 2.5\,\mathrm{cm}$ and $\pm 0.05\,\mathrm{G}$. The non-zero measured values of B_x and B_y suggest that the probe was slight off the z-axis. There also appears to be a slight systematic shift in the zero-crossing of the anti-Helmholtz coils likely due to an uncertainty in determining the physical center of the coils.

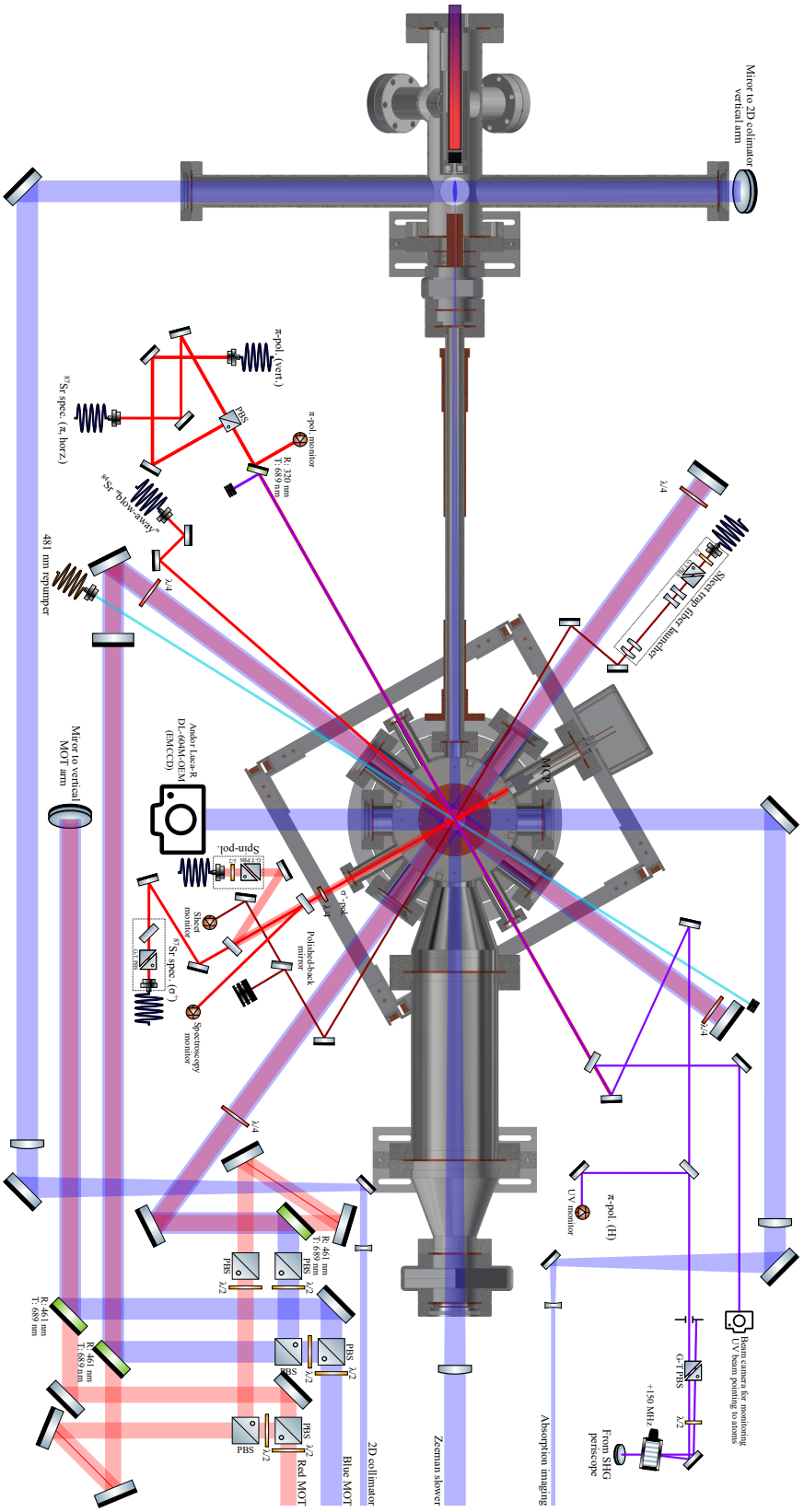

Figure 2.11: Cross-section of the vacuum system (viewed from above) and a simplified diagram of the various laser beams.

and using circularly-polarized pump and probe beams. Some details about our blue cooling system can be found in [93, 105].

Our current ECDL master laser[40] outputs about 40 mW. Although this laser generally remains single-mode when tuning between the various isotopes, we have been very disappointed with output mode quality which appears to be a Hermite-Gaussian TEM_{00} as seen in Fig. 2.12. Due to this poor output mode, a D-mirror was used to split the beam into two

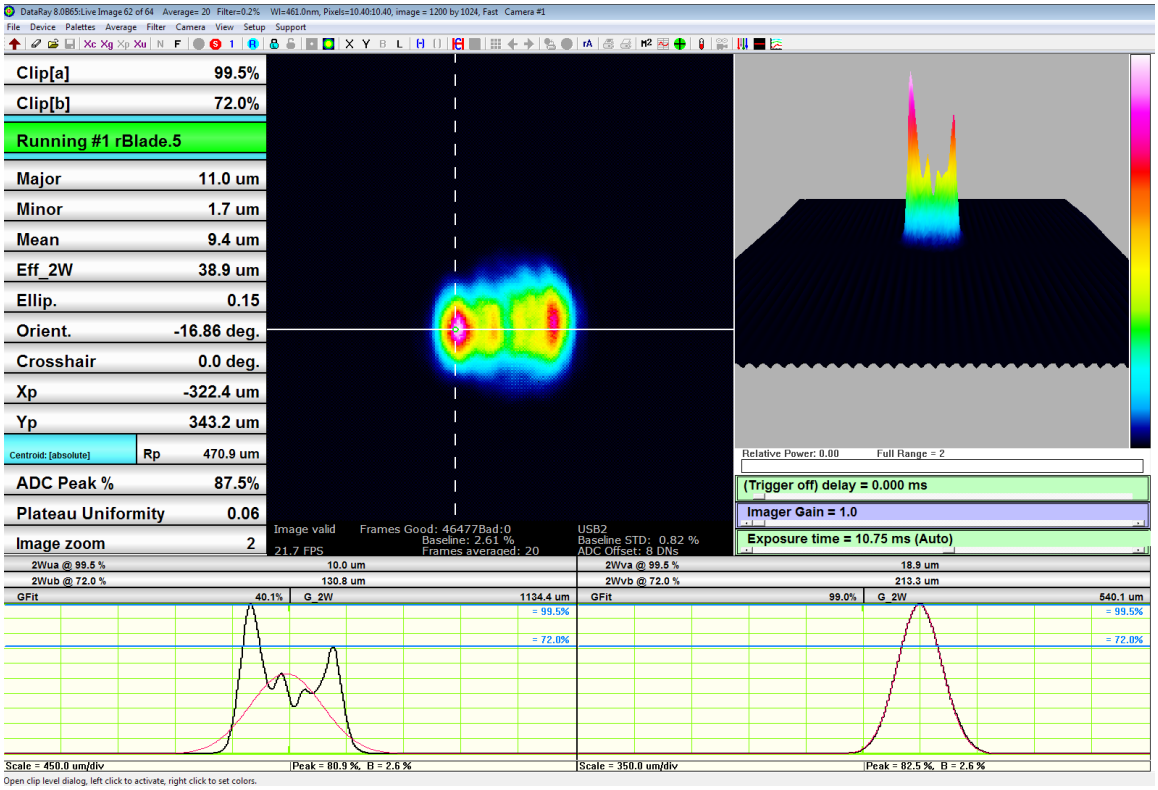

Figure 2.12: Output beam profile from the New Focus VP-0024 461 nm master laser. Although this image was taken after we received the laser back from repair, it still exhibits a similar output mode as when we first received the laser.

nearly-Gaussian beams, each of which was directed to a slave laser for injection locking. After using the laser for about six years, the piezo tuning element died and the laser had to be sent back for repairs. While the laser was undergoing repairs, the injection locking setup was modified so that the two slave lasers are now injection locked from the output

[40] New Focus TLB-6802: a Littman-Metcalf external cavity diode laser (ECDL).

of a single-mode polarization maintaining (SMPM) fiber so that we can easily change master lasers should this laser die again. We also noticed some strange grounding and noise issues with the current master laser system which seemed very sensitive to the particular cables connecting the feedback circuit to the laser driver[41]. We also have concerns about the long-term cost-effectiveness and reliability of the New Focus ECDL[42] and have purchased a Toptica 461 nm ECDL system[43] as a future replacement and to enable additional experiments.

Light from the master laser currently injection locks two slave lasers for boosting the available 461 nm power for the experiment. Currently, we use two New Focus TLB-6802-IJ[44] as the slave lasers, both of which output about 100 mW of power. We have previously tried homebuilding our own 461 nm slave laser with a can-opened blue diode[45] but found it to be unsatisfactory. The "MOT" slave is injection locked at the same frequency as the master laser and its power is split between the blue MOT, 2D collimator, and the imaging beam. The injection beam for the "Zeeman" slave is first shifted by -535 MHz relative to the master laser before injection locking the laser. This allows all the power out from the slave to be used for operating the Zeeman slower instead of taking a hit in power going through an AOM.

The entire 461 nm system is located at the opposite end of our table from the vacuum system and is boxed in an opaque enclosure to contain the blue light, even a little of which can lead to heating our samples. Mechanical shutters[46] are used to provide 100 % extinction.

[41] Similar grounding and noise issues with the New Focus laser was mentioned by Sara Campbell in Jun Ye's group. She documents their experiences in [90].

[42] During the piezo repair, New Focus recommended installation of a new diode and the initially quoted cost, for both the repair and new diode, was about half of buying a new ECDL system. This was significantly reduced after extended discussions with the company.

[43] The Toptica 461 nm laser is capable of outputting about 100 mW.

[44] From what we can tell, these are simply their standard TLB-6802 without the grating and probably using the Nichia NDB4216E non-AR coated diode which is specified to output about 100 mW.

[45] Nichia NDB4216E - a non-AR coated diode with about 100 mW of output power.

[46] Hard drive shutters are used as we've found them to be the most reliable.

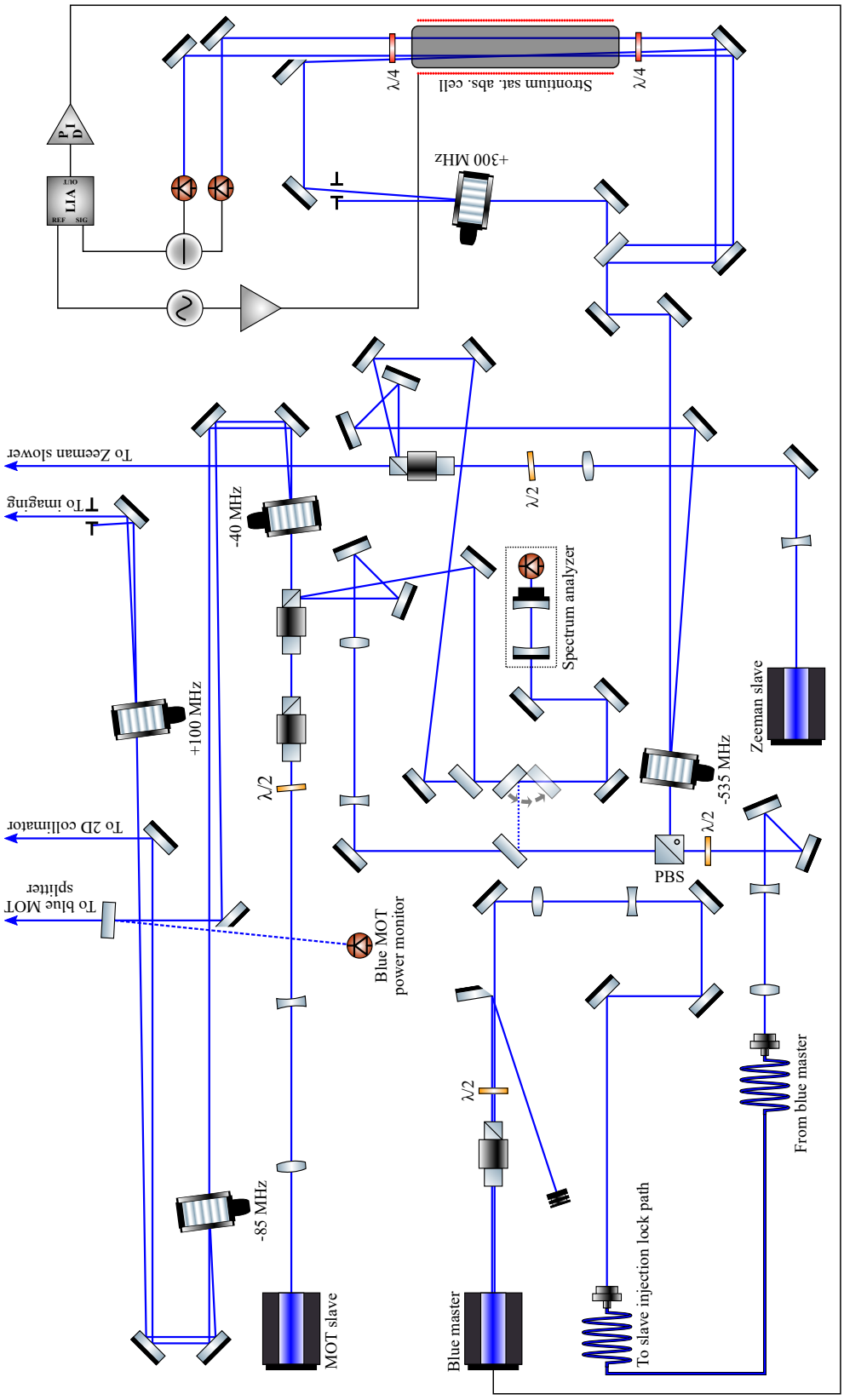

Figure 2.13: Simplified diagram of the 461 nm laser system in the opaque enclosure.

2.5.2 481 nm Repumping System

Before moving on to the narrow line red MOT, the atoms in the metastable reservoir are dark to both the 461 nm and the 689 nm cooling light and must be brought back to the ground state. The current 481 nm repumper system is shown in Fig. 2.14 with light provided by a Toptica DL 100[47] which outputs about 14 mW of power that is shared between the Rydberg, Neutral, and Plasma experiments. For now, this laser is stabilized to a Doppler-

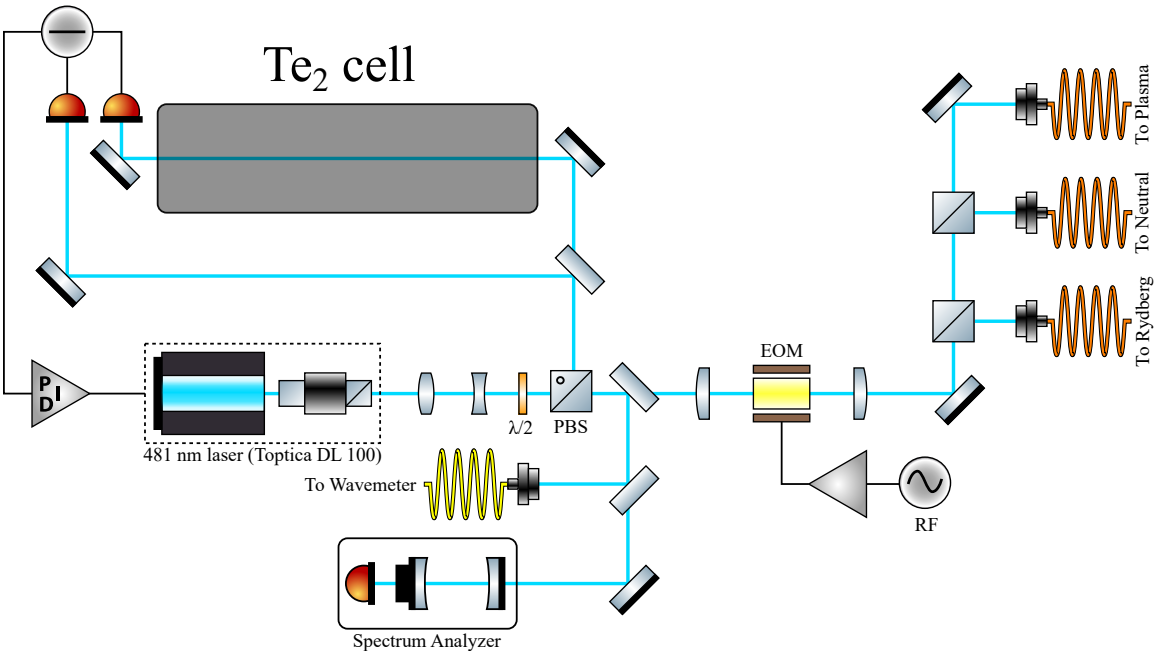

Figure 2.14: Simplified diagram of our current 481 nm repumper laser system. A portion of the light form the 481 nm external cavity diode laser (ECDL) is used to lock to a Doppler-broadened $^{130}Te_2$ line in a cell heated to about 555 °C. The rest of the light is sent through a free-space electro-optic modulator (EOM) at about 565 MHz which applies sidebands to the light in order to address the various isotopes and hyperfine states. The 481 nm light is delivered to the various experiments by multimode (MM) fibers.

broadened $^{130}Te_2$ line [131] that has a transition at 20 776.0886 cm^{-1} [164] which is close to the $(5s5p)\,^3P_2 \rightarrow (5p^2)\,^3P_2$ transition at 20 776.087 cm^{-1} [165]. Originally, when the laboratory was working with a single isotope, simply tuning the lock point to maximize the repumping efficiency for the isotope of interest was sufficient (typically ^{84}Sr since it's the

[47] The laser is equipped with a LD-0488-0060-1 diode.

least abundant). Now that we routinely work with multiple isotopes, a free-space electro-optic modulator (EOM) was introduced to to add sidebands to the 481 nm light in order to address the multiple bosonic isotopes and the hyperfine shift of ^{87}Sr.

2.5.3 689 nm "Red" Laser System

Some details about our narrow line cooling system can be found in [93] and additional resources can be found in [58, 85, 89, 90, 93]. The ^{87}Sr red MOT is particularly well described in [58] and will not be reproduced here.

689 nm Master Laser

A single 689 nm Toptica DL pro ECDL serves as our master laser and is shared between the Rydberg and Neutral experiments. The red master laser is first stabilized to a cavity resonance in a homebuilt high-finesse Fabry-Pérot (FP) cavity[48]. The length of the cavity, and therefore the frequency of the master laser, is then locked to a Doppler-free saturated absorption signal in a heated strontium cell. Since the $(5s^2)\,^1S_0 \rightarrow (5s5p)\,^3P_1$ transition is very weak, the cell is relatively long to allow enough absorption to occur. For most of the experiments described in this thesis, the red master laser was found to have a linewidth of about 30 kHz. A diagram of the red master laser system is presented in [93].

Due to the ease of building 689 nm slave lasers [93], we only need a single 689 nm stabilized master laser system to run both the Rydberg and Neutral experiments. From the red master table, two SMPM fibers run to each experiment with light at the following frequencies:

$f_{\mathbf{master}}$

The red master is locked to -82 MHz of the $(5s^2)\,^1S_0 \rightarrow (5s5p)\,^3P_1$ transition in ^{88}Sr. Slave lasers injection locked at this frequency are used for both trapping and

[48] The cavity has a finesse of about $F \gtrsim 2040$ and additional details can be found in [87].

spectroscopy with the bosonic isotopes. This light is also used to produce the ^{87}Sr red MOT "stir" beam.

$f_{\mathbf{master}} - 1440.440\,\mathrm{MHz}$

Light at this frequency is primarily used when addressing the $(5s^2)\,{}^1S_0, F = 9/2 \rightarrow (5s5p)\,{}^3P_1, F = 11/2$ transition in ^{87}Sr. The approximately $-1.4\,\mathrm{GHz}$ offset is generated by passing the light directly out of the 689 nm master laser though a free-space gigahertz AOM before being coupled in to SMPM fibers for delivery to the Rydberg and Neutral experiments. Currently, a single slave laser is injection locked at this frequency and is used to generate the ^{87}Sr "trap" red MOT light and for spectroscopy involving the $(5s5p)\,{}^3P_1, F = 11/2$ intermediate state.

We currently do not implement a fiber phase noise cancellation system [166, 167] so it's possible that the light reaching the slave lasers is broadened to kilohertz-levels over the $\approx$25 m fibers although it shouldn't be too difficult to implement in the future when necessary.

Rydberg Red Laser System

Once the red light arrives on the Rydberg table, typically only about 1 mW is available which is used to injection lock slave lasers to increase the available 689 nm power. The 689 nm slave lasers are relatively easy to build, as detailed in [93], and there are currently three slave lasers. We found that fiber-coupling the injection beams made them much less sensitive to mechanical drifts and greatly increased the ease of switching the frequency of the slave laser by changing the source of the injection beam. A rejected beam from the isolator is used to monitor the frequency modes of the slave lasers[49].

Figure 2.15 shows what the red MOT system looks like when set up for trapping any combination of isotopes. In practice, we don't always have all the red MOT AOMs lined

[49] In the future, I would recommend using a stray reflection or beam sampler after the isolator instead as the current arrangement could lead to a small amount of light from the spectrum analyzer cavity getting back to the slave lasers (especially since we share the spectrum analyzer cavity with multiple slaves) and possibly leading to laser instability.

up, typically only keeping the AOMs necessary for trapping the isotope(s) for a particular experiment while the other red MOT AOMs are used to generate various other beams (e.g., spectroscopy, "blow away", etc.). Since the red MOT is only operated for a few hundred milliseconds, the zeroth-order from the red MOT AOMs also provide the light for various other purposes as well (e.g., spectroscopy, loss, etc.). Without using a fiber combiner, we're able to devote a lot of power to the red MOT for each isotope, enabling us to use large red MOT beams. The drawback is that we're much more sensitive to misalignments, and the non-Gaussian intensity profiles out of the diodes lead to strange red-MOT shapes.

2.5.4 Optical Dipole Trap (ODT) System

Strontium in the ground $(5s^2)\,{}^1S_0$ state has no magnetic moment meaning it cannot be magnetically trapped, necessitating the use of optical traps. The current setup operates at 1064 nm with the high powers provided by a Nufern NuAMP SUB-1382 fiber amplifier which amplifies a few milliwatts of seed light up to about 50 W. Although there are modifications to reduce amplitude noise in the Nufern fiber amplifier as described in [168, 169], we use ours without any modifications. Due to the high IR powers, fused silica optics are used wherever possible[50].

Both free-space and fibered ODT systems have been used but after having to replace and realign the high-power IR lasers multiple times, we moved to an entirely fibered system so that the trap geometry and alignment on the atoms does not change. The drawback to the entirely fibered ODT system is that it is difficult to efficiently couple more than about 10 W continuously through a fiber without thermal effects degrading the coupling efficiency. A workaround to this issue is to only have high power through the fibers during transfer from the red MOT to produce the deepest trapping potential before quickly moving to the evaporation stage where the powers are ramped down.

[50] There still remain some BK7 elements such as the Brewster plates in the Thorlabs IO-5-1064-VHP optical isolator [168, 169].

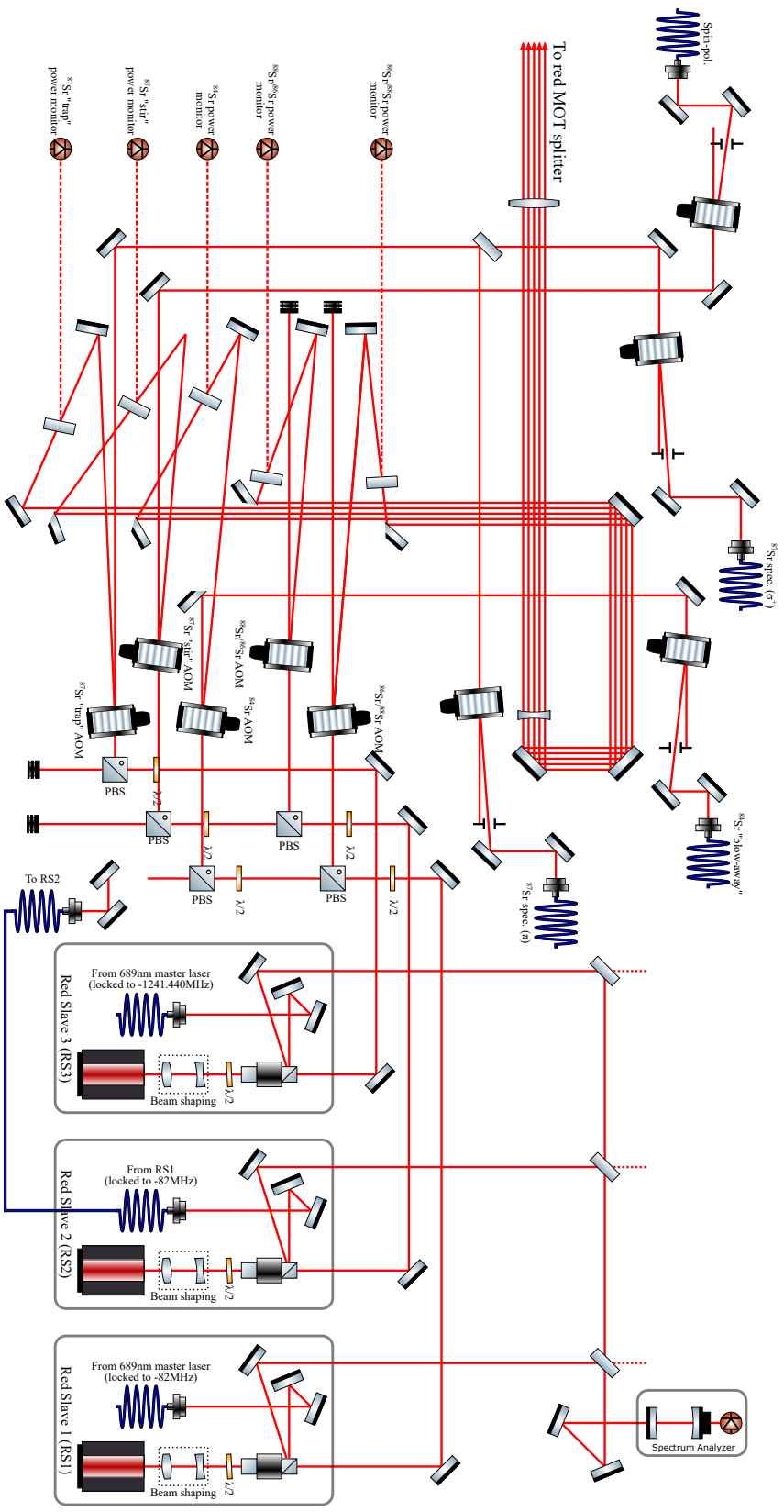

Figure 2.15: Simplified diagram of the red MOT system (when everything is put together) for multi-isotope trapping. The master laser frequency is referenced to the $(5s^2)\,{}^1S_0 \rightarrow (5s5p)\,{}^3P_1$ transition in ^{88}Sr.

For the high-power 1064 nm fibers, we've had good experiences using PMJ-A3AHPC, A3AHPC-1064-6/125-3AS-*L*-1 from OZ Optics. These fibers are air-gapped and feature an endcap on the ends that allows the beam to expand before it enters/exits the fiber, therefore reducing the power density at the fiber tip. The adjustable fiber tip position enables optimization of the coupling efficiency. Although the fiber tips are very delicate, we routinely achieve >7 W of output power from these fibers.

The current main ODT is comprised of a single high-aspect-ratio "sheet" trap with beam waists of about 28 µm (vertical) by 264 µm (horizontal). A beam profile is shown in Fig. 2.16. The design of the sheet trap, the aspect ratio in particular, was limited by the 1 in diameter beam shaping optics and the long distance to the atoms. The horizontal trap

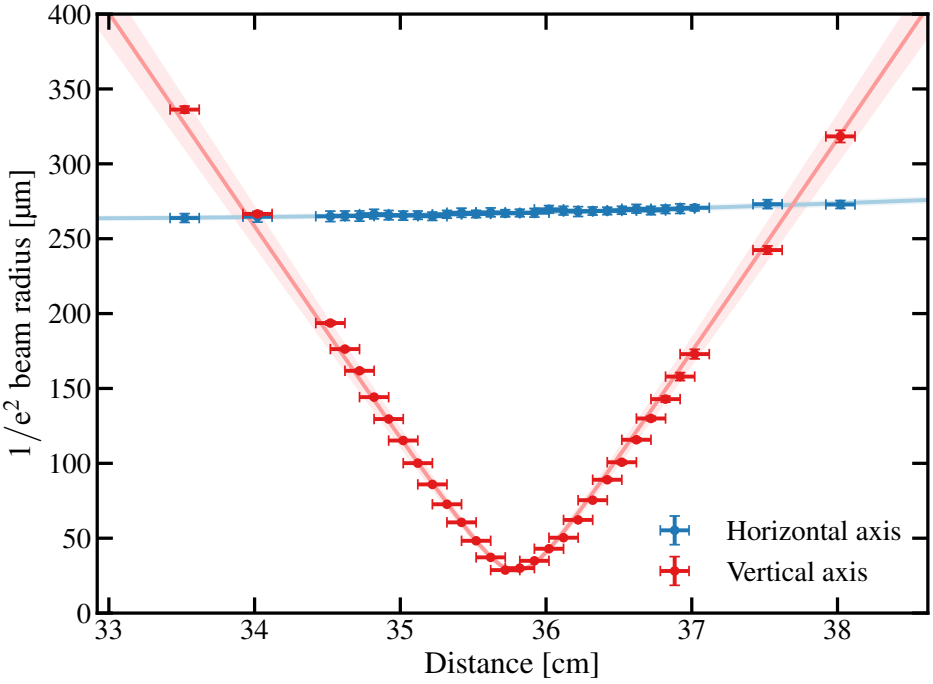

Figure 2.16: Beam profile of the sheet trap from which we fit to obtain the beam waists. For the vertical waist: $w = 28.0(10)$ µm, $z_0 = 35.795(9)$ cm, and $M^2 = 1.18(4)$. For the horizontal waist: $w = 263.5(9)$ µm, $z_0 = 32.3(4)$ cm, and $M^2 = 1.0$. Distances are measured from the end of the cage system assuming ±1 mm uncertainty.

frequency in the main ODT is increased with a circular ODT beam with waists of about 70 µm intersecting the sheet trap at a near vertical angle. The measured beam profile of the

vertical trap is shown in Fig. 2.17. For each experiment, we measure the trap oscillation

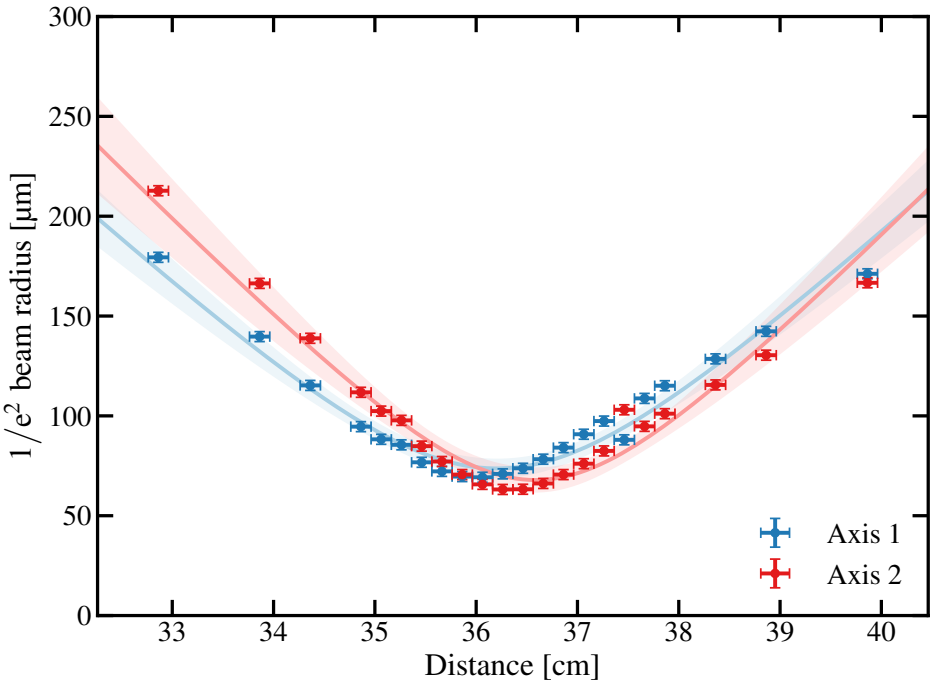

Figure 2.17: Beam profile of the vertical trap from which we fit to obtain the beam waists. For axis 1: $w = 74(4)\,\mu\text{m}$, $z_0 = 36.21(10)\,\text{cm}$, and $M^2 = 1.02(6)$. For axis 2: $w = 68(6)\,\mu\text{m}$, $z_0 = 36.58(11)\,\text{cm}$, and $M^2 = 1.05(8)$. A $\pm 1\,\text{mm}$ uncertainty was assumed in the measured distance and a $\pm 5\,\mu\text{m}$ uncertainty in the measured beam size.

frequencies for the sample of interest.

We attempted to circularly polarized the vertical ODT so that it would minimize the differential shifts and enable cooling in to the ODT [79, 170] but we have not yet observed any improvement. This lack of improvement is likely due to our 689 nm laser system being too broad to take advantage of the reduced shifts.

2.6 Making and Detecting Rydberg Atoms

After creating an ultracold sample of strontium, a 320 nm UV laser system is used to excite them to Rydberg states via the two-photon transition from the intermediate $(5s5p)\,^3P_1$ state. Once the Rydberg atoms are created, they are detected by applying

an electric field ramp that ionizes any Rydberg atoms and directs the resulting electrons towards a micro-channel plate (MCP) detector for counting.

2.6.1 320 nm UV Laser System

Strontium Rydberg atoms are produced using a two-photon transition where a 689 nm and a 320 nm photon drives atoms from the $(5s^2)\,^1S_0$ ground state to either a $(5sns)\,^3S_1$ or $(5snd)\,^3D_J$ Rydberg state. Generation of the 320 nm radiation starts with a tunable, narrow linewidth 1064 nm seed laser that is amplified to about 7.5 W by a fiber amplifier[51]. Two 1064 nm seed lasers have been used for experiments:

Koheras Basik BMY10PztSPm, KOH2038

This laser is capable of continuously scanning multiple gigahertz with both temperature and piezo tuning so it's preferred for experiments requiring scans over large frequency ranges. The narrowest 640 nm lines observed with this seed are around 1 MHz, likely limited by the slow feedback bandwidth of the piezo element.

NP Photonics Rock RFLM-50-3-1064.53-1-S-0

The Rock's piezo feedback bandwidth is quite a bit better than the Koheras with the narrowest features observed being ≈300 kHz. Although the feedback bandwidth results with a narrow 640 nm linewidth, temperature tuning is very slow which makes it difficult to continuously tune over large frequency ranges.

The output of the fiber amplifier pumps a Lockheed Martin Aculight Argos Model 2400 CW optical parametric oscillator (OPO) modified with a sum frequency generation (SFG) stage. Similar to the system described in [171], OPO-SFG is achieved by replacing the standard OPO crystal with a periodically poled, magnesium-oxide-doped lithium niobate crystal (MgO:PPLN) where the first section is designed for OPO and second section is designed for SFG. The cavity dichroics were also replaced to facilitate generation of 640 nm light. The

[51] IPG Photonics YAR-15K-1064-LP-SF ytterbium fiber amplifier.

OPO section uses the $\lambda_P = 1.064\,\mu m$ pump to generate $\lambda_S = 1.6\,\mu m$ and $\lambda_I = 3.2\,\mu m$ light followed by the SFG section then combining the $\lambda_S = 1.6\,\mu m$ with another $\lambda_P = 1.064\,\mu m$ to produce $\lambda_{SFG} = 640\,nm$.

As mentioned in [172], temperature tuning of the crystal is required for efficient 640 nm generation but the Argos system was only designed for heating. A workaround was developed where a water-cooling block is attached to the outside of the OPO cavity housing to lower the temperature enough to where the Argos' internal heater is capable of stabilizing the temperature (see Fig. 2.18). With this addition, we typically get about $(1 - 1.5)\,W$ of 640 nm light.

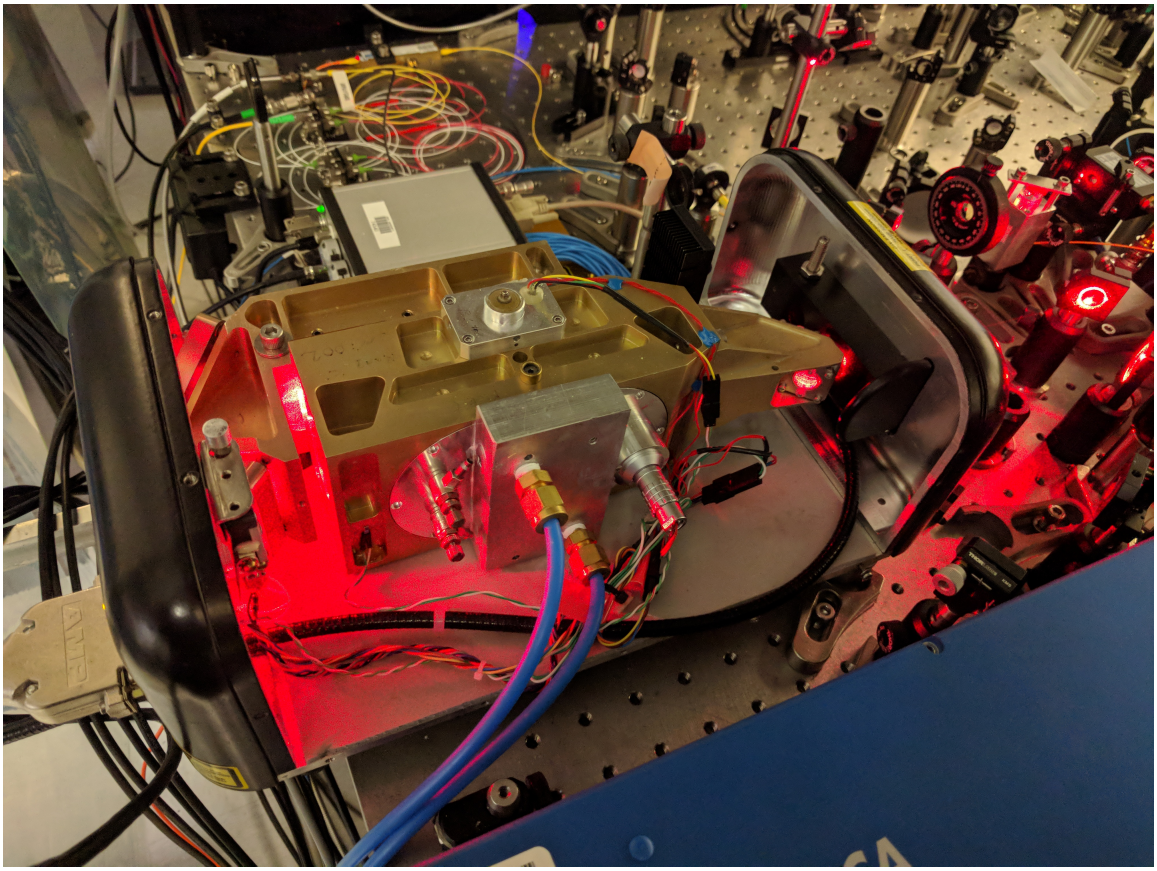

Figure 2.18: Picture of the Lockheed Martin Aculight Argos Model 2400 CW OPO with the custom water-cooling block attached to the cavity housing. The current tubing on the cooling block is too stiff to bend so the laser cover is left off. *** ADD OPTICAL LAYOUT IF I HAVE TIME ***

Stabilization of the 640 nm laser frequency is accomplished with a transfer cavity lock [173–175] where the length of a tunable optical cavity is stabilized by locking a cavity resonance to the 689 nm laser (which itself is stabilized to an atomic reference). The 640 nm laser is then stabilized by locking its frequency to a resonance of the cavity. Some of the details of our transfer cavity are documented in [172, 176]. Briefly, our transfer cavity is constructed from an Invar body with the cavity mirrors attached to a piezoelectric (PZT) stack on each end. The PZT on one end is used to stabilize the cavity length to the 689 nm laser while the other end provides a tunable offset cavity length that can be used to lock to different FSRs of the transfer cavity. Pound-Drever-Hall (PDH) [177, 178] is used to lock the cavity length to the 689 nm reference and to lock the 640 nm to the cavity. The optical layout at the transfer cavity is shown in Fig. 2.19. Tunability is achieved with a broadband

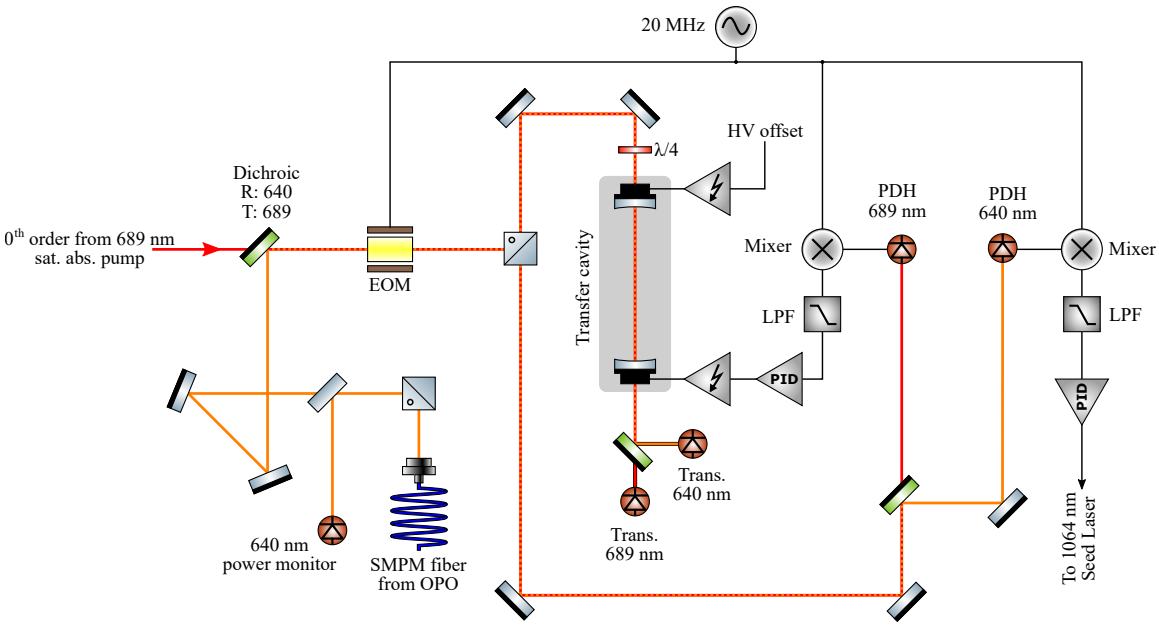

Figure 2.19: Simplified diagram of the transfer cavity setup for stabilizing the 640 nm laser system. The system is modified from the one presented in [172] with the addition of power control for reducing sensitivity to residual amplitude modulation (RAM). *** PUT FIBER EOM IN TO DIAGRAM ***

fiber EOM (fEOM) between the OPO laser output and the transfer cavity which places tunable gigahertz sidebands on the 640 nm light which can be locked to (e.g., see [179]). The 640 nm PDH error signal from the transfer cavity is fed back to the 1064 nm seed laser.

Although we have not done a full characterization of the linewidth of the 640 nm laser, the narrowest Rydberg lines we have seen are about 150 kHz (in 640 nm) with the Rock and can be considered an upper bound on the laser's short-term stability. Longer-term stability isn't as good where drifts of 500 kHz have been observed when scanning over the same Rydberg lines separated by a few days.

The 640 nm output from the OPO is coupled into a commercial Toptica second-harmonic generation (SHG) pro system, which doubles the 640 nm to 320 nm. When well-tuned, the system is capable of outputting >500 mW of power but it tends to degrade over time. Our typical operating powers are closer to about 100 mW and varies depending on the principal quantum number we are exciting.

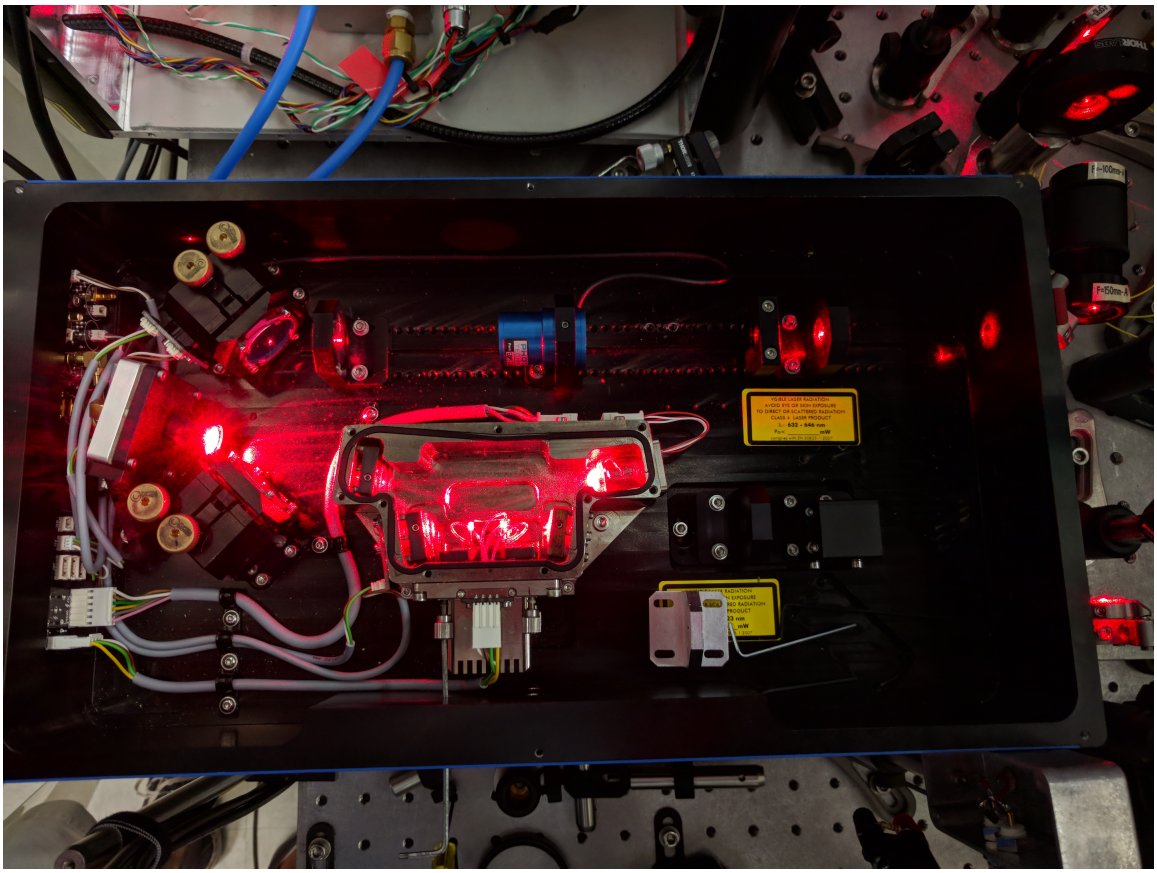

Figure 2.20: Picture of the Toptica second harmonic generation (SHG) pro bow tie doubling cavity. The normally-sealed SHG cavity was opened up for realigning the 640 nm to the SHG cavity.

2.6.2 Electric Field System

Due to the extreme $(n^\star)^7$ scaling of polarizability [28], Rydberg atoms are extremely sensitive to electric fields. In-vacuum electric field plates were installed to mitigate stray electric fields at the location of the atoms and for performing selective field ionization (SFI). The electric field plate system, shown in Figs. 2.21 and 2.22, follows similar designs described in [34, 65] using a split-ring electrode geometry with four quadrant electrodes above and four quadrant electrodes below the atoms. The split-ring electrodes and in

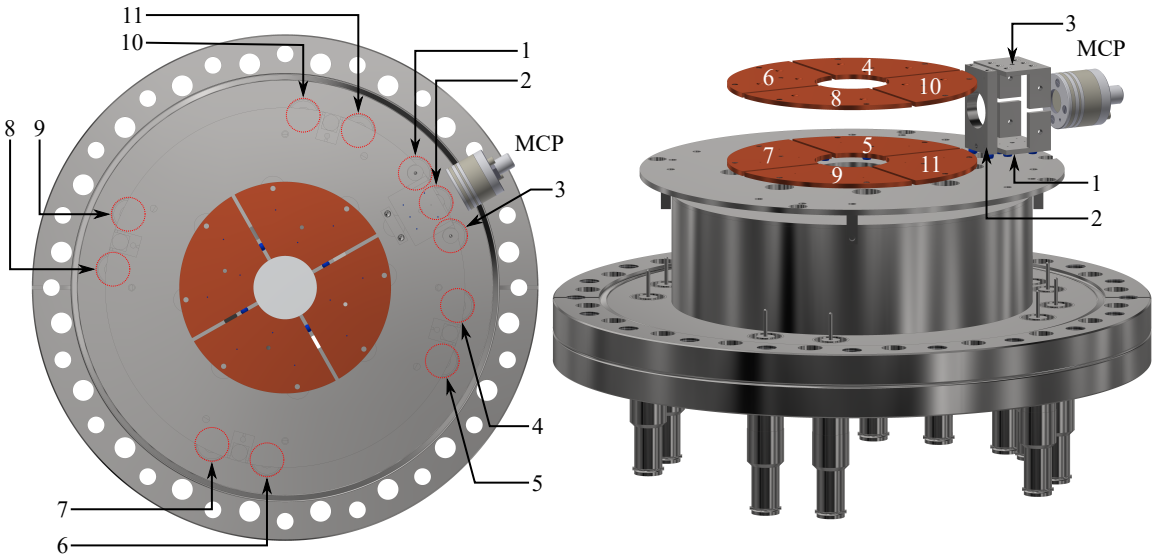

Figure 2.21: CAD renderings of the electric field plates with most of the supporting scaffold removed. Blue spheres represent the sapphire spacers used to isolate the high-voltage components from the grounded support structure. (Left) Top view of the eight electric field plates, Einzel lens, guiding plates, and MCP. The eleven 10 kV SHV feedthroughs are numbered clockwise. Red circles highlight the locations of the feedthroughs which are partially obstructed from view by the bottom scaffold plate. (Right) The electrodes are numbered corresponding to the feedthrough on the bottm flange.

vacuum wires are made from oxygen-free high conductivity (OFHC) copper with stainless steel making up the supporting scaffold, Einzel lens, and guiding plates. Additional details can be found in [180].

We currently have a (limited) ability to change how the electric field plates are ramped depending on whether want want to detect electrons or ions, and whether we want to

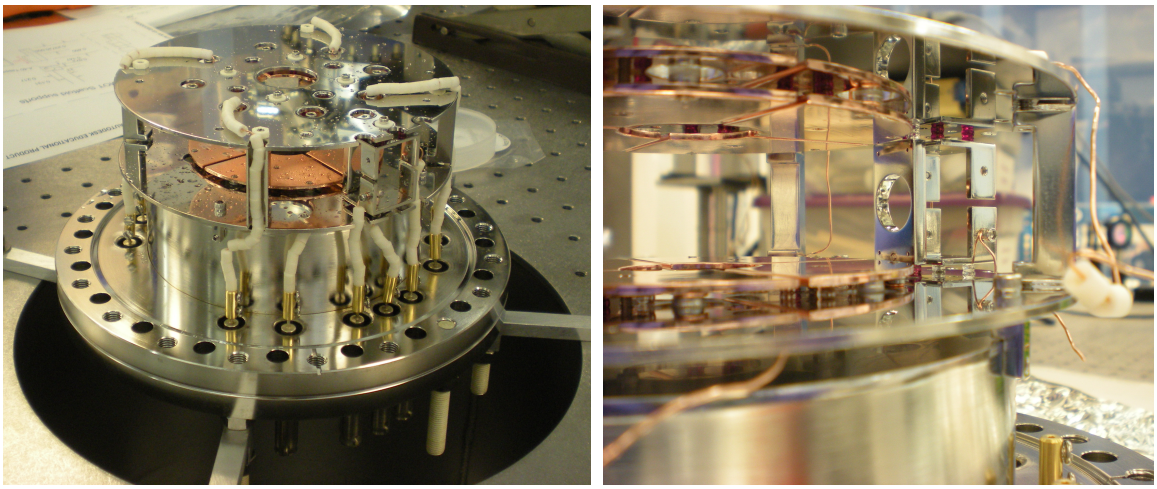

Figure 2.22: (Left) Overview of the actual electric field system mounted on the bottom flange of main chamber. Connections between the feedthroughs and the electric field plates are made with OFHC wires and insulated from the grounded supporting scaffold wtih ceramic fish spine beads. Beryllium-copper in-line barrel connectors with two cross-screws attach the wires to the feedthroughs. (Right) Close up of the eight electric field plates, Einzel lens, and guiding plates. The sapphire spheres (red or clear) which isolate the high-voltage parts from the grounded scaffold structure are also visible.

perform state-resolved selective field ionization (SFI). Most of the work presented in this thesis involves detecting electrons and using the integrated SFI spectra (i.e., simply counting all the electrons). When taking data, we monitor the SFI spectra to make sure that the entire Rydberg signal is captured but the data analysis simply uses the total Rydberg electron counts. An example SFI spectrum is shown in Fig. 2.25.

2.6.3 Charged Particle Detection

One of the major aspects which separates this experiment from most other neutral atom experiments is the ability to detect charged particles. Some of the previous work with strontium Rydberg experiments were carried out in the Neutral apparatus but since it lacked the ability to detect charged particles, atom loss in absorption images was used instead [47, 181, 182]. Our system was designed from the beginning to be able to detect charged particles have found the signal to be incredibly sensitive, providing the ability to detect signals spanning several orders of magnitude [56].

An overview of how the charged particle detection system works is shown in Fig. 2.23. The following procedure outlines how electrons are detected but the system can be configured to detect ions instead. After performing a Rydberg excitation on a sample, an electric field ramp is applied where the plates closer (further) from the MCP are ramped to positive (negative) high-voltage, ionizing any Rydberg atoms produced and directing the electrons towards the MCP. The length of the cables from the HV switch[52] to each of the feedthroughs are about the same length to keep the capacitances approximately equal. The high-voltage

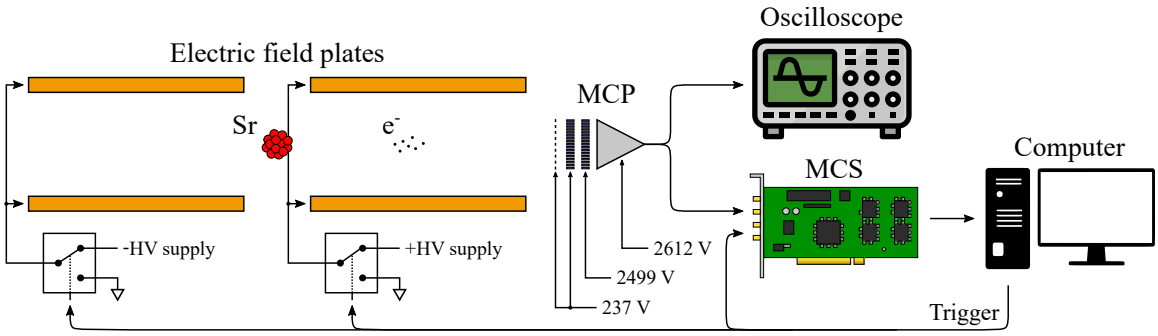

Figure 2.23: Simplified diagram of how the charged particle detection system works when set up for counting electrons.

supplies for the electric field plate ramps are adjusted depending on the principal quantum number of the Rydberg state being excited. Due to the cable capacitance, this also affects the ramp rate of the applied electric field but it doesn't significantly affect the integrated SFI spectrum which is the quantity of interest.

Charged particles are detected with an MCP[53]. For detecting electrons, the front plate is kept fixed at 200 V while the back of the MCP is fixed at 2650 V. The MCP is mounted to a 2.75 in flange with four HV feedthroughs with ceramic insulation. Currently, the MCP's output is first connected to a preamplifier[54] which is then fed in to an RF amplifier[55] to remove DC offsets before going to the MCS[56]. An example Rydberg signal from the MCS

[52] Willamette High Voltage PHVSW-005.
[53] Photonis Advanced Performance Detector (APD) 2 miniTOF. It's important to note that we purchased the version with PEEK components so care must be taken when performing a bake-out.
[54] Stanford Research Systems SR445.
[55] Mini-Circuits ZFL-500LN.
[56] FAST ComTec GmbH MCA-3 P7882.

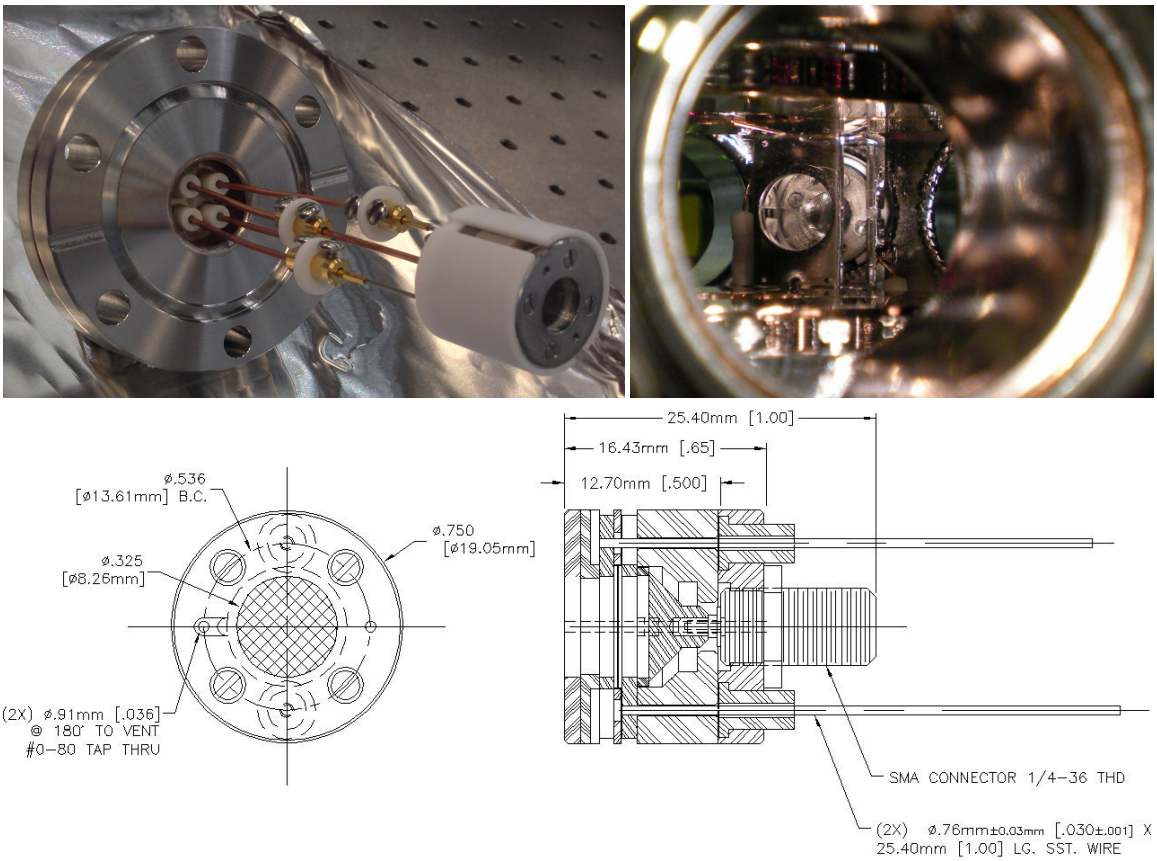

Figure 2.24: (Top left) The MCP mounted to a 2.75 in flange with high-voltage feedthroughs. Connections are made using beryllium-copper inline barrel connectors with ceramic washers placed between the screws to keep the connections from touching each other and the main vacuum chamber. (Top right) The MCP in the main chamber. (Bottom) Mechanical drawing of the APD 2 miniTOF MCP provided by Photonis USA.

is shown in Fig. 2.25.

As seen in Fig. 2.26, MCPs are known to "saturate" and become non-linear as the count rate increases. This non-linearity is important to characterize to determine when the signal changes from the linear regime to the non-linear regime which requires the non-linearity to be taken in to account. Performing a fit to the empirical model

$$y = A[1 - \exp(Bx)] \tag{2.2}$$

determines the constants $A = 44.0(17)$ and $B = -0.059(5)$, allowing for correction of undercounting in the non-linear regime. However, data are typically only recorded under

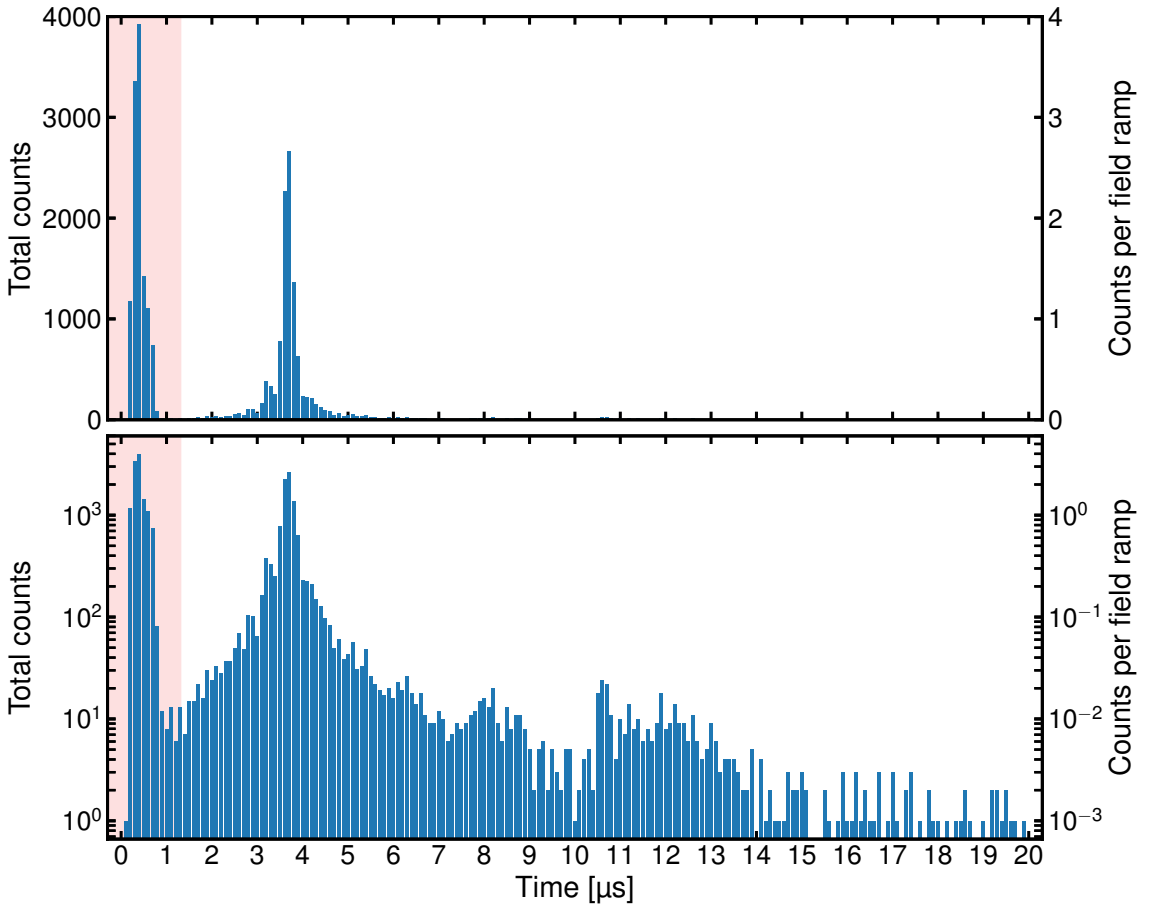

Figure 2.25: Example MCS signal from the $(5s38s)\,^3S_1, F = 11/2$ Rydberg line in ^{87}Sr for a single detuning in (top) linear scale and (bottom) log scale. There are 200 100 ns bins with the electric field ramp starting at $t = 0$ ns. To increase signal, we perform multiple excitation-detection sequences and sum the resulting counts bin-by-bin. Dividing by the total number of loops gives the counts per bin per loop (1000 loops were used in the data above). The MCS detects a large "kick" for first several bins (shaded region) so the data in those bins (shaded region) are dropped before proceeding with the analysis.

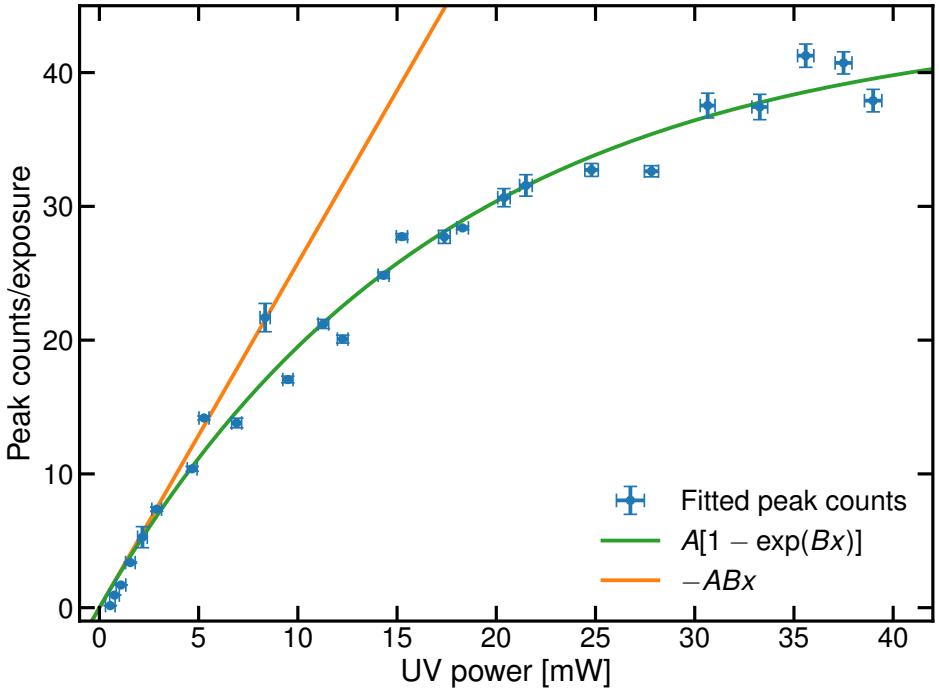

Figure 2.26: Peak integrated SFI spectrum per 10 µs exposure vs. UV excitation power exciting to the $(5s33s)\,^3S_1, F = 11/2$ state of ^{87}Sr in a $B_x \approx 1.1$ G bias field (689 nm power kept constant). The peak counts were obtained by fitting to the Zeeman-split spectra and extracting the height of the $m_F = 11/2$ line. Since 1000 10 µs exposures were used for each frequency point, the fitted peak counts was divided by 1000 to obtain the counts per exposure. Fitting to the empirical model $A[1 - \exp(Bx)]$ results in the coefficients $A = 44.0(17)$ and $B = -0.059(5)$.

conditions where the departures from linearity are relatively small.

2.7 Absorption Imaging

Although the primary signals of interest are obtained from the charged-particle detection system, absorption imaging[57] remains an important diagnostic tool for measuring the atom number and sample temperature (e.g., see [183]). The absorption imaging process involves taking at least two images: an "atom" image and a "background" image:

"Atom" image

[57] Our primary absorption imaging camera is an Andor Luca-R DL-604M-OEM.

The "atom" image is obtained by illuminating the cloud with a resonant pulse of 461 nm light, typically about 10 µs in duration. Since the light is resonant with the $(5s^2)\,^1S_0 \rightarrow (5s5p)\,^1P_1$ transition, the atoms scatter light out of the imaging beam and the resulting shadow is recorded on the camera.

"Background" image

The "background" image is obtained with a pulse of 461 nm identical in duration to the "atom" image (ideally, with the same intensity). This image provides a reference intensity map of the imaging beam without atoms and is generally taken about 100 ms after the "atom" image.

Once the "atom" and "background" images are obtained, the log of their ratio can be related to the density of atoms at a particular pixel which integrated along the imaging beam path (this is generally referred to as a "column" density). The sample temperature can be extracted by performing a "time-of-flight" measurement by introducing a time delay between releasing the atoms from the trap and the imaging pulses [184]. In general, absorption imaging is done with an imaging beam that is far below the saturation intensity of the atomic transition ($s \ll 1$) but it is possible to perform absorption imaging at high intensities [185, 186]. Some additional details of the absorption imaging process is given in [93] and the references therein.

For ultracold gases of strontium, it's particularly important to note that the (on-resonance) absorption cross-section for ^{87}Sr (σ_0^{87}) is different from the bosonic isotopes (σ_0^{88}). For the bosons, the Clebsch-Gordan factor for the $^1S_0 \rightarrow {}^1P_1$ is unity so the absorption cross-section is insensitive to laser polarization (at least in zero magnetic field). This is different in ^{87}Sr due to hyperfine structure where different imaging beam polarizations have different coupling strengths to the upper $(5s5p)\,^1P_1, F = 7/2$, $9/2$, and $11/2$ states. Not only does this make absorption imaging ^{87}Sr sensitive to the initial population of the various $(5s^2)\,^1S_0, F = 9/2, m_F$ substates, the $\tau = 5$ ns lifetime of the $(5s5p)\,^1P_1$ state can also lead to optical pumping effects which redistributes the m_F populations for an imaging

pulse a few microseconds in duration. Calculations using both a rate equation model and the full optical Bloch equations are presented in [86, 89] and show that, for a linearly polarized imaging beam, $\sigma_0^{87}(t_{\text{imaging}} \to \infty)/\sigma_0^{88} \to 0.59$ for both spin-polarized and unpolarized samples of ^{87}Sr.

3. Spectroscopy of ^{87}Sr Triplet Rydberg States

As mentioned in Section 1.2, strontium offers the possibility for exciting ULRRMs in ultracold bosonic and fermionic gases. In these samples, quantum statistics are expected to affect the excitation rate of ULRRMs where bosonic and fermionic samples are expected to exhibit enhanced and suppressed ULRRM excitation rates, respectively. The large nuclear spin of ^{87}Sr also provides an approximation to a classical gas, where the states are distributed among the $2I + 1 = 10$ m_F sublevels of the $(5s^2)\,^1S_0, F = 9/2$ ground state, as comparison. In order to produce ULRRMs in ultracold strontium gases, it is first necessary to locate and identify the parent Rydberg levels.

An ultracold bosonic gas is represented by ^{84}Sr due to the ease of evaporation but, in principle, any of the bosonic isotopes can be used[58]. Most spectroscopic studies of strontium Rydberg systems have focused on the most abundant isotope (^{88}Sr) which has $I = 0$. Not only is there a wealth of experimental measurements available for this isotope, the absence of nuclear spin leads to an excitation spectrum that is relatively well understood [36, 187–194]. Since the other bosonic isotopes also have $I = 0$, it is straightforward to locate Rydberg states in ^{84}Sr upon appropriate rescaling of the Rydberg constant and using the appropriate ionization limit.

In contrast, relatively few studies have been done on ^{87}Sr which has strong hyperfine interactions due to its large $I = 9/2$ nuclear spin. It is this hyperfine interaction that leads to mixing between states normally well-described by LS-coupling in the bosons, significantly complicating the Rydberg excitation spectrum. In previous experimental work [195–199], excitation was performed to singlet $(5sns)\,^1S_0$ and $(5snd)\,^1D_2$ Rydberg levels with triplet

[58] An "ideal" bosonic gas would be better represented with ^{88}Sr as $a_s \approx 0\,a_0$ but this isotope is difficult to evaporate.

states being observed due to state mixing. In order to better understand the ^{87}Sr Rydberg states, we mapped the triplet Rydberg series by two-photon excitation to $(5sns)\,^3S_1$ and $(5snd)\,^3D_{1,2,3}$ hyperfine states via the $(5s5p)\,^3P_1$ intermediate state. To our knowledge, this is the first measurement of ^{87}Sr Rydberg states by direct excitation utilizing the $(5s5p)\,^3P_1$ intermediate state.

3.1 Ionization Limit of ^{87}Sr

The first indication that the Rydberg levels of ^{87}Sr were not as simple as for the bosonic isotopes was the reported ionization limit, $E_{\text{ion}}^{87} = 45\,932.2861(10)\,\text{cm}^{-1}$ [165, 188], being well above those of the bosons as shown in Fig. 3.1 and Tab. B.7. Mass-scaling the ionization

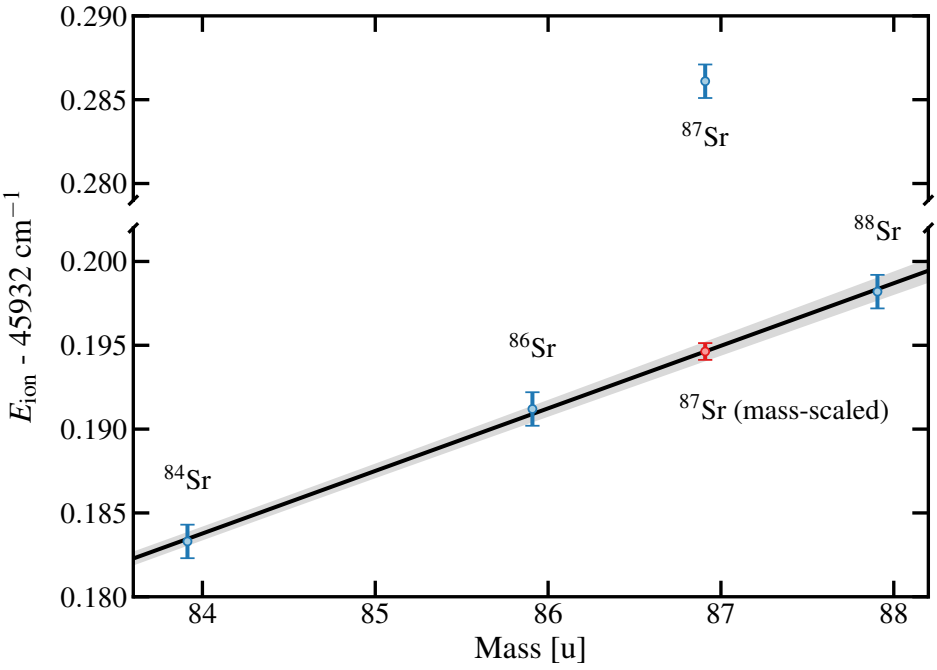

Figure 3.1: Reported isotope ionization limits E_{ion} vs. mass (blue points). A linear fit (black line) is used to estimate the E_{ion}^{87} for an assumed $I = 0$ ^{87}Sr atom from the ionization energies of the bosonic isotopes. Ionization energies from [165, 188] and atomic masses from [200] (see Tab. B.7 for additional information).

energies of the bosonic isotopes suggests that the ionization energy for an assumed $I = 0$ ^{87}Sr atom should be approximately $45\,932.1946(5)\,\text{cm}^{-1}$. This value is about 2.74 GHz

below the reported ionization energy.

The source of this discrepancy is likely related to the hyperfine interaction in the ground state of $^{87}Sr^{+}$. Since it has a rubidium-like structure with a single s valence electron outside a filled [Kr] core, the hyperfine interaction can be written as (see, e.g., [71, 201])

$$\hat{V}_{\rm hf} = A_{\rm hf}\hat{\mathbf{I}}\cdot\hat{\mathbf{J}} = A_{\rm hf}\hat{\mathbf{I}}\cdot\hat{\mathbf{S}} \tag{3.1}$$

where $\mathbf{J} = \mathbf{L} + \mathbf{S}$ and $A_{\rm hf}$ is the strength of the magnetic dipole hyperfine interaction with $\mathbf{L}$, $\mathbf{S}$, and $\mathbf{J}$ referring to the ground-state of $^{87}Sr^{+}$ (singly-ionized ^{87}Sr). Note that there are no higher order contributions (e.g., electric quadrupole) since the valence electron is in an s-state so only the contact interaction is non-zero [202]. Following the usual procedure by defining $\mathbf{F} = \mathbf{J} + \mathbf{I}$, the energy shift can be evaluated as

$$\langle\hat{V}_{\rm hf}\rangle = \frac{1}{2}A_{\rm hf}\,\langle\hat{\mathbf{F}}^2 - \hat{\mathbf{J}}^2 - \hat{\mathbf{I}}^2\rangle = \frac{1}{2}A_{\rm hf}[F(F+1)\ - J(J+1)\ - I(I+1)\,] \tag{3.2}$$

In the ground state of $^{87}Sr^{+}$, $S = s = 1/2$ and $I = 9/2$ meaning the the $(5s)\,^2S_{1/2}$ is split in to $F = 4$ and 5 components. Using $A_{\rm hf} = -1\,000\,473.673(11)\,\text{kHz}$[59] [203], the $F = 4$ and $F = 5$ states in $^{87}Sr^{+}$ are shifted by

$$\langle\hat{V}_{\rm hf}\rangle = \begin{cases} -\frac{11}{4}A_{\rm hf} = 2.751\,302\,601(30)\,\text{GHz}, & F = 4 \\ \frac{9}{4}A_{\rm hf} = -2.251\,065\,764(25)\,\text{GHz}, & F = 5 \end{cases} \tag{3.3}$$

Notice that $\langle\hat{V}_{\rm hf}(F=4)\,\rangle \approx 2.75\,\text{GHz}$ nearly matches the 2.74 GHz discrepancy between the reported ionization limit of ^{87}Sr and the ionization limit determined by mass-scaling from the bosonic isotopes. This seems reasonable since most of the earlier spectroscopic work on ^{87}Sr primarily focused on the singlet Rydberg states which converges to the upper $F = 4$ state of $^{87}Sr^{+}$ [198].

[59] Sunaoshi et al. determined $A_{\rm hf}$ by measuring the splitting of the $(5s)\,^2S_{1/2}, F = 4$ and $(5s)\,^2S_{1/2}, F = 5$ ground state of $^{87}Sr^{+}$ in an ion trap. They measured the splitting to be $E_{F=4} - E_{F=5} = 5\,002\,368.363(57)\,\text{kHz}$.

3.2 Publication: Spectroscopy of ^{87}Sr Triplet Rydberg States

Below is a reproduction of our work, published in [84], which was a combined experimental and theoretical study of $(5sns)\,^3S_1$ and $(5snd)\,^3D_{1,2,3}$ Rydberg states in ^{87}Sr. The experimental work was undertaken at Rice University with theory collaborates at the Institute for Theoretical Physics of the Vienna University of Technology. R.D., J.D.W., and S.K.K. took the experimental data, R.D. compiled and analyzed the data, and S.Y. developed the theoretical framework for ^{87}Sr and performed the calculations to extract the quantum defects from the experimental data. The paper was written collaboratively between R.D., S.Y., and F.B.D. S.Y. wrote the theoretical section, R.D. wrote the experimental section, and S.Y. and F.B.D. wrote the introduction, results, and conclusion sections. All three discussed the introduction, results, and conclusion.

Phys. Rev. A **98**, 042505 (2018)

R. Ding, J. D. Whalen, S. K. Kanungo, T. C. Killian, and F. B. Dunning

Department of Physics and Astronomy, Rice University, Houston, Texas 77005, USA

S. Yoshida and J. Burgdörfer

Institute for Theoretical Physics, Vienna University of Technology, A-1040 Vienna, Austria, European Union

3.2.1 Abstract

A combined experimental and theoretical spectroscopic study of high-n, $30 \lesssim n \lesssim 100$, triplet S and D Rydberg states in ^{87}Sr is presented. ^{87}Sr has a large nuclear spin $I = 9/2$, and at high-n the hyperfine interaction becomes comparable to, or even larger than, the fine structure and singlet-triplet splittings, which poses a considerable challenge both for precision spectroscopy and for theory. For high-n S states, the hyperfine shifts are evaluated nonperturbatively, taking advantage of earlier spectroscopic data for the $I = 0$ isotope ^{88}Sr,

which results in good agreement with the present measurements. For the D states, this procedure is reversed by first extracting from the present ^{87}Sr measurements the energies of the $^3D_{1,2,3}$ states to be expected for isotopes without hyperfine structure (^{88}Sr), which allows the determination of corrected quantum defects in the high-n limit.

3.2.2 Introduction

Rydberg excitation in dense cold-atom samples can lead to the formation of ultralong-range Rydberg molecules in which scattering of the Rydberg electron from neighboring ground-state atoms leads to the binding of one or more ground-state atoms in multiple possible vibrational levels [47, 52–55, 204–212] Measurements of such weakly bound Rydberg molecules have also been extended to dense Bose-Einstein condensates (BECs) and higher-n values where the Rydberg electron orbit can enclose tens to hundreds of ground-state atoms [56, 81, 213].

The interaction between the excited Rydberg electron and a ground-state atom can be described using a Fermi pseudopotential. For strontium, except at short ranges, s-wave scattering dominates due to the lack of a p-wave resonance. This results in an oscillating molecular potential that reflects the modulations in the electron probability density [53]. The largest, and deepest, potential well is located near the outer classical turning point and the wave function of the ground vibrational state of the Rydberg molecule is strongly localized in this region. Thus, the probability for forming a ground-state dimer molecule will depend on the likelihood of initially finding a pair of ground-state atoms at the appropriate internuclear separation R. By varying n and the location of the potential minimum, one can probe the pair correlation function in the ultracold gas. This provides an opportunity to examine the influence of quantum statistical properties on Rydberg molecule formation. Strontium is an attractive candidate for such a study because it possesses both bosonic (^{84}Sr, ^{86}Sr, and ^{88}Sr) and fermionic (^{87}Sr) isotopes, all of which have been cooled to degeneracy. The excitation spectra for the bosonic isotopes are particularly simple as they have zero

nuclear spin ($I = 0$) and therefore no hyperfine structure. In contrast, ^{87}Sr has nuclear spin $I = 9/2$, which results in hyperfine interactions that greatly complicate the excitation spectrum.

Several studies of Rydberg spectra for bosonic ^{88}Sr have been reported [59, 187, 189]. These studies primarily centered on lower-n states ($n \lesssim 40$) and focused on the perturbations introduced by channel interactions and their treatment using multichannel quantum-defect theory (MQDT). Information on higher-n levels was typically obtained by extrapolating the measured quantum defects using the Rydberg-Ritz formula. Such extrapolation is known to be an effective method for predicting the energies of high-n Rydberg states whose quantum defects are essentially n independent and therefore nearly constant. This, however, is not true for strontium D states whose quantum defects exhibit a relatively strong n dependence.

Experimental and theoretical studies of the spectrum for ^{87}Sr have also been reported [196–199, 214, 215]. These include measurements at low n, where the hyperfine interaction can be treated as a weak perturbation, and at high n ($n \sim 100$), where the hyperfine shift becomes comparable to or even larger than the energy spacing between adjacent unperturbed states. Analysis of the high-n spectrum therefore poses a considerable challenge and requires use of nonperturbative methods. One possible approach is to take advantage of the accurate spectral information available for the bosonic isotope ^{88}Sr and use it to estimate the spectrum for ^{87}Sr [196–199]. For S states this approach provides energy levels that agree reasonably well with measured data [196–199]. A similar method utilizing a truncated basis set has been used to study low-n ($n < 20$) ^{87}Sr D states [216].

However, the high-n levels were analyzed by MQDT [215] because no corresponding measured levels for the bosonic isotopes were available. Earlier spectroscopic studies utilized a heat pipe, which can introduce uncertainties due to Doppler and pressure broadening. Moreover, Stark shifts due to the presence of stray fields could not be controlled. Indeed, for high-n states, $n \gtrsim 100$, additional *ad hoc* corrections were introduced to obtain agreement

between the theoretical estimates and the experimental measurements.

In this work we measure and analyze the excitation spectrum for high-n ($50 \lesssim n \lesssim 100$) S and D Rydberg states created in an ^{87}Sr ultracold gas using two-photon excitation as a precursor to planned studies of Rydberg molecule formation in fermionic gases. Measurements using ultracold atoms are expected to be more accurate than measurements in a heat pipe because Doppler and pressure broadening are well suppressed and stray fields can also be controlled. In the present two-photon excitation scheme the intermediate $(5s5p)\,^3P_1$ state is used instead of the $(5s5p)\,^1P_1$ state employed in earlier studies. Since the $(5s5p)\,^3P_1$ state has a much longer lifetime than the $(5s5p)\,^1P_1$ state ($\tau = 21\,\mu$s and $\tau = 5\,$ns, respectively), broadening induced by scattering off the intermediate state is also suppressed.

We compare our experimental data with predictions derived from a semiempirical theoretical description that exploits spectroscopic data for the bosonic isotopes. This approach produces satisfactory agreement with the present measurements. We also derive improved Rydberg-Ritz formulas for both S and D states at very high n.

3.2.3 Theoretical Approach

An *ab initio* theoretical description of the electronic structure of strontium Rydberg atoms with a precision of $\sim$10 MHz or better is currently out of reach. Thus, in order to arrive at a quantitative and predictive description, it is necessary to resort to semiempirical methods. The theoretical approach adopted here follows that of earlier work by Beigang and co-workers [198, 199].

The underlying idea is to exploit the much simpler (and for S states, better known) electronic structure of the bosonic isotope ^{88}Sr as reference for ^{87}Sr to accurately account for the perturbations introduced by hyperfine interactions by direct diagonalization. The spectroscopic data for ^{88}Sr thus serve as an analog simulation of the full N-electron Schrödinger equation that accounts for electron correlation and configuration interactions, which are

tacitly assumed to be the same for all the isotopes. Isotope-specific interactions are then taken into account nonperturbatively by diagonalizing the full Hamiltonian which includes the hyperfine interaction. Accordingly, the Hamiltonian $H(87)$ for ^{87}Sr is written as

$$H(87) = H_0(88, m_{87}) + V_{\rm hf}, \tag{3.4}$$

where $H_0(88, m_{87})$ plays the role of the unperturbed Hamiltonian that yields the eigenstates and eigenenergies, i.e., spectral lines, for ^{88}Sr but rescaled by the isotope shift corresponding to the reduced mass $m_{87} = m_e M_{87}/(m_e + M_{87})$, where m_e is the electron mass, M_{87} is the mass of $^{87}Sr^+$ ion, and $V_{\rm hf}$ is the hyperfine interaction. Corrections beyond the elementary isotope shift, in particular, the mass polarization correction, can be estimated from earlier data for helium Rydberg states [217–219] and, upon rescaling to Sr, are found to be $\lesssim$1 MHz and can therefore be neglected.

The Hamiltonian $H(87)$ [Eq. (3.4)] is diagonalized using the basis states $|[(5s n\ell)\,^{2S+1}L_J, I]F\rangle$ constructed by the coupling of angular momenta $\vec{\mathbf{F}} = \vec{\mathbf{J}} + \vec{\mathbf{I}}$, where $\vec{\mathbf{I}}$ is the nuclear spin and $|(5s n\ell)\,^{2S+1}L_J\rangle$ are the eigenstates of $H_0(88, m_{87})$. We note that we retain the conventional Russell-Saunders $^{2S+1}L_J$ notation for the eigenstates of $H_0(88, m_{87})$ even though S and L are not exactly conserved quantum numbers in the presence of the spin-orbit interaction. In this basis $H_0(88, m_{87})$ is diagonal with corresponding eigenenergies

$$E^{(0)}_{n,S,L,J} = E^{(0)}_{\rm ion} - \frac{R(m_{87})}{(n - \mu^{(0)}_{n,S,L,J})^2}, \tag{3.5}$$

where $E^{(0)}_{\rm ion}$ is the energy corresponding to the first ionization threshold of ^{87}Sr assuming $I = 0$, $\mu^{(0)}_{n,S,L,J}$ is the quantum defect for the state $|(5s n\ell)\,^{2S+1}L_J\rangle$, and $R(m_{87}) = R_\infty m_{87}/m_e$ with the Rydberg constant R_∞. In the following we use either directly measured or extrapolated (at high-n) quantum defects for ^{88}Sr as input.

The hyperfine interaction results from the interaction between an electron and the electric and magnetic multipoles of the nucleus [220]. For singly excited high-n strontium atoms with two electrons outside closed shells, $V_{\rm hf}$ is governed by the interaction of the $5s$ valence and $n\ell$ Rydberg electrons with the ^{87}Sr nuclear spin $I = 9/2$. Because of the $(n^*)^{-3}$ scaling

of the hyperfine interaction [221], the hyperfine shift associated with the Rydberg electron for high-n values ($n > 20$) can be estimated to be $\lesssim$1 MHz and can therefore be safely neglected. ($n^* = n - \mu^{(0)}_{n,S,L,J}$ is the effective quantum number and $n^* \simeq 1.5$ for the $(5s^2)\,^1S_0$ ground state.) Therefore, the hyperfine interaction $V_{\rm hf}$ can be approximated by the contact interaction of the inner (or valence) $5s$ electron with the nucleus [199]

$$V_{\rm hf} \simeq a_{5s}\vec{\mathbf{s}}_{\rm in}\cdot\vec{\mathbf{I}}, \tag{3.6}$$

where $\vec{\mathbf{s}}_{\rm in}$ is the spin of the inner $5s$ electron. The hyperfine coupling constant can be extracted from the ionization limit yielding $a_{5s} \simeq -1.0005\,$GHz [203] [see the discussion following Eq. (3.10)]. Since the interaction of the Rydberg electron with the nuclear spin is negligibly small, the hyperfine interaction $V_{\rm hf}$ is approximately independent of n. This n independence of $V_{\rm hf}$ [Eq. (3.6)] has profound consequences for the Rydberg spectrum described by the isotope-rescaled Hamiltonian $H(87)$ [Eq. (3.4)]. The matrix elements of the reference Hamiltonian $H_0(88, m_{87})$ depend on the fine-structure splitting $\Delta E^{(0)}_J = |E^{(0)}_{n,S,L,J+1} - E^{(0)}_{n,S,L,J}|$ which, taking D states as an example, scales as (in GHz)

$$\Delta E^{(0)}_J \sim 4.4\times 10^5/{n^*}^{3.4} \tag{3.7}$$

in the high-n regime (see Fig. 3.2). The singlet-triplet splittings scale as (in GHz)

$$\Delta E^{(0)}_S = \left|E^{(0)}_{n,1,L,J} - E^{(0)}_{n,0,L,J}\right| \sim 1.8\times 10^6/{n^*}^3 \tag{3.8}$$

and the Coulomb splittings scale as (in GHz)

$$\Delta E^{(0)}_n = \left|E^{(0)}_{n+1,S,L,J} - E^{(0)}_{n,S,L,J}\right| \sim 5.8\times 10^6/{n^*}^3. \tag{3.9}$$

Therefore, as n^* increases, $V_{\rm hf}$ becomes comparable in size first to the fine structure splitting, then to the singlet-triplet splitting, and finally to the Coulomb splitting. This is illustrated in Fig. 3.2 and leads to strong state mixing. In consequence, Eq. (3.4) cannot in general be treated perturbatively but rather must be diagonalized.

The present approach is a variant of MQDT [61, 215] commonly used to analyze the energy levels of multielectron systems. In MQDT, instead of describing microscopically the

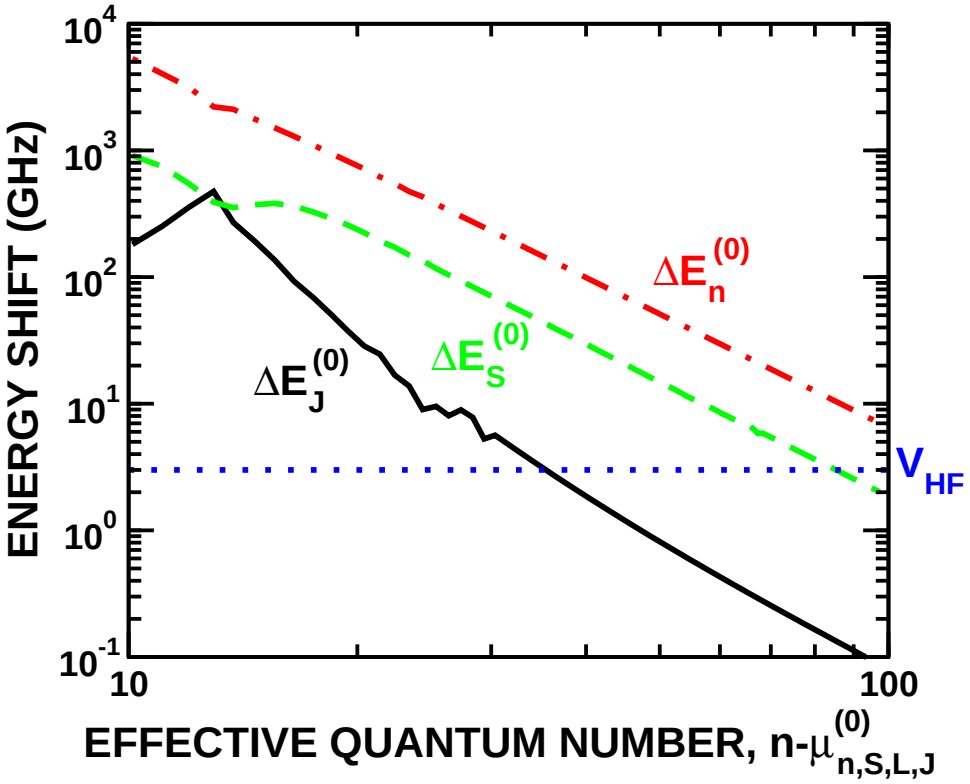

Figure 3.2: The n scaling of the fine-structure splitting $\Delta E_J^{(0)}$ (——), the spin singlet-triplet splitting $\Delta E_S^{(0)}$ (– – –), and the level separation $\Delta E_n^{(0)}$ (—·—) between like states in ^{88}Sr that differ in n by one. Also shown is the strength of the hyperfine interaction in ^{87}Sr (· · · ·). The splittings $\Delta E_J^{(0)}$ and $V_{\rm hf}$ refer to ^3D states with $J = 1$ and $J = 2$ and are evaluated using the measured data and their extrapolation.

core-electron interaction in each channel and the mixing of different channels, interactions are represented by a set of parameters (e.g., scattering phase shifts and K matrices) which are typically extracted from the measured data. In the current approach, a different set of parameters, i.e., the measured quantum defects [or, equivalently, energy levels Eq. (3.5)] of isotopes with vanishing nuclear spin are used.

An alternative approach to describe the energy levels in strontium is to use a two-active-electron (TAE) model [222] which treats the electron-electron interactions between the outer electrons microscopically while their interaction with the $N-2$ electron core is parameterized in terms of model potentials. The currently available model potentials yield quantum defects with an accuracy of $\sim$0.01. This uncertainty is larger than that present

in current experimental data, especially for low-n states. Therefore, we do not employ the TAE approximation in Eq. (3.4) for deriving results to compare with experiment. However, we do use TAE calculations to probe the validity of the approximations entering into our semiempirical description. For example, the approximation of the hyperfine interaction by the contact term [Eq. (3.6)] is confirmed by TAE calculations. Contributions from the interactions between the Rydberg electron and the magnetic dipole and electric quadrupole moments of the core ion are found to be of the order of 100 Hz (or smaller) around $n = 100$. Moreover, the mixing of $4dn\ell$ and $5pn\ell$ channels in the $|(5sn\ell)\,^{2S+1}L_J\rangle$ state is negligibly small (less than 0.02 %) and therefore the polarization of the second (inner) valence electron can be neglected.

In the following we consider two-photon excitation of ^{87}Sr from the ground state to S or D Rydberg states. In the limit $n \to \infty$ both the S and D Rydberg states converge to the $^{87}\mathrm{Sr}^+$ ($(5s)\,^2S_{1/2}$) ionization limit. Because of the hyperfine interaction, this ionization limit is split into two components with $F = 4$ or 5,

$$E_{\mathrm{ion}}(F) = E_{\mathrm{ion}}^{(0)} + \frac{a_{5s}}{2}\left(F(F+1) - I(I+1) - \frac{3}{4}\right), \tag{3.10}$$

where $E_{\mathrm{ion}}^{(0)}$ is the threshold for ^{87}Sr assuming its nuclear spin $I = 0$. From the splitting of the ionization thresholds $E_{\mathrm{ion}}(F = 4) - E_{\mathrm{ion}}(F = 5)$, the hyperfine constant a_{5s} is determined. (Note that F has integer values for $^{87}\mathrm{Sr}^+$ rather than half-integer values for ^{87}Sr.)

Energy Shift of S States

In ^{87}Sr, there are four S basis states present within a single Rydberg n manifold with, e.g., $m_F = 1/2$, i.e., $|[(5sns)\,^1S_0, I]F = I\rangle$ and $|[(5sns)\,^3S_1, I]F = I, I \pm 1\rangle$. (Note that the hyperfine interaction is independent of m_F.) For evaluation of the matrix elements of the hyperfine interaction V_{hf} in this basis, the angular integrals can be performed analytically [223]. Since F is an exact quantum number, substates of different F remain decoupled under the action of V_{hf}. Consequently, the hyperfine shifts of the states $F = I \pm 1$ are given

by the diagonal elements of the matrix $V_{\rm hf}$ (in GHz)

$$\langle[(5sns)\,^3S_1, I]F = I+1|\,V_{\rm hf}\,|[(5sns)\,^3S_1, I]F = I+1\rangle = \frac{1}{2}a_{5s}I \simeq -2.25 \tag{3.11}$$

and

$$\langle[(5sns)\,^3S_1, I]F = I-1|\,V_{\rm hf}\,|[(5sns)\,^3S_1, I]F = I-1\rangle = -\frac{1}{2}a_{5s}(I+1) \simeq 2.75. \tag{3.12}$$

Because of the orthogonality of the radial wave functions, states with different n belonging to the same spin multiplet are decoupled. In the limit $n \to \infty$, these states converge to the ionization limits $E_{\rm ion}(F = I \pm 1/2)$ [Eq. (3.10)] associated with the states $(5s)\,^2S_{1/2}$, $F = 5$ [Eq. (3.11)] or $F = 4$ [Eq. (3.12)] of the $^{87}Sr^+$ ion. For $F = I$, the hyperfine interaction causes singlet-triplet mixing and leads to a breakdown of the LS-coupling scheme. Since the radial functions belonging to different spin multiplets are not pairwise orthogonal, the matrix $V_{\rm hf}$ for the the subspace $F = I$ becomes

$$\langle[(5sn's)\,^1S_0, I]F = I|\,V_{\rm hf}\,|[(5sns)\,^1S_0, I]F = I\rangle = 0, \tag{3.13}$$

$$\langle[(5sn's)\,^3S_1, I]F = I|\,V_{\rm hf}\,|[(5sns)\,^3S_1, I]F = I\rangle = -\frac{1}{2}a_{5s}\delta_{n,n'}, \tag{3.14}$$

$$\langle[(5sn's)\,^1S_0, I]F = I|\,V_{\rm hf}\,|[(5sns)\,^3S_1, I]F = I\rangle = \frac{1}{2}a_{5s}\sqrt{I(I+1)}O_{n,n'}, \tag{3.15}$$

where $O_{n,n'}$ is the overlap between the singlet and the triplet radial wave functions and can be estimated semiclassically [224]. For example, $O_{n,n'} \simeq 0.98$ for $n = n'$, $O_{n,n'} \simeq 0.1$ for $|n - n'| = 1$, and continues to rapidly decrease with increasing $|n - n'|$.

Using this hyperfine interaction matrix together with the Hamiltonian $H_0(88, m_{87})$ derived from the measured energies for $n \leq 70$ $^1S_0$ states [188] and for $n \leq 40$ $^3S_1$ states [189] in ^{88}Sr as well as values obtained by extrapolation [59] to higher n using the Rydberg-Ritz formula, the Hamiltonian Eq. (3.4) is diagonalized. (Note that the Rydberg-Ritz formula is also used for low-n states when the measured data show large fluctuations.) $H_0(88, m_{87})$ is constructed by first converting the measured energies and ionization threshold [165] for ^{88}Sr to quantum defects using Eq. (3.5) with the Rydberg constant $R(m_{88})$ mass scaled for ^{88}Sr. These quantum defects are then converted back to energies appropriate to ^{87}Sr using the ionization threshold for ^{87}Sr and the corresponding ^{87}Sr mass-scaled Rydberg constant $R(m_{87})$.

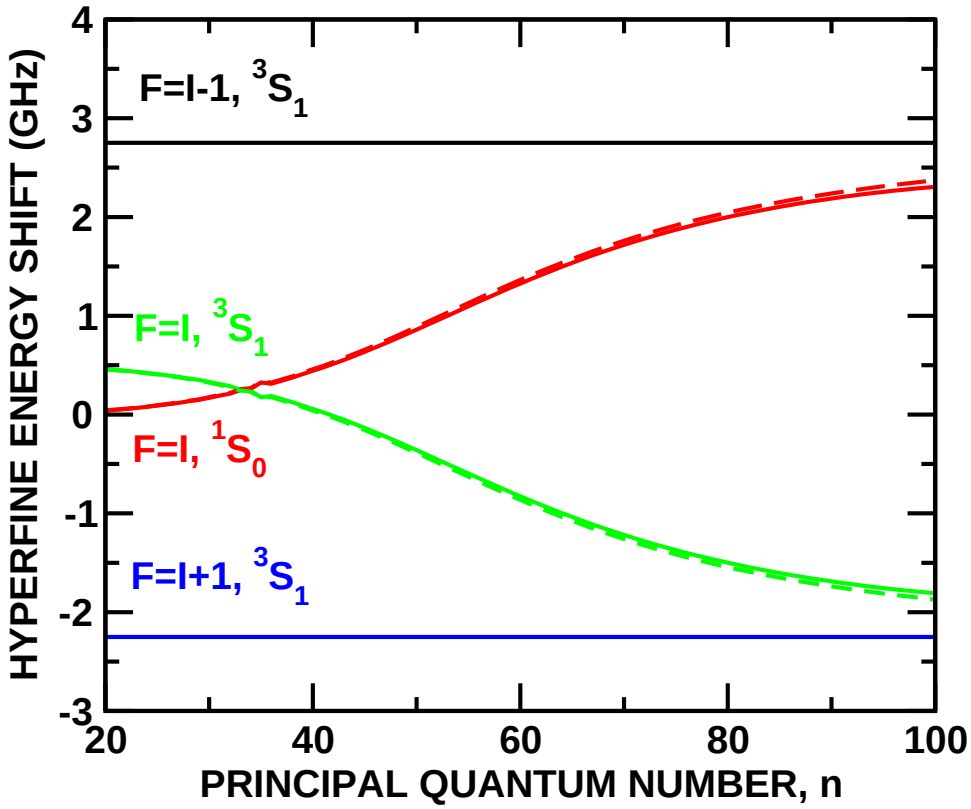

Figure 3.3: Solid lines show hyperfine energy shifts of the $(5sns)\,^{1,3}S$ states in ^{87}Sr relative to the eigenvalues of $H_0(88, m_{87})$ [see Eq. (3.4)]. The state labels for the mixed $F = I$ submanifold [Eqs. (3.13) to (3.15)] indicate the state with the largest overlap. Dashed lines show hyperfine energy shifts for $F = I$ states when mixing of adjacent n levels due to the hyperfine interaction is neglected, i.e., setting $O_{n,n'} = \delta_{n,n'}$ in Eq. (3.15).

The ionization threshold for ^{87}Sr has only been measured for the $(5s)\,^2S_{1/2}, F = 4$ state. The threshold $E^{(0)}_{\rm ion}$ is therefore estimated by subtracting the hyperfine shift $-(1/2)a_{5s}(I+1)$ [Eqs. (3.10) and (3.12)] from the measured value. Figure 3.3 shows the calculated hyperfine shift $E - E^{(0)}_{n,S,L,J}$, where E is an eigenenergy of the Hamiltonian $H(87)$. As reference we use the eigenvalues $E^{(0)}_{n,S,L,J}$ of $H_0(88, m_{87})$. In the case of singlet-triplet mixing (for $F = I$) we use the eigenvalue of the S state that features the largest overlap. For low-n states, the hyperfine interaction is much smaller than the singlet-triplet splitting. Therefore, the hyperfine interaction can be treated perturbatively and the first-order term in the energy shift vanishes for $^1S_0$ states [Eq. (3.13)] and is $-(1/2)a_{5s} \simeq 0.5\,$GHz for $^3S_1$ states [Eq. (3.14)] as observed in Fig. 3.3 for $n \simeq 20$. As n increases, the mixing of the singlet and triplet states

leads to strong deviations from the perturbative estimates and eventually, in the high-n limit, the shifts of the two $F = I$ states approach that of either the $F = I + 1$ or of the $F = I - 1$ state, the splitting of which corresponds to that of the ionization limits. For very high n the inter-n mixing becomes non-negligible. The comparison between the full calculation and the one in which inter-n mixing is switched off [i.e., $O_{n,n'} = \delta_{n,n'}$ in Eq. (3.15)], also shown in Fig. 3.3, reveals that only for $n > 80$ do the contributions from different n levels become visible. Around $n = 100$, the difference between the two calculations is $\sim$70 MHz. We note that the accuracy of the calculations is limited by the uncertainties in the measurement of the Rydberg states and the ionization thresholds as well as by the Rydberg-Ritz fitting used to derive the energies $E^{(0)}_{n,S,L,J}$. An order of magnitude estimate of the uncertainty can be obtained as follows. Taking, for example, the measured data [189] for $n \leq 40$ with an accuracy of $0.01\,\mathrm{cm}^{-1} \simeq 300\,\mathrm{MHz}$, this uncertainty translates into an error of at most 0.002 in the quantum defect. For high n, assuming that the quantum defect can be extrapolated with the same accuracy of 0.002, the resulting error in high Rydberg states would be $0.002/n^3$, corresponding to $\sim$35 MHz for $n \sim 70$ and $\sim$13 MHz for $n \sim 100$.

Energy Shift of D States

Extending the method used for the S states to D states presents considerable difficulties. The available measured levels for the ^3D states of ^{88}Sr are limited to $n \lesssim 40$ [189]. Moreover, the quantum defects extracted from these measurements feature a non-negligible n dependence which precludes the accurate extrapolation to very high-n states. In fact, attempts to employ quantum defects derived from earlier measurements of low-n states [59] to describe the present data for higher n failed to provide any reasonable degree of agreement. Therefore, for the ^3D states we apply the method outlined above, only in reverse. Following Eq. (3.4), we use the present experimental data for ^{87}Sr to determine spectroscopic information for the bosonic isotope. In practice, the quantum defects $\mu^{(0)}_{n,S,L,J}$ [Eq. (3.5)] are treated initially as free parameters and the eigenvalues of $H(87)$ are evaluated for each guess of $\mu^{(0)}_{n,S,L,J}$. By scanning through the parameter space in $\mu^{(0)}_{n,S,L,J}$ the set of

quantum defects that yield, for the hyperfine energy levels of ^{87}Sr, the best agreement with the measured data are identified. The quantum defects for the $n = 50$, 60, and 98 levels obtained in this manner are used to update the Rydberg-Ritz formula for the ^3D states, in particular for their high-n limits. These quantum defects are then tested against data for $n \simeq 50$ and 80 Rydberg states in ^{88}Sr. Moreover, the updated Rydberg-Ritz formula can be used to calculate the hyperfine structure for higher-n ^{87}Sr Rydberg D states and the resulting predictions tested against measured data for very high-n ($n \sim 100$, 280) D states [62, 215]. In our analysis, we include all singlet and triplet D states, i.e., $|[(5snd)\,^1D_2, I]F\rangle$ and $|[(5snd)\,^3D_{1,2,3}, I]F\rangle$ states with $|I - J| \leq F \leq I + J$.

For Rydberg D states, the spin-orbit interaction (see Fig. 3.2) leads to a breakdown of the LS coupling even in the absence of nuclear spin. This small but non-negligible coupling induces a weak mixing between the $^1D_2$ and the $^3D_2$ states [187, 215]. To account for this mixing, the D states for $I = 0$, i.e., eigenstates of the Hamiltonian $H_0(88, m_{87})$, are expanded as

$$\begin{aligned} |(5snd)\,^1D_2\rangle &= \cos\theta\,|n_1^*\,^1D_2\rangle + \sin\theta\,|n_1^*\,^3D_2\rangle\,, \\ |(5snd)\,^3D_2\rangle &= -\sin\theta\,|n_3^*\,^1D_2\rangle + \cos\theta\,|n_3^*\,^3D_2\rangle\,. \end{aligned} \tag{3.16}$$

The $|n_{1,3}^*\,^{1,3}D_2\rangle$ states denote pure singlet and triplet states while the mixed singlet or triplet states are denoted by $|(5snd)\,^{2S+1}D_2\rangle$. With the help of an independent TAE calculation we have verified that the radial wave functions of both pure singlet and triplet states $|n_{2S+1}^*\,^1D_2\rangle$ and $|n_{2S+1}^*\,^3D_2\rangle$ follow the same asymptotic behavior characterized by the same scattering phase shift or, equivalently, effective quantum number $n_{2S+1}^* = n - \mu^{(0)}_{n,S,L=2,J=2}$.

The mixing of singlet and triplet states is known to be strong around $n = 15$ and the value of θ is sensitive to the value of n [187]. Indeed, the singlet and the triplet states include a sizable admixture of the $4d6s$ configuration around $n = 15$, modifying the magnitude of the electron-electron interaction. Consequently, the spin-orbit interaction becomes comparable to the electron-electron interaction, leading to strong mixing of the singlet and triplet states. This results in a pronounced deviation of the singlet-triplet splitting from the n^{-3} scaling

around $n = 15$ (Fig. 3.2). For higher n, on the other hand, the singlet-triplet mixing becomes nearly n independent and θ is estimated to converge towards $\theta \sim -0.14$. (The TAE calculation yields a similar value, $\theta \sim -0.16$.) As will be shown later, the current experimental data can be well reproduced when θ is set to -0.14 and this value is used in the following calculations. Including this admixture, the matrix elements of the hyperfine operator $V_{\rm hf}$ in the D sector can be calculated (see Section 3.2.7).

Using the measured quantum defects for ^{88}Sr [188, 189] and the Rydberg-Ritz formula, the hyperfine structure is calculated and plotted in terms of quantum defects (see Fig. 3.4). This quantum defect should converge to a constant value as $n \to \infty$ provided that the Rydberg series is pure, i.e., converges to a well-defined ionization threshold. However, since for ^{87}Sr two ionization limits $E_{\rm ion}(F = 4, 5)$ [Eq. (3.10)] are present and the channels are strongly mixed by the hyperfine interaction, it is not straightforward to identify the proper ionization limit for each Rydberg series. We illustrate this point in Fig. 3.4, where the fractional part of the quantum defect ($\mu \mod 1$) relative to just one of the two thresholds $E_{\rm ion}(F = 4)$ is plotted. The quantum defect relative to $E_{\rm ion}(F = 4)$ is defined as

$$\mu(\nu_{F=4}) = n - \nu_{F=4} \quad \text{with} \quad \nu_{F=4} = \sqrt{\frac{R(m_{87})}{E_{\rm ion}(F = 4) - E}}, \tag{3.17}$$

where E is the eigenenergy of the Hamiltonian $H(87)$ [Eq. (3.4)] and is expressed in terms of the effective quantum number $\nu_{F=4}$ for the different F manifolds. A few different $\nu_{F=4}$ dependences in $\mu(\nu_{F=4})$ can be distinguished: A near constant $\mu(\nu_{F=4})$ as seen for $F = I-3$ indicates convergence to $E_{\rm ion}(F = 4)$ and a monotonically increasing $\mu(\nu_{F=4})$ ($F = I + 3$) signals the approach of the other ionization threshold $E_{\rm ion}(F = 5)$,

$$\mu(\nu_{F=4}) = n - \sqrt{\frac{R(m_{87})}{E_{\rm ion}(F = 5) + \Delta E_{\rm ion} - E}} \simeq \mu(\nu_{F=5}) + \frac{\Delta E_{\rm ion}}{2R(m_{87})}\nu_{F=5}^3, \tag{3.18}$$

with $\nu_{F=5} = \{R(m_{87})/[E_{\rm ion}(F = 5) - E]\}^{1/2}$ and $\Delta E_{\rm ion} = E_{\rm ion}(F = 4) - E_{\rm ion}(F = 5) > 0$. In the high-$n$ limit, while $\mu(\nu_{F=5})$ becomes a constant, $\mu(\nu_{F=4})$ increases with n. Around $\nu_{F=4} \simeq 110$, $\Delta E_{\rm ion}$ becomes comparable to n^{-3} and the quantum defect will be shifted by 1 (equivalent to approaching the same value for its fractional part) compared to its value

for lower n. Consequently, the inter-n mixing becomes strong and, correspondingly, the formation of avoided crossings is clearly observed. The existence of multiple thresholds affects the extraction of proper quantum defects as for high n the hyperfine interaction can become comparable to the energy splittings between states with $\Delta n \simeq 1$ and the asymptotic behavior of the quantum defects may become even more complicated.

3.2.4 Experimental Method

A schematic diagram of the present experimental arrangement is presented in Fig. 3.5. The cooling and trapping of strontium is described in detail elsewhere [79, 80, 117, 124, 140]. Briefly, starting from a Zeeman slowed atomic beam, ^{87}Sr atoms are first cooled and trapped using a "blue" magneto-optical trap (MOT) operating on the 461 nm $(5s^2)\,^1S_0 \rightarrow (5s5p)\,^1P_1$ transition. The atoms are then further cooled in a narrow-line "red" MOT utilizing the $(5s^2)\,^1S_0 \rightarrow (5s5p)\,^3P_1$ intercombination line at 689 nm. Approximately 1×10^6 atoms at $\sim$2 µK are captured before turning off all trapping fields for spectroscopy measurements.

Rydberg atoms are created by two-photon excitation using counterpropagating cross-linearly polarized 689 nm and 319 nm laser beams which drive transitions to the $(5sns)\,^3S_1$ and $(5snd)\,^3D_{1,2,3}$ Rydberg levels via the intermediate $(5s5p)\,^3P_1, F = 9/2$ or $11/2$ states. These intermediate states were selected to take advantage of selection rules to aid in identifying the Rydberg hyperfine states populated [see Fig. 3.5b]. The typical detunings of the 689 nm laser were $\Delta_{9/2} \sim 36$ MHz and $\Delta_{11/2} \sim 12$ MHz. The 689 nm laser was chopped into $(10 - 20)$ µs-long pulses to generate temporally localized groups of Rydberg atoms. The number of Rydberg atoms produced by each pulse was determined by using the electrodes in Fig. 3.5c to generate a ramped electric field sufficient to ionize the Rydberg atoms. The resulting electrons were directed towards, and detected by, a microchannel plate (MCP) whose output was fed into a multichannel scalar. Typically $(100 - 500)$ measurement cycles were performed before loading a new sample and changing the 319 nm laser frequency. Spectroscopic measurements at high n using ^{84}Sr showed that the stray fields in the trap-

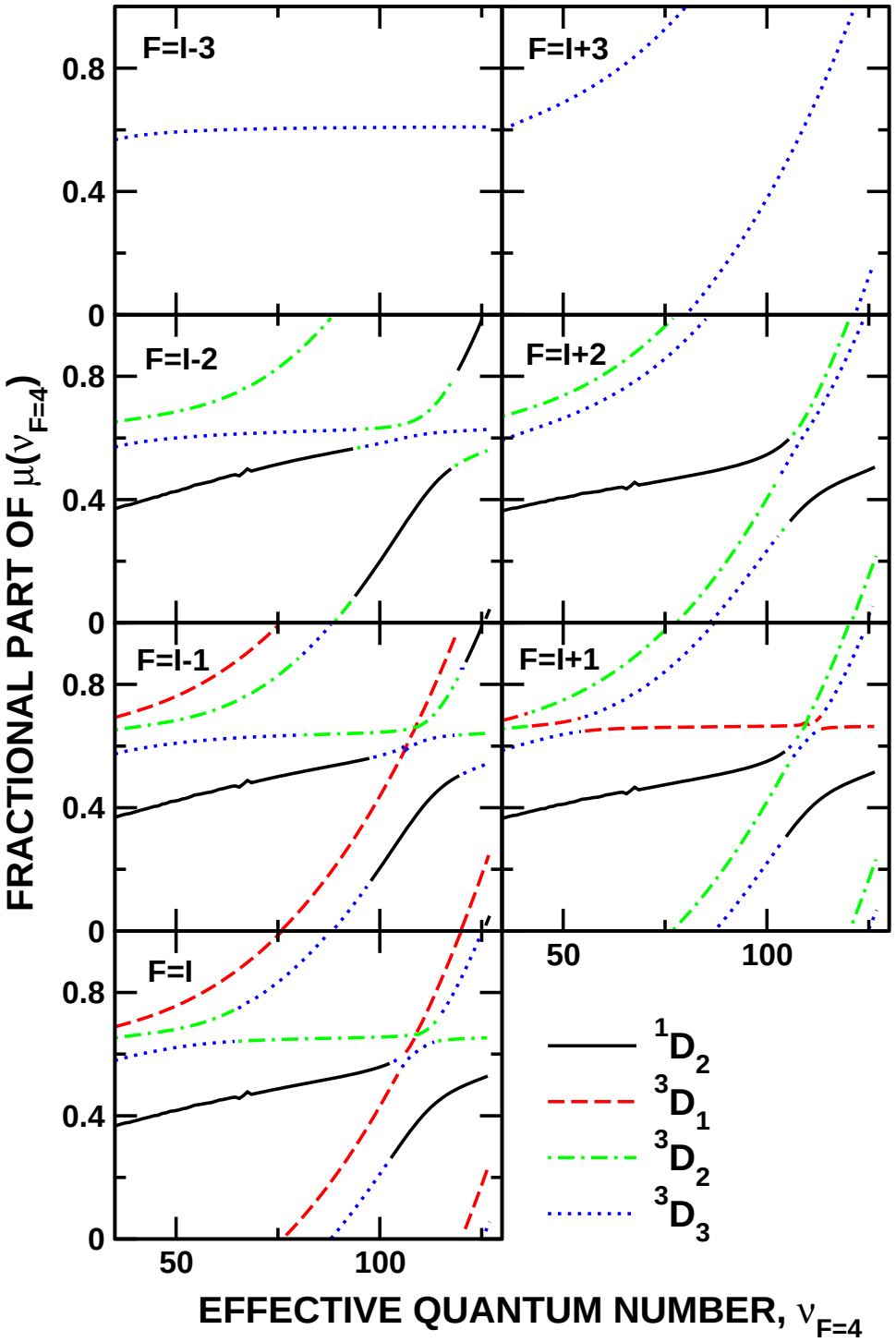

Figure 3.4: Solid lines show the fractional part of quantum defect $\mu(\nu_{F=4})$ evaluated relative to the $F = 4$ ionization threshold [see Eq. (3.17)] as a function of the effective quantum number $\nu_{F=4}$ for different F manifolds of Sr in the D sector. Each state is labeled by its dominant $^{2S+1}D_J$ state component.

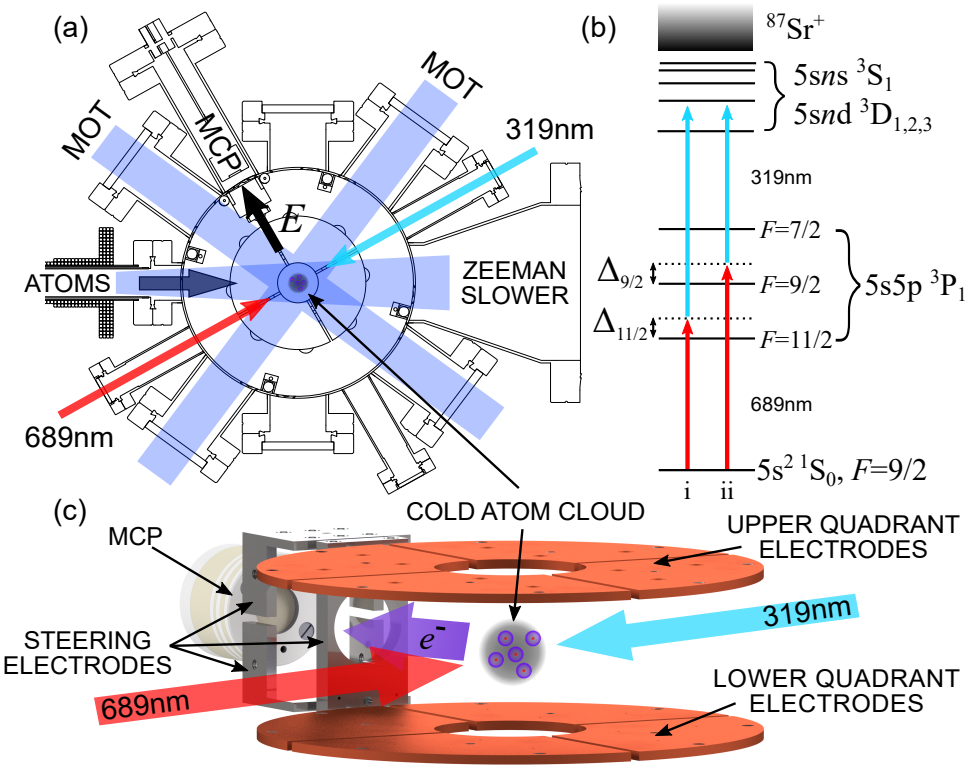

Figure 3.5: (a) Diagram of the experimental arrangement showing the 461 nm cooling beams and the counterpropagating 689 nm and 319 nm Rydberg excitation lasers. (b) Two-photon excitation scheme utilizing either the (i) $(5s5p)\,^3P_1, F = 11/2$ or (ii) $(5s5p)\,^3P_1, F = 9/2$ intermediate states. The detunings $\Delta_{11/2} \sim 12$ MHz and $\Delta_{9/2} \sim 36$ MHz remain fixed. (c) Arrangement of the electrodes used for ionizing Rydberg atoms and guiding the electrons towards the MCP detector.

ping region were less than 10 mV cm^{-1}. Any resultant Stark shifts should therefore be at most a few megahertz even at $n \sim 90$.

The 319 nm radiation was generated by frequency doubling the output of a 638 nm optical parametric oscillator (OPO). A sample of the output is sent though a broadband fiber electro-optic modulator from which one of the sidebands was locked to a transfer cavity, allowing the 319 nm laser to be scanned over multiple gigahertz. The transfer cavity was stabilized using a 689 nm master laser locked to the $(5s^2)\,^1S_0 \rightarrow (5s5p)\,^3P_1$ transition in ^{88}Sr. The linewidth of the 319 nm laser is estimated to be $\lesssim$500 kHz based on the narrowest observed spectroscopic features.

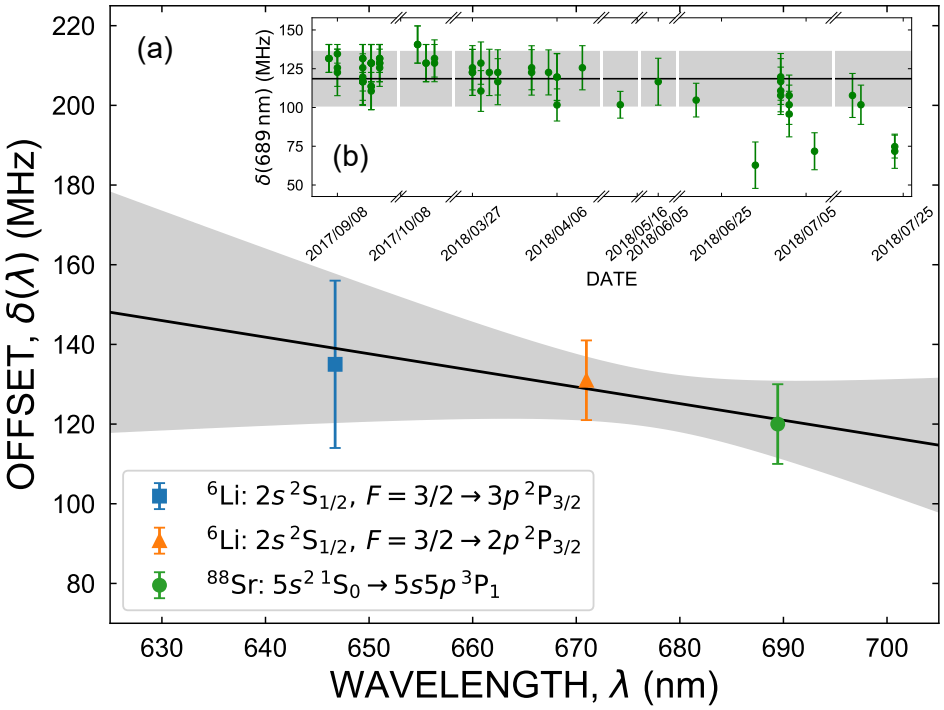

Figure 3.6: (a) Wavelength dependence of the offset δ between the measured and published transition frequencies used to calibrate the wavemeter. The black line shows the linear fit used to obtain the offset at 638 nm and the shaded region the uncertainty in the wavemeter calibration obtained from Monte Carlo simulations (see the text). The inset shows the offset of the 689 nm transition in ^{88}Sr measured at different times.

A wavemeter (EXFO WA-1500) was used to measure the wavelength of the 638 nm output from the OPO and hence determine the Rydberg state energies with a resolution-limited statistical uncertainty (σ_{stat}) of about ± 15 MHz (± 30 MHz) at 638 nm (319 nm). In order to estimate systematic offsets in the wavemeter, the frequencies of lasers locked to atomic transitions in ^{88}Sr ($(5s^2)\,^1S_0 \rightarrow (5s5p)\,^3P_1$ at 689 nm [165, 225]) and in ^{6}Li ($(2s)\,^2S_{1/2}, F = 3/2 \rightarrow (2p)\,^2P_{3/2}$ at 671 nm and $(2s)\,^2S_{1/2}, F = 3/2 \rightarrow (3p)\,^2P_{3/2}$ at 646 nm/2 = 323 nm [226–228]) were measured and then compared to the published values for the same transitions and the differences δ between the measured and published frequencies are shown in Fig. 3.6. A linear fit yields an offset of $\approx$140 MHz at 638 nm. In an attempt to estimate the systematic uncertainty in this calibration factor, a Monte Carlo sampling was adopted in which linear fits to points drawn at random from the Gaussian uncertainty distributions

appropriate to each point in the calibration were repeated, resulting in a systematic uncertainty ($\sigma_{\rm sys}$) of about ± 25 MHz (± 50 MHz) at 638 nm (319 nm). To check for drifts in the wavemeter calibration, each 638 nm wavelength measurement was followed by a reference measurement of the 689 nm master laser. As shown in the inset in Fig. 3.6b, the day-to-day variations were relatively small compared to the wavemeter's systematic uncertainty. Whereas our wavemeter limits the measurements of individual term energies to $\sim$60 MHz, line separations can be measured to kilohertz-level accuracies when scanning within a single free spectral range (FSR) of the transfer cavity and to megahertz-level accuracies when piecing together scans over successive FSRs.

3.2.5 Results and Discussion

Table 3.1 lists the measured term energies for multiple $(5sns)\,^{1,3}S$ states with $30 \lesssim n \lesssim 99$. Figure 3.7 shows quantum defects $\mu^{(0)}_{n,S,L,J}$ for the $(5sns)\,^3S_1$ states either measured for ^{88}Sr [188, 189] or obtained using the corresponding Rydberg-Ritz formula [59] together with those extracted from the current measurement of the $(5sns)\,^3S_1, F = 11/2$ states for ^{87}Sr. Since the hyperfine energy shift for the $(5sns)\,^3S_1, F = 11/2$ states is constant [Eq. (3.11)], the quantum defects $\mu^{(0)}_{n,S,L,J}$ of the corresponding bosonic isotope can be uniquely determined. The quantum defects obtained in this manner deviate from the values predicted by the earlier Rydberg-Ritz formula displaying a slow decrease in $\mu^{(0)}_{n,S,L,J}$ with increasing n. In line with the earlier discussion [Eq. (3.18)], such a systematic decrease in $\mu^{(0)}_{n,S,L,J}$ with n is typically observed when the ionization threshold is slightly shifted. In the current study the previously reported ionization threshold for ^{87}Sr [165, 188] is used in Eq. (3.5) to convert between the energy and the quantum defect. After subtracting the hyperfine energy correction its value is $E^{(0)}_{\rm ion} = 45\,932.1943\,{\rm cm}^{-1}$. The present measured energy levels can be converted to a converged, nearly constant quantum defect if a slightly higher threshold energy $E^{(0)}_{\rm ion} \simeq 45\,932.1956\,{\rm cm}^{-1}$ is used (see Fig. 3.7). This would correspond to an energy shift of $\sim$40 MHz. (We note that other sources of uncertainty such as specific isotope effects, mass polarization contributions, or stray field effects can be ruled out.) Due

to the fluctuations in the measured quantum defects (Fig. 3.7) for high n, the ionization threshold can be determined only within an error of $\sim \pm 20\,\mathrm{MHz}$.

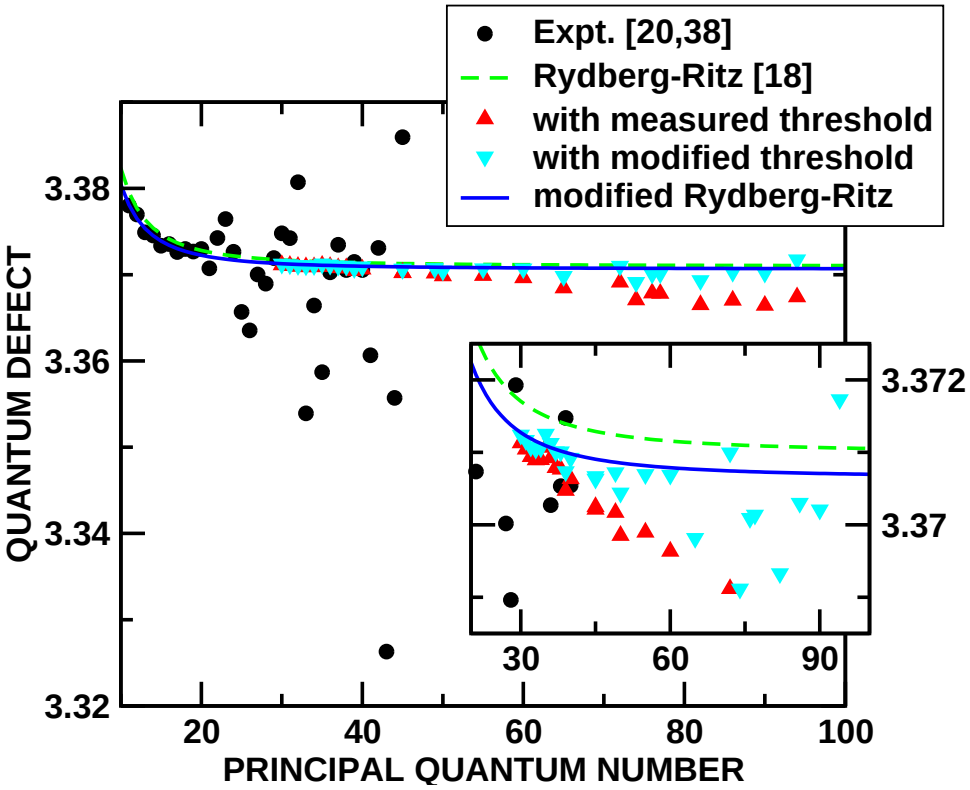

Figure 3.7: Quantum defects $\mu^{(0)}_{n,S,L,J}$ for the $(5sns)\,^3S_1$ levels: measurements from earlier work [188, 189] (•), present measurements of the $(5sns)\,^3S_1, F = 11/2$ states derived from the earlier ionization limit [165] (▲), and present measurements with modified ionization limit (see text) (▼). Also shown are the predictions using the Rydberg-Ritz formula from [59] (– – –) and the modified Rydberg-Ritz formula (——). The inset shows the higher-n region on an expanded scale. (Note that references [18], [20], and [38] in the figure legend correspond to [59], [189], and [188], respectively.)

Another feature observed in Fig. 3.7 is a nearly constant shift of the measured $\mu^{(0)}_{n,S,L,J}$ from the Rydberg-Ritz prediction for low-lying states $30 < n < 40$. Since the quantum defects at low n are insensitive to small differences in the ionization threshold, the observed shift suggests the Rydberg-Ritz formula for the ^3S states needs to be updated. The combined data from the earlier measurements [188, 189] for ^{88}Sr and the current measurements for ^{87}Sr can be well fit using the Rydberg-Ritz expression

$$\mu^{(0)}_{n,S,L,J} = \mu_0 + \frac{\alpha}{(n-\mu_0)^2} + \frac{\beta}{(n-\mu_0)^4} \tag{3.19}$$

and the values of μ_0, α, and β given in Tab. 3.3, which also includes the corresponding values derived from the earlier measurements at lower n [59]. The change in quantum defect is small ($\sim$0.0035) but, when converted to energy, the difference can be non-negligible for low-n states ($\sim$80 MHz for $n = 30$). Table 3.1 includes theoretical predictions based on diagonalization of the rescaled Hamiltonian Eq. (3.4). The calculations use the modified Rydberg-Ritz formula for $\mu^{(0)}_{n,S,L,J}$ together with the measured ionization threshold [165, 188]. On average, the present theoretical estimates lie slightly below the measured energy levels and, in the high-n limit, their differences converge to a near-constant value of $(40 - 50)$ MHz. This provides another indication that the ionization threshold should be modified.

Table 3.1: Experimentally measured and theoretically calculated energies of selected $(5sns)\,^1S_0$ and $(5sns)\,^3S_1$ states in ^{87}Sr. Here ΔE_{expt} and ΔE_{theor} are the measured and predicted separations from the $(5sns)\,^3S_1, F = 11/2$ state of the same n which is used as a reference. The uncertainties shown include both the statistical and systematic uncertainties in the wavemeter calibration.

Series	n	Term	F	E_{expt} [cm^{-1}]	ΔE_{expt} [GHz]	E_{theor} [cm^{-1}]	ΔE_{theor} [GHz]
$5sns$	40	$^1S_0$	9/2	45 850.8762(21)	16.35(8)	45 850.8702	16.22
	60			45 898.1444(22)	7.28(9)	45 898.1421	7.26
	72			45 909.0252(20)	6.10(9)	45 909.0240	6.1
	74			45 910.3230(21)	5.98(9)	45 910.3211	5.99
	76			45 911.5148(20)	5.91(8)	45 911.5127	5.89
	77			45 912.0738(20)	5.84(9)	45 912.0725	5.85
	78			45 912.6114(20)		45 912.6100	5.81
	82			45 914.5606(22)	5.66(9)	45 914.5589	5.67
	86			45 916.2336(21)	5.56(8)	45 916.2321	5.56
	90			45 917.6802(19)	5.46(8)	45 917.6791	5.47
	94			45 918.9402(19)	5.40(8)	45 918.9388	5.39
	98			45 920.0438(22)	5.325(5)	45 920.0423	5.327
$5sns$	40	$^3S_1$	7/2	45 850.4974(21)	4.99(8)	45 850.4960	5.0
	60			45 898.0688(21)	5.02(8)	45 898.0668	5.0
$5sns$	40	$^3S_1$	9/2	45 850.4078(21)	2.31(8)	45 850.4061	2.31
	50			45 881.7138(22)	1.88(9)	45 881.7119	1.89
	72			45 908.8546(21)	0.99(9)	45 908.8528	0.97
	74			45 910.1518(22)	0.85(9)	45 910.1516	0.91
	76			45 911.3460(19)	0.85(8)	45 911.3445	0.85
	77			45 911.9068(21)	0.83(9)	45 911.9049	0.83
	78			45 912.4444(19)		45 912.4429	0.8

Continued on next page.

Table 3.1 – *Continued from previous page.*

Series	n	Term	F	E_{expt} [cm^{-1}]	ΔE_{expt} [GHz]	E_{theor} [cm^{-1}]	ΔE_{theor} [GHz]
	82			45 914.3958(21)	0.72(9)	45 914.3935	0.71
	86			45 916.0696(21)	0.64(8)	45 916.0677	0.63
	90			45 917.5172(21)	0.57(8)	45 917.5155	0.56
	94			45 918.7774(22)	0.52(9)	45 918.7759	0.51
	98			45 919.8816(22)	0.463 02(7)	45 919.8800	0.461 64
$5sns$	30	$^3S_1$	11/2	45 777.3637(20)		45 777.3621	
	31			45 788.3644(21)		45 788.3624	
	32			45 798.2325(22)		45 798.2302	
	33			45 807.1179(19)		45 807.1158	
	34			45 815.1469(21)		45 815.1452	
	35			45 822.4253(21)		45 822.4252	
	36			45 829.0469(20)		45 829.0460	
	37			45 835.0865(21)		45 835.0851	
	38			45 840.6098(14)		45 840.6085	
	39			45 845.6759(22)		45 845.6734	
	40			45 850.3308(15)		45 850.3291	
	42			45 858.5807(21)		45 858.5793	
	43			45 862.2455(20)		45 862.2439	
	44			45 865.6435(21)		45 865.6413	
	45			45 868.7988(15)		45 868.7968	
	49			45 879.4140(19)		45 879.4124	
	50			45 881.6510(21)		45 881.6488	
	55			45 890.9526(20)		45 890.9511	
	60			45 897.9014(19)		45 897.9000	
	65			45 903.2294(19)		45 903.2272	
	72			45 908.8216(22)		45 908.8205	
	74			45 910.1236(22)		45 910.1213	
	76			45 911.3178(19)		45 911.3161	
	77			45 911.8790(21)		45 911.8774	
	82			45 914.3718(22)		45 914.3699	
	86			45 916.0482(19)		45 916.0467	
	90			45 917.4982(19)		45 917.4967	
	94			45 918.7600(21)		45 918.7590	
	98			45 919.8662(22)		45 919.8646	
	99			45 920.1210(22)		45 920.1196	

To remove the uncertainty in the ionization limit from the comparison between experiment and theory, we also include in Tab. 3.1 the measured energy differences between the $(5sns)\,^1S_0, F = 9/2$ or the $(5sns)\,^3S_1, F = 7/2,\ 9/2$ states and the corresponding $(5sns)\,^3S_1, F = 11/2$ states together with the values predicted by theory. As seen in

Tab. 3.1, the discrepancies between these values are typically well below $0.0005\,\mathrm{cm}^{-1} \simeq 15\,\mathrm{MHz}$. Therefore, in the following, we focus on relative energies in our analysis of D states.

Figure 3.8 shows the positions of the measured $(5snd)\,^3D$ spectral lines for $n = 50$, 60, 97, and 98 relative to the energy of the $(5sns)\,^3S_1, F = 11/2$ state. The corresponding term values are listed in Tab. 3.2. The $n = 50$ and 60 states were excited via the intermediate $(5s5p)\,^3P_1, F = 9/2$ state, allowing the creation of states with $F = 7/2$, $9/2$, and $11/2$. The $n = 97$ and 98 states were excited via the intermediate $(5s5p)\,^3P_1, F = 11/2$ state, allowing the creation of $F = 9/2$, $11/2$, and $13/2$ states. Figure 3.8 also includes the best theoretical fit to the data that could be obtained. This was realized by first determining the values of the quantum defects $\mu^{(0)}_{n,S,L,J}$ that best reproduce the measured energy levels and then using these to update the Rydberg-Ritz expression Eq. (3.19) for the n dependence of the quantum defect at high n (see Tab. 3.3). The predicted levels shown in Fig. 3.8 are derived using the updated Rydberg-Ritz formulas. However, since the measured quantum defects of ^{88}Sr $^1D_2$ states (with $I = 0$) are available up to $n = 70$, the Rydberg-Ritz expression from [59] is used for these states. The measured quantum defects for the ^3D states are shown in Fig. 3.9 together with the values given by both the present and the earlier Rydberg-Ritz expressions. The differences between the predicted quantum defects [Eq. (3.19)] based on the present data for ^{87}Sr and previous data for ^{88}Sr [59] appear to be small $\sim$0.02. However, when converted to energy, this small difference translates into discrepancies of 130 MHz for $n = 100$ and 1 GHz for $n = 50$ well outside the uncertainty of the current experiment.

The present Rydberg-Ritz formulas can also be tested against earlier measured quantum defects for D states in ^{87}Sr ($n > 100$) [215]. The data are reproduced to within an average difference of $\sim$60 MHz. When the modified ionization limit discussed above is used to evaluate the quantum defect, the average difference is reduced to $\sim$25 MHz. These residual differences could be caused by stray fields present in the heat pipe used for the earlier work. Additionally, the current theoretical model can predict the hyperfine structure of D states around $n \simeq 280$, which can again be compared with the earlier measurements [62]. Due to

Table 3.2: Comparison of measured and calculated positions of $(5snd)\,^3D_{1,2,3}$ lines for $n = 50$, 60, and ~ 98. The splittings $\Delta E_{\rm expt}$ between those lines that could be measured during a single FSR scan of the 319 nm laser frequency or, for $n \sim 98$, where neighboring scans could be accurately patched together are included together with the corresponding theoretical predictions. For the $n = 98 - 99$ scan, all differences are referenced to the $(5sns)\,^3S_1, F = 11/2$ level.

Series	n	Term	F	$E_{\rm expt}$ [cm^{-1}]	$\Delta E_{\rm expt}$ [MHz]	$E_{\rm theor}$ [cm^{-1}]	$\Delta E_{\rm theor}$ [MHz]
$5snd$	50	$^3D_1$	7/2	45 883.1440(22)	−295.60(7)	45 883.1414	−299.01
	50	$^3D_1$	9/2	45 883.1538(22)	0	45 883.1514	0
	50	$^3D_2$	11/2	45 883.1685(22)	439.39(7)	45 883.1662	443.71
$5snd$	50	$^3D_2$	7/2	45 883.2882(21)	0	45 883.2855	0
	50	$^3D_2$	9/2	45 883.2922(21)	118.91(7)	45 883.2893	114.7
	50	$^3D_1$	11/2	45 883.2972(21)	269.12(7)	45 883.2942	260.55
$5snd$	50	$^3D_3$	11/2	45 883.3849(22)	−890.64(7)	45 883.3814	−890.22
	50	$^3D_3$	9/2	45 883.4146(22)	0	45 883.4111	0
$5snd$	50	$^3D_3$	7/2	45 883.4374(22)		45 883.4339	
$5snd$	60	$^3D_1$	7/2	45 898.7367(21)	−183.64(7)	45 898.7347	−178.89
	60	$^3D_1$	9/2	45 898.7428(21)	0	45 898.7407	0
	60	$^3D_2$	11/2	45 898.7521(21)	277.34(7)	45 898.7497	270.37
$5snd$	60	$^3D_2$	7/2	45 898.8568(22)	−79.40(7)	45 898.8544	−72.67
	60	$^3D_2$	9/2	45 898.8594(22)	0	45 898.8569	0
	60	$^3D_3$	11/2	45 898.8618(22)	71.37(7)	45 898.8588	58.8
$5snd$	60	$^3D_1$	11/2	45 898.9223(22)	−626.40(7)	45 898.9197	−609.77
	60	$^3D_3$	9/2	45 898.9432(22)	0	45 898.9400	0
	60	$^3D_3$	7/2	45 898.9608(22)	526.18(7)	45 898.9573	517.37
$5sns$	98	$^3S_1$	11/2	45 919.8662(22)	0	45 919.8646	0
	98	$^3S_1$	9/2	45 919.8816(22)	463.02(7)	45 919.8800	461.64
$5snd$	97	$^3D_1$	11/2	45 919.9565(22)	2707.6(35)	45 919.9552	2716.6
	97	$^3D_2$	9/2	45 919.9593(22)	2792.4(35)	45 919.9579	2796.2
	97	$^1D_2$	9/2	45 919.9896(22)	3701(4)	45 919.9879	3697
	97	$^1D_2$	11/2	45 919.9925(22)	3785(4)	45 919.9909	3786
	97	$^1D_2$	13/2	45 919.9946(22)	3850(4)	45 919.9933	3857
$5sns$	98	$^1S_0$	9/2	45 920.0438(22)	5325(5)	45 920.0423	5327
$5snd$	98	$^3D_1$	9/2	45 920.0474(22)	5432(5)	45 920.0460	5439
	98	$^3D_2$	11/2	45 920.0501(22)	5512(5)	45 920.0485	5514
	98	$^3D_2$	13/2	45 920.0544(22)	5641(5)	45 920.0526	5636
	98	$^3D_3$	13/2	45 920.0916(22)	6756(6)	45 920.0901	6761
	98	$^3D_3$	11/2	45 920.0956(22)	6877(6)	45 920.0943	6886
	98	$^3D_3$	9/2	45 920.0982(22)	6954(6)	45 920.0971	6970
$5sns$	99	$^3S_1$	11/2	45 920.1210(22)	7639(6)	45 920.1196	7643

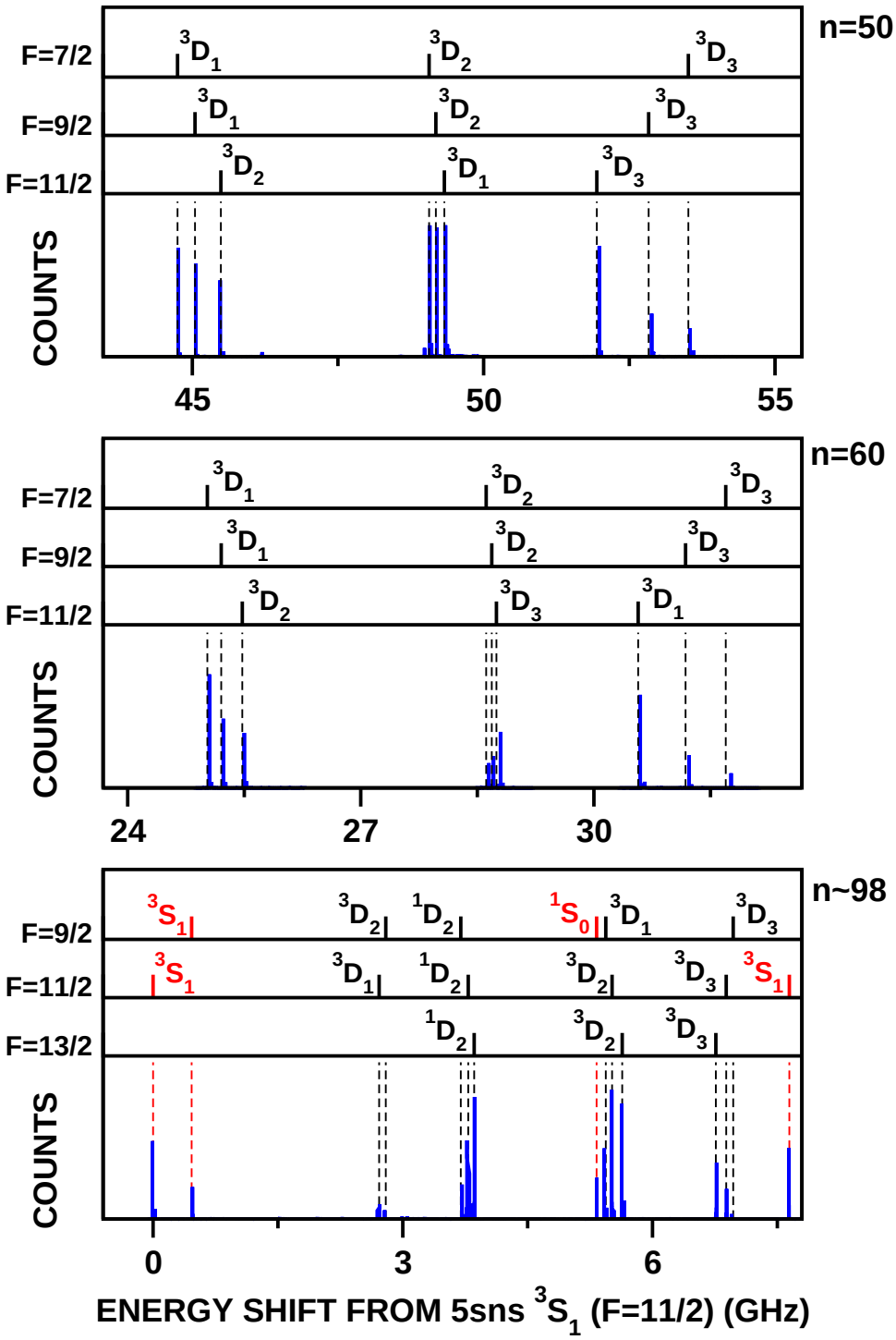

Figure 3.8: Shown in blue are the measured spectra for $(5snd)\,^3D$ states of ^{87}Sr in the vicinity of (a) $n = 50$, (b) $n = 60$, and (c) $n = 98$. Energies are given relative to the $5s50s$, $5s60s$, and $5s98s$ $^3S_1, F = 11/2$ states, respectively. Rydberg excitation was performed following scheme (ii) in (a) and (b) and scheme (i) in (c). The vertical bars above the data show the calculated positions for the various hyperfine states (see the text). The measured levels and splittings are given in Tab. 3.2.

the uncertainty in the ionization threshold, the exact energies cannot be evaluated but the size of the hyperfine splittings is well reproduced within an error of 10 MHz.

Finally, the improved Rydberg-Ritz formulas for the ^3D states determined from the present data for ^{87}Sr can be used to determine spectroscopic information for ^{88}Sr. When we compare energies for the $5s50d$ and $5s80d$ $^3D_{1,2}$ states derived using the present updated Rydberg-Ritz formulas with earlier measurements [229, 230] the agreement is significantly improved over that obtained using the earlier Rydberg-Ritz parametrization, the differences between theory and experiment being reduced by several hundred megahertz.

As a further test of the present theoretical approach, Tab. 3.2 includes the frequency separations between selected pairs of levels that could be measured during a single FSR scan of the 319 nm laser and that are known to high precision. Table 3.2 also includes the corresponding theoretical predictions. In all but one case the measured and theoretical separations agree to better than ±10 MHz.

Table 3.3: Values of the parameters μ_0, α, and β for the Rydberg-Ritz formula obtained in this and earlier work.

Series	Term	μ_0	α	β	Reference
$(5sns)$	$^1S_0$	3.268 96(2)	−0.138(7)	0.9(6)	[59]
$(5sns)$	$^3S_1$	3.370 65	0.443	−0.553	this work
		3.371(2)	0.5(2)	$-1(2)\times10^1$	[59]
$(5snd)$	$^1D_2$	2.3807(2)	−39.41(6)	$-109(2)\times10^1$	[59]
$(5snd)$	$^3D_1$	2.673	−5.4	−8166	this work
		2.658(6)	3(2)	$-8.8(7)\times10^3$	[59]
$(5snd)$	$^3D_2$	2.662	−15.4	−9804	this work
		2.636(5)	−1(2)	$-9.8(9)\times10^3$	[59]
$(5snd)$	$^3D_3$	2.612	−41.4	−15 363	this work
		2.63(1)	−42.3(3)	$-18(1)\times10^3$	[59]

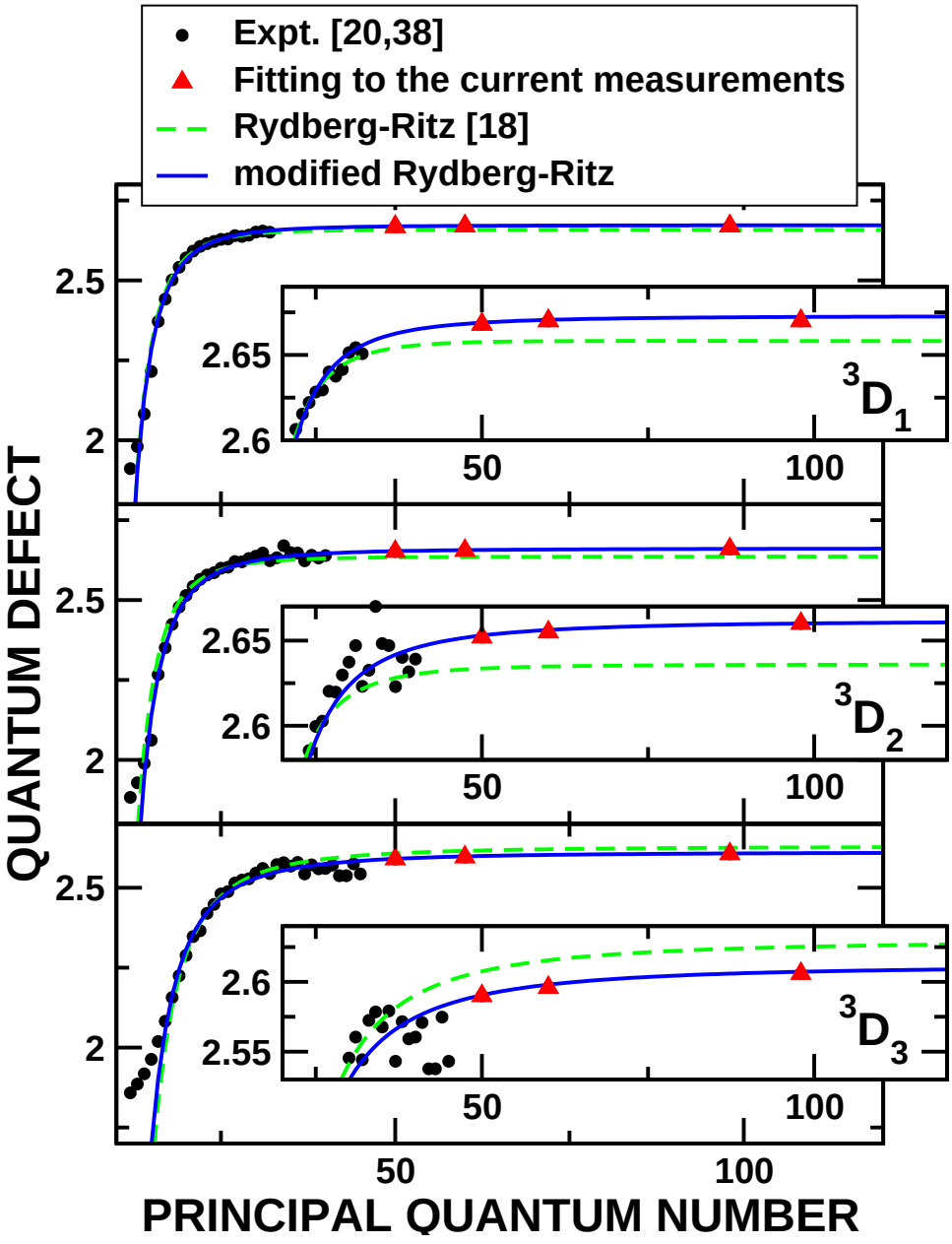

Figure 3.9: Quantum defects $\mu^{(0)}_{n,S,L,J}$ for the $(5snd)\,^3D_{1,2,3}$ levels: measurements from earlier work [188, 189] (•), present measurements (▲), predictions using the Rydberg-Ritz formulas developed previously [59] (– – –), and predictions based on the present updated Rydberg-Ritz formulas (see the text) (——). The insets show the high-n region on an expanded scale. (Note that references [18], [20], and [38] in the figure legend correspond to [59], [189], and [188], respectively.)

3.2.6 Summary

The present work demonstrates that the energies of high-n ^{87}Sr Rydberg states can be accurately determined by diagonalizing an isotope-rescaled Hamiltonian. This Hamiltonian is constructed using spectral information for the bosonic isotope (^{88}Sr) which has vanishing nuclear spin combined with the hyperfine interaction present in ^{87}Sr. The present approach can be implemented for fermionic atoms whenever the energy levels for an isotope with vanishing nuclear spin are available. The method can also be applied in reverse, allowing determination of spectroscopic information, in particular quantum defects, for bosonic isotopes from the hyperfine-resolved spectrum of the fermionic isotope. The major limitation on the accuracy of the present analysis is the uncertainty in the hyperfine-resolved ionization threshold. This uncertainty can be removed by focusing on energy differences to a reference level whereupon accuracies of the order of a few megahertz can be achieved.

Acknowledgments

Research supported by the AFOSR (Grant No. FA9550-17-1-0366), the NSF (Grant No. 1600059), the Robert A. Welch Foundation (Grants No. C-0734 and No. C-1844), and the FWF (Austria) (Grants No. FWF-SFB041 ViCoM and No. FWF-SFB049 NextLite). The Vienna scientific cluster was used for the calculations. We thank Ya-Ting Chang, Danyel Cavazos, and Randall G. Hulet for use of their equipment in calibrating our wavemeter.

3.2.7 Appendix: Matrix Elements of the Hyperfine Operator $V_{\mathbf{hf}}$

The matrix elements of the hyperfine operator V_{HF} can be evaluated analytically [223] and they are listed in the following. For the diagonal elements of $J = 2$ states we find

$$\langle [(5sn'd)\,{}^1D_2, I]F|\, V_{\mathrm{hf}}\, |[(5snd)\,{}^1D_2, I]F\rangle = -a_{5s}\lambda K \cos(\theta+\xi)\sin\theta\delta_{n,n'}, \tag{3.20}$$

$$\langle [(5sn'd)\,{}^3D_2, I]F|\, V_{\mathrm{hf}}\, |[(5snd)\,{}^3D_2, I]F\rangle = a_{5s}\lambda K \sin(\theta+\xi)\cos\theta\delta_{n,n'}, \tag{3.21}$$

with $K = F(F+1) - J(J+1) - I(I+1)$, $\lambda = (2\ell+1)/[4\ell(\ell+1)]$, $\xi = \arcsin[1/(2\ell+1)]$, and $\ell = 2$. The diagonal elements of $J = 1$, 3 states are

$$\langle[(5sn'd)\,^3D_1, I]F|\,V_{\rm hf}\,|[(5snd)\,^3D_1, I]F\rangle = -\frac{1}{4\ell}a_{5s}K\delta_{n,n'}, \tag{3.22}$$

$$\langle[(5sn'd)\,^3D_3, I]F|\,V_{\rm hf}\,|[(5snd)\,^3D_3, I]F\rangle = \frac{1}{4(\ell+1)}a_{5s}K\delta_{n,n'}. \tag{3.23}$$

The off-diagonal elements between states with the same $J = 2$ are

$$\langle[(5sn'd)\,^1D_2, I]F|\,V_{\rm hf}\,|[(5snd)\,^3D_2, I]F\rangle = -\frac{\lambda}{2}a_{5s}K\cos(2\theta+\xi)O_{n,n'} \tag{3.24}$$

and those with different J are

$$\langle[(5sn'd)\,^1D_2, I]F|\,V_{\rm hf}\,|[(5snd)\,^3D_1, I]F\rangle = -\frac{1}{4\ell}a_{5s}K_-\sin(\theta-\eta)O_{n,n'}, \tag{3.25}$$

$$\langle[(5sn'd)\,^1D_2, I]F|\,V_{\rm hf}\,|[(5snd)\,^3D_3, I]F\rangle = \frac{1}{4(\ell+1)}a_{5s}K_+\cos(\theta-\eta)O_{n,n'}, \tag{3.26}$$

$$\langle[(5sn'd)\,^3D_2, I]F|\,V_{\rm hf}\,|[(5snd)\,^3D_1, I]F\rangle = \frac{1}{4\ell}a_{5s}K_-\cos(\theta-\eta)O_{n,n'}, \tag{3.27}$$

$$\big\langle[(5sn'd)\,^3D_2, I]F\big|\,V_{\rm hf}\,\big|[(5snd)\,^3D_3, I]F\big\rangle = \frac{1}{4(\ell+1)}a_{5s}K_+\sin(\theta-\eta)O_{n,n'}, \tag{3.28}$$

$$\big\langle[(5sn'd)\,^3D_1, I]F\big|\,V_{\rm hf}\,\big|[(5snd)\,^3D_3, I]F\big\rangle = 0,$$

with

$$\eta = \arcsin\sqrt{\frac{\ell}{2\ell+1}},$$

$$K_- = \sqrt{[\ell^2-(F-I)^2][(F+I+1)^2-\ell^2]},$$

and

$$K_+ = \sqrt{[(\ell+1)^2-(F-I)^2][(F+I+1)^2-(\ell+1)^2]}.$$

Similar to the S states, the overlap integral $O_{n,n'}$ of the radial wave functions can be evaluated semiclassically [224] and depends only on the effective quantum number $n - \mu^{(0)}_{n,S,L,J}$.

3.3 Additional Materials

The following subsections include additional material not included in the published paper.

3.3.1 n Scaling of Various Splittings

As mentioned in the paper, various energy splittings decrease with increasing n whereas the hyperfine interaction remains constant. This is illustrated in Fig. 3.2 where the experimentally determined fine-structure, singlet-triplet, and Coulomb splitting in ^{88}Sr are plotted. Figure 3.10 shows the same information as Fig. 3.2 (plotted for n instead of n^*) but with more splittings and was computed using the most recently reported ionization limit and quantum defects for ^{88}Sr from [36, 59]. The strength of hyperfine interaction can

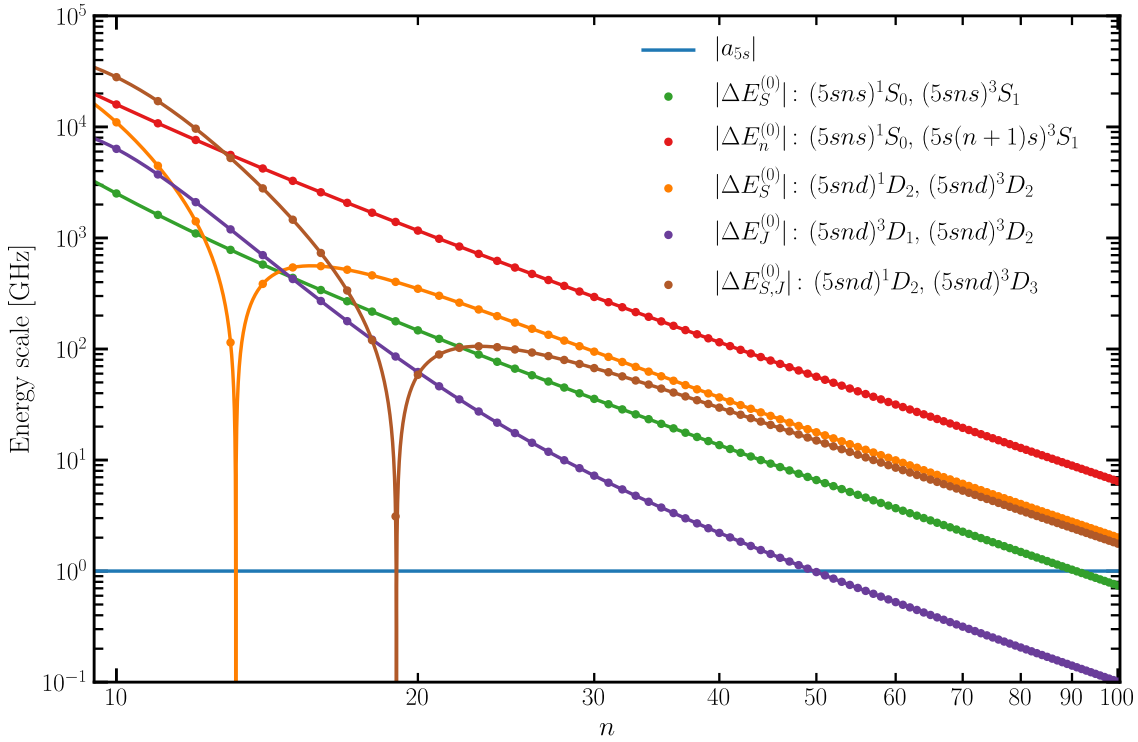

Figure 3.10: The n scaling of various splittings in ^{88}Sr calculated using the most recently reported quantum defects and ionization energy [36, 59]. The splittings between various states are represented by $\Delta E_X^{(0)}$ between the given states where $X = S$ is the singlet-triplet splitting, $X = J$ is the fine structure splitting, and $X = n$ is the Coulomb splitting. The energy scale of the hyperfine interaction in ^{87}Sr is approximately constant and is taken to be $|a_{5s}| \approx 1\,\text{GHz}$ [203].

be related to the contact interaction of the inner $5s$ electron with the $^{87}Sr^+$ core and is taken to be $|a_{5s}| \simeq 1\,\text{GHz}$ [203].

From examining Fig. 3.10, it's possible to estimate where hyperfine state mixing will occur by finding when $|a_{5s}|$ becomes comparable to a particular energy splitting. This suggests, for example, that hyperfine mixing should occur between the $(5snd)\,^1D_2$ and the $(5snd)\,^3D_2$ states near $n = 14$ and between the $(5snd)\,^1D_2$ and the $(5snd)\,^3D_3$ states near $n = 20$. Indeed, both interactions have been observed experimentally with large shifts reported in the spectra of ^{87}Sr $(5snd)\,^1D_2$ hyperfine Rydberg states around $n = 16$ [196, 197] and $n = 19$ [216].

3.3.2 $\hat{V}_{\mathbf{hf}}$ for Singly Excited Rydberg States

The hyperfine interaction can be expressed as [69, 201, 231]

$$\hat{V}_{\mathrm{hf}} = A\hat{\mathbf{I}} \cdot \hat{\mathbf{J}} = \sum_i A_i \hat{\mathbf{I}} \cdot \hat{\mathbf{j}}_i = \sum_i A_i \hat{\mathbf{I}} \cdot \left(\hat{\mathbf{l}}_i + \hat{\mathbf{s}}_i\right) \tag{3.29}$$

for electron $i \in \{1, 2\}$ with the (magnetic dipole) hyperfine constant A_i. Therefore the contribution of each electron to the total hyperfine shift is

$$\langle \hat{V}_{\mathrm{hf}} \rangle_i = A_i \langle \hat{\mathbf{I}} \cdot \hat{\mathbf{j}}_i \rangle = \frac{A_i}{2}[f_i(f_i+1) - I(I+1) - j_i(j_i+1)] \tag{3.30}$$

We now consider a singly-excited Rydberg state where the "inner" electron is in the $|ms\rangle$ state and the "outer" electron is in the $|nl\rangle$ state (with $n \gg m$). Since $\langle \hat{V}_{\mathrm{hf}} \rangle_i \sim 1/n^3$ [69, 221, 231], the interaction of the "outer" electron with the nuclear spin quickly decreases with n meaning $\langle \hat{V}_{\mathrm{hf}} \rangle_{\mathrm{outer}} = A_{\mathrm{outer}} \langle \hat{\mathbf{I}} \cdot \hat{\mathbf{j}}_{\mathrm{outer}} \rangle \approx 0$. Therefore, the hyperfine interaction can be approximated as

$$\langle \hat{V}_{\mathrm{hf}} \rangle \simeq \langle \hat{V}_{\mathrm{hf}} \rangle_{\mathrm{inner}} = A_{\mathrm{inner}} \langle \hat{\mathbf{I}} \cdot \hat{\mathbf{s}}_{\mathrm{inner}} \rangle \implies \hat{V}_{\mathrm{hf}} \simeq A_{\mathrm{inner}} \hat{\mathbf{I}} \cdot \hat{\mathbf{s}}_{\mathrm{inner}} \tag{3.31}$$

For ^{87}Sr, the inner electron is in the $5s$ state with $A_{\mathrm{inner}} = A_{5s} = -1\,000\,473.673(11)\,\mathrm{kHz}$ obtained from the hyperfine splitting of the $(5s)\,^2S_{1/2}, F = 4$ and 5 ground states in $^{87}\mathrm{Sr}^+$ [203].

Following from the derivation presented by Shuhei Yoshida, it should be noted that $\hat{V}_{\mathrm{hf}}$

can be expanded as

$$\hat{V}_{\rm hf} = A_{\rm inner}\hat{\mathbf{I}}\cdot\hat{\mathbf{s}}_{\rm inner} = \frac{1}{2}A_{\rm inner}\left(\hat{s}_{{\rm inner},+}\hat{I}_- + \hat{s}_{{\rm inner},-}\hat{I}_+ + 2\hat{s}_{{\rm inner},z}\hat{I}_z\right) \tag{3.32}$$

where $\hat{J}_\pm = \hat{J}_x \pm i\hat{J}_y$ and $\hat{J}_z$ are the ladder operators for a spin $\mathbf{J}$. This will be helpful when computing the matrix elements of $\hat{V}_{\rm hf}$. Note that $\hat{V}_{\rm hf}$ leaves the total angular momentum m_F unchanged, only coupling states with the same m_F.

3.3.3 Singly Excited S State Hyperfine Mixing Matrix

The matrix elements for hyperfine mixing of the $(5sns)\,^1S_0$ and the $(5sns)\,^3S_1$ states are not too difficult to evaluate and the derivation outlined below is based on the one presented by Shuhei Yoshida.

For the singly excited S states, the four basis states are $|(5sns)\,^3S_1, F = I-1\rangle$, $|(5sns)\,^1S_0, F = I\rangle$, $|(5sns)\,^3S_1, F = I\rangle$, and $|(5sns)\,^3S_1, F = I+1\rangle$. Using Eq. (3.32), it can be shown that $\hat{V}_{\rm hf}$ has the following effect on the basis states (the case of $m_F = F$ was evaluated for simplicity)

$$\hat{V}_{\rm hf}\left|(5sns)\,^3S_1, F = I-1\right\rangle = -\frac{1}{2}A_{5s}(I+1)\left|(5sns)\,^3S_1, F = I-1\right\rangle \tag{3.33}$$

$$\hat{V}_{\rm hf}\left|(5sns)\,^1S_0, F = I\right\rangle = \frac{1}{2}A_{5s}\sqrt{I(I+1)}\left|(5sns)\,^3S_1, F = 9/2\right\rangle \tag{3.34}$$

$$\hat{V}_{\rm hf}\left|(5sns)\,^3S_1, F = I\right\rangle = \frac{1}{2}A_{5s}\left(\sqrt{I}(I+1)\left|(5sns)\,^1S_0, F = I\right\rangle - \left|(5sns)\,^3S_1, F = I\right\rangle\right) \tag{3.35}$$

$$\hat{V}_{\rm hf}\left|(5sns)\,^3S_1, F = I+1\right\rangle = \frac{1}{2}A_{5s}I\left|(5sns)\,^3S_1, F = I+1\right\rangle \tag{3.36}$$

Therefore the total hyperfine interaction Hamiltonian can be written as

$$\hat{V}_{\rm hf} = \frac{1}{2}A_{5s}\begin{pmatrix} -(I+1) & 0 & 0 & 0 \\ 0 & 0 & \sqrt{I\,(I+1)} & 0 \\ 0 & \sqrt{I\,(I+1)} & -1 & 0 \\ 0 & 0 & 0 & I \end{pmatrix} \tag{3.37}$$

From Eq. (3.37), it is clear that the $|(5sns)\,^3S_1, F = I - 1\rangle$ and the $|(5sns)\,^3S_1, F = I + 1\rangle$ states are not mixed, resulting in the states exhibiting a constant shift. Conversely, the submatrix for the two $F = I$ states has off-diagonal elements meaning those states are coupled by $\hat{V}_{\text{hf}}$.

3.3.4 Singly Excited D State Hyperfine Mixing Matrix

A procedure similar to the one used to derive the $\hat{V}_{\text{hf}}$ matrix elements for singly excited S states can be applied to obtain $\hat{V}_{\text{hf}}$ for the singly excited D states but the process is quite a bit more difficult. Starting from the LS-coupled basis, there are 20 states spread across the various $|(5snd)\,^1D_2, m_J\rangle$, $|(5snd)\,^3D_1, m_J\rangle$, $|(5snd)\,^3D_2, m_J\rangle$, and $|(5snd)\,^3D_3, m_J\rangle$ sublevels. Incorporating the $2I + 1 = 10$ nuclear spin states of ^{87}Sr results in a total of 200 states which can be coupled by $\hat{V}_{\text{hf}}$. This is even before including mixing between the various D states [187, 215, 216]. Therefore, the reader is referred to [215] which provides a summary of calculating $\hat{V}_{\text{hf}}$ for the singly excited D states and [223] which provides analytical matrix elements of $\hat{V}_{\text{hf}}$ for two electrons in an sl configuration.

3.3.5 Calibration of the EXFO WA-1500 Wavemeter

All light used in the calibration measurements was delivered to the EXFO WA-1500 wavemeter using single mode (SM) optical fibers[60]. We had previously used a multimode fiber but found that the wavemeter readings were inconsistent, most likely due to the speckle output pattern or to slight beam pointing deviations. Switching to a SM fiber mitigated these issue and we were able to consistently obtain wavenumber measurements limited by the resolution of the wavemeter with a statistical uncertainty of about $\sigma_{\text{stat}} = \pm 0.0005\,\text{cm}^{-1} = \pm 15\,\text{MHz}$ for the wavelengths we measured. Since the 319 nm light is generated by frequency-doubling from 638 nm, the statistical uncertainty should be doubled to about $\sigma_{\text{stat}} = \pm 0.001\,\text{cm}^{-1} = \pm 30\,\text{MHz}$.

[60] Thorlabs SM600 FC/PC single mode fiber.

Since the wavemeter is used to determine the absolute energy of the 638 nm photon, potential systematic offsets also needed to be characterized. We initially attempted to perform Doppler-free spectroscopy of molecular iodine ($^{127}I_2$) using the $P65$ (7–4) line at 15 672.517 398(25) cm^{-1} [232], which is near the 638 nm wavelength required to excite the $(5s40s)\,^3S_1$ strontium Rydberg state. Unfortunately, we were unable to observe narrow Doppler-free signals when scanning the 638 nm laser through a our iodine cell using a simple saturated absorption setup[61]. A longer cell and a more sensitive detection method may be necessary since most reported $^{127}I_2$ spectroscopy studies in this wavelength range utilized cells longer than 30 cm in addition implementing some sort of modulation spectroscopy to improve the signal-to-noise ratio (e.g., see [74, 232, 234]). Since the publication of our paper, the Weidemüller group was able to calibrate their wavemeter with Doppler-free iodine spectroscopy for measurements of the $(5sns)\,^3S_1$, $(5snd)\,^3D_1$, and $(5snd)\,^3D_2$ Rydberg energies in ^{88}Sr [36].

Although the iodine spectroscopy was unsuccessful, we were able to calibrate the wavemeter by measuring the wavelengths of lasers locked to atomic transitions in ^{88}Sr (689 nm) and in ^{6}Li (671 nm and 323 nm). The 689 nm reference comes from the red master laser locked to the $^1S_0 \rightarrow {}^3P_1$ in ^{88}Sr in the Killian laboratory for strontium experiments. Ya-Ting Chang, Danyel Cavazos, and Dr. Randy Hulet were kind enough to let us run a fiber[62] between the Killian and Hulet laboratories in order to measure the wavelengths of their 671 nm and 323 nm = 2 × 646 nm lithium cooling lasers. The 671 nm is used for a standard D_2 MOT while the 646 nm is frequency doubled to 323 nm for a UV MOT [233]. The long fiber was required so that the EXFO WA-1500 could be calibrated in-place under similar conditions as when measuring Rydberg energies. In addition to keeping the wavemeter in-place, the wavelength calibration measurements were performed within about 2 h to reduce environmental influences. The results, presented in Tab. 3.4, were used to calculate the frequency offset $\delta(\nu) = \nu_{\text{measured}} - \nu_{\text{reference}}$ shown in Fig. 3.6.

[61] This matches similar experiences reported by Jason Nguyen and Henry Luo in the Hulet lab when they were considering using an iodine cell to lock their 646 nm laser for a ^{6}Li UV MOT [233].

[62] Also a Thorlabs SM600 FC/PC SM fiber.

Table 3.4: Values used to calibrate the WA-1500 on a single day (2018/03/09). All measurements were performed within about 2 h. The value of the 689 nm transition in ^{88}Sr were taken from [165, 225]. The values of the 671 nm and 323 nm = 2 × 646 nm transitions in ^{6}Li were taken from [226–228].

λ [nm]	Atom	Transition	Reference [cm^{-1}]	Measured [cm^{-1}]
689	^{88}Sr	$(5s^2)\,^1S_0 \rightarrow (5s5p)\,^3P_1$	14 504.338 241 59(33)	14 504.342 24(35)
671	^{6}Li	$(2s)\,^2S_{1/2}, F = 3/2 \rightarrow (2p)\,^2P_{3/2}$	14 903.629 524 2(7)	14 903.633 91(33)
323 (646)	^{6}Li	$(2s)\,^2S_{1/2}, F = 3/2 \rightarrow (3p)\,^2P_{3/2}$	30 925.1703(10) (15 462.5851(5))	30 925.1792(10) (15 462.5896(5))

3.3.6 Comparison of Measured Quantum Defects

Table 3.5 compiles a list of strontium quantum defects for the singly excited $(5sns)\,S$ and $(5snd)\,D$ states. Comparing the quantum defects reported in [36, 59, 194], which were obtained from measurements in ^{88}Sr, to those extracted from the $(5sns)\,^3S_1, F = 11/2$ in ^{87}Sr shows generally good agreement.

Table 3.5: Values of the parameters δ_0, δ_2, and δ_4 for the Rydberg-Ritz formula Eq. (3.19). The quantum defects from [36, 59, 194] were extracted from measurements in ^{88}Sr whereas this work extracted quantum defects from the $(5sns)\,^3S_1, F = 11/2$ in ^{87}Sr.

Series	Term	δ_0	δ_2	δ_4	Ref.
$5sns$	$^1S_0$	3.268 96(2)	−0.138(7)	0.9(6)	[59]
$5sns$	$^3S_1$	3.371(2)	0.5(2)	$-1(2) \times 10^1$	[59]
		3.370 65	0.443	−0.553	this work
		3.369 24(2)	0.52(2)	−0.1(3)	[194]
		3.370 778(4)	0.418(1)	−0.3(1)	[36]
$5snd$	$^1D_2$	2.3807(2)	−39.41(6)	$-109(2) \times 10^1$	[59]
$5snd$	$^3D_1$	2.658(6)	3(2)	$-8.8(7) \times 10^3$	[59]
		2.673	−5.4	−8166	this work
		2.664(7)	−1(9)	$-8(2) \times 10^3$	[194]
		2.675 17(20)	−13.15(26)	$-4.444(91) \times 10^3$	[36]
$5snd$	$^3D_2$	2.636(5)	−1(2)	$-9.8(9) \times 10^3$	[59]
		2.662	−15.4	−9804	this work
		2.661 42(30)	−16.77(38)	$-6.656(134) \times 10^3$	[36]
$5snd$	$^3D_3$	2.63(1)	−42.3(3)	$-18(1) \times 10^3$	[59]
		2.612	−41.4	−15 363	this work

Figures 3.11 to 3.16 expand on Figs. 3.7 and 3.9, presenting a comparison of the quantum defects obtained from measurements in ^{88}Sr with those extracted from the energies of the observed hyperfine states in the ^{87}Sr data presented above. The ^{88}Sr quantum defects were extracted from the reported Rydberg energies using the Rydberg formula Eq. (3.5) with the most recently reported ionization limit $E_{\text{ion}}^{(0)} = 45\,932.200\,24(33)\,\text{cm}^{-1}$ [36] and the mass-scaled Rydberg constant $R(m_{88}) = 109\,736.630\,867\,5(7)\,\text{cm}^{-1}$ (see Appendix B.4). Quantum defects were obtained from the ^{87}Sr data by first subtracting the calculated hyperfine energy shift to obtain an effective $I = 0$ Rydberg state energy, and then applying Eq. (3.5) with the mass-scaled Rydberg constant $R(m_{87}) = 109\,736.623\,013\,5(7)\,\text{cm}^{-1}$ (see Appendix B.4) and ionization limit $E_{\text{ion}}^{(0)} = 45\,932.1956\,\text{cm}^{-1}$.

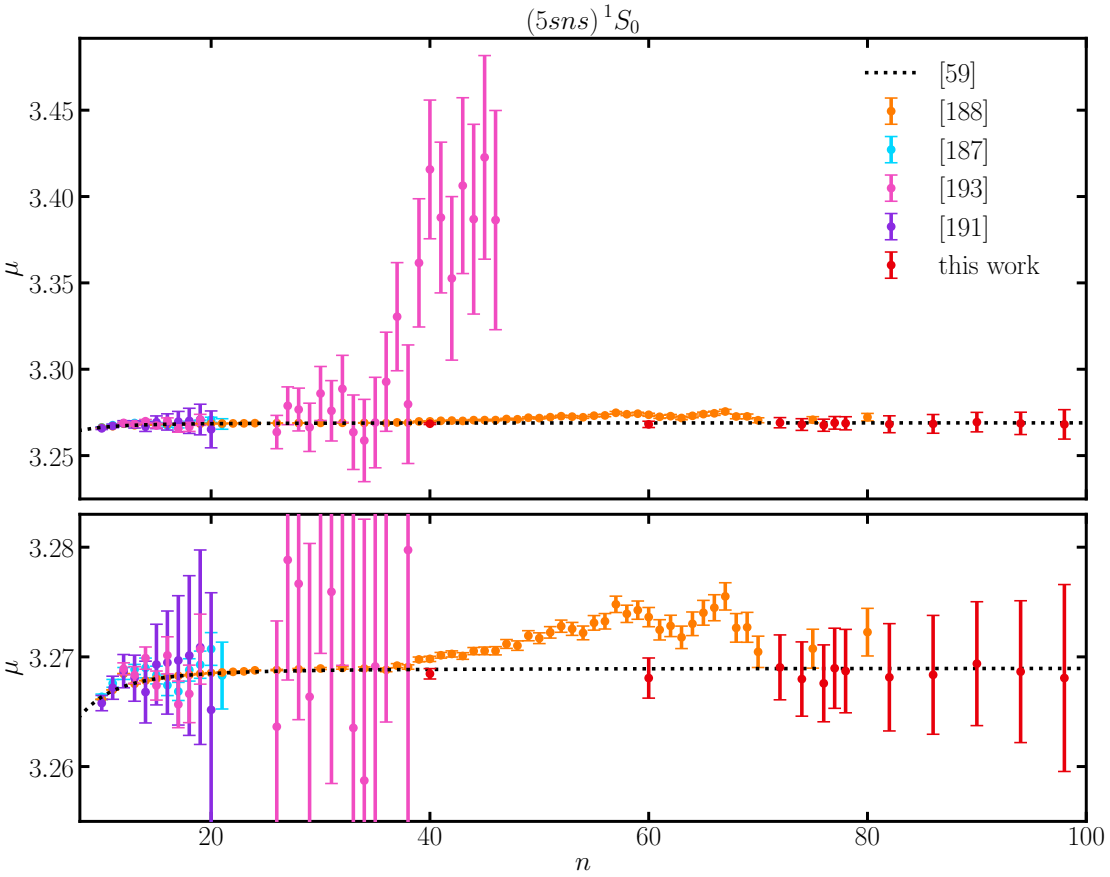

Figure 3.11: Quantum defects for the $(5sns)\,^1S_0$ Rydberg series. For ^{88}Sr, the quantum defects were calculated from the term energies reported in [187, 188, 191, 193]. The quantum defects derived from the ^{87}Sr data were obtained after removing the hyperfine shift.

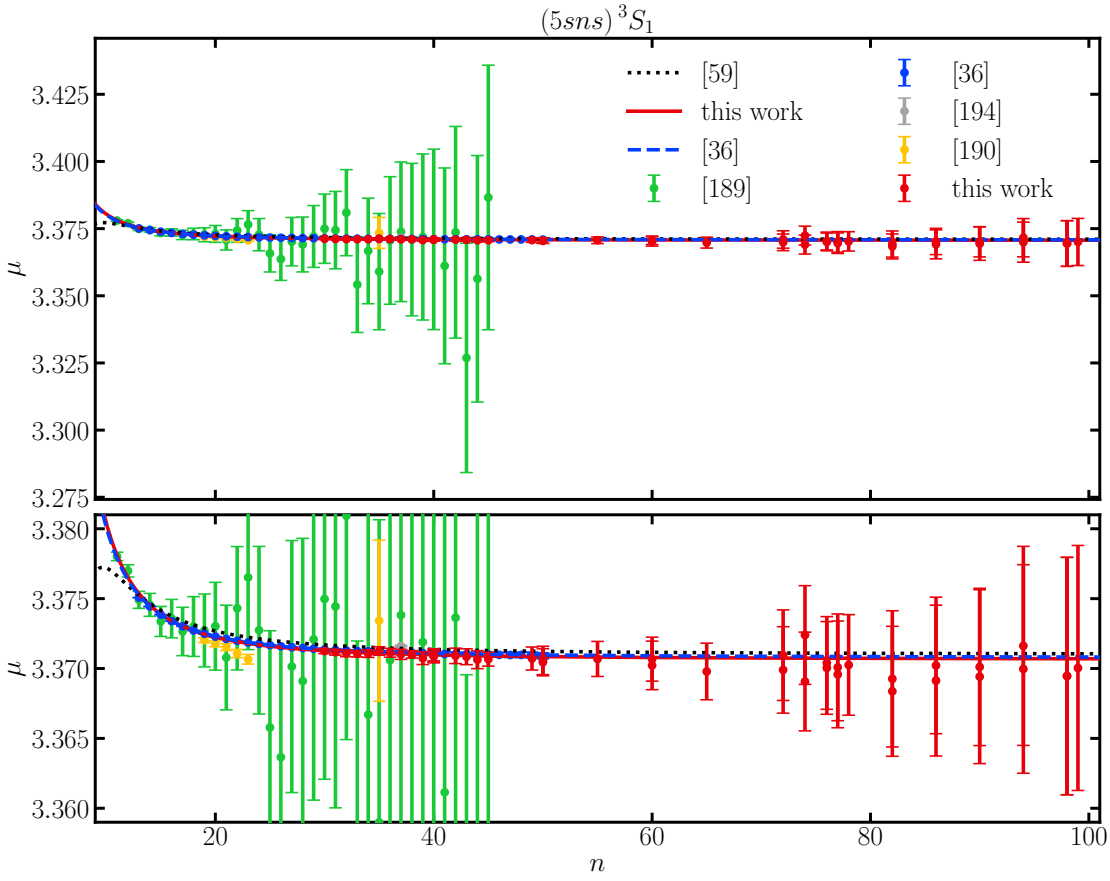

Figure 3.12: Quantum defects for the $(5sns)\,^3S_1$ Rydberg series. For ^{88}Sr, the quantum defects were calculated from the term energies reported in [36, 189, 190, 194]. The quantum defects derived from the ^{87}Sr data were obtained after removing the hyperfine shift.

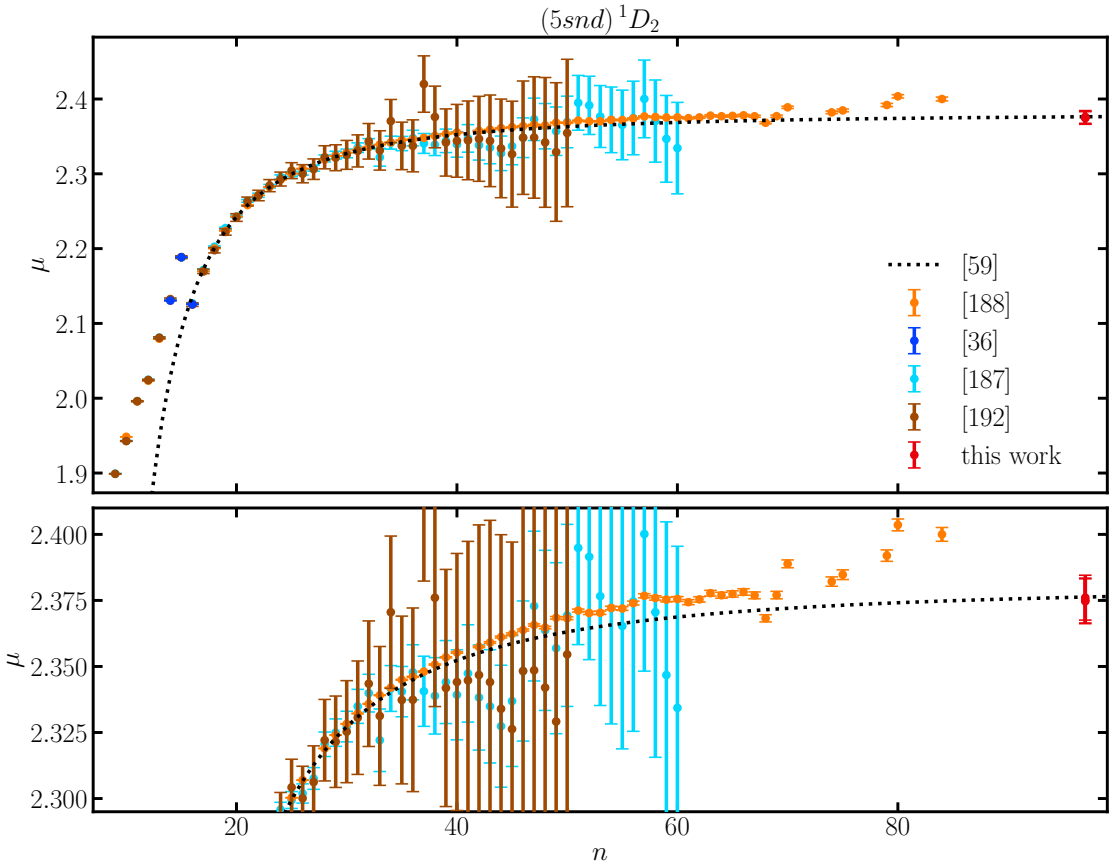

Figure 3.13: Quantum defects for the $(5snd)\,^1D_2$ Rydberg series. For ^{88}Sr, the quantum defects were calculated from the reported term energies. The quantum defects derived from the ^{87}Sr data were obtained after removing the hyperfine shift.

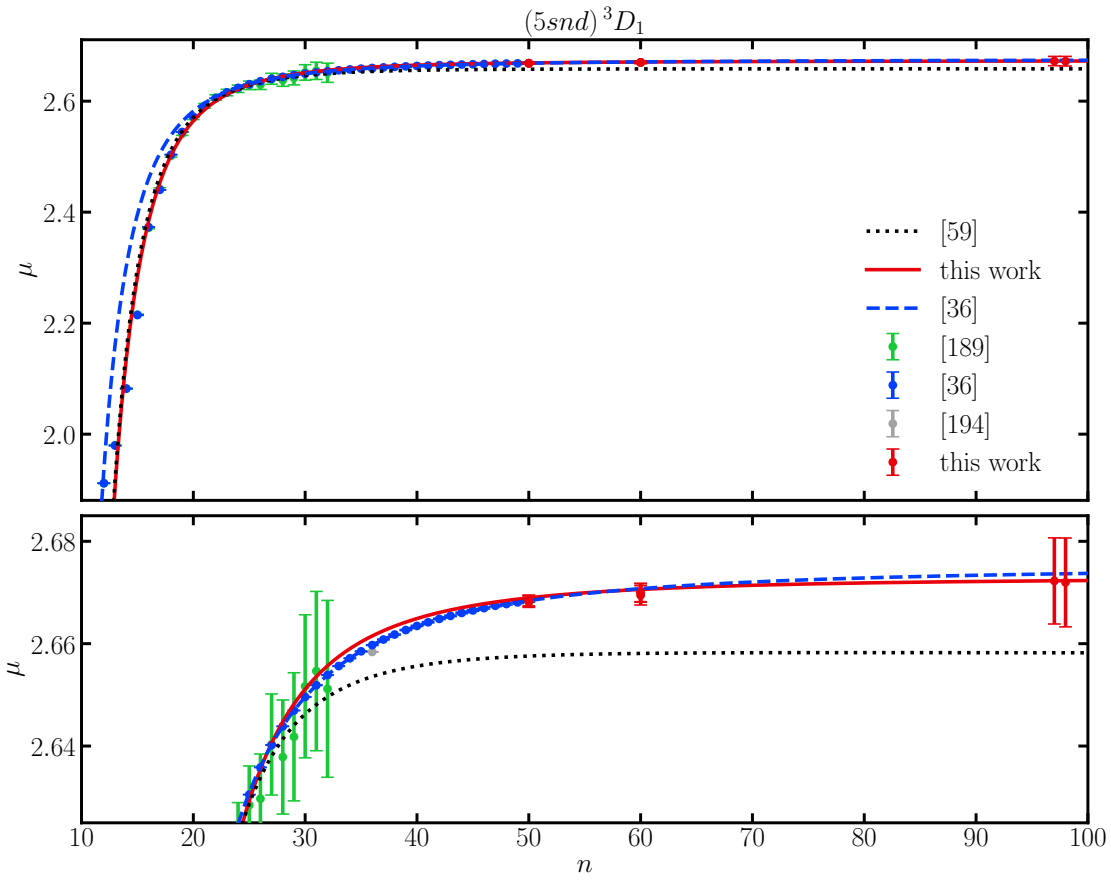

Figure 3.14: Quantum defects for the $(5snd)\,^3D_1$ Rydberg series. For ^{88}Sr, the quantum defects were calculated from the reported term energies. The quantum defects derived from the ^{87}Sr data were obtained after removing the hyperfine shift.

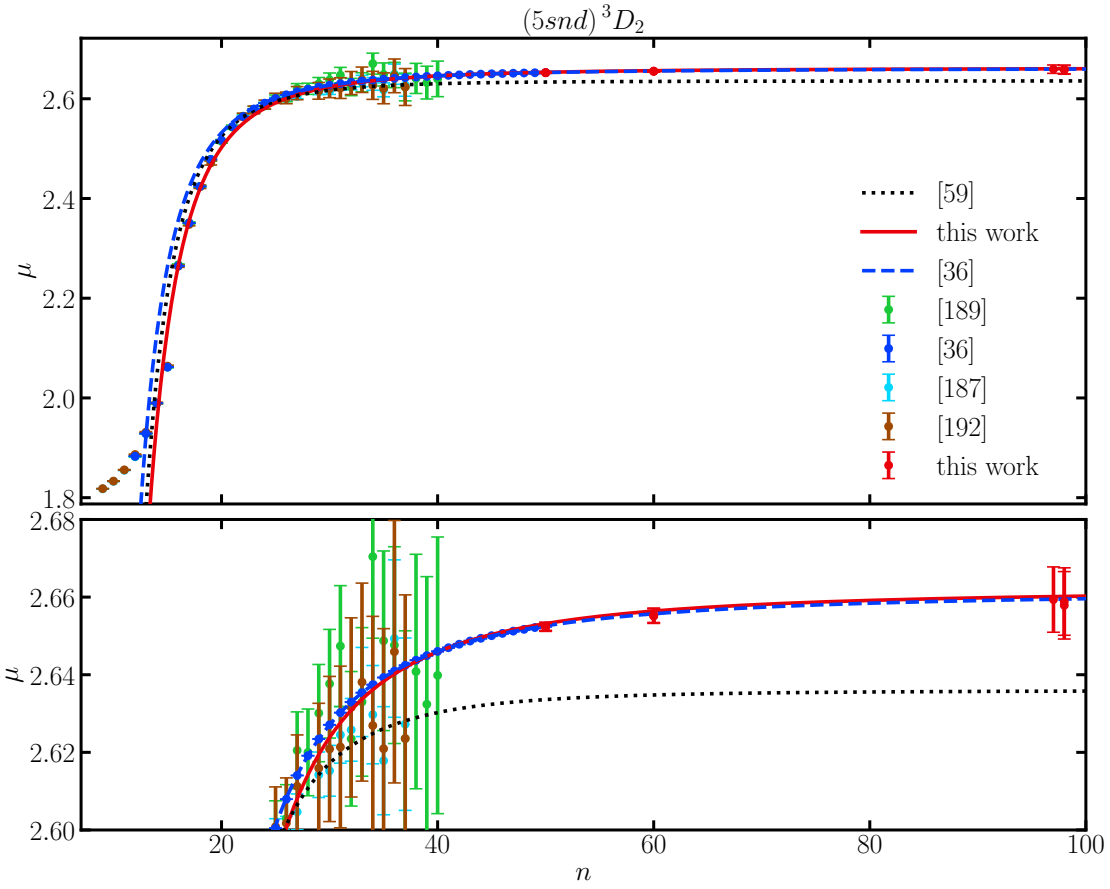

Figure 3.15: Quantum defects for the $(5snd)\,^3D_2$ Rydberg series. For ^{88}Sr, the quantum defects were calculated from the reported term energies. The quantum defects derived from the ^{87}Sr data were obtained after removing the hyperfine shift.

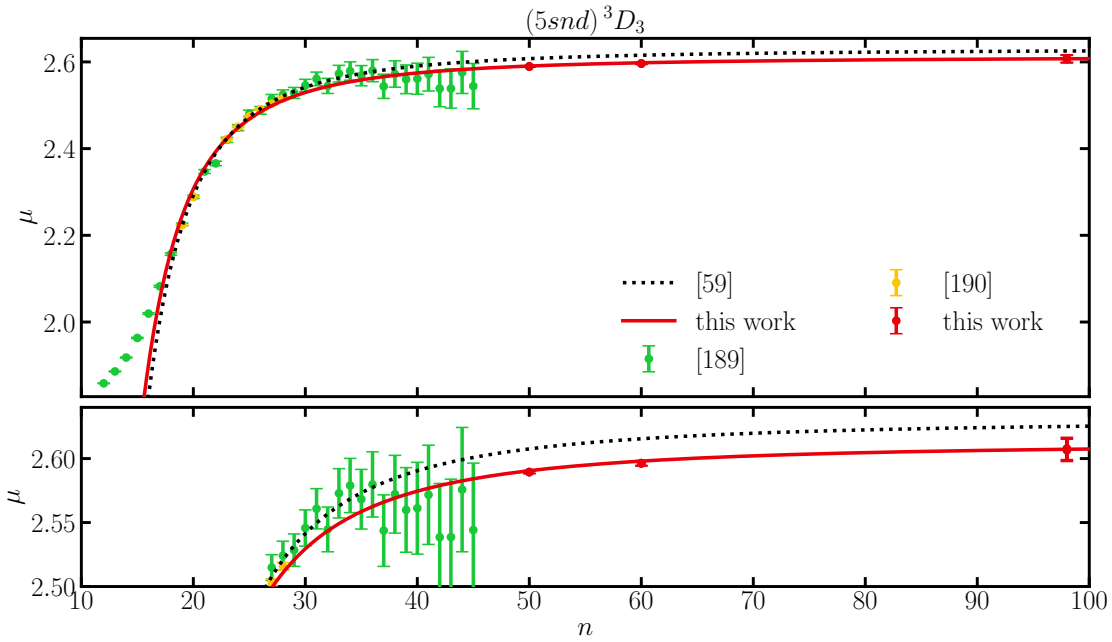

Figure 3.16: Quantum defects for the $(5snd)\,^3D_3$ Rydberg series. For ^{88}Sr, the quantum defects were calculated from the reported term energies. The quantum defects derived from the ^{87}Sr data were obtained after removing the hyperfine shift.

4. Vibrationally-Excited Rydberg Molecules in Cold Gases of ^{87}Sr

Many interesting phenomena in quantum systems have length scales associated with their underlying interactions. Perhaps one of the most fundamental results from either Bose-Einstein or Fermi-Dirac statistics which lead to the bunching or antibunching of particles [235]. Another interesting phenomena is the "fermionization" of strongly-interacting bosons in a one-dimensional gas [236]. In these examples, the interactions affect the likelihood of finding one particle within a fixed distance of another, i.e., they become spatially correlated. As a result, tools that provide information about the spatial correlations in such systems are extremely valuable and can furnish new insights into the behavior of quantum gases.

Possibly one of the most ingenious ways of probing correlations due to quantum statistics was demonstrated with metastable helium atoms. By dropping both ultracold and quantum degenerate Bose and Fermi gases onto a time-resolved position-sensitive MCP detector, the two-body and three-body spatial correlations of the dropped cloud (or the momentum correlations of the initial cloud) were able to be reconstructed [237–239]. Although powerful, this techniques requires atoms to be in a metastable state with enough energy to trigger the MCP channels. It is also not *in situ*, needing the samples to be at equilibrium prior to dropping in order for the reconstruction to make sense, thus limiting the possibility of observing the temporal development of spatial correlations.

Alternative, less destructive, *in situ* techniques have also been developed and employed but these are generally restricted by the dimensionality of a system or the length scales accessible. For the shortest length scales (i.e., $R = 0$ contact interactions), inelastic loss due to three-body recombination has been shown to be sensitive to the effects of $g^{(3)}(R)$ as evidenced by the different loss rates observed in nondegenerate compared to degenerate Bose

gases [240]. For length scales comparable to the sizes of molecular bonds (i.e., $R \sim R_{\mathrm{vdW}} \lesssim 10\,\mathrm{nm}$), photoassociative spectroscopy (PAS) can be used since efficient photoassociation requires the constituent atoms to have a separation distance comparable to the range of the molecular potential (the van der Waals length R_{vdW}) [241, 242]. If the effect can be observed in a two- (or one-) dimensional lattice structure, quantum gas microscopes (QGM) have the capability of directly detecting the presence or absence of atoms on a particular lattice site and, therefore, are able to directly measure spatial correlations [243–245]. Since QGMs require an optical lattice, their accessible length scales are generally restricted by the wavelength of light used to form the lattice ($R \gtrsim 266\,\mathrm{nm}$). Figure 4.1 illustrates some of the tools and their typical effective length scales.

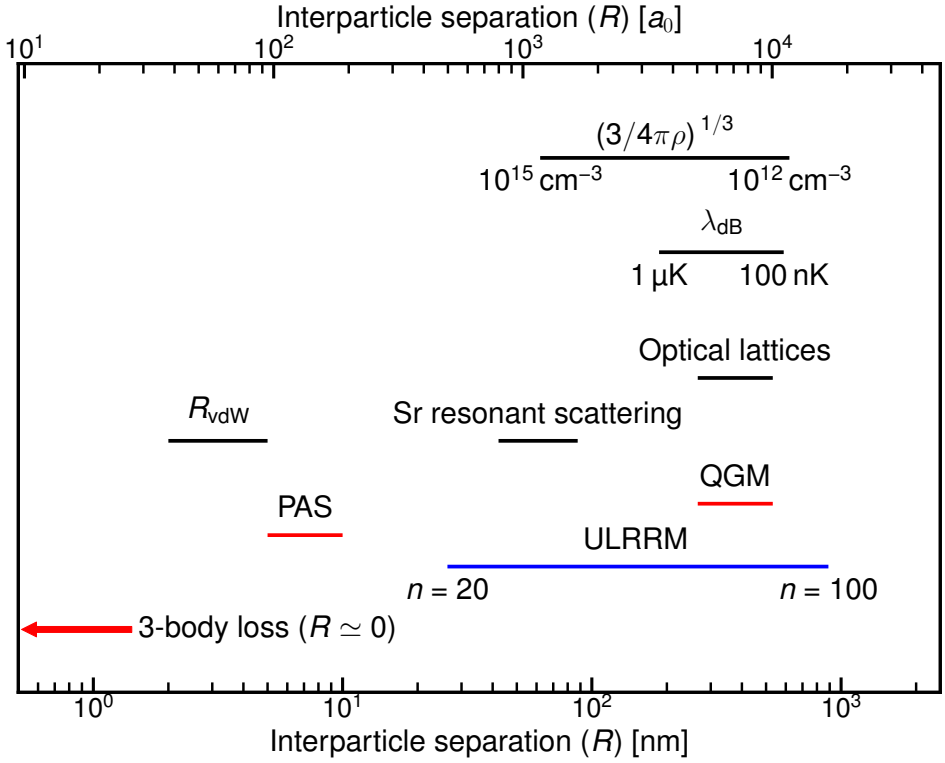

Figure 4.1: A (non-exhaustive) list of lengths scales in typical ultracold gas experiments. Black lines show the length scales associated with various interactions and red lines illustrate the effective ranges of various techniques. The blue line indicates the length scales accessible with ULRRMs at different values of principal quantum numbers (n).

As seen in Fig. 4.1, the techniques mentioned above cannot probe length scales $10\,\mathrm{nm} \lesssim$

$R \lesssim 266\,\text{nm}$. Such length scales, however, can be explored with ULRRMs. Analogous to how PAS can be used to probe correlations on the order of the molecular potential R_{vdW}, the formation rate of ULRRMs can be applied to probe spatial correlations on the length scale of the ULRRM molecular potential. The advantage of ULRRMs is that the ULRRM molecular potential is related to the size of the parent Rydberg atom, allowing many different interparticle separations to be explored by simply varying the principal quantum number. This tunability gives ULRRMs a huge advantage, allowing them to probe particle correlations on length scales previously inaccessible using alternate techniques.

This chapter contains work that is currently in progress. As such, the presented data, analysis, and results should be considered preliminary.

4.1 Probing of Spatial Correlations with ULRRMs

In an ideal noninteracting gas, the atoms are expected to exhibit quantum statistical effects in their density distributions depending on whether they are bosonic, fermionic, or classical. For the two-body case, this effect on the density distribution is typically characterized by the pair correlation function $g^{(2)}(R)$ and can be written (for the ideal noninteracting case) as

$$g^{(2)}(R) = 1 + \epsilon \mathrm{e}^{-2\pi R^2/{\lambda_{\text{dB}}}^2} \tag{4.1}$$

where $\epsilon = +1$, -1, and 0 for bosons, fermions, and classical gases, respectively, and $\lambda_{\text{dB}} = h/\sqrt{2\pi m k_B T}$ is the thermal de Broglie wavelength. For a more detailed discussion, see [235][63].

It was shown in [249] that the excitation rate of ULRRMs is sensitive to spatial correlations on length scales of the Rydberg electron orbital radius, i.e., $R \sim R_n \approx 2(n-\delta)^2$. In particular, these studies were performed using the most deeply-bound vibrational ($\nu = 0$) dimer state which is spatially well-localized in the outer lobe of the Rydberg electron wave function as seen in Fig. 4.2. Since the state is radially well-localized, by varying n (and

[63] I found the derivations in [246–248] to be helpful.

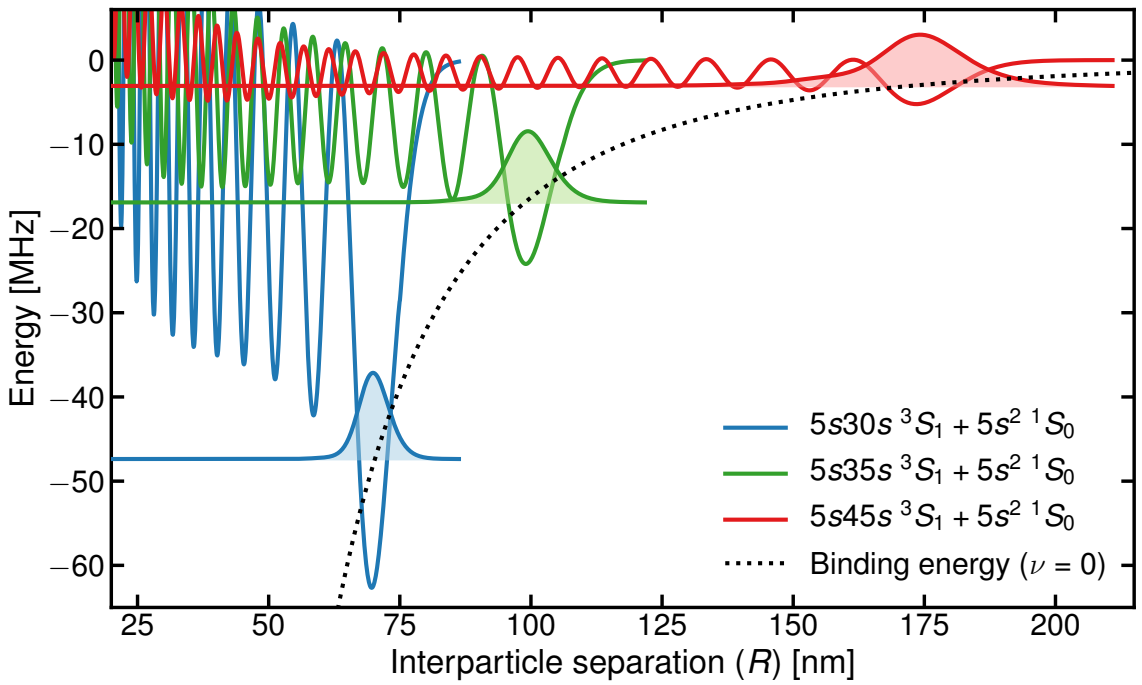

Figure 4.2: Calculated radial molecular potentials of a $(5sns)\,^3S_1 + (5s^2)\,^1S_0$ ULRRM and the $\nu = 0$ radial vibrational wave functions for $n = 30$, 35, and 45. As seen in the figure, the position of the well-localized $\nu = 0$ vibrational state depends on n. The binding energy of the $\nu = 0$ states is also shown with the $(n^*)^{-6}$ scaling (dotted line).

therefore R_n) the optimum interatomic pair separation between atoms for formation of $\nu = 0$ ULRRMs can be tuned. Therefore, differences in the initial spatial correlations between bosonic, fermionic, and classical gases can be observed as changes in the ULRRM excitation rates.

The probability of exciting a Rydberg molecule in an ultracold gas can be modeled similarly to photoassociation processes [241, 242, 250] and a schematic is outlined in Fig. 4.3. Starting from a pair of colliding atoms, their scattering wave function can be written as $|\chi_0^E\rangle$ where, well-outside the interatomic potential, they can be described by free-particle wave functions wave vector $k = \sqrt{2\mu E/\hbar^2}$ separated by R in the center-of-mass frame. It is this scattering wave function which contains information about the symmetry of the initial states. The probability of photoexcitation to a particular ULRRM state with wave function

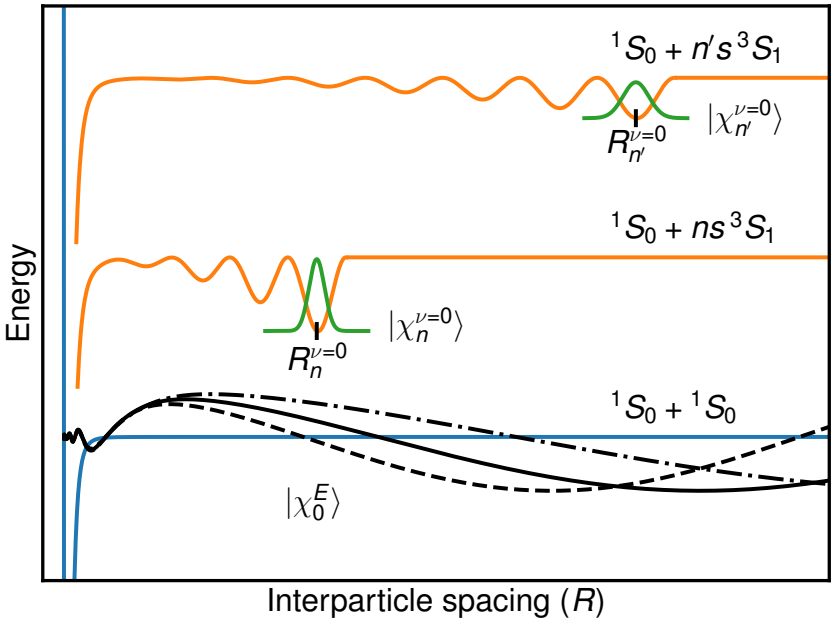

Figure 4.3: Schematic illustration of the excitation process of two free atoms to a vibrational ULRRM state. Two colliding free atoms in the $(5s^2)\,^1S_0 - (5s^2)\,^1S_0$ interaction potential (blue) have the energy-dependent scattering wave function $|\chi_0^E\rangle$ (black) with free particle wave vector $k = \sqrt{2\mu E/\hbar^2}$ for collision energy E (a thermal average of the initial colliding wave functions is represented by the different $|\chi_0^E\rangle$ curves). ULRRM potentials for $(5s^2)\,^1S_0 + (5sns)\,^3S_1$ states are shown for n and n' (orange) along with the wave functions for the most deeply-bound $\nu = 0$ states $|\chi_n^\nu\rangle$ (green) which are spatially-localized at $R_n^{\nu=0}$. Figure adapted from [249].

$|\chi_n^\nu\rangle$ can be thought of in terms of an effective Franck-Condon factor $\mathcal{F}_n^\nu = \langle\chi_0^E|\chi_n^\nu\rangle$

$$|\mathcal{F}_n^\nu|^2 = \left|\langle\chi_0^E|\chi_n^\nu\rangle\right|^2 = \left|\int_0^\infty \mathrm{d}R\, R^2 \chi_0^E(R)\,\chi_n^\nu(R)\right|^2 \tag{4.2}$$

Taking a thermal average over the initial collision energies of the two-particle states ($\langle\cdots\rangle_E$) leads to

$$\left\langle|\mathcal{F}_n^\nu|^2\right\rangle_E = \left\langle\left|\langle\chi_0^E|\chi_n^\nu\rangle\right|^2\right\rangle_E = \left\langle\left|\int_0^\infty \mathrm{d}R\, R^2 \chi_0^E(R)\,\chi_n^\nu(R)\right|^2\right\rangle_E \tag{4.3}$$

As described in [249], due to the $\nu = 0$ state being well-localized around R_n, it can be approximated as $\chi_n^{\nu=0}(R) \approx \delta(R - R_n)$. Evaluating Eq. (4.3) under this approximation

gives[64]

$$\left\langle \left| \mathcal{F}_n^{\nu=0} \right|^2 \right\rangle_E = \left\langle \left| \int_0^\infty \mathrm{d}R\, R^2 \chi_0^E(R)\, \chi_n^{\nu=0}(R) \right|^2 \right\rangle_E$$
$$\approx \left\langle \left| \chi_0^E(R_n) \right|^2 \right\rangle_E \left| \int_0^\infty \mathrm{d}R\, R^2 \chi_n^{\nu=0}(R) \right|^2$$
$$= g^{(2)}(R_n) \left| \int_0^\infty \mathrm{d}R\, R^2 \chi_n^{\nu=0}(R) \right|^2 \tag{4.4}$$

where, in the last line, the relation $\langle |\chi_0^E(R_n)|^2 \rangle_E = g^{(2)}(R_n)$, with $g^{(2)}(R_n)$ the pair-correlation function for separation R_n, was used. This replacement is nontrivial but can be made when the sample is thermal and $\chi_n^{\nu=0}(R)$ is well-localized on the scale of the initial collisional state $\chi_0^E(R)$ [249]. For the higher vibrational states $\nu > 0$, the approximation $\chi_n^{\nu=0}(R) \approx \delta(R_n)$ cannot be made since they are delocalized and, therefore, Eq. (4.3) must be evaluated with the full $|\chi_n^\nu\rangle$ ULRRM wave function.

4.2 Experimental Procedure

The experimental procedures used for studies of vibrationally-excited ULRRMs are similar to those presented in [249] and so will only be briefly covered. The production of cold gases of both spin-polarized and unpolarized ^{87}Sr begins by loading a mixture of ^{87}Sr and ^{84}Sr in to the magnetic trap. As described in Section 2.1.2, both isotopes are loaded by operating a blue 461 nm MOT on the $(5s^2)\,{}^1S_0 \rightarrow (5s5p)\,{}^1P_1$ transition tuned to the first isotope and then changing the laser frequency to trap the second isotope. Laser cooling on the 461 nm transition populates the magnetic trap with atoms following the weak $(5s5p)\,{}^1P_1 \rightarrow (5s4d)\,{}^1D_2 \rightarrow (5s5p)\,{}^3P_2$ decay path. After the atoms are collected in the magnetic trap, both isotopes are repumped with a pulse of 481 nm light resonant with the $(5s5p)\,{}^3P_2 \rightarrow (5p^2)\,{}^3P_2$ transition and second-stage narrow line laser cooling proceeds simultaneously for both isotopes on the $(5s^2)\,{}^1S_0 \rightarrow (5s5p)\,{}^3P_1$ transition at 689 nm. Narrow line cooling produces samples at temperatures of about 2 µK which are then loaded in to

[64] When evaluating Eq. (4.4), it helps to notice that $\int_0^\infty \mathrm{d}R\, R^2 \chi_0^E(R)\, A\delta(R - R_n) = R_n^2 \chi_0^E(R_n)\, A = \chi_0^E(R_n) \int_0^\infty \mathrm{d}R\, R^2 A\delta(R - R_n)$.

the ODT before all laser cooling light is extinguished.

Once loaded in to the ODT, sample preparation for the spin-polarized and unpolarized gases differ slightly. For the unpolarized sample, the atoms are held in the ODT for a short period of time to allow for free-evaporation before starting forced evaporation. For the spin-polarized sample, an approximately 7 G magnetic bias field is ramped on during the free-evaporation hold, providing both a quantization axis and Zeeman splitting the $(5s5p)\,^3P_1, F = 9/2$ states by approximately 600 kHz between adjacent m_F levels. Spin-polarization is achieved by optically pumping on the $(5s^2)\,^1S_0, F = 9/2 \rightarrow (5s5p)\,^3P_1, F = 9/2$ transition, individually addressing each $\Delta m_F = +1$ transition with σ^+-polarized 689 nm light. After spin-polarization, the bias magnetic field is ramped down to $B_{\mathrm{pol}} \approx 1$ G to maintain a quantization axis and forced evaporation is performed.

The effectiveness of spin-polarization is evaluated spectroscopically by exciting trapped atoms to a $(5sns)\,^3S_1, F = 11/2$ Rydberg state in the $B_{\mathrm{pol}} \approx 1$ G bias magnetic field. For this setup, excitation is performed with counterpropagating 689 nm and 320 nm beams both with π-polarization to drive $\Delta m_F = 0$ transitions. The 689 nm photon is $\Delta/2\pi = 14.85(100)$ MHz blue-detuned of intermediate $(5s5p)\,^3P_1, F = 11/2$ state and the frequency of the 320 nm laser is scanned. During excitation, the ODT was turned off to eliminate AC Stark shifts and turned back on to recapture the remaining ground-state atoms after any Rydberg atoms produced are field ionized and detected with the MCP. In order to increase signal, the π-π excitation and measurement cycles are performed 1000 times before before a new sample is loaded and the 320 nm laser frequency changed. A comparison of excitation in an unpolarized and spin-polarized sample is shown in Fig. 4.4. Model fits to the data show that the optical pumping transfers >90 % of the population into the $(5s^2)\,^1S_0, F = 9/2, m_F = 9/2$ state. It should be noted that the repeated π-π excitations do cause some population redistribution among the m_F states so the fit values place a lower bound on the effectiveness of optical pumping.

After forced evaporation, both spin-polarized and unpolarized samples are at about

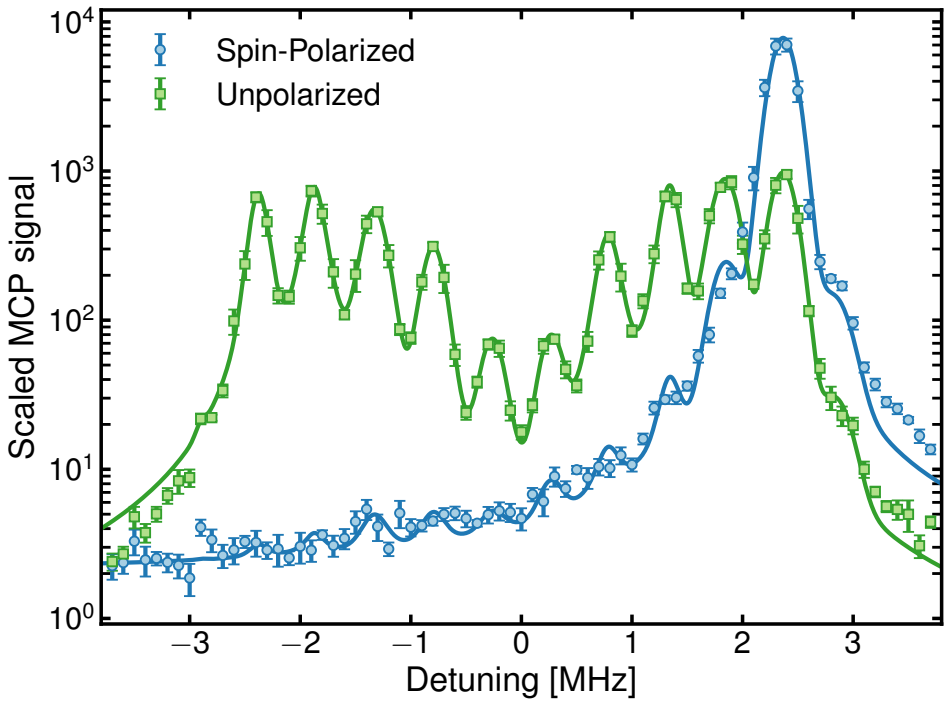

Figure 4.4: Experimental spectra and fit of excitation to the $(5s33s)\,^3S_1, F = 11/2$ state from both an unpolarized (green) and a spin-polarized (blue) samples. A bias magnetic field $B_{\text{pol}} \approx 1\,\text{G}$ Zeeman splits the Rydberg state. Excitation is performed with π-polarized counterpropagating 689 nm and 320 nm beams. Ideally, only $\Delta m_F = 0$ transitions are driven with the π-π excitation scheme so only 10 peaks should be visible in the unpolarized spectra. The small features on the extreme left and right ($m_F = \pm 11/2$) are likely due to imperfect polarization.

900 nK. Prior to Rydberg excitation, a pulse of 689 nm light resonant with the $(5s^2)\,^1S_0 \rightarrow (5s5p)\,^3P_1$ transition in ^{84}Sr is applied to remove the isotope from the ODT. Due to the large isotope shifts, minimal heating was observed in ^{87}Sr.

With the exception of the ≈1 G magnetic bias field used to maintain the spin-polarization (no bias field is applied when studing an unpolarized sample), the same two-photon Rydberg excitation scheme is applied to both the spin-polarized and unpolarized gases. The first photon is at 689 nm with σ^+-polarization and is blue-detuned from the intermediate $(5s5p)\,^3P_1, F = 11/2$ state by about $\Delta/2\pi = 14.85(100)$ MHz. The second photon is at 320 nm with π-polarization and is tuned to excite ULRRMs of the parent $(5sns)\,^3S_1, F = 11/2$ Rydberg state. Excitation powers were kept low to avoid saturating the MCP so the signal-

to-noise ratio was increased by performing 1000 excitation and detection cycles on a sample before a new sample is prepared and the frequency of the 320 nm laser changed. Again, the ODT is turned off during Rydberg excitation to eliminate AC Stark shifts before being turned back on after the field ionization and detection to recapture remaining ground-state atoms.

4.3 Spectroscopy of $\nu = 1$ and $\nu = 2$ ULRRMs

Spectroscopy was performed by exciting ULRRMs of the parent $(5sns)\,^3S_1, F = 11/2$ Rydberg state for $n = 31-41$. In the experiment, the photoexcitation signal of the ULRRM dimers can be modeled as

$$\mathcal{S}_n^\nu(f) = \alpha I_{689\,\mathrm{nm}} I_{320\,\mathrm{nm}} \mathcal{N}_2 \beta_n \mathcal{C} \left\langle |\mathcal{F}_n^\nu|^2 \right\rangle_E L(f) \tag{4.5}$$

where α is the detection efficiency, $I_{689\,\mathrm{nm}}$ and $I_{320\,\mathrm{nm}}$ are the intensities of the two-photon excitation lasers, β_n is proportional to the square of the reduced two-photon electronic-transition matrix element, $\mathcal{N}_2 \equiv \int \mathrm{d}^3 r\, \rho(R)^{\,2}$ is the volume integral of the square of the density distribution, $\mathcal{C}$ is a Clebsch-Gordan factor, and $L(f)$ is a normalized lineshape function. To eliminate dependences on the specific lineshape, the quantity of interest is the integrals of the observed excitation signal

$$\mathcal{S}_n^\nu = \int \mathrm{d}f\, \mathcal{S}_n^\nu(f) = \alpha I_{689\,\mathrm{nm}} I_{320\,\mathrm{nm}} \mathcal{N}_2 \beta_n \mathcal{C} \left\langle |\mathcal{F}_n^\nu|^2 \right\rangle_E \tag{4.6}$$

For a particular n, β_n should remain the same for both spin-polarized and unpolarized samples and the Clebsch-Gordan factor $\mathcal{C}$ can be calculated. By monitoring the atom number, temperature, $I_{689\,\mathrm{nm}}$, and $I_{320\,\mathrm{nm}}$, corrections can be applied to the observed signals to reduce potential systematic errors.

The first corrections applied to the "raw" MCP signal involves accounting for any under-counting due to MCP saturation using the model described in Section 2.6.3. Slow changes in the two-photon excitation rate are easily removed by dividing the signal by $I_{689\,\mathrm{nm}}$ and

$I_{320\,\mathrm{nm}}$ recorded on a DAQ[65]. Applying these corrections results in a "scaled" MCP signal. An example two-photon excitation spectra to the $(5s34s)\,^3S_1, F = 11/2$ parent Rydberg state from both a spin-polarized and an unpolarized ^{87}Sr sample is shown in Fig. 4.5, demonstrating the effects of removing dependences on $I_{689\,\mathrm{nm}}$, $I_{320\,\mathrm{nm}}$, and MCP saturation. Fitting is performed on the scaled MCP signals to obtain the integral of the particular ULRRM line of interest (represented by $\mathcal{S}_n^\nu$ in Eq. (4.6)). Fits to the spectra in Fig. 4.5 are shown in Fig. 4.6.

Before extracting a value for the integral, we must still determine the two-body density-dependent correction term $\mathcal{N}_2$ to reduce the effects of atom number and temperature variations for the different samples. To make a comparison between spin-polarized and unpolarized signals, it is also necessary to determine the ratio of their detection efficiencies $\alpha_{\mathrm{pol}}/\alpha_{\mathrm{unpol}}$.

4.3.1 Two-Body Density Correction: $\mathcal{N}_2$

During data collection, both the atom number and sample temperature are recorded with absorption imaging on the $(5s^2)\,^1S_0 \rightarrow (5s5p)\,^1P_1$ transition. All the samples have the same final ODT trapping parameters prior to Rydberg excitation. The vertical trap frequency was measured to be $f_z \approx 300\,\mathrm{Hz}$ and radial trap frequency is about $f_r \approx 130\,\mathrm{Hz}$. Knowing these parameters, the density-dependent $\mathcal{N}_2$ factor can be calculated and applied to the ULRRM signals.

For a thermal gas in a three-dimensional harmonic trap, the density distribution is given by

$$\rho(\mathbf{r}) = \frac{N}{\pi^{3/2} R_x R_y R_z} \mathrm{e}^{-x^2/R_x^2} \mathrm{e}^{-y^2/R_y^2} \mathrm{e}^{-z^2/R_z^2} \tag{4.7}$$

where N is the total atom number and $R_i^2 = 2k_B T/m\omega_i^2$ where $f_i = \omega_i/2\pi$ is the trap frequency [7]. For the dimers, the total signal should be proportional to $[\rho(\mathbf{r})\,]^2$ integrated

[65] We actually record voltages $V_{689\,\mathrm{nm}}$ and $V_{320\,\mathrm{nm}}$ from monitor photodiodes which are proportional to $I_{689\,\mathrm{nm}}$ and $I_{320\,\mathrm{nm}}$, respectively.

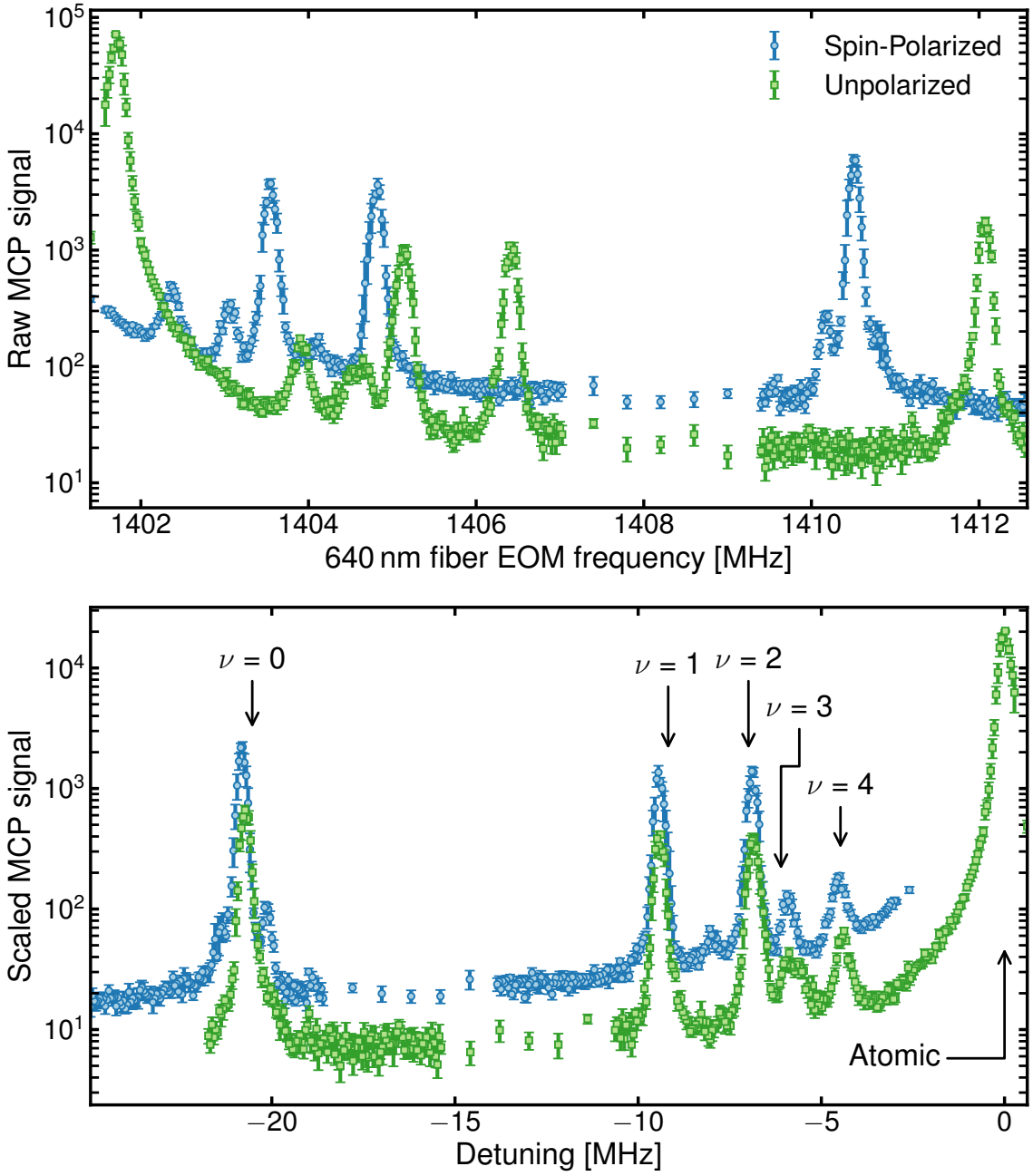

Figure 4.5: Upper figure shows the signals obtained directly from the MCP accumulated from 1000 excitation and detection cycles when scanning the 640 nm fiber EOM frequency (the "raw" MCP signal). Lower figure shows the "scaled" MCP signals after removing the Zeeman shift and accounting for MCP saturation as well as both $I_{689\,\mathrm{nm}}$ and $I_{320\,\mathrm{nm}}$. ^{87}Sr atom number was approximately the same for both the spin-polarized and unpolarized samples. Data shown is for excitation to the $(5s34s)\,^3S_1, F = 11/2$ parent state. The theoretically calculated positions of the various vibrational dimer states ν are indicated by arrows (lower figure).

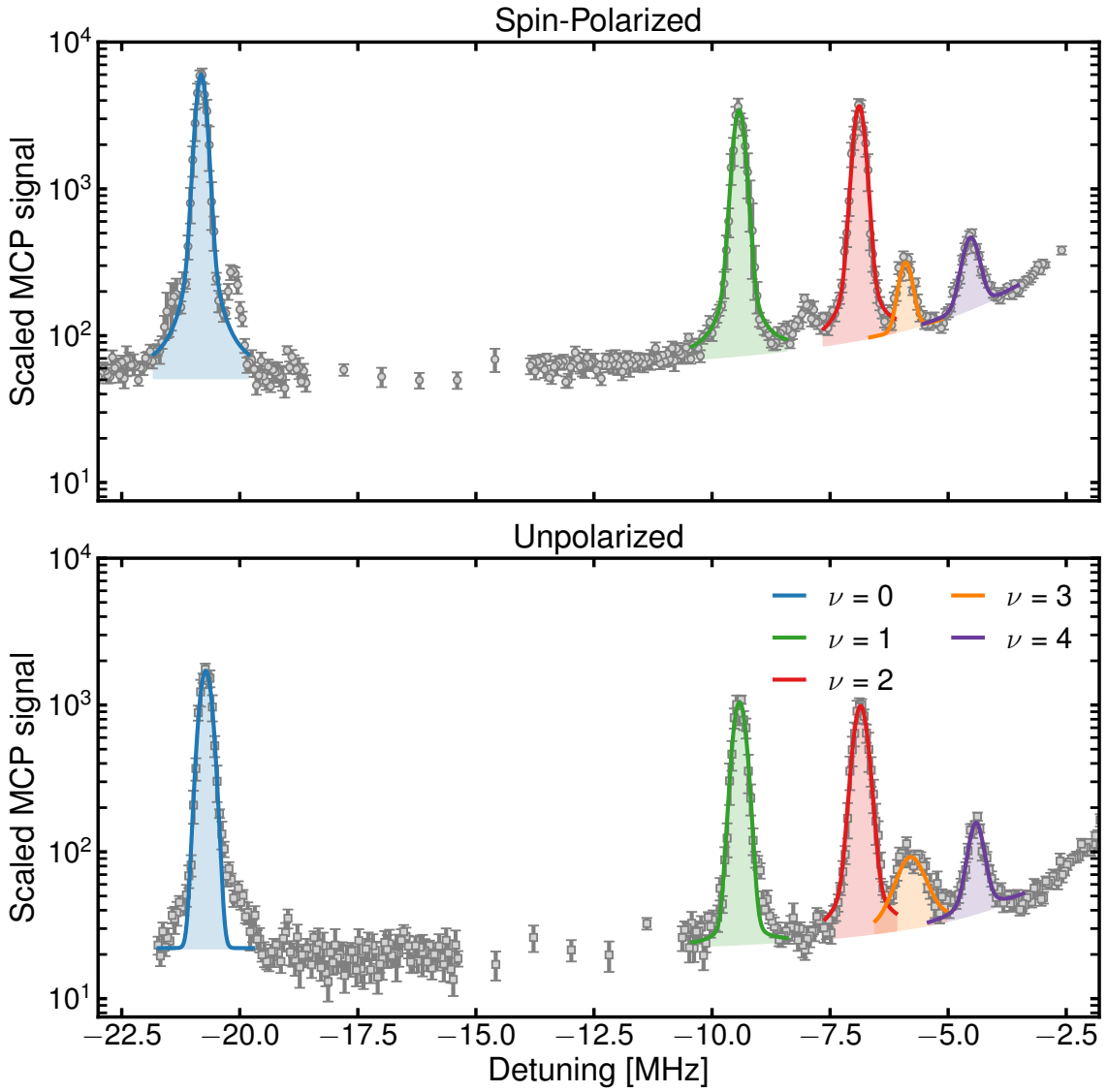

Figure 4.6: Fits to the spin-polarized (upper panel) and unpolarized (lower panel) $(5s34s)\,^3S_1, F = 11/2$ spectra shown in Fig. 4.5. Solid lines show the fit results and the shaded regions represent the integrals used to extract $\mathcal{S}^{\nu}_{n=34}$.

over all space. Performing this integration yields

$$\mathcal{N}_2 = \int \mathrm{d}^3 r\, \rho(\mathbf{r})^2 = \frac{N^2}{(2\pi)^{3/2} R_x R_y R_z} \propto \frac{N^2}{T^{3/2}} \tag{4.8}$$

Therefore, we can scale the measured signal by $N^2/T^{3/2}$ in order to account for the signal dependence on atom number and temperature. Recall that the same trapping parameters was used for both the spin-polarized and unpolarized samples and therefore the dependences on the trap frequencies drop out. This correction is applied to all the dimer data.

4.3.2 Examining Polarized-Polarized and Unpolarized-Unpolarized Ratios

In order to eliminate any dependency of $\mathcal{S}_n^\nu$ on the detection efficiency α, spin-polarized signals were compared to spin-polarized signals and unpolarized signals were compared to unpolarized signals within a principal quantum number. In particular, the ratios of the $\nu = 1$ and 2 states were compared to the $\nu = 0$ with the ratio defined as

$$\frac{\mathcal{S}_{n,x}^\nu}{\mathcal{S}_{n,x}^{\nu=0}} = \frac{\alpha_x I_{689\,\mathrm{nm}} I_{320\,\mathrm{nm}} \mathcal{N}_2 \beta_n \mathcal{C}_x \left\langle \left| \mathcal{F}_{n,x}^\nu \right|^2 \right\rangle_E}{\alpha_x I_{689\,\mathrm{nm}} I_{320\,\mathrm{nm}} \mathcal{N}_2 \beta_n \mathcal{C}_x \left\langle \left| \mathcal{F}_{n,x}^{\nu=0} \right|^2 \right\rangle_E} = \frac{I_{689\,\mathrm{nm}} I_{320\,\mathrm{nm}} \mathcal{N}_2 \left\langle \left| \mathcal{F}_{n,x}^\nu \right|^2 \right\rangle_E}{I_{689\,\mathrm{nm}} I_{320\,\mathrm{nm}} \mathcal{N}_2 \left\langle \left| \mathcal{F}_{n,x}^{\nu=0} \right|^2 \right\rangle_E} \tag{4.9}$$

where x represents the spin-polarized ($\mathcal{S}_{n,\mathrm{pol}}^\nu$) or unpolarized ($\mathcal{S}_{n,\mathrm{unpol}}^\nu$) signal. The dependence on α_x is eliminated because the data come from either polarized or unpolarized samples only. Monitoring the intensities $I_{689\,\mathrm{nm}}$ and $I_{320\,\mathrm{nm}}$ allows those factors to be scaled out of a particular measurement. The recorded atom number and temperature are used to calculate $\mathcal{N}_2$. Therefore, the $\langle |\mathcal{F}_{n,x}^\nu|^2 \rangle_E / \langle |\mathcal{F}_{n,x}^{\nu=0}|^2 \rangle_E$ must be the dominant contributing factor to $\mathcal{S}_{n,x}^\nu / \mathcal{S}_{n,x}^{\nu=0}$.

The measured ratios when varying the principal quantum number over $n = 31 - 41$ is shown in Fig. 4.7. The $\mathcal{S}_{n,x}^{\nu=1}/\mathcal{S}_{n,x}^{\nu=0}$ and $\mathcal{S}_{n,x}^{\nu=2}/\mathcal{S}_{n,x}^{\nu=0}$ ratios exhibit very different n-dependencies common to both the spin-polarized and unpolarized samples. While the $\mathcal{S}_{n,x}^{\nu=1}/\mathcal{S}_{n,x}^{\nu=0}$ ratio exhibits the expected excitation reduction for lower n, the $\mathcal{S}_{n,x}^{\nu=2}/\mathcal{S}_{n,x}^{\nu=0}$ ratio is counterintuitive and was found to be enhanced for lower n.

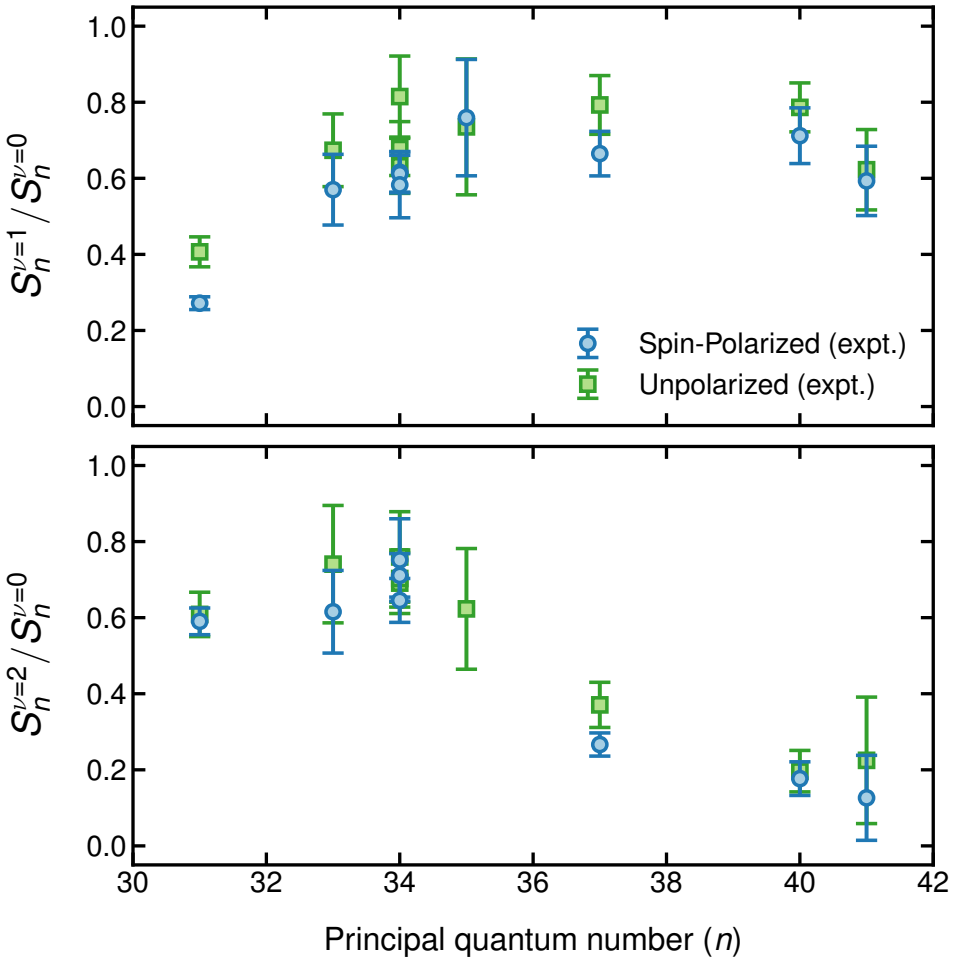

Figure 4.7: Experimentally measured ratios of the $\nu = 1$ (upper panel) and $\nu = 2$ (lower panel) vibrational states compared to the $\nu = 0$ state of the same n for both spin-polarized (blue circles) and unpolarized (green squares) samples.

This n-scaling of the ratios common to both the spin-polarized and unpolarized samples can be qualitatively understood by examining the radial vibrational wave functions[66]. Figure 4.8 shows ULRRM potentials and the $\nu = 0$, 1, and 2 radial vibrational wave functions for a representative selection of n. The $\nu = 0$ state is localized in the outermost well of the ULRRM potential near $R_n^{\nu=0} \simeq 1.87(n-\delta)^2 a_0$[67] meaning the contribution to $\langle |\mathcal{F}_{n,x}^{\nu=0}|^2 \rangle_E$ comes exclusively from the region around $R_n^{\nu=0}$. As a result of this relatively simple n-

[66] In analogy with standard photoassociation where varying the vibrational state ν provides information about both the initial free-free scattering state and the molecular state.

[67] This scaling is obtained from fitting the theoretically calculated ULRRM radial vibrational wave functions.

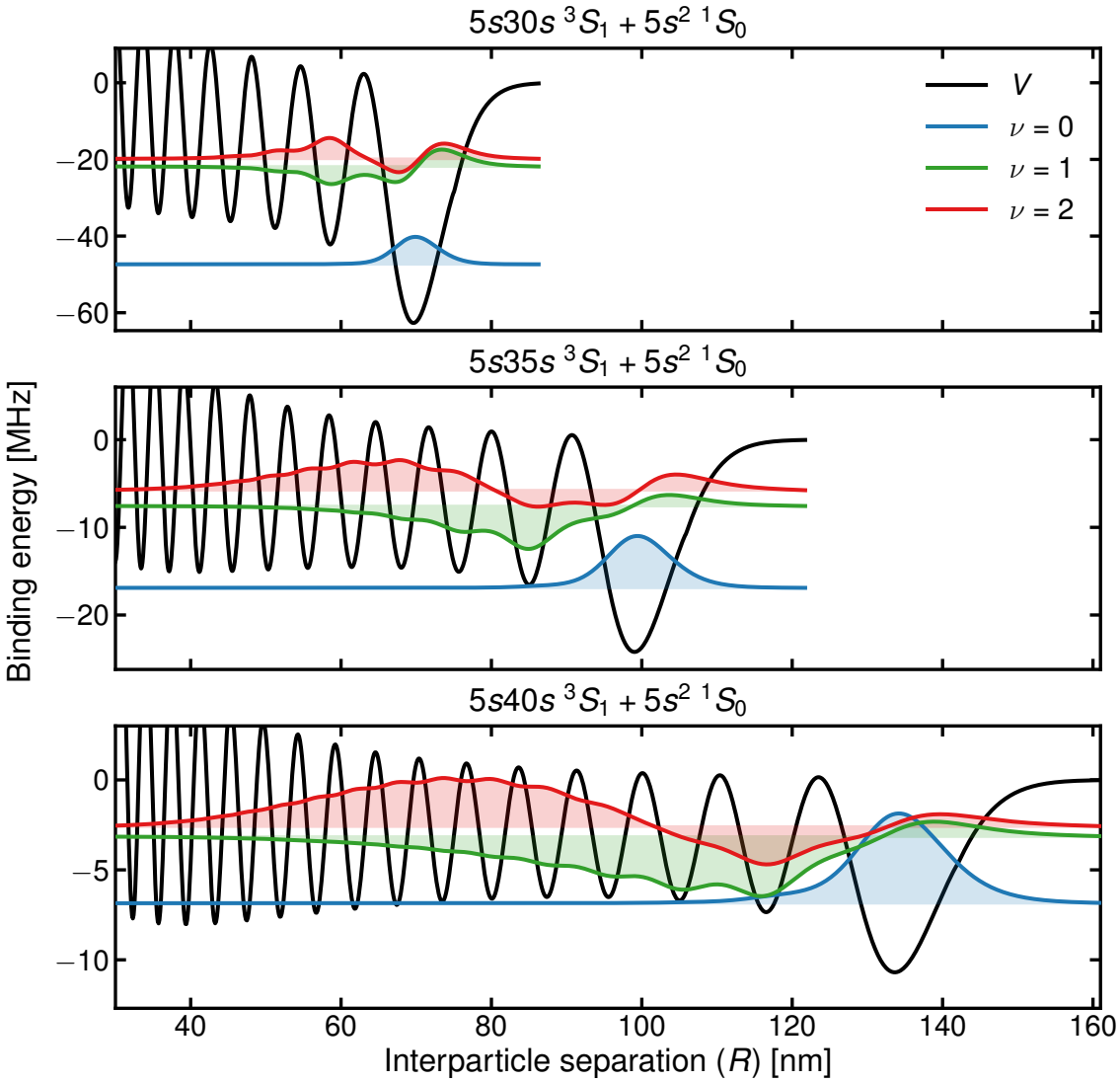

Figure 4.8: Illustrative ULRRM potentials (V) radial vibrational wave functions for $\nu = 0$, 1, and 2 for a $(5sns)\,^3S_1 + (5s^2)\,^1S_0$ dimer. Notice that the binding energies span different ranges in the three figures.

dependence, it is straightforward to interpret the effects of the initial spatial distribution of atoms on the excitation rate to the $\nu = 0$ ULRRM state across different n.

This simple interpretation for the $\mathcal{S}_{n,x}^{\nu=1}/\mathcal{S}_{n,x}^{\nu=0}$ and $\mathcal{S}_{n,x}^{\nu=2}/\mathcal{S}_{n,x}^{\nu=0}$ ratios is not as easy due to the delocalized nature of the $\nu = 1$ and $\nu = 2$ wave functions. It can be seen in Fig. 4.8 that the $\nu = 1$ state can be considered somewhat localized around a particular (or a few adjacent) well(s) of the ULRRM potential and therefore $\langle|\mathcal{F}_{n,x}^{\nu=1}|^2\rangle_E$ can be expected (and was observed) to follow a similar n-scaling behavior as the $\nu = 0$ state (i.e., decreasing $\mathcal{S}_{n,x}^{\nu=1}/\mathcal{S}_{n,x}^{\nu=0}$ at lower n). The $\nu = 2$ state is much more delocalized with no obvious n-dependence so the "simple" picture used to understand the $\mathcal{S}_{n,x}^{\nu=1}/\mathcal{S}_{n,x}^{\nu=0}$ ratio is not applicable for the $\mathcal{S}_{n,x}^{\nu=2}/\mathcal{S}_{n,x}^{\nu=0}$ ratio. It should be noted that both the $\nu = 1$ and $\nu = 2$ wave functions have a node around $R_n^{\nu=0}$ meaning the contribution to $\langle|\mathcal{F}_{n,x}^{\nu=1}|^2\rangle_E$ and $\langle|\mathcal{F}_{n,x}^{\nu=2}|^2\rangle_E$ at this position is reduced.

While the n-dependence of the ratios that are common to both the spin-polarized and unpolarized samples provides information about the initial colliding atomic wave function and the ULRRM wave function, the differences in $\mathcal{S}_{n,\mathrm{pol}}^{\nu}/\mathcal{S}_{n,\mathrm{pol}}^{\nu=0}$ and $\mathcal{S}_{n,\mathrm{unpol}}^{\nu}/\mathcal{S}_{n,\mathrm{unpol}}^{\nu=0}$ provides information regarding the effects of correlations. Most notably, it can be seen in Fig. 4.7 that there is a weak but consistent systematic reduction of the polarized ratios compared to the unpolarized ratios in both $\mathcal{S}_{n}^{\nu=1}/\mathcal{S}_{n}^{\nu=0}$ and $\mathcal{S}_{n,x}^{\nu=2}/\mathcal{S}_{n,x}^{\nu=0}$ ratios across the range of n explored. This is evidence suggesting that the spin-polarized sample is experiencing stronger effects of antibunching compared to the unpolarized sample.

4.3.3 Electron Detection Efficiency Ratio: $\alpha_{\mathrm{pol}}/\alpha_{\mathrm{unpol}}$

In order to compare the spin-polarized data to the unpolarized data, the electron detection efficiency α needs to be determined. Although it would be extremely useful to know the exact value of α, only the ratio $\alpha_{\mathrm{pol}}/\alpha_{\mathrm{unpol}}$ is needed since we are interested in how the spin-polarized samples differ from the unpolarized samples. The ratio $\alpha_{\mathrm{pol}}/\alpha_{\mathrm{unpol}}$ accounts for the differences in detection efficiency between the spin-polarized sample and

unpolarized samples with the former measurements taken in a $B_{\text{pol}} \approx 1\,\text{G}$ bias magnetic field oriented towards the MCP (to maintain spin-polarization) and the latter in no bias field ($B_{\text{unpol}} = 0\,\text{G}$). Naïvely, the spin-polarized samples are expected to exhibit a larger signal than the unpolarized sample simply due to the Lorentz force of the magnetic field, oriented towards the MCP, helping guide the electrons towards the detector. Towards this end, we measured the two-photon excitation signals with ^{84}Sr due to its simpler electronic structure in both B_{pol} and B_{unpol} configurations.

The measurements with ^{84}Sr used the same beam paths and geometry as the ULRRM measurements in ^{87}Sr. Two-photon excitation following the $(5s^2)\,^1S_0 \rightarrow (5s5p)\,^3P_1 \rightarrow (5s37s)\,^3S_1$ path was used. The first 689 nm photon has σ^+-polarization and is blue-detuned from the intermediate state by $\Delta/2\pi = 14.93(100)\,\text{MHz}$. The second 320 nm photon has π-polarization. Figure 4.9 shows spectra obtained with and without the bias magnetic field when 689 nm is held fixed while the 320 nm frequency is scanned across the Rydberg atomic line. From the data shown in the figure, the values $\mathcal{S}(B_{\text{pol}}) = 369(9)$ and $\mathcal{S}(B_{\text{unpol}}) = 278(7)$ were extracted for fits to the Rydberg line. Taking their ratio gives $\alpha(B_{\text{pol}})\,/\alpha(B_{\text{unpol}}) = 1.33(5)$.

Before reporting a detection efficiency difference for the B_{pol} and B_{unpol} conditions, there are still a few things to check and consider. A possible source of systematic error in this determination of the ratio could be due to poor polarization of either (or both) the 689 nm and 320 nm excitation lasers. This seems unlikely as there is very little signal at $\Delta/2\pi = 0\,\text{MHz}$ when the the magnetic field is applied (blue circles), suggesting that the polarizations are likely reasonably well-aligned to the quantization axis. This also matches our previous spin-polarization tests which found the σ^+ beam path to have relatively good circular polarization. The 320 nm path passes through a high-extinction ratio calcite polarizer[68] that cleans up its polarization.

Another thing to consider is that the Zeeman effect could change the intermediate

[68] Thorlabs' GLB10 Glan-Laser alpha-BBO calcite polarizer.

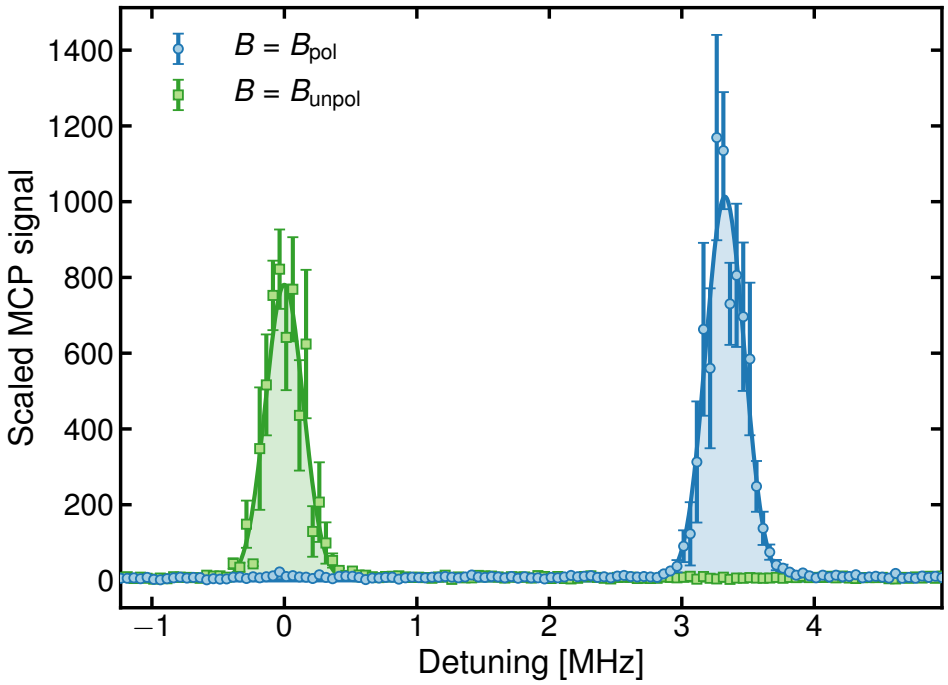

Figure 4.9: The ^{84}Sr $(5s37s)\,^3S_1$ atomic Rydberg line with $B_{\mathrm{pol}} \approx 1\,\mathrm{G}$ (blue circles) and $B_{\mathrm{unpol}} \approx 0\,\mathrm{G}$ (green squares) bias magnetic fields. The MCP signal was scaled accounting for both the 689 nm and 320 nm powers while the atom number was constant for all the measurements. Gaussian fits (lines) were used to extract the integrals, resulting with $\mathcal{S}(B_{\mathrm{pol}}) = 369(9)$ (blue shaded region) and $\mathcal{S}(B_{\mathrm{unpol}}) = 278(7)$ (green shaded region).

detuning with the effect scaling as $\Gamma_{\mathrm{sc}} \sim 1/\Delta^2$. From Fig. 4.9, the observed shift of the $(5s37s)\,^3S_1, m_J = 1$ state with and without the magnetic field is 3.326(6) MHz. Since the $(5s37s)\,^3S_1$ state has $g_J = 2$, this corresponds to $B_{\mathrm{pol}} = 1.1882(20)\,\mathrm{G}$, which agrees with previous calibration measurements obtained by performing spectroscopy on the $(5s^2)\,^1S_0 \rightarrow (5s5p)\,^3P_1$ transition. Considering the detuning $\Delta_{\mathrm{unpol}}/2\pi = 14.9(10)\,\mathrm{MHz}$ in the B_{unpol} case, the intermediate state detuning from the $(5s^2)\,^1S_0 \rightarrow (5s5p)\,^3P_1, m_J = 1$ is expected to be reduced to $\Delta_{\mathrm{pol}}/2\pi = 12.4(10)\,\mathrm{MHz}$ in the B_{pol} case. Therefore, the $\mathcal{S}(B_{\mathrm{pol}})$ is expected to be about a factor of $\Delta^2_{\mathrm{unpol}}/\Delta^2_{\mathrm{pol}} = 1.44(4)$ larger than $\mathcal{S}(B_{\mathrm{unpol}})$ due to the reduced detuning.

Since the the value of $\Delta^2_{\mathrm{unpol}}/\Delta^2_{\mathrm{pol}}$ is close to the measured value $\mathcal{S}(B_{\mathrm{pol}})\,/\mathcal{S}(B_{\mathrm{unpol}})$, this would suggest that the enhancement of the signal obtained in B_{pol} is due to the Zeeman shift reducing the intermediate state detuning instead of due to the Lorentz force guiding

more electrons to the MCP. Fortuitously, the experimental parameters used to determine $\alpha_{\rm pol}/\alpha_{\rm unpol}$ in ^{84}Sr are almost identical to the conditions used for the ULRRM measurements in ^{87}Sr. In both measurements, the 689 nm laser was blue-detuned from the intermediate state by approximately 14.9 MHz in no magnetic field (i.e., $\Delta_{\rm unpol}/2\pi \approx 14.9\,{\rm MHz}$). With the Zeeman shifts of the intermediate states being the same, $g_J m_J = 3/2$ for the $(5s5p)\,^3P_1, m_J = 1$ state in ^{84}Sr and $g_F m_F = 3/2$ for the $(5s5p)\,^3P_1, F = 11/2, m_F = 11/2$ state in ^{87}Sr, we can reasonably expect that the enhancement of spin-polarized signal (with $B = B_{\rm pol}$) compared to the unpolarized signal (with $B = B_{\rm unpol}$) to also be given by $\alpha(B_{\rm pol})\,/\alpha(B_{\rm unpol}) = 1.33(5)$.

4.3.4 Preliminary Comparison of $\mathcal{S}^{\nu}_{n,\mathbf{pol}}$ to $\mathcal{S}^{\nu}_{n,\mathbf{unpol}}$

A preliminary comparison of the spin-polarized to unpolarized ratios $\mathcal{S}^{\nu}_{n,\rm pol}/\mathcal{S}^{\nu}_{n,\rm unpol}$ for the $\nu = 0$, 1, and 2 vibrational states is shown in Fig. 4.10. The spin-polarized to unpolarized ratios in the figure account for the $\alpha(B_{\rm pol})\,/\alpha(B_{\rm unpol}) = 1.33(5)$ factor and the difference in Clebsch-Gordan coupling strength to the Rydberg state[69].

With the exception of the data taken at $n = 31$, both the $\mathcal{S}^{\nu=0}_{n,\rm pol}/\mathcal{S}^{\nu=0}_{n,\rm unpol}$ and the $\mathcal{S}^{\nu=1}_{n,\rm pol}/\mathcal{S}^{\nu=1}_{n,\rm unpol}$ ratios exhibit a pronounced decrease in their values at smaller n (i.e., smaller interparticle separations R), which is additional evidence of antibunching. Figure 4.10 also shows the expected $g^{(2)}(R)$ for fermions at $T = 850(100)\,{\rm nK}$ with $R^{\nu=0}_n$ given previously for the $\nu = 0$ state. For comparison, $0.8g^{(2)}(R)$ is also shown which has qualitatively better agreement with the observations. Currently, it is unclear why the $\nu = 0$ ratio appears to converge $\approx$0.8 as n increases instead of 1 expected from $g^{(2)}(R)$.

[69] $\mathcal{C}_{\rm pol} = 11/13$ and $\mathcal{C}_{\rm unpol} = 46/275$.

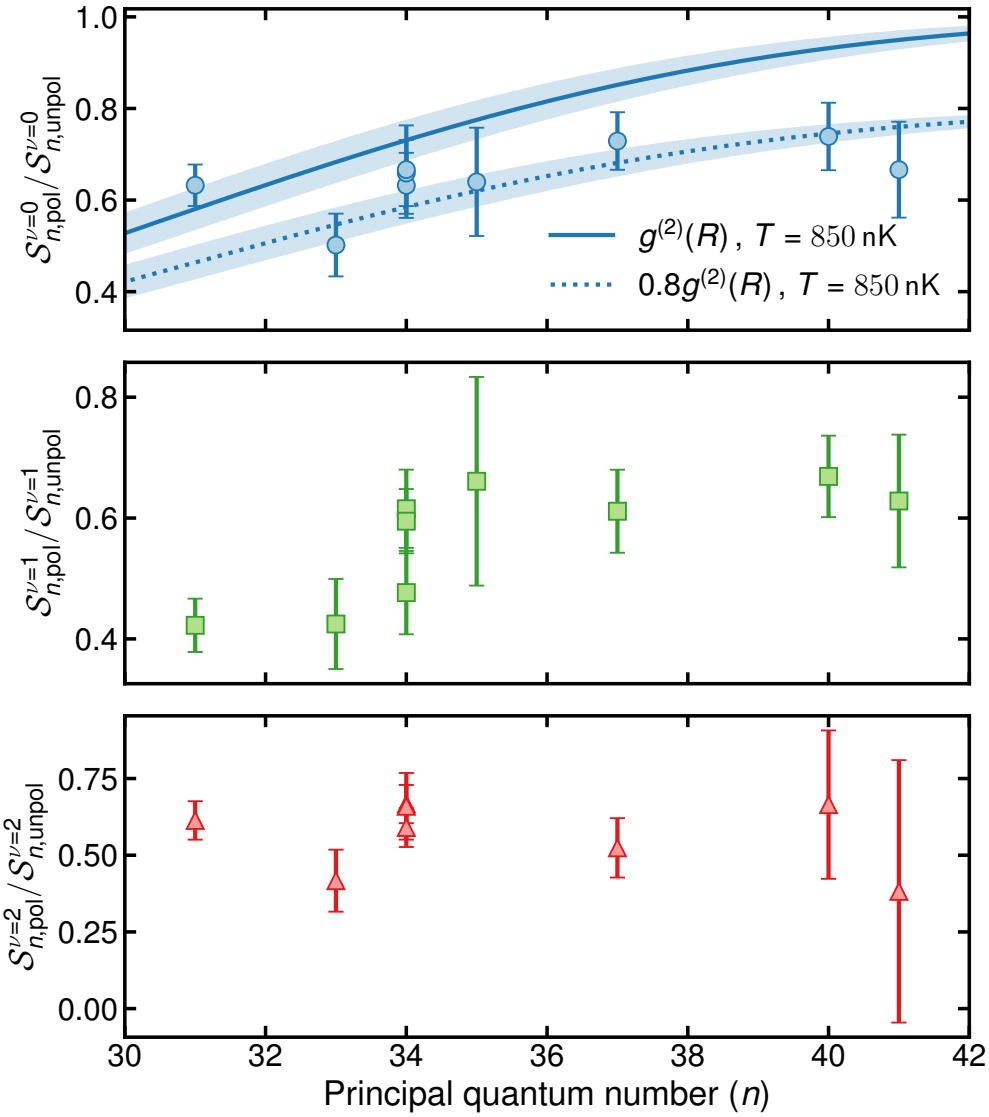

Figure 4.10: Comparison of the ratio $\mathcal{S}^{\nu}_{n,\mathrm{pol}}/\mathcal{S}^{\nu}_{n,\mathrm{unpol}}$ for $\nu = 0$, 1, and 2 across multiple principal quantum numbers (n). The extracted spin-polarized to unpolarized ratios accounts for both $\alpha(B_{\mathrm{pol}})/\alpha(B_{\mathrm{unpol}}) = 1.33(5)$ and for differences in the Clebsch-Gordan couplings. For the $\nu = 0$ ratios, $g^{(2)}(R)$ (solid line) and $0.8g^{(2)}(R)$ (dotted line) for fermions is shown where $R_n \simeq 1.87(n-\delta)^2 a_0$ and $T = 850(100)$ nK (the shaded region corresponds to the expected uncertainty).

4.4 Conclusion

We have presented preliminary measurements of the photoexcitation rates of the dimer $\nu = 1$ and $\nu = 2$ vibrationally-excited ULRRM states. By comparing ratios instead of signals, sensitivities to common factors can be reduced or eliminated. Comparison of spin-polarized to spin-polarized samples and unpolarized to unpolarized samples, shown in Fig. 4.7, highlights common n-dependencies of the ULRRM excitation rate of a particular vibrational state in both spin-polarized and unpolarized samples. It also provided the first evidence of antibunching with the systematically lower spin-polarized ratios compared to the unpolarized ratios across n.

Comparison spin-polarized to unpolarized signals is more difficult as the measurement requires more accurate knowledge of, and is sensitive to, experimental factors which are not common between the conditions under which data is obtained for the spin-polarized and unpolarized samples. Figure 4.10 does indicate that the $\nu = 1$ polarized-unpolarized ratio follows the general trend of the $\nu = 0$ ratios but slightly reduced, again, in agreement with intuition of the $\nu = 1$ state experiencing additional suppression. The delocalized $\nu = 2$ state does not appear to show much of a consistent trend, likely resulting from the structure exhibited by the wave function.

The presented measurements were very challenging due to long-term drifts in the 320 nm Rydberg laser frequency and to a previously unnoticed changes in beam pointing when tuning to different n. Additional work exploring the vibrational states ULRRM states is worthwhile since they do exhibit more complicated dependencies compared to the $\nu = 0$ state. Once experimental challenges are overcome, these states can be used to test theoretical calculations of both the ULRRM radial vibrational wave functions and how the effects of quantum statistics affect their production rate.

5. Summary

This thesis has demonstrated that strontium is an exciting system for studying long-range interactions associated with Rydberg atoms. Starting from the atom itself, as detailed in Ch. 1, strontium has a variety of properties not available in other atomic species. These include a number of stable bosonic and fermionic isotopes, narrow and ultra-narrow transitions for both laser cooling and for Rydberg excitation, and many accessible Rydberg states due to having two valence electrons with varying interactions strengths and anisotropies.

Chapter 2 described the various techniques employed for producing cold and ultracold gases of strontium. In particular, details relevant for the current strontium Rydberg experiment were covered. Over the past few years, the strontium Rydberg experiment has grown from barely being able to sustain a blue MOT (Fig. 5.1) to an experiment capable of reaching the ultracold temperatures necessary for creating and detecting Rydberg molecules (Fig. 5.2).

Chapter 3 explored the effects of hyperfine interactions on the Rydberg states of ^{87}Sr. Compared to the relatively well-understood structure of ^{88}Sr, the $I = 9/2$ nuclear spin in ^{87}Sr leads to strong hyperfine interactions which mix the Rydberg states normally well-described by LS-coupling. Working with theory collaborators, we were able to develop an understanding of the hyperfine Rydberg states that was essential for producing the first fermionic ULRRMs in a gas of ^{87}Sr.

We concluded in Ch. 4 with current efforts exploring the effects of quantum statistics on the excitation of ULRRMs. Experiments involving the vibrationally excited $\nu = 1$ states suggest that, while they are sensitive to the effects of quantum statistics, it is difficult to extract quantitative information without accurate knowledge of the ULRRM wave functions.

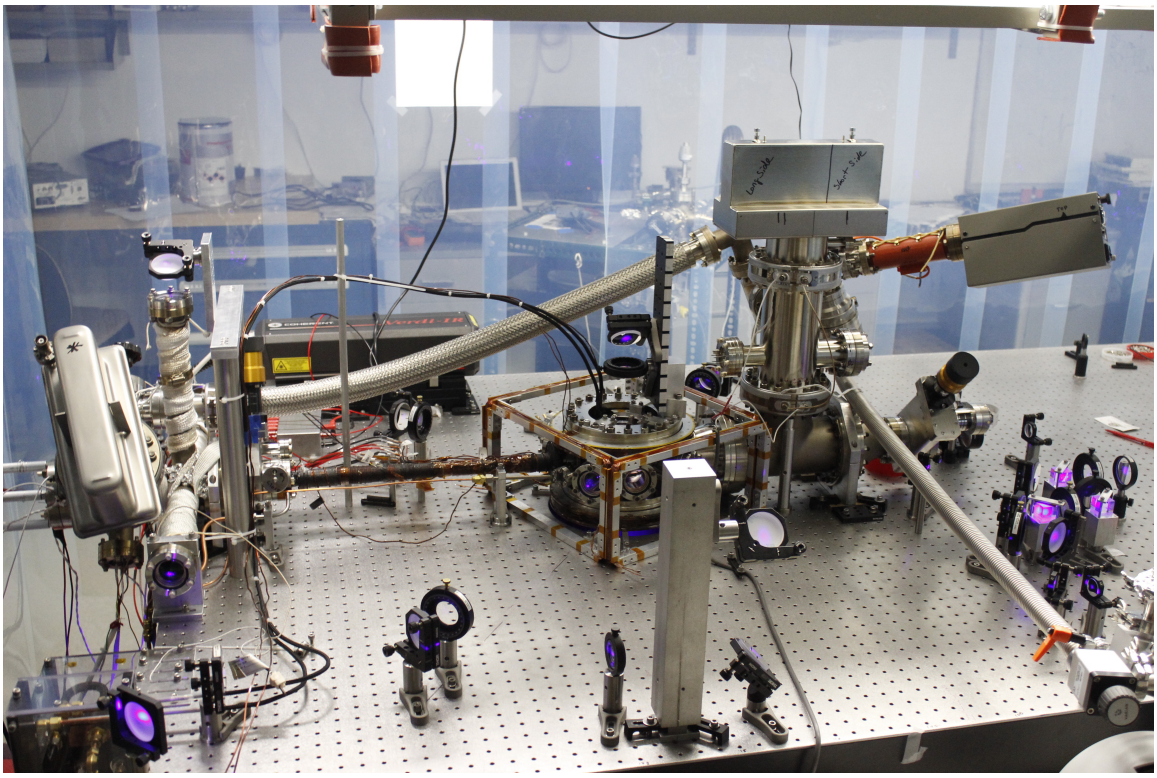

Figure 5.1: Picture of the Rydberg apparatus taken on 2014/05/29 just before we started preparing to bake the vacuum system. We had observed our first blue MOT the previous day before. The pink appearance of the 461 nm beams are likely due to the camera's sensor saturating.

We also presented progress towards probing two-body correlations with the delocalized $\nu = 1$ and 2 vibrational state, an extension of the work presented in [249].

5.1 Future Directions

This section contains various ideas for future work with strontium Rydberg atoms and molecules. Many of the experiments listed below are achievable with the current Rydberg apparatus or may require some straightforward upgrades.

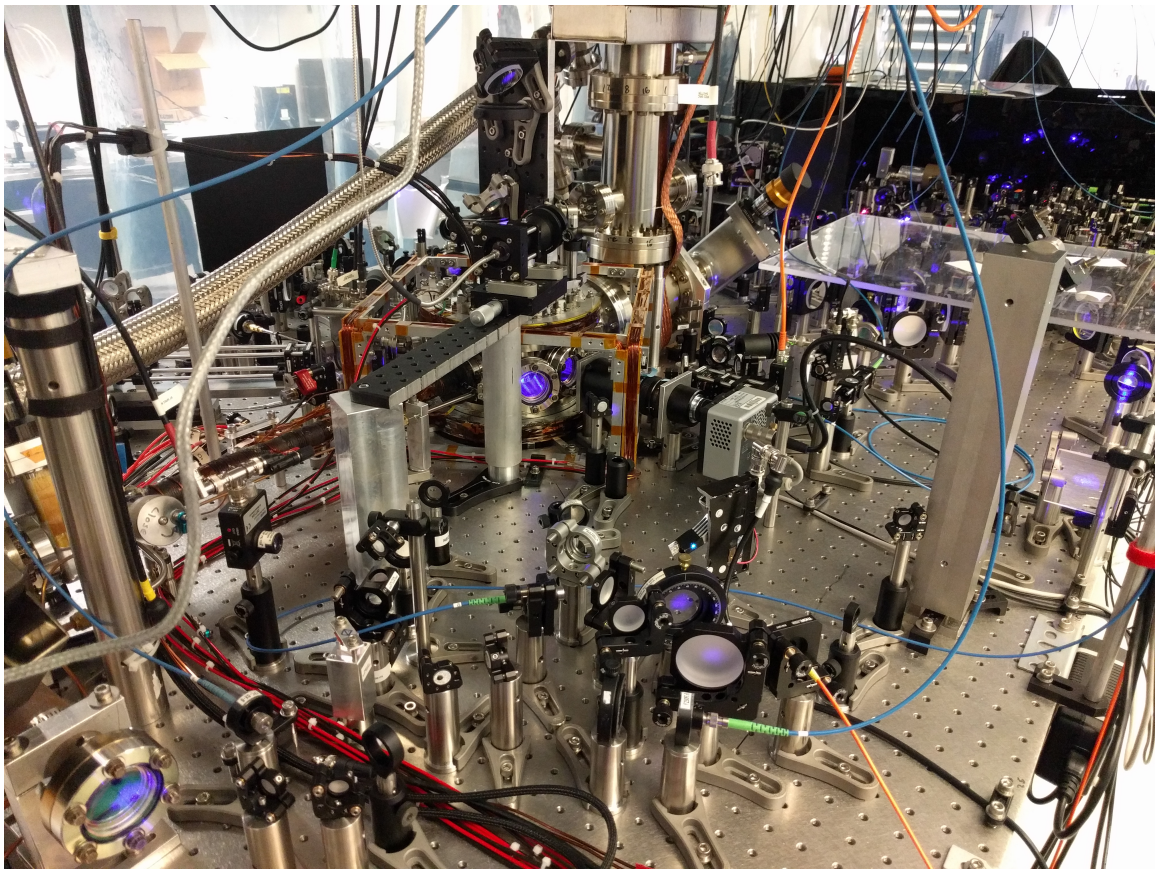

Figure 5.2: A more recent picture of the Rydberg apparatus taken on 2018/09/20. The table got a lot more crowded with many additions to the system.

5.1.1 Probing Effects of N-Body Spatial Correlations on Formation Rates of ULRRMs

One of the most straightforward directions for future exploration is to extend the work presented in [249] beyond probing two-body spatial correlations to higher-order N-body effects. This work demonstrated that the production rate for the well-localized $\nu = 0$ vibrational dimer ULRRM states are sensitive to the two-body spatial correlations arising from quantum statistics of the initial gas. By exciting to different principal quantum numbers, which changes the location of the $\nu = 0$ state, a measurement of $g^{(2)}(R)$ can be extracted. A similar experiment can be carried out by exciting to a N-mer ULRRM state which should be sensitive to $g^{(N)}(R)$ spatial correlations.

Considering our explorations of the vibrationally excited ULRRM states, it would make sense to continue to use the well-localized $\nu = 0$ state to eliminate the additional complexity associated with the delocalized $\nu > 0$ states. Obtaining sufficient signal-to-noise ratios for an N-mer state will be challenging considering the dimer signal is about one tenth of the atomic signal so the trimers are expected to be about ten times weaker. Nevertheless, work towards this goal is currently underway with promising measurements in a Fermi gas (spin-polarized ^{87}Sr), a Bose gas (^{84}Sr), and a nearly classical gas (unpolarized ^{87}Sr).

5.1.2 High-Resolution Spectroscopy of ULRRMs

Improvements to the 320 nm laser systems used to produce Rydberg atoms and molecules could lead to the observation of very weak effects. In the current work, it was assumed that the embedded neutral atom does not significantly modify the Rydberg electron wave function but it is not clear at what point this approximation becomes invalid. Under the current approximation, the binding energies of an N-mer state is simply N times the binding energy of the dimer state (e.g., a trimer $\nu = 0$ has the same binding energy as two dimer $\nu = 0$ states). Deviations from these expected binding energies could be a signature that the approximation is no longer valid.

Highly accurate measurements of the binding energies could be used to improve theoretical calculations of the ULRRM wave functions. During experiments involving the excited ULRRM states, it was found that although the theory predicts the binding energies of the $\nu = 0$ state well, discrepancies exist in the predicted energies of the $\nu = 1$ and $\nu = 2$ states. Measurements of the binding energies could potentially be used to constrain the model potential and the resulting wave functions.

Another possibility is the observation of effects of angular momentum on ULRRMs (which has not been previously considered) formation in Bose and Fermi gases. For fermions in particular, they are expected to fill the various vibrational ULRRM states following shell structure as Pauli statistics exclude fermions from occupying the same state (a “rotational

blockade"') whereas no suppression should exist for bosons [251].

5.1.3 Wave Packet Dynamics with ULRRMs

Due to the ability to drive Rydberg to Rydberg transitions with microwave radiation, one could study how the ULRRM vibrational states evolve when the parent Rydberg atom is changed from one state to another. Since changing the Rydberg state changes the molecular potential experienced by the ground-state atom(s) embedded in the Rydberg electron wave function and therefore the vibrational states, one could consider the microwaves as projecting the initial wave function into a different potential landscape. For example, starting from the well-localized $\nu = 0$ ULRRM state with the parent Rydberg atom in the $(5sns)\,^3S_1$ state, microwave radiation can excite the parent Rydberg atom to a $(5sn's)\,^3S_1$ state which would then project the initially well-localized $\nu = 0$ state at on to the ULRRM vibrational wave functions of the $(5sn's)\,^3S_1$ state.

Another possibility is to excite the parent Rydberg atom to a state with different symmetry. For example, microwave excitation could be used to drive the $\nu = 0$ ULRRM state of the initial $(5sns)\,^3S_1$ state to $(5snp)\,^3P_{0,1,2}$ which should drastically alter the allowed states since the Rydberg electron wave function now has an angular dependence.

5.1.4 Rydberg Dressing

One of the most exciting areas of research involves modification of interaction between ground-state atoms by coupling to highly-excited Rydberg states [252–256]. The idea is that the coupling process "dresses" the ground-state atoms by mixing in a fraction of strongly-interacting Rydberg character while mitigating the challenges of actually producing Rydberg atoms (e.g., decoherence and reduced sample lifetimes). Rydberg dressing has been proposed as a potential route towards the observation of a three-dimensional soliton [257], the realization of a supersolid phase [258], and for enhanced metrology [73, 259].

Although Rydberg dressing has been experimentally demonstrated with two atoms in optical tweezers [260] and on a two-dimensional lattice [261], experimental realization of Rydberg dressing in a bulk gas has been difficult. Due to the distribution of atoms in a bulk gas, it was observed that Rydberg dressing in a bulk gas leads to a sudden onset of decoherence [181, 182, 262] with the effects being attributed to the production of "contaminant" Rydberg atoms through an to avalanche process involving resonant interactions [263]. If these challenges can be overcome, Rydberg dressing is a promising method for incorporating tunable long-range interactions without the need for controling exotic atomic species or molecules.

A.1 Symbols used in optical diagrams

Table A.1 shows the various symbols used in the optical diagrams and their meanings. The idea for this table came from seeing one presented in [89].

Table A.1: Most of the optical component symbols used in this thesis. The symbols are from [264].

Object	Symbol
Laser	
Isolator	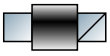
Lenses	
Mirrors	
D-mirror	
Dichroic mirrors	
Flipper mirror	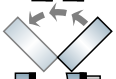
PZT mirrors	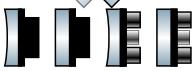
Half-wave plate (HWP) ($\lambda/2$)	
Quarter-wave plate (QWP) ($\lambda/4$)	
Non-polarizing beam splitters (BS)	
Polarizing beam splitter (PBS)	
Glan-Taylor polarizer (PBS)	
Beam dump	
Photodetector	

Continued on next page.

Table A.1 continued from previous page

Object	Symbol
Acousto-optic modulator (AOM)	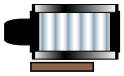
Electro-optic modulator (EOM)	
Fiber coupler	
Polarization-maintaining (PM) fiber	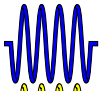
Single-mode (SM) fiber	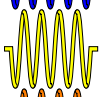
Multi-mode (MM) fiber	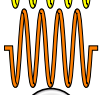
Signal generator	
Generic amplifier	
High-voltage amplifier	
PID servo	
PDH module	
Lock-in amplifier	

B. Strontium Data

Values for various properties of strontium are presented below. Hopefully this appendix will serve as a quick reference for various values as well as providing references to additional information.

B.1 Physical Properties

There are four naturally occurring stable isotopes of strontium of both bosons and fermions. The three bosonic isotopes (^{88}Sr, ^{86}Sr, and ^{84}Sr) all have no nuclear spin ($I = 0$) while the fermionic isotope (^{87}Sr) has $I = 9/2$. Table B.1 gives the atomic masses, abundances, and nuclear spins (I) for strontium from [265]. The relative atomic masses of

Table B.1: Atomic masses, abundances, and nuclear spins (I) of the four stable isotopes of strontium. Some physical properties of four naturally occurring isotopes of strontium [265].

Isotope	Atomic mass [u]	Abundance [%]	I
^{88}Sr	87.905 612 5(12)	82.58(35)	0
^{87}Sr	86.908 877 5(12)	7.00(20)	9/2
^{86}Sr	85.909 260 6(12)	9.86(20)	0
^{84}Sr	83.913 419 1(13)	0.56(2)	0

the isotopes presented in [265] comes from [266]. Other references which may be helpful are [267, 268].

B.2 Scattering Properties

The s-wave scattering lengths of various pairs of isotopes is presented in Tab. B.2 along with references.

Table B.2: Measured s-wave scattering lengths (a_s) of strontium for various pairs of isotopes given in a_0 (an extended version of Tab. 2.3).

Isotope pair	a_s [269]	a_s [154]	a_s [270]
^{88}Sr-^{88}Sr	−1.4(6)	−2.00(27)	
^{87}Sr-^{87}Sr	96.2(1)	96.198(68)	
^{86}Sr-^{86}Sr	823(24)	798(12)	810.6(3)(9)
^{84}Sr-^{84}Sr	122.7(3)	122.762(92)	
^{88}Sr-^{87}Sr	55.0(2)	54.819(92)	
^{88}Sr-^{86}Sr	97.4(1)	97.374(69)	
^{88}Sr-^{84}Sr	1790(130)	1658(54)	
^{87}Sr-^{86}Sr	162.5(5)	162.25(21)	
^{87}Sr-^{84}Sr	−56(1)	−57.61(61)	
^{86}Sr-^{84}Sr	31.9(3)	31.65(14)	

B.3 Electronic Properties

Strontium has two principal transitions from the $(5s^2)\,^1S_0$ ground state, one at 461 nm and another at 689 nm. The bosonic isotopes (^{88}Sr, ^{86}Sr, and ^{84}Sr) have no hyperfine structure since $I = 0$ and their total angular momentum is given by $\mathbf{J} = \mathbf{L} + \mathbf{S}$. The $I = 9/2$ nuclear spin of ^{87}Sr leads to hyperfine interactions ($\hat{V}_{\rm hf}$) so the total angular momentum is now given by $\mathbf{F} = \mathbf{I} + \mathbf{J}$. The shift due to $\hat{V}_{\rm hf}$ can be expressed as (see e.g., [71, 201])

$$\langle \hat{V}_{\rm hf} \rangle = \frac{1}{2} A_{\rm hf} K + B_{\rm hf} \frac{\frac{3}{2}K(K+1) - 2I(I+1)\,J(J+1)}{4I(2I-1)\,J(2J-1)} \tag{B.1}$$

with $K = F(F+1) - I(I+1) - J(J+1)$. The hyperfine constants $A_{\rm hf}$ and $B_{\rm hf}$ represent the strengths of the magnetic dipole hyperfine and the electric-quadrupole interactions, respectively.

The isotope shifts of the 461 nm $(5s^2)\,^1S_0 \rightarrow (5s5p)\,^1P_1$ transition relative to ^{88}Sr presented in Tab. 2.1 were obtained by combining the values from Tabs. B.3 and B.4. Table B.3 gives the isotope shifts of the bosons and the center-of-gravity for ^{87}Sr (i.e., assumimg $I = 0$).

Absolute transition frequencies of the 689 nm $(5s^2)\,^1S_0 \rightarrow (5s5p)\,^3P_1$ transition are

Table B.3: Isotope shifts of the 461 nm $(5s^2)\,^1S_0 \rightarrow (5s5p)\,^1P_1$ transition relative to ^{88}Sr. Due to the hyperfine structure of ^{87}Sr, the isotope shift is given relative to the center-of-gravity of the upper $(5s5p)\,^1P_1$ state. Transitions to a specific $(5s5p)\,^1P_1, F$ state can be calculated with the A and B hyperfine constants in Tab. B.4.

Isotope	Lower level	Upper level	$\nu - \nu_{88}$ [MHz]	Ref.
^{88}Sr	$(5s^2)\,^1S_0$	$(5s5p)\,^1P_1$	0	
^{87}Sr	$(5s^2)\,^1S_0$	$(5s5p)\,^1P_1$	−46.3(20)	[271]
			−49.2(36)	[272]
			−44.6(4)	[273]
^{86}Sr	$(5s^2)\,^1S_0$	$(5s5p)\,^1P_1$	−124.8(3)	[271]
			−124.5(13)	[272]
			−126.3(2)	[273]
^{84}Sr	$(5s^2)\,^1S_0$	$(5s5p)\,^1P_1$	−270.8(14)	[271]
			−270.6(24)	[272]
			−273.2(3)	[273]

Table B.4: ^{87}Sr hyperfine A_{hf} and B_{hf} coefficients for the $(5s5p)\,^1P_1$ state and calculated shifts from the center-of-gravity (ΔE_{HF}).

A_{hf} [MHz]	B_{hf} [MHz]	Ref.	Lower level	Upper level	ΔE_{HF} [MHz]
−3.4(4)	39(4)	[274]	$(5s^2)\,^1S_0, F = 9/2$	$(5s5p)\,^1P_1, F = 7/2$	36.6(29)
				$(5s5p)\,^1P_1, F = 11/2$	−5.5(21)
				$(5s5p)\,^1P_1, F = 9/2$	−22.6(27)
−3.334(25)	40.29(21)	[273]	$(5s^2)\,^1S_0, F = 9/2$	$(5s5p)\,^1P_1, F = 7/2$	36.80(17)
				$(5s5p)\,^1P_1, F = 11/2$	−4.93(12)
				$(5s5p)\,^1P_1, F = 9/2$	−23.53(14)

shown in Tab. B.5. The isotope shifts relative to ^{88}Sr presented in Tab. 2.2 were derived by subtracting the absolute transition frequencies. Note that some references measured relative isotope shifts with higher precision than the absolute transition frequencies. For example, [225] gives the ^{88}Sr-^{86}Sr isotope shift to be 163 817.4(2) kHz (i.e., sub-kilohertz uncertainty) whereas the absolute energy of the transition in ^{88}Sr was measured to be 434 829 121 311(10) kHz (i.e., ±10 kHz uncertainty).

Table B.5: Absolute frequencies of the 689 nm $(5s^2)\,{}^1S_0 \rightarrow (5s5p)\,{}^3P_1$ transition.

Isotope	Lower level	Upper level	Frequency [kHz]	Ref.
^{88}Sr	$(5s^2)\,{}^1S_0$	$(5s5p)\,{}^3P_1$	434 829 121 311(10)	[165, 225]
			434 829 121 300(20)	[126]
			434 829 121 312.334(39)	[275]
			434 829 121 313(20)	[276]
^{87}Sr	$(5s^2)\,{}^1S_0, 9/2$	$(5s5p)\,{}^3P_1, 7/2$	434 830 473 270(55)	[126, 165]
			434 830 473 218(55)	[276]
	$(5s^2)\,{}^1S_0, 9/2$	$(5s5p)\,{}^3P_1, 9/2$	434 829 343 010(50)	[126, 165]
			434 829 342 986(65)	[276]
	$(5s^2)\,{}^1S_0, 9/2$	$(5s5p)\,{}^3P_1, 11/2$	434 827 879 860(55)	[126, 165]
			434 827 879 826(60)	[276]
^{86}Sr	$(5s^2)\,{}^1S_0$	$(5s5p)\,{}^3P_1$	434 828 957 494(10)	[165, 225]
			434 828 957 493(25)	[276]
^{84}Sr	$(5s^2)\,{}^1S_0$	$(5s5p)\,{}^3P_1$	434 828 769 718(111)	[276]

B.4 Rydberg Properties

This section contains values which may be useful for working with Rydberg states of strontium atoms.

B.4.1 Strontium Rydberg Constant

The value of the Rydberg constant is $R_\infty = 109\,737.315\,685\,08(65)\,\mathrm{cm}^{-1}$ [277] for an infinitely heavy nucleus. Replacing the electron mass (m_e) with the reduced mass $\mu = m_e M/(m_e + M)$ where M is the mass of the nucleus gives

$$R_M = \frac{\mu}{m_e} R_\infty = \frac{M}{m_e + M} R_\infty \tag{B.2}$$

Using the electron mass $m_e = 9.109\,383\,56(11) \times 10^{-31}\,\mathrm{kg}$, u $= 1.660\,539\,040(20) \times 10^{-27}\,\mathrm{kg}$, and the masses of the strontium isotopes in Tab. B.1, the mass-corrected Rydberg constants can be calculated and are given in Tab. B.6. Note that the CODATA values presented in [277] were recently revised for 2018 [278].

Table B.6: Calculated mass-corrected Rydberg constants for strontium. Values of the fundamental constants $R_\infty = 109\,737.315\,685\,08(65)\,\mathrm{cm}^{-1}$, $m_e = 9.109\,383\,56(11) \times 10^{-31}\,\mathrm{kg}$, and $\mathrm{u} = 1.660\,539\,040(20) \times 10^{-27}\,\mathrm{kg}$ are from [277].

Isotope	R [cm^{-1}]
^{88}Sr	109 736.630 867 5(7)
^{87}Sr	109 736.623 013 5(7)
^{86}Sr	109 736.614 953 8(7)
^{84}Sr	109 736.598 287 4(7)

B.4.2 Ionization Limits

The currently published values for the ionization energies (E_{ion}) of strontium are given in Tab. B.7. Note that for ^{87}Sr, due to the $I = 9/2$ nuclear spin, F has half-integer values for neutral ^{87}Sr whereas F has integer values for the ion $^{87}\mathrm{Sr}^+$.

Table B.7: Ionization limits of the various strontium isotopes. Note that for ^{87}Sr, the ionization energy $45\,932.1956\,\mathrm{cm}^{-1}$ [84] is for an assumed $I = 0$ atom.

Isotope	Initial state (SrI)	Final state (SrII)	E_{ion} [cm^{-1}]	Ref.
^{88}Sr	$(5s^2)\,^1S_0$	$(5s)\,^2S_{1/2}$	45 932.1982(10)	[165, 188]
			45 932.200 24(33)	[36]
^{87}Sr	$(5s^2)\,^1S_0, F = 9/2$	$(5s)\,^2S_{1/2}, F = 4$	45 932.2861(10)	[165, 188]
		$(5s)\,^2S_{1/2}$	45 932.1956	[84]
^{86}Sr	$(5s^2)\,^1S_0$	$(5s)\,^2S_{1/2}$	45 932.1912(10)	[165, 188]
^{84}Sr	$(5s^2)\,^1S_0$	$(5s)\,^2S_{1/2}$	45 932.1833(10)	[165, 188]

C. Various Drawings

C.1 Dual MOT Coils

Cross-section drawing of the dual MOT coils. Some spacing was left between the individual coil wraps in the drawing to account for non-perfect wrapping. The CAD drawing should be good enough for numerically calculating the MOT field.

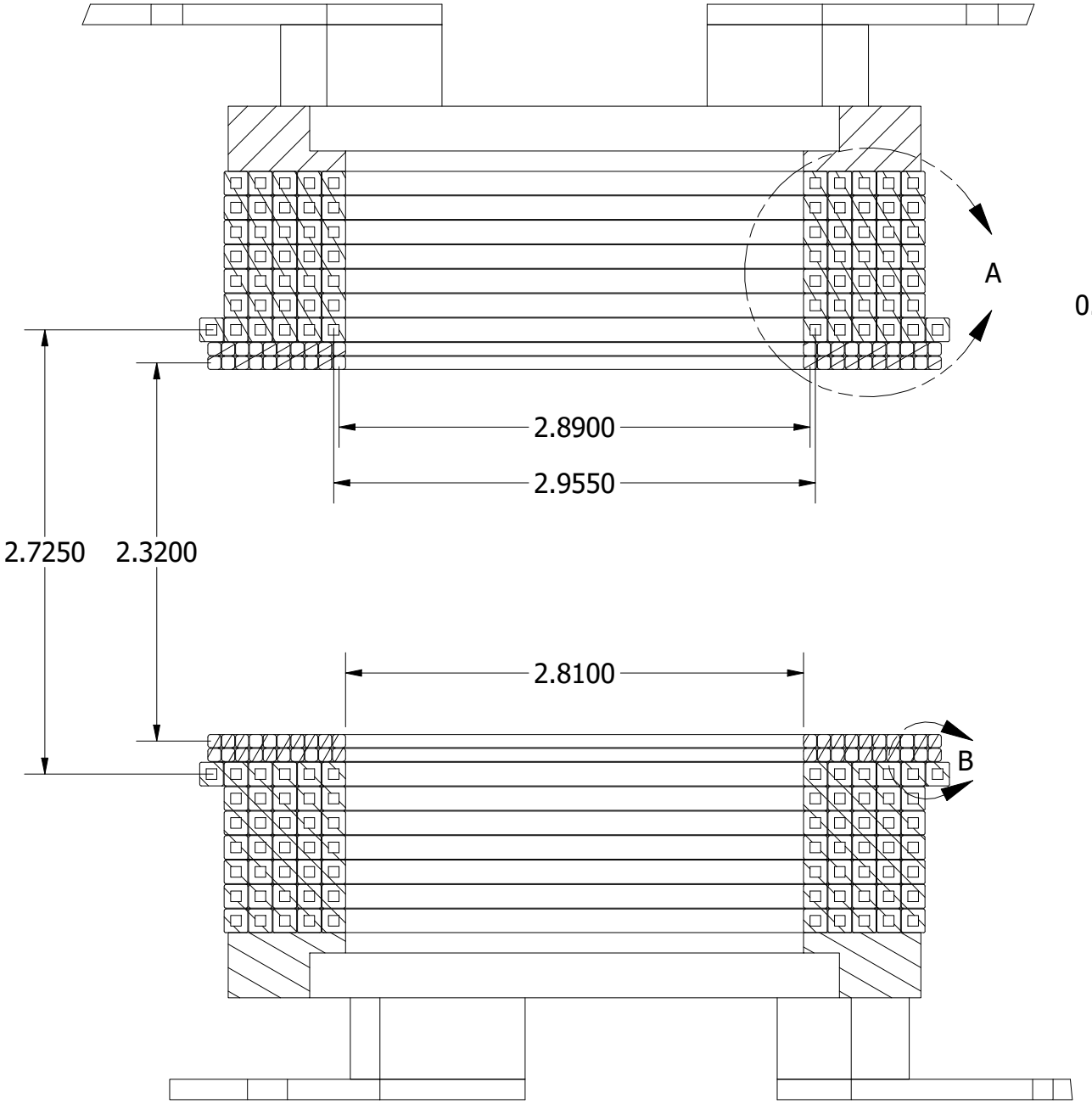
A
2.8900
2.9550
2.7250
2.3200
2.8100
B

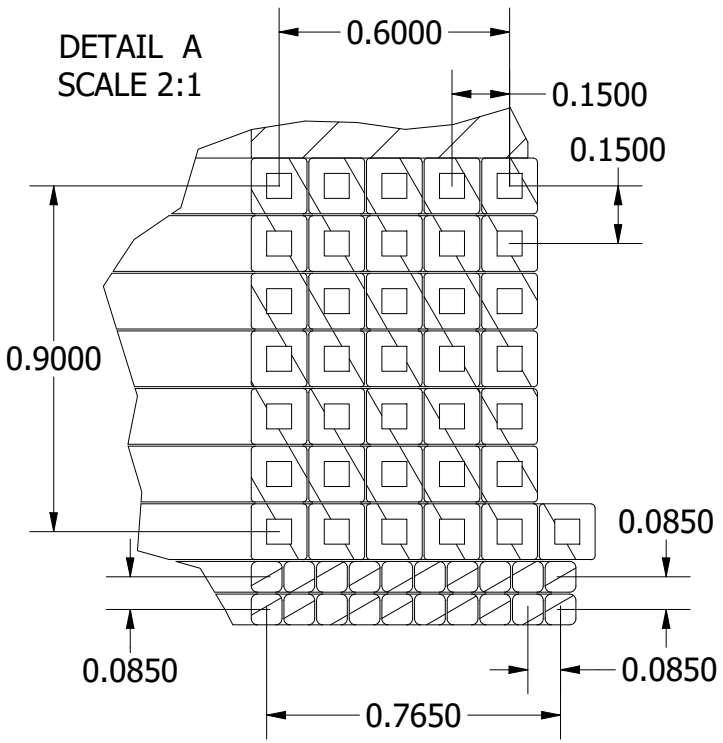
DETAIL A
SCALE 2:1
0.6000
0.1500
0.1500
0.9000
0.0850
0.0850
0.0850
0.7650

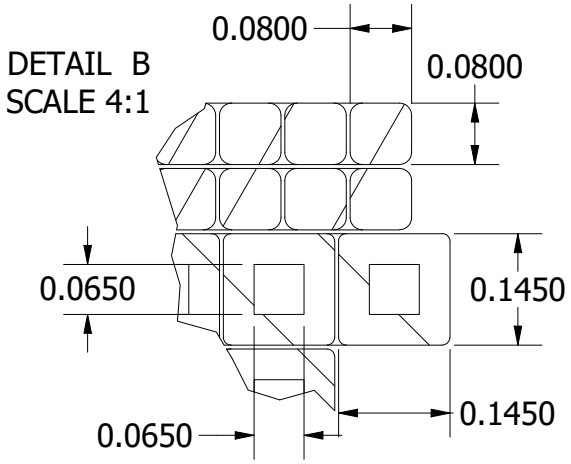
DETAIL B
SCALE 4:1
0.0800
0.0800
0.0650
0.1450
0.1450
0.0650

Bibliography

[1] Q. Chen, J. Stajic, S. Tan, and K. Levin, "BCS-BEC crossover: From high temperature superconductors to ultracold superfluids", Physics Reports **412**, 1–88 (2005).

[2] V. Gurarie and L. Radzihovsky, "Resonantly paired fermionic superfluids", Annals of Physics **322**, 2–119 (2007).

[3] T. Bourdel, L. Khaykovich, J. Cubizolles, J. Zhang, F. Chevy, M. Teichmann, L. Tarruell, S. J. J. M. F. Kokkelmans, and C. Salomon, "Experimental Study of the BEC-BCS Crossover Region in Lithium 6", Physical Review Letters **93**, 050401 (2004).

[4] M. Greiner, O. Mandel, T. Esslinger, T. W. Hänsch, and I. Bloch, "Quantum phase transition from a superfluid to a Mott insulator in a gas of ultracold atoms", Nature **415**, 39–44 (2002).

[5] K. E. Strecker, G. B. Partridge, A. G. Truscott, and R. G. Hulet, "Formation and propagation of matter-wave soliton trains", Nature **417**, 150–153 (2002).

[6] L. Khaykovich, F. Schreck, G. Ferrari, T. Bourdel, J. Cubizolles, L. D. Carr, Y. Castin, and C. Salomon, "Formation of a Matter-Wave Bright Soliton", Science **296**, 1290–1293 (2002).

[7] C. J. Pethick and H. Smith, *Bose-Einstein Condensation in Dilute Gases* (Cambridge University Press, 2008).

[8] J. Dalibard, *Collisional dynamics of ultra-cold atomic gases, Course cxl: bose – einstein condensation in gases*, Proceedings of the International School of Physics Enrico Fermi, Varenna, 1998.

[9] D. Jaksch, J. I. Cirac, P. Zoller, S. L. Rolston, R. Côté, and M. D. Lukin, "Fast Quantum Gates for Neutral Atoms", Physical Review Letters **85**, 2208 (2000).

[10] D. DeMille, "Quantum Computation with Trapped Polar Molecules", Physical Review Letters **88**, 067901 (2002).

[11] S. de Léséleuc, S. Weber, V. Lienhard, D. Barredo, H. P. Büchler, T. Lahaye, and A. Browaeys, "Accurate Mapping of Multilevel Rydberg Atoms on Interacting Spin-1/2 Particles for the Quantum Simulation of Ising Models", Physical Review Letters **120**, 113602 (2018).

[12] P. Schauss, "Quantum simulation of transverse ising models with Rydberg atoms", Quantum Science and Technology **3**, 023001 (2018).

[13] T. Lahaye, C. Menotti, L. Santos, M. Lewenstein, and T. Pfau, "The physics of dipolar bosonic quantum gases", Reports on Progress in Physics **72**, 126401 (2009).

[14] M. Aymar and O. Dulieu, "Calculation of accurate permanent dipole moments of the lowest $^{1,3}\Sigma^+$ states of heteronuclear alkali dimers using extended basis sets", The Journal of Chemical Physics **122**, 204302 (2005).

[15] L. D. Marco, G. Valtolina, K. Matsuda, W. G. Tobias, J. P. Covey, and J. Ye, "A degenerate Fermi gas of polar molecules", Science **363**, 853–856 (2019).

[16] D. McCarron, "Laser cooling and trapping molecules", Journal of Physics B: Atomic, Molecular and Optical Physics **51**, 212001 (2018).

[17] M. R. Tarbutt, "Laser cooling of molecules", arXiv:1902.05628 (2018).

[18] L. Anderegg, B. L. Augenbraun, Y. Bao, S. Burchesky, L. W. Cheuk, W. Ketterle, and J. M. Doyle, "Laser cooling of optically trapped molecules", Nature Physics **14**, 890–893 (2018).

[19] A. Griesmaier, J. Werner, S. Hensler, J. Stuhler, and T. Pfau, "Bose-Einstein Condensation of Chromium", Physical Review Letters **94**, 160401 (2005).

[20] B. Naylor, A. Reigue, E. Maréchal, O. Gorceix, B. Laburthe-Tolra, and L. Vernac, "Chromium dipolar Fermi sea", Physical Review A **91**, 011603 (2015).

[21] K. Aikawa, A. Frisch, M. Mark, S. Baier, A. Rietzler, R. Grimm, and F. Ferlaino, "Bose-Einstein Condensation of Erbium", Physical Review Letters **108**, 210401 (2012).

[22] K. Aikawa, A. Frisch, M. Mark, S. Baier, R. Grimm, and F. Ferlaino, "Reaching Fermi Degeneracy via Universal Dipolar Scattering", Physical Review Letters **112**, 010404 (2014).

[23] M. Lu, N. Q. Burdick, S. H. Youn, and B. L. Lev, "Strongly Dipolar Bose-Einstein Condensate of Dysprosium", Physical Review Letters **107**, 190401 (2011).

[24] M. Lu, N. Q. Burdick, and B. L. Lev, "Quantum Degenerate Dipolar Fermi Gas", Physical Review Letters **108**, 215301 (2012).

[25] M. Lepers, H. Li, J.-F. Wyart, G. Quéméner, and O. Dulieu, "Ultracold Rare-Earth Magnetic Atoms with an Electric Dipole Moment", Physical Review Letters **121**, 063201 (2018).

[26] K. Baumann, C. Guerlin, F. Brennecke, and T. Esslinger, "Dicke quantum phase transition with a superfluid gas in an optical cavity", Nature **464**, 1301–1306 (2010).

[27] R. Mottl, F. Brennecke, K. Baumann, R. Landig, T. Donner, and T. Esslinger, "Roton-Type Mode Softening in a Quantum Gas with Cavity-Mediated Long-Range Interactions", Science **336**, 1570–1573 (2012).

[28] T. F. Gallagher, *Rydberg Atoms* (Cambridge University Press, 1994).

[29] T. Kazimierczuk, D. Fröhlich, S. Scheel, H. Stolz, and M. Bayer, "Giant Rydberg excitons in the copper oxide Cu_2O", Nature **514**, 343–347 (2014).

[30] N. Šibalić, J. D. Pritchard, C. S. Adams, and K. J. Weatherill, "ARC: An open-source library for calculating properties of alkali Rydberg atoms", Computer Physics Communications **220**, 319–331 (2017).

[31] J. R. Rydberg, *Recherches sur la constitution des spectres d'émission des éléments chimiques*, franska, Vol. Band 23 No 11, Kungliga vetenskapsakademiens handlingar 11 (Kungliga Vetenskapsakademien, 1890).

[32] J. R. Rydberg, "On the Structure of the Line-Spectra of the Chemical Elements", The London, Edinburgh, and Dublin Philosophical Magazine and Journal of Science **29**, 331–337 (1890).

[33] T. F. Gallagher, "Rydberg atoms", Reports on Progress in Physics **51**, 143–188 (1988).

[34] R. Löw, H. Weimer, J. Nipper, J. B. Balewski, B. Butscher, H. P. Büchler, and T. Pfau, "An experimental and theoretical guide to strongly interacting Rydberg gases", Journal of Physics B: Atomic, Molecular and Optical Physics **45**, 113001 (2012).

[35] C.-J. Lorenzen and K. Niemax, "Quantum Defects of the $n^2P_{1/2,3/2}$ Levels in ^{39}K I and ^{85}Rb I", Physica Scripta **27**, 300–305 (1983).

[36] L. Couturier, I. Nosske, F. Hu, C. Tan, C. Qiao, Y. H. Jiang, P. Chen, and M. Weidemüller, "Measurement of the strontium triplet Rydberg series by depletion spectroscopy of ultracold atoms", Physical Review A **99**, 022503 (2019).

[37] D. B. Branden, T. Juhasz, T. Mahlokozera, C. Vesa, R. O. Wilson, M. Zheng, A. Kortyna, and D. A. Tate, "Radiative lifetime measurements of rubidium Rydberg states", Journal of Physics B: Atomic, Molecular and Optical Physics **43**, 015002 (2009).

[38] F. Camargo, J. D. Whalen, R. Ding, H. R. Sadeghpour, S. Yoshida, J. Burgdörfer, F. B. Dunning, and T. C. Killian, "Lifetimes of ultra-long-range strontium Rydberg molecules", Physical Review A **93**, 022702 (2016).

[39] E. Amaldi and E. Segrè, "Effetto della Pressione Sui Termini Elevati Degli Alcalini", Il Nuovo Cimento **11**, 145–156 (1934).

[40] E. Amaldi and E. Segrè, "Effect of Pressure on High Terms of Alkaline Spectra", Nature **133**, 141–141 (1934).

[41] T. C. Liebisch, M. Schlagmüller, F. Engel, H. Nguyen, J. Balewski, G. Lochead, F. Böttcher, K. M. Westphal, K. S. Kleinbach, T. Schmid, A. Gaj, R. Löw, S. Hofferberth, T. Pfau, J. Pérez-Ríos, and C. H. Greene, "Controlling Rydberg atom

excitations in dense background gases", Journal of Physics B: Atomic, Molecular and Optical Physics **49**, 182001 (2016).

[42] J. P. Shaffer, S. T. Rittenhouse, and H. R. Sadeghpour, "Ultracold Rydberg molecules", Nature Communications **9** (2018).

[43] M. Yan, B. J. DeSalvo, B. Ramachandhran, H. Pu, and T. C. Killian, "Controlling Condensate Collapse and Expansion with an Optical Feshbach Resonance", Physical Review Letters **110**, 123201 (2013).

[44] S. Stellmer, F. Schreck, and T. C. Killian, "Degenerate quantum gases of strontium", 1–80 (2014).

[45] E. Fermi, "Sopra lo Spostamento per Pressione delle Righe Elevate delle Serie Spettrali", Il Nuovo Cimento **11**, 157–166 (1934).

[46] A. Omont, "On the theory of collisions of atoms in Rydberg states with neutral particles", Journal de Physique **38**, 1343–1359 (1977).

[47] B. J. DeSalvo, J. A. Aman, F. B. Dunning, T. C. Killian, H. R. Sadeghpour, S. Yoshida, and J. Burgdörfer, "Ultra-long-range Rydberg molecules in a divalent atomic system", Physical Review A **92**, 031403 (2015).

[48] V. Bendkowsky, "Ultralong range Rydberg molecules: investigation of a novel binding", en, Ph.D. Thesis (University of Stuttgart, 2010).

[49] J. Balewski, "Hochauflösende Photoassoziationsspektroskopie von Rydberg-Dimeren und Trimeren", Diplomarbeit (University of Stuttgart, 2009).

[50] C. Fey, F. Hummel, and P. Schmelcher, "Ultralong-range rydberg molecules", arXiv (2019).

[51] M. T. Eiles, "Trilobites, butterflies, and other exotic specimens of long-range rydberg molecules", Journal of Physics B: Atomic, Molecular and Optical Physics **52**, 113001 (2019).

[52] C. H. Greene, A. S. Dickinson, and H. R. Sadeghpour, "Creation of Polar and Nonpolar Ultra-Long-Range Rydberg Molecules", Physical Review Letters **85**, 2458 (2000).

[53] V. Bendkowsky, B. Butscher, J. Nipper, J. P. Shaffer, R. Löw, and T. Pfau, "Observation of ultralong-range Rydberg molecules", Nature (London) **458**, 1005–1008 (2009).

[54] J. Tallant, S. T. Rittenhouse, D. Booth, H. R. Sadeghpour, and J. P. Shaffer, "Observation of Blueshifted Ultralong-Range Cs_2 Rydberg Molecules", Physical Review Letters **109**, 173202 (2012).

[55] A. Gaj, A. T. Krupp, J. B. Balewski, R. Löw, S. Hofferberth, and T. Pfau, "From molecular spectra to a density shift in dense rydberg gases", Nature Communications **5** (2014).

[56] F. Camargo, R. Schmidt, J. D. Whalen, R. Ding, G. Woehl, S. Yoshida, J. Burgdörfer, F. B. Dunning, H. R. Sadeghpour, E. Demler, and T. C. Killian, "Creation of Rydberg Polarons in a Bose Gas", Physical Review Letters **120**, 083401 (2018).

[57] R. Schmidt, J. D. Whalen, R. Ding, F. Camargo, G. Woehl, S. Yoshida, J. Burgdörfer, F. B. Dunning, E. Demler, H. R. Sadeghpour, and T. C. Killian, "Theory of excitation of Rydberg polarons in an atomic quantum gas", Physical Review A **97**, 022707 (2018).

[58] S. Stellmer, "Degenerate quantum gases of strontium", Ph.D. Thesis (University of Innsbruck, Jan. 2013).

[59] C. L. Vaillant, M. P. A. Jones, and R. M. Potvliege, "Long-range Rydberg-Rydberg interactions in calcium, strontium and ytterbium", Journal of Physics B: Atomic, Molecular and Optical Physics **45**, 135004 (2012).

[60] C. L. Vaillant, M. P. A. Jones, and R. M. Potvliege, "Multichannel quantum defect theory of strontium bound Rydberg states", Journal of Physics B: Atomic, Molecular and Optical Physics **47**, 155001 (2014).

[61] F. Robicheaux, D. W. Booth, and M. Saffman, "Theory of long-range interactions for Rydberg states attached to hyperfine-split cores", Physical Review A **97**, 022508 (2018).

[62] S. Ye, X. Zhang, T. C. Killian, F. B. Dunning, M. Hiller, S. Yoshida, S. Nagele, and J. Burgdörfer, "Production of very-high-n strontium Rydberg atoms", Physical Review A **88**, 043430 (2013).

[63] U. Eichmann, V. Lange, and W. Sandner, "Dipole structure of planetary atoms", Physical Review Letters **68**, 21 (1992).

[64] J. Millen, G. Lochead, and M. P. A. Jones, "Two-Electron Excitation of an Interacting Cold Rydberg Gas", Physical Review Letters **105**, 213004 (2010).

[65] J. Millen, "A cold strontium Rydberg gas", Ph.D. Thesis (Durham University, 2011).

[66] G. Lochead, D. Boddy, D. P. Sadler, C. S. Adams, and M. P. A. Jones, "Number-resolved imaging of excited-state atoms using a scanning autoionization microscope", Physical Review A **87**, 053409 (2013).

[67] G. Lochead, "Excited state spatial distributions in a cold strontium gas", Ph.D. Thesis (Durham University, 2012).

[68] H. J. Metcalf and P. van der Straten, *Laser Cooling and Trapping* (Springer New York, 1999).

[69] B. H. Bransden and C. J. Joachain, *Physics of Atoms and Molecules* (Prentice Hall, Apr. 24, 2003).

[70] C. J. Foot, *Atomic Physics* (Oxford University Press, 2005), 344 pp.

[71] D. A. Steck, *Quantum and Atom Optics*, `http://steck.us/teaching`.

[72] T. R. Gentile, B. J. Hughey, D. Kleppner, and T. W. Ducas, "Experimental study of one- and two-photon Rabi oscillations", Physical Review A **40**, 5103 (1989).

[73] L. I. R. Gil, R. Mukherjee, E. M. Bridge, M. P. A. Jones, and T. Pohl, "Spin Squeezing in a Rydberg Lattice Clock", Physical Review Letters **112**, 103601 (2014).

[74] O. Onishchenko, S. Pyatchenkov, A. Urech, C.-C. Chen, S. Bennetts, G. A. Siviloglou, and F. Schreck, "Frequency of the ultranarrow $^1S_0 - {}^3P_2$ transition in ^{87}Sr", Physical Review A **99**, 052503 (2019).

[75] S. Stellmer, M. K. Tey, B. Huang, R. Grimm, and F. Schreck, "Bose-Einstein Condensation of Strontium", Physical Review Letters **103**, 200401 (2009).

[76] Y. N. M. de Escobar, P. G. Mickelson, M. Yan, B. J. DeSalvo, S. B. Nagel, and T. C. Killian, "Bose-Einstein Condensation of ^{84}Sr", Physical Review Letters **103**, 200402 (2009).

[77] P. G. Mickelson, Y. N. M. de Escobar, M. Yan, B. J. DeSalvo, and T. C. Killian, "Bose-Einstein condensation of ^{88}Sr through sympathetic cooling with ^{87}Sr", Physical Review A **81**, 051601 (2010).

[78] S. Stellmer, M. K. Tey, R. Grimm, and F. Schreck, "Bose-Einstein condensation of ^{86}Sr", Physical Review A **82**, 041602 (2010).

[79] S. Stellmer, R. Grimm, and F. Schreck, "Production of quantum-degenerate strontium gases", Physical Review A **87**, 013611 (2013).

[80] B. J. DeSalvo, M. Yan, P. G. Mickelson, Y. N. M. de Escobar, and T. C. Killian, "Degenerate Fermi Gas of ^{87}Sr", Physical Review Letters **105**, 030402 (2010).

[81] B. Butscher, V. Bendkowsky, J. Nipper, J. B. Balewski, L. Kukota, R. Löw, T. Pfau, W. Li, T. Pohl, and J. M. Rost, "Lifetimes of ultralong-range Rydberg molecules in vibrational ground and excited states", Journal of Physics B: Atomic, Molecular and Optical Physics **44**, 184004 (2011).

[82] E. L. Hamilton, C. H. Greene, and H. R. Sadeghpour, "Shape-resonance-induced long-range molecular Rydberg states", Journal of Physics B: Atomic, Molecular and Optical Physics **35**, L199–L206 (2002).

[83] J. D. Whalen, F. Camargo, R. Ding, T. C. Killian, F. B. Dunning, J. Pérez-Ríos, S. Yoshida, and J. Burgdörfer, "Lifetimes of ultralong-range strontium Rydberg molecules in a dense Bose-Einstein condensate", Physical Review A **96**, 042702 (2017).

[84] R. Ding, J. D. Whalen, S. K. Kanungo, T. C. Killian, F. B. Dunning, S. Yoshida, and J. Burgdörfer, "Spectroscopy of ^{87}Sr triplet Rydberg states", Physical Review A **98**, 042505 (2018).

[85] M. M. Boyd, "High Precision Spectroscopy of Strontium in an Optical Lattice: Towards a New Standard for Frequency and Time", Ph.D. Thesis (University of Colorado at Boulder, 2007).

[86] P. G. Mickelson, "Trapping and Evaporation of ^{87}Sr and ^{88}Sr Mixtures", Ph.D. Thesis (William Marsh Rice University, 2010).

[87] Y. N. M. de Escobar, "Bose-Einstein Condensation of ^{84}Sr", Ph.D. Thesis (William Marsh Rice University, 2012).

[88] D. Boddy, "First observations of Rydberg blockade in a frozen gas of divalent atoms", Ph.D. Thesis (Durham University, 2014).

[89] D. S. Barker, "Degenerate Gases of Strontium for Studies of Quantum Magnetism", en, Ph.D. Thesis (University of Maryland, 2016).

[90] S. L. Campbell, "A Fermi-degenerate three-dimensional optical lattice clock", Ph.D. Thesis (University of Colorado at Boulder, 2017).

[91] A. D. Ludlow, "The Strontium Optical Lattice Clock: Optical Spectroscopy with Sub-Hertz Accuracy", Ph.D. Thesis (University of Colorado at Boulder, 2008).

[92] M. Schioppo, N. Poli, M. Prevedelli, S. Falke, C. Lisdat, U. Sterr, and G. M. Tino, "A compact and efficient strontium oven for laser-cooling experiments", Review of Scientific Instruments **83**, 103101 (2012).

[93] R. Ding, "Narrow Line Cooling of ^{84}Sr", Master's Thesis (William Marsh Rice University, 2016).

[94] R. Senaratne, "Quantum Simulation of Strongly-Driven Systems Using Ultracold Lithium and Strontium", Ph.D. Thesis (University of California, Santa Barbara, June 2018).

[95] V. I. Balykin, V. S. Letokhov, and A. I. Sidorov, "Radiative collimation of an atomic beam by two-dimensional cooling by a laser beam", Journal of Experimental and Theoretical Physics Letters **40** (1984).

[96] V. I. Balykin, V. S. Letokhov, V. G. Minogin, Y. V. Rozhdestvensky, and A. I. Sidorov, "Radiative collimation of atomic beams through two-dimensional cooling of atoms by laser-radiation pressure", Journal of the Optical Society of America B **2**, 1776 (1985).

[97] P. D. Lett, W. D. Phillips, S. L. Rolston, C. E. Tanner, R. N. Watts, and C. I. Westbrook, "Optical molasses", Journal of the Optical Society of America B **6**, 2084 (1989).

[98] M. A. Joffe, W. Ketterle, A. Martin, and D. E. Pritchard, "Transverse cooling and deflection of an atomic beam inside a Zeeman slower", Journal of the Optical Society of America B **10**, 2257 (1993).

[99] M. D. Hoogerland, J. P. J. Driessen, E. J. D. Vredenbregt, H. J. L. Megens, M. P. Schuwer, H. C. W. Beijerinck, and K. A. H. van Leeuwen, "Bright thermal atomic beams by laser cooling: A 1400-fold gain in beam flux", Applied Physics B Laser and Optics **62**, 323–327 (1996).

[100] T. Yang, K. Pandey, M. S. Pramod, F. Leroux, C. C. Kwong, E. Hajiyev, Z. Y. Chia, B. Fang, and D. Wilkowski, "A high flux source of cold strontium atoms", The European Physical Journal D **69** (2015).

[101] S. Dörscher, A. Thobe, B. Hundt, A. Kochanke, R. L. Targat, P. Windpassinger, C. Becker, and K. Sengstock, "Creation of quantum-degenerate gases of ytterbium in a compact 2D-/3D-magneto-optical trap setup", Review of Scientific Instruments **84**, 043109 (2013).

[102] G. Lamporesi, S. Donadello, S. Serafini, and G. Ferrari, "Compact high-flux source of cold sodium atoms", Review of Scientific Instruments **84**, 063102 (2013).

[103] I. Nosske, L. Couturier, F. Hu, C. Tan, C. Qiao, J. Blume, Y. H. Jiang, P. Chen, and M. Weidemüller, "Two-dimensional magneto-optical trap as a source for cold strontium atoms", Physical Review A **96**, 053415 (2017).

[104] I. Nosske, L. Couturier, F. Hu, C. Tan, C. Qiao, J. Blume, Y. H. Jiang, P. Chen, and M. Weidemüller, "Erratum: Two-dimensional magneto-optical trap as a source for cold strontium atoms [Phys. Rev. A **96** , 053415 (2017)]", Physical Review A **97**, 039901 (2018).

[105] F. Camargo, "Strontium Laser Cooling and Trapping Apparatus", Master's Thesis (William Marsh Rice University, 2015).

[106] W. D. Phillips and H. Metcalf, "Laser Deceleration of an Atomic Beam", Physical Review Letters **48**, 596 (1982).

[107] C. J. Dedman, J. Nes, T. M. Hanna, R. G. Dall, K. G. H. Baldwin, and A. G. Truscott, "Optimum design and construction of a Zeeman slower for use with a magneto-optic trap", Review of Scientific Instruments **75**, 5136–5142 (2004).

[108] S. C. Bell, M. Junker, M. Jasperse, L. D. Turner, Y.-J. Lin, I. B. Spielman, and R. E. Scholten, "A slow atom source using a collimated effusive oven and a single-layer variable pitch coil Zeeman slower", Review of Scientific Instruments **81**, 013105 (2010).

[109] G. Reinaudi, C. B. Osborn, K. Bega, and T. Zelevinsky, "Dynamically configurable and optimizable Zeeman slower using permanent magnets and servomotors", Journal of the Optical Society of America B **29**, 729 (2012).

[110] I. R. Hill, Y. B. Ovchinnikov, E. M. Bridge, E. A. Curtis, and P. Gill, "Zeeman slowers for strontium based on permanent magnets", Journal of Physics B: Atomic, Molecular and Optical Physics **47**, 075006 (2014).

[111] V. Lebedev and D. M. Weld, "Self-assembled Zeeman slower based on spherical permanent magnets", Journal of Physics B: Atomic, Molecular and Optical Physics **47**, 155003 (2014).

[112] S. P. Krzyzewski, T. G. Akin, P. Dahal, and E. R. I. Abraham, "A clip-on Zeeman slower using toroidal permanent magnets", Review of Scientific Instruments **85**, 103104 (2014).

[113] B. Ohayon and G. Ron, "Investigation of different magnetic field configurations using an electrical, modular Zeeman slower", Review of Scientific Instruments **86**, 103110 (2015).

[114] S. A. Hopkins, K. Butler, A. Guttridge, S. Kemp, R. Freytag, E. A. Hinds, M. R. Tarbutt, and S. L. Cornish, "A versatile dual-species Zeeman slower for caesium and ytterbium", Review of Scientific Instruments **87**, 043109 (2016).

[115] E. L. Raab, M. Prentiss, A. Cable, S. Chu, and D. E. Pritchard, "Trapping of Neutral Sodium Atoms with Radiation Pressure", Physical Review Letters **59**, 2631 (1987).

[116] X. Xu, T. H. Loftus, J. W. Dunn, C. H. Greene, J. L. Hall, A. Gallagher, and J. Ye, "Single-Stage Sub-Doppler Cooling of Alkaline Earth Atoms", Physical Review Letters **90**, 193002 (2003).

[117] X. Xu, T. H. Loftus, J. L. Hall, A. Gallagher, and J. Ye, "Cooling and trapping of atomic strontium", Journal of the Optical Society of America B **20**, 968 (2003).

[118] T. Kisters, K. Zeiske, F. Riehle, and J. Helmcke, "High-resolution spectroscopy with laser-cooled and trapped calcium atoms", Applied Physics B Lasers and Optics **59**, 89–98 (1994).

[119] X. Xu, T. H. Loftus, M. J. Smith, J. L. Hall, A. Gallagher, and J. Ye, "Dynamics in a two-level atom magneto-optical trap", Physical Review A **66**, 011401 (2002).

[120] A. Cooper, J. P. Covey, I. S. Madjarov, S. G. Porsev, M. S. Safronova, and M. Endres, "Alkaline-Earth Atoms in Optical Tweezers", Physical Review X **8**, 041055 (2018).

[121] L. R. Hunter, W. A. Walker, and D. S. Weiss, "Observation of an Atomic Stark-Electric-Quadrupole Interference", Physical Review Letters **56**, 823 (1986).

[122] M. Yasuda and H. Katori, "Lifetime Measurement of the $^3P_2$ Metastable State of Strontium Atoms", Physical Review Letters **92**, 153004 (2004).

[123] T. Loftus, J. R. Bochinski, and T. W. Mossberg, "Magnetic trapping of ytterbium and the alkaline-earth metals", Physical Review A **66**, 013411 (2002).

[124] S. B. Nagel, C. E. Simien, S. Laha, P. Gupta, V. S. Ashoka, and T. C. Killian, "Magnetic trapping of metastable $^3P_2$ atomic strontium", Physical Review A **67**, 011401 (2003).

[125] D. S. Barker, B. J. Reschovsky, N. C. Pisenti, and G. K. Campbell, "Enhanced magnetic trap loading for atomic strontium", Physical Review A **92**, 043418 (2015).

[126] I. Courtillot, A. Quessada-Vial, A. Brusch, D. Kolker, G. D. Rovera, and P. Lemonde, "Accurate spectroscopy of Sr atoms", The European Physical Journal D **33**, 161–171 (2005).

[127] P. G. Mickelson, Y. N. M. de Escobar, P. Anzel, B. J. DeSalvo, S. B. Nagel, A. J. Traverso, M. Yan, and T. C. Killian, "Repumping and spectroscopy of laser-cooled Sr atoms using the $(5s5p)^3P_2$-$(5s4d)^3D_2$ transition", Journal of Physics B: Atomic, Molecular and Optical Physics **42**, 235001 (2009).

[128] S. Stellmer and F. Schreck, "Reservoir spectroscopy of $5s5p\,^3P_2 - 5snd\,^3D_{1,2,3}$ transitions in strontium", Physical Review A **90**, 022512 (2014).

[129] P. H. Moriya, M. O. Araújo, F. Todão, M. Hemmerling, H. Keßler, R. F. Shiozaki, R. C. Teixeira, and P. W. Courteille, "Comparison between 403 nm and 497 nm repumping schemes for strontium magneto-optical traps", Journal of Physics Communications **2**, 125008 (2018).

[130] E. Mason, "Generation of Repumping Light for Ultracold Strontium Experiments", Bachelor's Thesis (University of California, Santa Barbara, 2013).

[131] P. Wongwaitayakornkul, "A Tellurium Frequency Reference For Re-pumping During Laser-cooling of Strontium", Bachelor's Thesis (William Marsh Rice University, 2013).

[132] L. Couturier, I. Nosske, F. Hu, C. Tan, C. Qiao, Y. H. Jiang, P. Chen, and M. Weidemüller, "Laser frequency stabilization using a commercial wavelength meter", Review of Scientific Instruments **89**, 043103 (2018).

[133] F. Hu, I. Nosske, L. Couturier, C. Tan, C. Qiao, P. Chen, Y. H. Jiang, B. Zhu, and M. Weidemüller, "Analyzing a single-laser repumping scheme for efficient loading of a strontium magneto-optical trap", Physical Review A **99**, 033422 (2019).

[134] S. M. Heider and G. O. Brink, "Hyperfine structure of ^{87}Sr in the $^3P_2$ metastable state", Physical Review A **16**, 1371 (1977).

[135] M. A. Norcia, A. W. Young, and A. M. Kaufman, "Microscopic Control and Detection of Ultracold Strontium in Optical-Tweezer Arrays", Physical Review X **8**, 041054 (2018).

[136] R. K. Hanley, "Creation of a strontium microtrap: Towards a spin-squeezed atomic clock", Ph.D. Thesis (Durham University, 2018).

[137] N. C. Jackson, R. K. Hanley, M. Hill, C. S. Adams, and M. P. A. Jones, "Number-resolved imaging of ^{88}Sr atoms in a long working distance optical tweezer", arXiv:1904.03233 (2019).

[138] W. Bowden, R. Hobson, I. R. Hill, A. Vianello, M. Schioppo, A. Silva, H. S. Margolis, P. E. G. Baird, and P. Gill, "A pyramid mot with integrated optical cavities as a cold atom platform for an optical lattice clock", arXiv:1907.13429 (2019).

[139] T. H. Loftus, T. Ido, M. M. Boyd, A. D. Ludlow, and J. Ye, "Narrow line cooling and momentum-space crystals", Physical Review A **70**, 063413 (2004).

[140] T. Mukaiyama, H. Katori, T. Ido, Y. Li, and M. Kuwata-Gonokami, "Recoil-Limited Laser Cooling of ^{87}Sr Atoms near the Fermi Temperature", Physical Review Letters **90**, 113002 (2003).

[141] M. A. Norcia, "New tools for precision measurement and quantum science with narrow linewidth optical transitions", Ph.D. Thesis (University of Colorado, 2018).

[142] M. A. Norcia, J. R. K. Cline, J. P. Bartolotta, M. J. Holland, and J. K. Thompson, "Narrow-line laser cooling by adiabatic transfer", New Journal of Physics **20**, 023021 (2018).

[143] J. P. Bartolotta, M. A. Norcia, J. R. K. Cline, J. K. Thompson, and M. J. Holland, "Laser cooling by sawtooth-wave adiabatic passage", Physical Review A **98**, 023404 (2018).

[144] J. A. Muniz, M. A. Norcia, J. R. K. Cline, and J. K. Thompson, "A Robust Narrow-Line Magneto-Optical Trap using Adiabatic Transfer", arXiv:1806.00838 (2018).

[145] S. Snigirev, A. J. Park, A. Heinz, I. Bloch, and S. Blatt, "Fast and dense magneto-optical traps for strontium", Physical Review A **99**, 063421 (2019).

[146] D. S. Barker, N. C. Pisenti, B. J. Reschovsky, and G. K. Campbell, "Three-photon process for producing a degenerate gas of metastable alkaline-earth-metal atoms", Physical Review A **93**, 053417 (2016).

[147] A. Robert, O. Sirjean, A. Browaeys, J. Poupard, S. Nowak, D. Boiron, C. I. Westbrook, and A. Aspect, "A Bose-Einstein Condensate of Metastable Atoms", Science **292**, 461–464 (2001).

[148] F. P. D. Santos, J. Léonard, J. Wang, C. J. Barrelet, F. Perales, E. Rasel, C. S. Unnikrishnan, M. Leduc, and C. Cohen-Tannoudji, "Bose-Einstein Condensation of Metastable Helium", Physical Review Letters **86**, 3459 (2001).

[149] J. M. McNamara, T. Jeltes, A. S. Tychkov, W. Hogervorst, and W. Vassen, "Degenerate Bose-Fermi Mixture of Metastable Atoms", Physical Review Letters **97**, 080404 (2006).

[150] R. Grimm, M. Weidemüller, and Y. B. Ovchinnikov, "Optical dipole traps for neutral atoms", Feb. 24, 1999.

[151] H. Katori, T. Ido, and M. Kuwata-Gonokami, "Optimal Design of Dipole Potentials for Efficient Loading of Sr Atoms", Journal of the Physical Society of Japan **68**, 2479–2482 (1999).

[152] J. Ye, H. J. Kimble, and H. Katori, "Quantum State Engineering and Precision Metrology Using State-Insensitive Light Traps", Science **320**, 1734–1738 (2008).

[153] N. D. Oppong, "Towards a degenerate Fermi gas of strontium-87 in a 3D optical lattice", Master's Thesis (University of Colorado at Boulder, 2015).

[154] A. Stein, H. Knöckel, and E. Tiemann, "The $^1S + {}^1S$ asymptote of Sr_2 studied by Fourier-transform spectroscopy", The European Physical Journal D **57**, 171–177 (2010).

[155] N. Poli, R. E. Drullinger, G. Ferrari, J. Léonard, F. Sorrentino, and G. M. Tino, "Cooling and trapping of ultracold strontium isotopic mixtures", Physical Review A **71**, 061403 (2005).

[156] G. Ferrari, R. E. Drullinger, N. Poli, F. Sorrentino, and G. M. Tino, "Cooling of Sr to high phase-space density by laser and sympathetic cooling in isotopic mixtures", Physical Review A **73**, 023408 (2006).

[157] A. D. Ludlow, M. M. Boyd, J. Ye, E. Peik, and P. O. Schmidt, "Optical atomic clocks", Reviews of Modern Physics **87**, 637 (2015).

[158] R. Mukherjee, J. Millen, R. Nath, M. P. A. Jones, and T. Pohl, "Many-body physics with alkaline-earth Rydberg lattices", Journal of Physics B: Atomic, Molecular and Optical Physics **44**, 184010 (2011).

[159] T. Topcu and A. Derevianko, "Possibility of triple magic trapping of clock and Rydberg states of divalent atoms in optical lattices", Journal of Physics B: Atomic, Molecular and Optical Physics **49**, 144004 (2016).

[160] R. Senaratne, S. V. Rajagopal, Z. A. Geiger, K. M. Fujiwara, V. Lebedev, and D. M. Weld, "Effusive atomic oven nozzle design using an aligned microcapillary array", Review of Scientific Instruments **86**, 023105 (2015).

[161] P. Cheiney, O. Carraz, D. Bartoszek-Bober, S. Faure, F. Vermersch, C. M. Fabre, G. L. Gattobigio, T. Lahaye, D. Guéry-Odelin, and R. Mathevet, "A Zeeman slower

design with permanent magnets in a Halbach configuration", Review of Scientific Instruments **82**, 063115 (2011).

[162] Y. Shimada, Y. Chida, N. Ohtsubo, T. Aoki, M. Takeuchi, T. Kuga, and Y. Torii, "A simplified 461-nm laser system using blue laser diodes and a hollow cathode lamp for laser cooling of Sr", Review of Scientific Instruments **84**, 063101 (2013).

[163] T. Hosoya, M. Miranda, R. Inoue, and M. Kozuma, "Injection locking of a high power ultraviolet laser diode for laser cooling of ytterbium atoms", Review of Scientific Instruments **86**, 073110 (2015).

[164] J. Cariou and P. Luc, *Atlas du spectre d'absorption de la molecule de tellure, Partie 2: 18500-21200 cm^{-1}* (Laboratoire Aime-Cotton CNRS II, 1980).

[165] J. E. Sansonetti and G. Nave, "Wavelengths, Transition Probabilities, and Energy Levels for the Spectrum of Neutral Strontium (Sr I)", Journal of Physical and Chemical Reference Data **39**, 033103 (2010).

[166] L.-S. Ma, P. Jungner, J. Ye, and J. L. Hall, "Delivering the same optical frequency at two places: accurate cancellation of phase noise introduced by an optical fiber or other time-varying path", Optics Letters **19**, 1777 (1994).

[167] B. Rauf, M. C. V. López, P. Thoumany, M. Pizzocaro, and D. Calonico, "Phase noise cancellation in polarisation-maintaining fibre links", Review of Scientific Instruments **89**, 033103 (2018).

[168] A. Mazurenko, "Probing Long Range Antiferromagnetism and Dynamics in the Fermi-Hubbard Model", Ph.D. Thesis (Harvard University, 2017).

[169] A. Mazurenko, S. Blatt, F. Huber, M. F. Parsons, C. S. Chiu, G. Ji, D. Greif, and M. Greiner, "Implementation of a stable, high-power optical lattice for quantum gas microscopy", Review of Scientific Instruments **90**, 033101 (2019).

[170] T. Ido and H. Katori, "Recoil-Free Spectroscopy of Neutral Sr Atoms in the Lamb-Dicke Regime", Physical Review Letters **91**, 053001 (2003).

[171] S. Mieth, A. Henderson, and T. Halfmann, "Tunable, continuous-wave optical parametric oscillator with more than 1W output power in the orange visible spectrum", Optics Express **22**, 11182 (2014).

[172] B. J. DeSalvo, "Ultralong-Range Molecules and Rydberg Blockade in Ultracold ^{84}Sr", Ph.D. Thesis (William Marsh Rice University, 2015).

[173] E. Riedle, S. H. Ashworth, J. T. Farrell, and D. J. Nesbitt, "Stabilization and precise calibration of a continuous-wave difference frequency spectrometer by use of a simple transfer cavity", Review of Scientific Instruments **65**, 42–48 (1994).

[174] P. Bohlouli-Zanjani, K. Afrousheh, and J. D. D. Martin, "Optical transfer cavity stabilization using current-modulated injection-locked diode lasers", Review of Scientific Instruments **77**, 093105 (2006).

[175] T. Leopold, L. Schmöger, S. Feuchtenbeiner, C. Grebing, P. Micke, N. Scharnhorst, I. D. Leroux, J. R. C. López-Urrutia, and P. O. Schmidt, "A tunable low-drift laser stabilized to an atomic reference", Applied Physics B **122** (2016).

[176] C. G. Zha, "Characterizing a Fabry-Perot Transfer Cavity", Bachelor's Thesis (William Marsh Rice University, 2013).

[177] R. W. P. Drever, J. L. Hall, F. V. Kowalski, J. Hough, G. M. Ford, A. J. Munley, and H. Ward, "Laser phase and frequency stabilization using an optical resonator", Applied Physics B Photophysics and Laser Chemistry **31**, 97–105 (1983).

[178] E. D. Black, "An introduction to Pound-Drever-Hall laser frequency stabilization", American Journal of Physics **69**, 79–87 (2001).

[179] P. D. Gregory, P. K. Molony, M. P. Köppinger, A. Kumar, Z. Ji, B. Lu, A. L. Marchant, and S. L. Cornish, "A simple, versatile laser system for the creation of ultracold ground state molecules", New Journal of Physics **17**, 055006 (2015).

[180] F. Camargo, "Rydberg Molecules and Polarons in Ultracold Strontium Gases", Ph.D. Thesis (William Marsh Rice University, Apr. 2017).

[181] B. J. DeSalvo, J. A. Aman, C. Gaul, T. Pohl, S. Yoshida, J. Burgdörfer, K. R. A. Hazzard, F. B. Dunning, and T. C. Killian, "Rydberg-blockade effects in Autler-Townes spectra of ultracold strontium", Physical Review A **93**, 022709 (2016).

[182] J. A. Aman, B. J. DeSalvo, F. B. Dunning, T. C. Killian, S. Yoshida, and J. Burgdörfer, "Trap losses induced by near-resonant Rydberg dressing of cold atomic gases", Physical Review A **93**, 043425 (2016).

[183] T. Pyragius, "Developing and building an absorption imaging system for Ultracold Atoms", arXiv preprint arXiv:1209.3408 (2012).

[184] I. Yavin, M. Weel, A. Andreyuk, and A. Kumarakrishnan, "A calculation of the time-of-flight distribution of trapped atoms", American Journal of Physics **70**, 149–152 (2002).

[185] G. Reinaudi, T. Lahaye, Z. Wang, and D. Guéry-Odelin, "Strong saturation absorption imaging of dense clouds of ultracold atoms", Optics Letters **32**, 3143 (2007).

[186] K. Hueck, N. Luick, L. Sobirey, J. Siegl, T. Lompe, H. Moritz, L. W. Clark, and C. Chin, "Calibrating high intensity absorption imaging of ultracold atoms", Optics Express **25**, 8670 (2017).

[187] P. Esherick, "Bound, even-parity $J = 0$ and $J = 2$ spectra of Sr", Physical Review A **15**, 1920 (1977).

[188] R. Beigang, K. Lücke, A. Timmermann, P. J. West, and D. Frölich, "Determination of absolute level energies of $5sns\ ^1\mathrm{S}_0$ and $5snd\ ^1\mathrm{D}_2$ Rydberg series of Sr", Optics Communications **42**, 19–24 (1982).

[189] R. Beigang, K. Lücke, D. Schmidt, A. Timmermann, and P. J. West, "One-Photon Laser Spectroscopy of Rydberg Series from Metastable Levels in Calcium and Strontium", Physica Scripta **26**, 183–188 (1982).

[190] S. Kunze, R. Hohmann, H.-J. Kluge, J. Lantzsch, L. Monz, J. Stenner, K. Stratmann, K. Wendt, and K. Zimmer, "Lifetime measurements of highly excited Rydberg states

of strontium I", Zeitschrift für Physik D Atoms, Molecules and Clusters **27**, 111–114 (1993).

[191] C. J. Dai and X. A. Zhao, "Study of Sr $5sns\ ^1S_0$ Rydberg series", Journal of Quantitative Spectroscopy and Radiative Transfer **54**, 1019–1025 (1995).

[192] C. J. Dai, "Perturbed $5snd\ ^{1,3}D_2$ Rydberg series of Sr", Physical Review A **52**, 4416 (1995).

[193] G. Philip and J.-P. Connerade, "The controlled excitation of forbidden transitions in the two-photon spectrum of strontium by using collisions and electric fields", Optics Communications **279**, 141–149 (2007).

[194] N. C. Jackson, "Rydberg spectroscopy and dressing in an ultracold strontium gas", Ph.D. Thesis (Durham University, 2018).

[195] R. Beigang, E. Matthias, and A. Timmermann, "Odd-Even Staggering of Isotope Shifts in the $5sns\ ^1\mathrm{S}_0$ Rydberg Series of Strontium", Zeitschrift für Physik A Atoms and Nuclei **301**, 93–94 (1981).

[196] R. Beigang, E. Matthias, and A. Timmermann, "Influence of Singlet-Triplet Mixing on the Hyperfine Structure of $5snd$ Rydberg States in ^{87}Sr", Physical Review Letters **47**, 326 (1981).

[197] R. Beigang, E. Matthias, and A. Timmermann, "Influence of Singlet-Triplet Mixing on the Hyperfine Structure of $5snd$ Rydberg States in ^{87}Sr", Physical Review Letters **48**, 290 (1982).

[198] R. Beigang and A. Timmermann, "Level shifts of $msns$ Rydberg states induced by hyperfine interaction in odd alkaline-earth isotopes", Physical Review A **25**, 1496 (1982).

[199] R. Beigang, W. Makat, A. Timmermann, and P. J. West, "Hyperfine-Induced n Mixing in High Rydberg States of ^{87}Sr", Physical Review Letters **51**, 771 (1983).

[200] M. A. Zucker, A. R. Kishore, R. Sukumar, and R. A. Dragoset, *Elemental Data Index*, version 2.5, National Institute of Standards and Technology, (Dec. 2015) `http://physics.nist.gov/EDI`.

[201] G. K. Woodgate, *Elementary Atomic Structure* (OXFORD UNIV PR, Aug. 11, 1983), 238 pp.

[202] E. Arimondo, M. Inguscio, and P. Violino, "Experimental determinations of the hyperfine structure in the alkali atoms", Reviews of Modern Physics **49**, 31 (1977).

[203] H. Sunaoshi, Y. Fukashiro, M. Furukawa, M. Yamauchi, S. Hayashibe, T. Shinozuka, M. Fujioka, I. Satoh, M. Wada, and S. Matsuki, "A precision measurement of the hyperfine structure of $^{87}Sr^{+}$", Hyperfine Interactions **78**, 241–245 (1993).

[204] W. Li, T. Pohl, J. M. Rost, S. T. Rittenhouse, H. R. Sadeghpour, J. Nipper, B. Butscher, J. B. Balewski, V. Bendkowsky, R. Löw, and T. Pfau, "A Homonuclear Molecule with a Permanent Electric Dipole Moment", Science **334**, 1110–1114 (2011).

[205] M. A. Bellos, R. Carollo, J. Banerjee, E. E. Eyler, P. L. Gould, and W. C. Stwalley, "Excitation of Weakly Bound Molecules to Trilobitelike Rydberg States", Physical Review Letters **111**, 053001 (2013).

[206] H. Saßmannshausen, F. Merkt, and J. Deiglmayr, "Experimental Characterization of Singlet Scattering Channels in Long-Range Rydberg Molecules", Physical Review Letters **114**, 133201 (2015).

[207] A. T. Krupp, A. Gaj, J. B. Balewski, P. Ilzhöfer, S. Hofferberth, R. Löw, T. Pfau, M. Kurz, and P. Schmelcher, "Alignment of D-State Rydberg Molecules", Physical Review Letters **112**, 143008 (2014).

[208] D. A. Anderson, S. A. Miller, and G. Raithel, "Photoassociation of Long-range nD Rydberg Molecules", Physical Review Letters **112**, 163201 (2014).

[209] D. Booth, S. T. Rittenhouse, J. Yang, H. R. Sadeghpour, and J. P. Shaffer, "Production of trilobite Rydberg molecule dimers with kilo-Debye permanent electric dipole moments", Science **348**, 99–102 (2015).

[210] M. T. Eiles and C. H. Greene, "Ultracold Long-Range Rydberg Molecules with Complex Multichannel Spectra", Physical Review Letters **115**, 193201 (2015).

[211] M. T. Eiles, H. Lee, J. Pérez-Ríos, and C. H. Greene, "Anisotropic blockade using pendular long-range Rydberg molecules", Physical Review A **95**, 052708 (2017).

[212] F. B. Dunning, T. C. Killian, S. Yoshida, and J. Burgdörfer, "Recent advances in Rydberg physics using alkaline-earth atoms", Journal of Physics B: Atomic, Molecular and Optical Physics **49**, 112003 (2016).

[213] K. S. Kleinbach, F. Engel, T. Dieterle, R. Löw, T. Pfau, and F. Meinert, "Ionic impurity in a Bose-Einstein Condensate at Submicrokelvin Temperatures", Physical Review Letters **120**, 193401 (2018).

[214] R. Beigang, "High-resolution Rydberg-state spectroscopy of stable alkaline-earth elements", Journal of the Optical Society of America B **5**, 2423 (1988).

[215] J.-Q. Sun, K. T. Lu, and R. Beigang, "Hyperfine structure of extremely high Rydberg msnd ^{1}D$_2$, ^{3}D$_1$, ^{3}D$_2$ and ^{3}D$_3$ series in odd alkaline-earth isotopes", Journal of Physics B: Atomic, Molecular and Optical Physics **22**, 2887–2901 (1989).

[216] R. Beigang, D. Schmidt, and A. Timmermann, "Hyperfine induced perturbation of the 5s19d Rydberg state of ^{87}Sr", Journal of Physics B: Atomic and Molecular Physics **15**, L201–L206 (1982).

[217] D. R. Cok and S. R. Lundeen, "Magnetic and electric fine structure in helium Rydberg states", Physical Review A **19**, 1830 (1979).

[218] D. R. Cok and S. R. Lundeen, "Erratum: Magnetic and electric fine structure in helium Rydberg states", Physical Review A **24**, 3283 (1981).

[219] T. van der Veldt, W. Vassen, and W. Hogervorst, "Mass-polarization effects in the $1s2s$ ^1S and ^3S states of helium", Physical Review A **41**, 4099 (1990).

[220] C. Schwartz, "Theory of Hyperfine Structure", Physical Review **97**, 380 (1955).

[221] J. Güdde, A. Klinkmüller, P. J. West, and E. Matthias, "Second-order magnetic contributions to the hyperfine splitting of the $5snd$ $^1D_2$ states in ^{87}Sr", Physical Review A **47**, 4725 (1993).

[222] G. Fields, X. Zhang, F. B. Dunning, S. Yoshida, and J. Burgdörfer, "Autoionization of very-high-n strontium Rydberg states", Physical Review A **97**, 013429 (2018).

[223] A. Lurio, M. Mandel, and R. Novick, "Second-Order Hyperfine and Zeeman Corrections for an (sl) Configuration", Physical Review **126**, 1758 (1962).

[224] S. A. Bhatti, C. L. Cromer, and W. E. Cooke, "Analysis of the Rydberg character of the $5d7d$ $^1D_2$ state of barium", Physical Review A **24**, 161 (1981).

[225] G. Ferrari, P. Cancio, R. Drullinger, G. Giusfredi, N. Poli, M. Prevedelli, C. Toninelli, and G. M. Tino, "Precision Frequency Measurement of Visible Intercombination Lines of Strontium", Physical Review Letters **91**, 243002 (2003).

[226] C. J. Sansonetti, C. E. Simien, J. D. Gillaspy, J. N. Tan, S. M. Brewer, R. C. Brown, S. Wu, and J. V. Porto, "Absolute Transition Frequencies and Quantum Interference in a Frequency Comb Based Measurement of the ^{6,7}Li D Lines", Physical Review Letters **107**, 023001 (2011).

[227] C. J. Sansonetti, C. E. Simien, J. D. Gillaspy, J. N. Tan, S. M. Brewer, R. C. Brown, S. Wu, and J. V. Porto, "Erratum: Absolute Transition Frequencies and Quantum Interference in a Frequency Comb Based Measurement of the ^{6,7}Li D Lines [Phys. Rev. Lett. **107**, 023001 (2011)]", Physical Review Letters **109**, 259901 (2012).

[228] L. J. Radziemski, R. Engleman, and J. W. Brault, "Fourier-transform-spectroscopy measurements in the spectra of neutral lithium, ^{6}Li I and ^{7}Li I (Li I)", Physical Review A **52**, 4462 (1995).

[229] J. Millen, G. Lochead, G. R. Corbett, R. M. Potvliege, and M. P. A. Jones, "Spectroscopy of a cold strontium Rydberg gas", Journal of Physics B: Atomic, Molecular and Optical Physics **44**, 184001 (2011).

[230] E. M. Bridge, N. C. Keegan, A. D. Bounds, D. Boddy, D. P. Sadler, and M. P. A. Jones, "Tunable cw UV laser with < 35 kHz absolute frequency instability for precision spectroscopy of Sr Rydberg states", Optics Express **24**, 2281 (2016).

[231] I. I. Sobelman, *Atomic Spectra and Radiative Transitions* (Springer-Verlag, 1992), 376 pp.

[232] C. J. Sansonetti, "Precise measurements of hyperfine components in the spectrum of molecular iodine", Journal of the Optical Society of America B **14**, 1913 (1997).

[233] P. M. Duarte, R. A. Hart, J. M. Hitchcock, T. A. Corcovilos, T.-L. Yang, A. Reed, and R. G. Hulet, "All-optical production of a lithium quantum gas using narrow-line laser cooling", Physical Review A **84**, 061406 (2011).

[234] Y.-C. Huang, Y.-C. Guan, T.-H. Suen, J.-T. Shy, and L.-B. Wang, "Absolute frequency measurement of molecular iodine hyperfine transitions at 647 nm", Applied Optics **57**, 2102 (2018).

[235] M. Naraschewski and R. J. Glauber, "Spatial coherence and density correlations of trapped bose gases", Physical Review A **59**, 4595 (1999).

[236] T. Kinoshita, T. Wenger, and D. S. Weiss, "Observation of a One-Dimensional Tonks-girardeau Gas", Science **305**, 1125–1128 (2004).

[237] M. Schellekens, R. Hoppeler, A. Perrin, J. V. Gomes, D. Boiron, A. Aspect, and C. I. Westbrook, "Hanbury Brown Twiss Effect for Ultracold Quantum Gases", Science **310**, 648–651 (2005).

[238] T. Jeltes, J. M. McNamara, W. Hogervorst, W. Vassen, V. Krachmalnicoff, M. Schellekens, A. Perrin, H. Chang, D. Boiron, A. Aspect, and C. I. Westbrook, "Comparison of the Hanbury Brown-Twiss effect for bosons and fermions", Nature **445**, 402–405 (2007).

[239] S. S. Hodgman, R. G. Dall, A. G. Manning, K. G. H. Baldwin, and A. G. Truscott, "Direct measurement of long-range third-order coherence in bose-einstein condensates", Science **331**, 1046–1049 (2011).

[240] E. A. Burt, R. W. Ghrist, C. J. Myatt, M. J. Holland, E. A. Cornell, and C. E. Wieman, "Coherence, Correlations, and Collisions: What One Learns about Bose-Einstein Condensates from Their Decay", Physical Review Letters **79**, 337 (1997).

[241] K. M. Jones, E. Tiesinga, P. D. Lett, and P. S. Julienne, "Ultracold photoassociation spectroscopy: Long-range molecules and atomic scattering", Reviews of Modern Physics **78**, 483–535 (2006).

[242] K. M. Jones, E. Tiesinga, P. D. Lett, and P. S. Julienne, "Publisher's Note: Ultracold photoassociation spectroscopy: Long-range molecules and atomic scattering [Rev. Mod. Phys. **78**, 483 (2006)]", Reviews of Modern Physics **78**, 1041 (2006).

[243] W. S. Bakr, A. Peng, M. E. Tai, R. Ma, J. Simon, J. I. Gillen, S. Folling, L. Pollet, and M. Greiner, "Probing the Superfluid-to-Mott Insulator Transition at the Single-Atom Level", Science **329**, 547–550 (2010).

[244] A. Omran, M. Boll, T. A. Hilker, K. Kleinlein, G. Salomon, I. Bloch, and C. Gross, "Microscopic Observation of Pauli Blocking in Degenerate Fermionic Lattice Gases", Physical Review Letters **115**, 263001 (2015).

[245] A. Mazurenko, C. S. Chiu, G. Ji, M. F. Parsons, M. Kanász-Nagy, R. Schmidt, F. Grusdt, E. Demler, D. Greif, and M. Greiner, "A cold-atom fermi–hubbard antiferromagnet", Nature (London) **545**, 462–466 (2017).

[246] M. Schellekens, "The Hanbury Brown and Twiss Effect for Cold Atoms", Ph.D. Thesis (Laboratoire Charles Fabry de l'Institut d'Optique, 2007).

[247] T. Jeltes, "Quantum Statistical Effects in Ultracold Gases of Metastable Helium", Ph.D. Thesis (Vrije Universiteit Amsterdam, 2008).

[248] V. Krachmalnicof, "Two experiments on quantum correlations in gases of metastable helium: fermion antibunching and a study of boson pair correlations in the collision of two condensates", Ph.D. Thesis (Université Paris Sud - Paris XI, 2009).

[249] J. D. Whalen, S. K. Kanungo, R. Ding, M. Wagner, R. Schmidt, H. R. Sadeghpour, S. Yoshida, J. Burgdörfer, F. B. Dunning, and T. C. Killian, "Probing nonlocal spatial correlations in quantum gases with ultra-long-range Rydberg molecules", Physical Review A **100**, 011402 (2019).

[250] E. R. I. Abraham, W. I. McAlexander, J. M. Gerton, R. G. Hulet, R. Côté, and A. Dalgarno, "Singlet s-wave scattering lengths of ^{6}Li and ^{7}Li", Physical Review A **53**, R3713–R3715 (1996).

[251] J. Sous, H. R. Sadeghpour, T. C. Killian, E. Demler, and R. Schmidt, "Rydberg impurity in a Fermi gas: Quantum statistics and rotational blockade", arXiv:1907.07685 (2019).

[252] J. E. Johnson and S. L. Rolston, "Interactions between Rydberg-dressed atoms", Physical Review A **82**, 033412 (2010).

[253] J. Honer, H. Weimer, T. Pfau, and H. P. Büchler, "Collective Many-Body Interaction in Rydberg Dressed Atoms", Physical Review Letters **105**, 160404 (2010).

[254] J. B. Balewski, A. T. Krupp, A. Gaj, S. Hofferberth, R. Löw, and T. Pfau, "Rydberg dressing: understanding of collective many-body effects and implications for experiments", New Journal of Physics **16**, 063012 (2014).

[255] C. Gaul, B. J. DeSalvo, J. A. Aman, F. B. Dunning, T. C. Killian, and T. Pohl, "Resonant Rydberg Dressing of Alkaline-Earth Atoms via Electromagnetically Induced Transparency", Physical Review Letters **116**, 243001 (2016).

[256] S. Helmrich, A. Arias, N. Pehoviak, and S. Whitlock, "Two-body interactions and decay of three-level Rydberg-dressed atoms", Journal of Physics B: Atomic, Molecular and Optical Physics **49**, 03LT02 (2016).

[257] F. Maucher, N. Henkel, M. Saffman, W. Królikowski, S. Skupin, and T. Pohl, "Rydberg-Induced Solitons: Three-Dimensional Self-Trapping of Matter Waves", Physical Review Letters **106**, 170401 (2011).

[258] G. Pupillo, A. Micheli, M. Boninsegni, I. Lesanovsky, and P. Zoller, "Strongly Correlated Gases of Rydberg-Dressed Atoms: Quantum and Classical Dynamics", Physical Review Letters **104** (2010).

[259] A. Arias, G. Lochead, T. M. Wintermantel, S. Helmrich, and S. Whitlock, "Realization of a Rydberg-Dressed Ramsey Interferometer and Electrometer", Physical Review Letters **122**, 053601 (2019).

[260] Y.-Y. Jau, A. M. Hankin, T. Keating, I. H. Deutsch, and G. W. Biedermann, "Entangling atomic spins with a Rydberg-dressed spin-flip blockade", Nature Physics **12**, 71–74 (2015).

[261] J. Zeiher, R. van Bijnen, P. Schauß, S. Hild, J.-y. Choi, T. Pohl, I. Bloch, and C. Gross, "Many-body interferometry of a Rydberg-dressed spin lattice", Nature Physics **12**, 1095–1099 (2016).

[262] E. A. Goldschmidt, T. Boulier, R. C. Brown, S. B. Koller, J. T. Young, A. V. Gorshkov, S. L. Rolston, and J. V. Porto, "Anomalous Broadening in Driven Dissipative Rydberg Systems", Physical Review Letters **116**, 113001 (2016).

[263] T. Boulier, E. Magnan, C. Bracamontes, J. Maslek, E. A. Goldschmidt, J. T. Young, A. V. Gorshkov, S. L. Rolston, and J. V. Porto, "Spontaneous avalanche dephasing in large Rydberg ensembles", Physical Review A **96**, 053409 (2017).

[264] A. Franzen, *Componentlibrary*, http://www.gwoptics.org/ComponentLibrary/, 2006.

[265] J. S. Coursey, D. J. Schwab, J. J. Tsai, and R. A. Dragoset, *Atomic Weights and Isotopic Compositions*, version 4.1, National Institute of Standards and Technology, (2015) `http://physics.nist.gov/Comp`.

[266] M. Wang, G. Audi, A. H. Wapstra, F. G. Kondev, M. MacCormick, X. Xu, and B. Pfeiffer, "The Ame2012 atomic mass evaluation", Chinese Physics C **36**, 1603–2014 (2012).

[267] R. Rana, M. Höcker, and E. G. Myers, "Atomic masses of strontium and ytterbium", Physical Review A **86**, 050502 (2012).

[268] M. Wang, G. Audi, F. G. Kondev, W. J. Huang, S. Naimi, and X. Xu, "The AME2016 atomic mass evaluation (II). Tables, graphs and references", Chinese Physics C **41**, 030003 (2017).

[269] Y. N. Martinez de Escobar, P. G. Mickelson, P. Pellegrini, S. B. Nagel, A. Traverso, M. Yan, R. Côté, and T. C. Killian, "Two-photon photoassociative spectroscopy of ultracold ^{88}Sr", Physical Review A **78**, 062708 (2008).

[270] J. A. Aman, J. C. Hill, R. Ding, K. R. A. Hazzard, T. C. Killian, and W. Y. Kon, "Photoassociative spectroscopy of a halo molecule in ^{86}Sr", Physical Review A **98**, 053441 (2018).

[271] E. R. Eliel, W. Hogervorst, T. Olsson, and L. R. Pendrill, "High resolution laser spectroscopy of low-lying p-states in Sr I and Ba I", Zeitschrift für Physik A Atoms and Nuclei **311**, 1–6 (1983).

[272] F. Buchinger, R. Corriveau, E. B. Ramsay, D. Berdichevsky, and D. W. L. Sprung, "Influence of the $N = 50$ shell closure on mean square charge radii of strontium", Physical Review C **32**, 2058 (1985).

[273] B. A. Bushaw and W. Nörtershäuser, "Resonance ionization spectroscopy of stable strontium isotopes and ^{90}Sr via $5s^2\ {}^1S_0 \rightarrow 5s5p\ {}^1P_1 \rightarrow 5s5d\ {}^1D_2 \rightarrow 5s11f\ {}^1F_3 \rightarrow Sr^+$", Spectrochimica Acta Part B: Atomic Spectroscopy **55**, 1679–1692 (2000).

[274] H.-J. Kluge and H. Sauter, "Levelcrossing Experiments in the First Excited $^1P_1$ States of the Alkaline Earths", Zeitschrift für Physik **270**, 295–309 (1974).

[275] T. Ido, T. H. Loftus, M. M. Boyd, A. D. Ludlow, K. W. Holman, and J. Ye, "Precision Spectroscopy and Density-Dependent Frequency Shifts in Ultracold Sr", Physical Review Letters **94**, 153001 (2005).

[276] L. Hui, G. Feng, W. Ye-Bing, T. Xiao, R. Jie, L. Ben-Quan, X. Qin-Fang, X. Yu-Lin, and C. Hong, "Precision frequency measurement of $^1S_0$-$^3P_1$ intercombination lines of Sr isotopes", Chinese Physics B **24**, 013201 (2015).

[277] P. J. Mohr, D. B. Newell, and B. N. Taylor, "CODATA recommended values of the fundamental physical constants: 2014", Reviews of Modern Physics **88**, 035009 (2016).

[278] E. Tiesinga, P. J. Mohr, D. B. Newell, and B. N. Taylor, *The 2018 CODATA Recommended Values of the Fundamental Physical Constants*, version 8.0, National Institute of Standards and Technology, (2) `http://physics.nist.gov/constants`.